UNIVERSITY *of the*
WESTERN CAPE

INVESTIGATION OF THE ACOUSTIC IMPEDANCE VARIATIONS OF THE UPPER SHALLOW MARINE SANDSTONE RESERVOIRS IN THE BREDASDORP BASIN, OFFSHORE SOUTH AFRICA

A Thesis in Petroleum Geology

By
MOSES MAGOBA

A thesis submitted in fulfilment of the requirements for the degree of Doctor of Philosophy in the Department of Earth Sciences, University of the Western Cape

SUPERVISOR: Dr Mimonitu Opuwari
CO-SUPERVISOR: Dr Nicolas Waldmann

ABSTRACT

Investigation of the acoustic impedance variations in the upper shallow marine sandstone reservoirs was extensively studied from 10 selected wells, namely: F-O1, F-O2, E-M4, E-CN1, E-G1, E-W1, F-A10, F-A11, F-A13, and F-L1 in the Bredasdorp Basin, offshore, South Africa. The studied wells were selected randomly across the upper shallow marine interval with the purpose of conducting a regional study to assess the variations in the acoustic impedance across the reservoirs using wireline log and core data. The datasets used in this study were geophysical wireline logs, conventional core analysis, geological well completion reports, core plugs, and core samples. The physical rock properties such as lithology, fluid type, and hydrocarbon bearing zone were identified while different parameters like the volume of clay, porosity, and water saturation were quantitatively estimated. The reservoirs were penetrated at a different depth ranging from a shallow depth of 2442m at well F-L1 to a deeper depth of 4256.7m at well E-CN1. The average volume of clay, average effective porosity from wireline log, and average water saturation ranged from 8.6%- 43%, 9%- 16% and 12%- 68%, respectively. Porosity distribution was fairly equal across the field from east to west except in well F-A10, F-A13, and F-A11 where a much higher porosity was shown with F-A13 showing the highest average value of 16%. Wells E-CN1, E-W1, F-O1, F-L1 and E-G1 had lower porosity with E-CN1 showing the lowest average value of 9%.

The acoustic properties of the reservoirs were determined from geophysical wireline logs in order to calculate acoustic impedance and also investigate factors controlling density and acoustic velocities of these sediments. The acoustic impedance proved to be highest on the central to the western side of the field at E-CN1 with an average value of 11832 g/cm3s whereas, well F-A13 reservoir in the eastern side of the field proved to have the lowest average acoustic impedance of 9821 g/cm3s. There was a good linear negative relationship between acoustic impedance and porosity, compressional velocity vs porosity and porosity vs bulk density. A good linear negative relationship between acoustic impedance and porosity was obtained where the reservoir was homogenous, thick sandstone. However, interbedded shale units within the reservoir appeared to hinder a reliable correlation between acoustic impedance and porosity. The cross-plots results showed that porosity was one of the major factors controlling bulk density, compressional velocity (Vp) and acoustic impedance. The Gassmann equation was used for the determination of the effects of fluid substitution on acoustic properties using rock frame properties. Three fluid substitution models (brine, oil, and gas)

were determined for pure sandstones and were used to measure the behaviour of the different sandstone saturations. A significant decrease was observed in Vp when the initial water saturation was substituted with a hydrocarbon (oil or gas) in all the wells. The value of density decreased quite visibly in all the wells when the brine (100% water saturation) was substituted with gas or oil. The fluid substitution affected the rock property significantly. The Vp slightly decreases when brine was substituted with water in wells F-A13, F-A10, F-O2, F-O1 F-A11, F-L1, and E-CN1. Wells E-G1, E-W1, and E-M4 contain oil and gas and therefore showed a notable decrease from brine to oil and from oil to gas respectively. Shear velocity (Vs) remained unaffected in all the wells. The acoustic impedance logs showed a decrease when 100% water saturation was replaced with a hydrocarbon (oil or gas) in all the wells. Clay presence significantly affects the behaviour of the acoustic properties of the reservoir rocks as a function of mineral type, volume, and distribution. The presence of glauconite mineral was observed in all the wells. Thirty-two thin sections, XRD and SEM/EDS from eight out of ten wells were studied to investigate lithology, diagenesis and the effect of mineralogy on porosity and acoustic properties (Compressional velocity and bulk density) within the studied reservoir units. Cementation (calcite and quartz), dissolution, compaction, clay mineral authigenesis, and stylolitization were the most significant diagenetic processes affecting porosity, velocity, and density. Well E-CN1 reservoir quality was very poor due to the destruction of intergranular porosity by extensive quartz and illite cementation, and compaction whereas well F-A13 show a highly porous sandstone reservoir with rounded monocrystalline quartz grain and only clusters of elongate to disc-like, authigenic chlorite crystals partly filling a depression within altered detrital grains.

Overall, the results show that the porosity, lithology mineralogy, compaction and pore fluid were the major factors causing the acoustic impedance variations in the upper shallow marine sandstone reservoirs.

Keywords: Compressional velocity, Porosity, Bulk density, Acoustic impedance, Mineralogy, Pore fluid, Glauconite, and Upper Shallow Marine sandstone.

DECLARATION

I declare *Investigation of the acoustic impedance variations of Upper Shallow Marine sandstone reservoirs in the Bredasdorp Basin, offshore South Africa* is my own work, that it has not been submitted before for any degree or examination in any other university, and that all the sources I have used or quoted have been indicated and acknowledged by means of complete references.

Moses Magoba March 2019

……

Signature

ACKNOWLEDGMENTS

I wish to express my deepest gratitude to my supervisors DR MIMONITU OPUWARI and DR NICOLAS WALDMAN for their patience, assistance, and guidance throughout this study. Special thanks also go to Petroleum Agency of South Africa (PASA) and Petrophysics and basin analysis laboratory, the University of Haifa for making the data available and providing the space and equipment to run all my experiments for this study.

I would like to thanks my sister DR ROZWIVHONA MAGOBA for taking her time to review this work. To my big brother DR REMBULUWANI MAGOBA, you have been the best brother anyone can ask for, the role you played in my life for all these years is really appreciated.

A special thanks to all my fellow postgraduate students in the geology department at the University of the Western Cape for their encouragement and support. I give my heartfelt thanks to HAKUNDWI MANDENDE, SEDZANI NETHENZHENI, NEHEMIA DOMINICK, OLUWATOYIN AYODELE, DR CHRIS SAMAKINDE, MURENDENI MUGIVHI, STEPHANE TSAKOU and NOTHANDO MGUNI for the very supportive role they have played during my study at the University of Western Cape.

Lastly, I dedicate this work to my siblings LITSHANI MAGOBA, TEVHEDZANI MAGOBA, and MPFUNZENI MAGOBA and my parents ALFRED and ELISA MAGOBA without them this would not have been possible.

TO GOD BE THE GLORY.

TABLE OF CONTENTS

ABSTRACT i
DECLARATION iii
ACKNOWLEDGMENTS iv
TABLE OF CONTENTS v
LIST OF FIGURES ix
LIST OF TABLES xiv
1 INTRODUCTION 1
1.1 BACKGROUND INFORMATION 1
1.2 BASICS 2
2.1.1 1.2.1 Thesis Outline 2
1.2.2 Chapter 1 2
1.2.3 Chapter 2 2
1.2.4 Chapter 3 3
1.2.5 Chapter 4 3
1.2.6 Chapter 5 3
1.2.7 Chapter 6 3
1.2.8 Chapter 7 3
1.3 LOCATION OF THE STUDY AREA 3
1.4 STATEMENT OF RESEARCH PROBLEM 5
1.5 AIMS AND OBJECTIVES 5
REFERENCES 7
2 GEOLOGICAL BACKGROUND OF THE BREDASDORP BASIN 8
2.1 INTRODUCTION 8
2.2 BASIN EVOLUTION 8
2.2.1 RIFT TECTONICS AND SEDIMENTATION (D TO 1AT1) 9
2.2.2 TRANSITIONAL –EARLY DRIFT TECTONICS AND SEDIMENTATION STAGE (1AT1 TO 5AT1) 10
2.2.3 5AT1 TO 13AT1 (BARREMIAN TO EARLY APTIAN) 10
2.2.4 LATE DRIFT TECTONICS AND SEDIMENTATION (13AT1 TO PRESENT DAY) 10
2.3 DEPOSITIONAL SETTING 11
2.4 THE GEOLOGY OF THE UPPER SHALLOW MARINE SANDSTONES 12

REFERENCES 15
3 LITERATURE REVIEW 16
3.1 INTRODUCTION 16
3.2 CORING 16
3.3 WELL LOGS 17
3.4 CHARACTERISTICS OF THE SELECTED WIRELINE LOGS 18
3.4.1 GAMMA RAY 18
3.4.2 RESISTIVITY LOG 18
3.4.3 SONIC LOG 20
3.4.4 DENSITY LOG 21
3.4.5 NEUTRON LOG 22
3.4.6 CALIPER LOG 23
REFERENCES 24
4 PETROPHYSICAL INTERPRETATION OF SHALLOW MARINE SANDSTONE RESERVOIRS 26
4.1 INTRODUCTION 27
4.2 AIMS AND OBJECTIVES 29
4.3 MATERIALS AND METHODS 29
4.3.1 DATA ANALYSIS 29
4.3.2 CLAY VOLUME ESTIMATION 31
4.3.3 POROSITY DETERMINATION FROM WIRELINE LOGS 32
4.3.4 POROSITY DETERMINATION FROM LABORATORY MEASUREMENTS 33
4.3.5 WATER SATURATION DETERMINATION 36
4.4 RESULTS AND INTERPRETATION 37
4.4.1 ANALYSIS AND INTERPRETATION OF CONVENTIONAL CORE RESULTS 37
4.4.2 INTERPRETATION OF CORE POROSITY 44
4.4.3 SPECIAL CORE ANALYSIS (SCAL) 50
4.4.4 QUALITATIVE INTERPRETATION 56
4.4.5 QUANTITATIVE INTERPRETATION 62
4.4.6 GENERAL DISTRIBUTION OF PETROPHYSICAL PROPERTIES ACROSS THE FIELD IN 3D VIEW 80
4.5 CONCLUSION 83
4.6 REFERENCES 84

5 EFFECT OF POROSITY ON ACOUSTIC PROPERTIES AND FLUID SUBSTITUTION MODELLING 86
5.1 INTRODUCTION 88
5.2 AIMS AND OBJECTIVES 89
5.3 MATERIALS AND METHOD 89
5.3.1 DATA SET 89
5.3.2 ESTIMATION OF COMPRESSIONAL VELOCITY AND ACOUSTIC IMPEDANCE FROM WIRELINE LOGS 89
5.4 WELL LOG RESULTS AND INTERPRETATION 93
5.4.1 INTRODUCTION TO WELL LOG ANALYSIS 93
5.4.2 F-O2 WELL LOG INTERPRETATION 93
5.4.3 E-M4 WELL LOG INTERPRETATION 94
5.4.4 E-CN1 WELL LOG INTERPRETATION 95
5.4.5 E-G1 WELL LOG INTERPRETATION 96
5.4.6 E-W1 WELL LOG INTERPRETATION 97
5.4.7 F-A10 WELL LOG INTERPRETATION 98
5.4.8 F-O1 WELL LOG INTERPRETATION 99
5.4.9 F-A11 WELL LOG INTERPRETATION 100
5.4.10 F-A13 WELL LOG INTERPRETATION 101
5.4.11 F-L1 WELL LOG INTERPRETATION 102
5.4.12 BULK DENSITY, COMPRESSIONAL VELOCITY, AND ACOUSTIC IMPEDANCE DISTRIBUTION PATTERN 103
5.5 CROSS-PLOTS RESULTS AND INTERPRETATION 106
5.5.1 F-O1 CROSS-PLOTS INTERPRETATION 106
5.5.2 F-O2 CROSS-PLOTS INTERPRETATION 107
5.5.3 E-G1 CROSSPLOTS INTERPRETATION 108
5.5.4 E-M4 CROSS-PLOTS INTERPRETATION 109
5.5.5 E-W1 CROSSPLOTS INTERPRETATION 110
5.5.6 E-CN1 CROSS-PLOTS INTERPRETATION 111
5.5.7 F-A10 CROSSPLOTS INTERPRETATION 112
5.5.8 F-A11 CROSS-PLOTS INTERPRETATION 113
5.5.9 F-A13 CROSSPLOTS INTERPRETATION 114
5.5.10 F-L1 CROSSPLOTS INTERPRETATION 115
5.5.11 MULTI-WELL CROSSPLOT OF POROSITY VS ACOUSTIC IMPEDANCE 116
5.6 EFFECT OF PORE FLUID ON ACOUSTIC IMPEDANCE 117

5.6.1 GASSMANN FLUID SUBSTITUTION MODELLING 118
5.7 CONCLUSION 129
5.8 REFFERENCES 130
6 EFFECT OF MINERALOGY ON VELOCITY, DENSITY AND POROSITY 131
6.1 INTRODUCTION 132
6.2 AIMS AND OBJECTIVES 133
6.3 MATERIALS AND METHODS 134
6.3.1 THIN SECTION ANALYSIS 134
6.3.2 XRD ANALYSIS SAMPLE PREPARATION 134
6.3.3 SEM-EDS ANALYSIS 137
6.4 RESULTS AND INTERPRETATION 137
6.4.1 F-O1 MINERALOGY INTERPRETATION 137
6.4.2 F-O2 MINERALOGY INTERPRETATION 143
6.4.3 E-CN1 MINERALOGY INTERPRETATION 148
6.4.4 E-G1 MINERALOGY INTERPRETATION 153
6.4.5 E-W1 MINERALOGY INTERPRETATION 158
6.4.6 F-A10 MINERALOGY INTERPRETATION 163
6.4.7 F-A13 MINERALOGY INTERPRETATION 168
6.4.8 E-M4 MINERALOGY INTERPRETATION 173
6.5 CONCLUSION 174
6.6 REFERENCES 175
7 GENERAL CONCLUSION AND RECOMMENDATIONS 177
7.1 RECOMMENDATIONS 178
APPENDIX A- GAMMA RAY HISTOGRAM PLOTS I
APPENDIX B- CONVENTIONAL CORE ANALYSIS RESULTS III
APPENDIX C- Gassmann fluid substitution results XXXV
Appendix D- XRD ANALYSIS XLV
APPENDIX E- SEM/EDS ANALYSIS LI
APPENDIX F-CORE PHOTOS LX
APPENDIX G- SHEAR VELOCITY QC LXV

LIST OF FIGURES

Figure 1-1: Flow chart illustrating the structure of the thesis. 2
Figure 1-2: Map showing the location of the selected wells in the Bredasdorp Basin (PASA, 2004/2005). 4
Figure 2-1: Major tectonic elements of the Outeniqua Basin (PASA, 2012). 8
Figure 2-2: Half graben formation from a series of normal faults dipping in the same direction (Modified from Houston, 1986). 9
Figure 2-3: General Chronostratigraphy of the Bredasdorp Basin (Mudaly, et al., 2009). 11
Figure 2-4: Generalised chronostratigraphy of the Bredasdorp Basin (Mudaly, et al., 2009). 13
Figure 2-5: Simplified chronostratigraphy of the Bredasdorp Basin (Mudaly, et al., 2009). 14
Figure 3-1: Illustration of the borehole formation and resistivity measurements (https://www.eoas.ubc.ca/~fjones/aglosite/objects/meth_10c/boreholes.htm) August 2019 19
Figure 3-2: Borehole compensated sonic tools (Glover, 2009) 21
Figure 3-3: Schematic diagram of a formation density tool (Glover, 2009) 22
Figure 3-4: The Compensated Neutron Log (CNL) tool (Glover, 2009) 23
Figure 3-5: Two arm caliper instrument (http://www.geologging.com/wp-content/uploads/2017/04/3-arm-Caliper.pdf) February 2019. 23
Figure 4-1: Flowchart illustrating a sequence of steps taken during petrophysical analysis. 30
Figure 4-2: Multi-well histogram plot displaying the minimum and maximum gamma ray values. 31
Figure 4-3: Calliper scale measuring the length and the diameter of the core plug. 35
Figure 4-4: Scale measuring the dry weight of the core plug. 35
Figure 4-5: Porosimeter instrument used to measure the porosity of the core plugs. 36
Figure 4-6: Histogram of well F-O1 grain densities. 38
Figure 4-7: Histogram of well F-O2 grain densities. 39
Figure 4-8: Histogram of well E-M4 grain densities. 40
Figure 4-9: Histogram of well E-CN1 grain densities. 41
Figure 4-10: Histogram of E-W1 grain densities. 42
Figure 4-11: Histogram of well F-A10 grain densities. 43
Figure 4-12: Histogram of F-A13 grain densities. 44
Figure 4-13: F-O1 core porosity histogram plot. 45
Figure 4-14: F-O2 core porosity histogram plot. 45
Figure 4-15: E-M4 core porosity histogram plot. 46
Figure 4-16: E-CN1 core porosity histogram plot. 47
Figure 4-17: E-G1 core porosity histogram plot. 47
Figure 4-18: E-W1 core porosity histogram plot. 48
Figure 4-19: F-A10 core porosity histogram plot. 49
Figure 4-20: F-A13 core porosity histogram plot. 49
Figure 4-21: Well F-O1 porosity at overburden pressure versus porosity at room conditions. 52

Figure 4-22: Well F-O2 porosity at overburden pressure versus porosity at room conditions. 53
Figure 4-23: Well F-A13 porosity at overburden pressure versus porosity at room conditions. 55
Figure 4-24: The petrophysical logs interpretation of Upper Shallow Marine sandstone (3701.9-3810.6m), a 1AT1 formation of well F-O1. 57
Figure 4-25: The petrophysical logs interpretation of Upper Shallow Marine sandstone (3615.5-3685.4m), a 1AT1 formation of well F-O2. 58
Figure 4-26: The petrophysical logs interpretation of Upper Shallow Marine sandstone (2558.1m-2665.8m), a 1AT1 formation of well E-M4. 58
Figure 4-27: The petrophysical logs interpretation of Upper Shallow Marine sandstone (4081-4246.7m), a 1AT1 formation of well E-CN1....59
Figure 4-28: The petrophysical logs interpretation of upper Shallow Marine Sandstone (3149.4-3164.6m), a 1AT1 formation of well E-G1. 59
Figure 4-29: The petrophysical logs interpretation of Upper Shallow Marine sandstone (3144.8-3188.1m), a 1AT1 formation of well E-W1. 60
Figure 4-30: The petrophysical logs interpretation of Upper Shallow Marine sandstone (2712.2-2949.6m), a 1AT1 formation of well F-A10. 60
Figure 4-31: The petrophysical logs interpretation of Upper Shallow Marine sandstone (2761.1-2818.8m), a 1AT1 formation of well F-A11. 61
Figure 4-32: The petrophysical logs interpretation of Upper Shallow Marine sandstone (2610.3-2720.4m), a 1AT1 formation of well F-A13. 61
Figure 4-33: The petrophysical logs interpretation of Upper Shallow Marine sandstone (2442-2606.3m), a 1AT1 formation of well F-L1. 62
Figure 4-34: Calculated reservoir results of well F-O1. 63
Figure 4-35: Calculated reservoir results of well F-O2. 65
Figure 4-36: Calculated reservoir results of well E-M4. 67
Figure 4-37: Calculated reservoir results for well E-CN1. 69
Figure 4-38: Calculated reservoir results of E-G1 well. 71
Figure 4-39: Calculated reservoir results of well E-W1. 72
Figure 4-40: Calculated reservoir results of well F-A10. 74
Figure 4-41: Calculated reservoir results of well F-A11. 76
Figure 4-42: Calculated reservoir results of well F-A13. 77
Figure 4-43: Calculated reservoir results of well F-L1....79
Figure 4-44: 3D parameter view showing the volume of clay content across the field....81
Figure 4-45: 3D parameter view showing porosity distribution across the field. 81
Figure 4-46: 3D parameter view showing water saturation distribution across the field. 82
Figure 5-1: Illustration of steps followed for the Vp and Vs calculations. 90
Figure 5-2: Shear velocity QC cross-plot calculation. 91
Figure 5-3: Relationship between velocity and depth in well F-A13. 92
Figure 5-4: Gamma-ray, Bulk density, Compressional velocity and acoustic impedance logs of well F-O2. 94
Figure 5-5: Gamma-ray, Bulk density, Compressional velocity and acoustic impedance logs of well E-M4. 95

Figure 5-6: Gamma-ray, Bulk density, Compressional velocity and acoustic impedance logs of well E-CN1. 96
Figure 5-7: Gamma-ray, Bulk density, Compressional velocity and acoustic impedance logs of well E-G1. 97
Figure 5-8: Gamma-ray, Bulk density, Compressional velocity and acoustic impedance logs of well E-W1. 98
Figure 5-9: Gamma-ray, Bulk density, Compressional velocity and acoustic impedance logs of well F-10. 99
Figure 5-10: Gamma-ray, Bulk density, Compressional velocity and acoustic impedance logs of well F-O1. 100
Figure 5-11: Gamma ray, Bulk density, Compressional velocity and acoustic impedance logs of well F-A11. 101
Figure 5-12: Gamma-ray, Bulk density, Compressional velocity and acoustic impedance logs of well F-13. 102
Figure 5-13: Gamma-ray, Bulk density, Compressional velocity and acoustic impedance logs of well F-L1. 102
Figure 5-14: Average bulk density distribution. 104
Figure 5-15: Compressional velocity distribution. 105
Figure 5-16: Average Acoustic impedance distribution 105
Figure 5-17: Cross-plots of (A) Compressional velocity vs bulk density (B) Porosity vs bulk density (C) Porosity vs acoustic impedance and (D) Compressional velocity vs Porosity. 107
Figure 5-18: Cross-plots of (A) Compressional velocity vs bulk density (B) Porosity vs bulk density (C) Compressional velocity vs Porosity and (D) Porosity vs acoustic impedance. 108
Figure 5-19: Cross-plots of (A) Compressional velocity vs Porosity, (B) Porosity vs acoustic impedance, (C) Compressional velocity vs bulk density (D) Porosity vs bulk density. 109
Figure 5-20: Cross-plots of (A) Compressional velocity vs bulk density, (B) Compressional velocity vs porosity, (C) Porosity vs acoustic impedance and (D) Porosity vs bulk density. 110
Figure 5-21: Cross-plots of (A) Compressional velocity vs Porosity, (B) Compressional velocity vs bulk density, (C) Porosity vs bulk density and (D) Porosity vs acoustic impedance. 111
Figure 5-22: Cross-plots of (A) Compressional velocity vs bulk density, (B) Porosity vs bulk density, (C) Compressional velocity vs Porosity and (D) Porosity vs acoustic impedance. 112
Figure 5-23: Cross-plots of (A) Compressional velocity vs bulk density, (B) Porosity vs bulk density, (C) Compressional velocity vs Porosity and (D) Porosity vs acoustic impedance. 113
Figure 5-24: Cross-plots of (A) Compressional velocity vs porosity, (B) Compressional velocity vs bulk density, (C) Porosity vs bulk density and (D) Porosity vs acoustic impedance. 114
Figure 5-25: Cross-plots of (A) Compressional velocity vs bulk density, (B) Porosity vs bulk density, (C) Compressional velocity vs Porosity and (D) Porosity vs acoustic impedance. 115

Figure 5-26: Cross-plots of (A) Compressional velocity vs bulk density, (B) Porosity vs bulk density, (C) Compressional velocity vs Porosity and (D) Porosity vs acoustic impedance. 116
Figure 5-27: A multi-well cross-plot of porosity versus acoustic impedance. 117
Figure 5-28: Shear velocity QC cross plots showing the relationship between Vp and Vs calculated using the Greenberg and Castagna (1992) relationship. 120
Figure 5-29: Elastic impedance logs for F-O1 well showing the calculated parameters (Vp, Vs, Al and Poison ratio) at different saturation levels (100% water saturation and gas) in reservoir interval. 121
Figure 5-30: Elastic impedance logs for F-O2 well showing the calculated parameters (Vp, Vs, Al and Poison ratio) at different saturation levels (100% water saturation and gas) in reservoir interval. 122
Figure 5-31: Elastic impedance logs for E-M4 well showing the calculated parameters (Vp, Vs, Al and Poison ratio) at different saturation levels (100% water saturation and gas and oil) in reservoir interval. 122
Figure 5-32: Elastic impedance logs for E-G1 well showing the calculated parameters (Vp, Vs, Al and Poison ratio) at different saturation levels (100% water saturation and gas and oil) in reservoir interval. 123
Figure 5-33: Elastic impedance logs for E-W1 well showing the calculated parameters (Vp, Vs, Al and Poison ratio) at different saturation levels (100% water saturation and gas and oil) in reservoir interval. 123
Figure 5-34: Elastic impedance logs for E-CN1 well showing the calculated parameters (Vp, Vs, Al and Poison ratio) at different saturation levels (100% water saturation and gas) in reservoir interval. 124
Figure 5-35: Elastic impedance logs for F-A13 well showing the calculated parameters (Vp, Vs, Al and Poison ratio) at different saturation levels (100% water saturation and gas) in reservoir interval. 124
Figure 5-36: Elastic impedance logs for F-A10 well showing the calculated parameters (Vp, Vs, Al and Poison ratio) at different saturation levels (100% water saturation and gas) in reservoir interval. 125
Figure 5-37: Elastic impedance logs for F-L1 well showing the calculated parameters (Vp, Vs, Al and Poison ratio) at different saturation levels (100% water saturation and gas) in reservoir interval. 125
Figure 5-38: Elastic impedance logs for F-A11 well showing the calculated parameters (Vp, Vs, Al and Poison ratio) at different saturation levels (100% water saturation and gas) in reservoir interval. 126
Figure 6-1: Mortar and pestle with a rock sample. 134
Figure 6-2: Illustration of the clay sample preparation for XRD analysis. 136
Figure 6-3: SEM/EDS Equipment used for analysis. 137
Figure 6-4: F-O1 petrography results (Fadipe, 2012). 139
Figure 6-5: F-O1 XRD analysis of 3705m. 140
Figure 6-6: F-O1 XRD analysis of 3720.52m. 140
Figure 6-7: F-O1 XRD analysis of 3712.46m. 140
Figure 6-8: SEM and EDS analysis of 3625.5m. 141
Figure 6-9: SEM and EDS analysis of 3705m. 142
Figure 6-10: F-O2 petrography analysis (Fadipe, 2012). 144

Figure 6-11: F-O2 XRD analysis of 3626.42m. 145
Figure 6-12: F-O2 SEM and EDS analysis of 3642m showing Glauconite. 146
Figure 6-13: F-O2 SEM and EDS of Chlorite analysis at 3626m. Q= Quartz, PL=Plagioclase. 147
Figure 6-14: E-CN1 petrography analysis of (A) 4006.5m, (B) 4257m, (C) 4254m and (D) 5259.5m. 149
Figure 6-15: E-CN1 XRD analysis of 4006.5m. G= Glauconite, I= Illite, Q= Quartz, and Ms= Muscovite. 149
Figure 6-16: E-CN1 XRD analysis of 4253.5m. G= Glauconite, I= Illite, Q= Quartz and Ms= Muscovite. 150
Figure 6-17: E-CN1 XRD analysis of 4257m. G= Glauconite, I= Illite, Q= Quartz, C= Chlorite and Ms= Muscovite. 150
Figure 6-18: E-CN1 SEM and EDS analysis of illite at 4006.5m. 151
Figure 6-19: SEM and EDS analysis of 4253.5m. 152
Figure 6-20: E-G1 petrography analysis of (A) 3615.4m, (B) 3161.5m, (C) 3166.5m and (D) 3616m with a magnification of 10X. 154
Figure 6-21: E-G1 XRD analysis of 3165.4m. 155
Figure 6-22: E-G1 XRD analysis of 3166.5m. 155
Figure 6-23: E-G1 SEM and EDS analysis of Chlorite at depth 3161.5m. 156
Figure 6-24: E-G1 SEM and EDS analysis of depth 3165.4m. Q= Quartz, Mp= Microporosity. 157
Figure 6-25: E-W1 petrography analysis of (A) 3174m (4X), (B) 3181.5m (4X), (C) 3186.5m (10X) and (D) 3189m (10X) with 4X and 10X magnifications. Ca= calcite cement 159
Figure 6-26: E-W1 XRD analysis of 3186.65m. 159
Figure 6-27: E-W1 XRD analysis of 3174m. 160
Figure 6-28: E-W1 SEM and EDS analysis of 3174m. 161
Figure 6-29: E-W1 SEM and EDS analysis of 3181m. 162
Figure 6-30: Petrographical analysis of (A) 2719.5m (10X), (B) 2730.5m (10X), (C) 2743m (4X), and (D) 2755.5m (10 X) with 4X and 10 X magnifications. 164
Figure 6-31: F-A10 XRD analysis at 2730.5m. C=Chlorite, V=Vermiculite, G= Glauconite, I= Illite, Q= Quartz and Ms= Muscovite. 164
Figure 6-32: F-A10 XRD analysis at 2743m. C=Chlorite, G= Glauconite, I= Illite, Q= Quartz. 165
Figure 6-33: F-A10 SEM and EDS for 2730.5m. 166
Figure 6-34: F-A10 SEM and EDS analysis at 2755.5m showing ragged-edged, authigenic chlorite platelets stacked face-to-face in a rare beehive-like structure. 167
Figure 6-35: F-A13 petrographical analysis of (A) 2615m, (B) 2624.5m, (C) 2646.5m and (D) 2656m. 169
Figure 6-36: F-A13 XRD analysis of 2646.5m. G=Glauconite, C=Chlorite, I=illite, Q=Quartz and MS= Muscovite. 169
Figure 6-37: F-A13 XRD analysis of 2656m. G=Glauconite, C=Chlorite, I=illite, Q=Quartz 170
Figure 6-38: F-A13 SEM/EDS analysis of 2656m. 171
Figure 6-39: F-A13 SEM/EDS analysis of 2615m. 172
Figure 6-40: E-M4 petrophysical analysis of 2567m (A, B) and 2573m (C, D). 173

LIST OF TABLES

Table 4-1: Characteristics of wireline logs 30
Table 4-2: Matrix densities of common lithology (Schlumberger, 2018).....38
Table 4-3: Well F-O1 core data used for porosity overburden correction.....51
Table 4-4: Well F-O2 core data used for porosity overburden correction.....53
Table 4-5: Well F-A13 core data used for porosity overburden correction. 54
Table 4-6: F-O1 core porosity results obtained from Helium porosimeter. 64
Table 4-7: F-O2 core porosity results obtained from Helium porosimeter. 66
Table 4-8: E-M4 core porosity results obtained from Helium porosimeter. 68
Table 4-9: E-CN1 core porosity results obtained from Helium porosimeter. 70
Table 4-10: E-W1 core porosity results obtained from Helium porosimeter. 73
Table 4-11: F-A10 core porosity results obtained from Helium porosimeter. 75
Table 4-12: F-A13 core porosity results obtained from Helium porosimeter. 78
Table 4-13: Porosity values for reservoir characterization (Modified from Rider, 1986). 80
Table 4-14: Reservoir summary results of all the studied wells 80
Table 5-1: Average values of bulk density, compressional velocity, and acoustic impedance. 103
Table 5-2: Reservoir temperature, pressure and salinity used in the substitution model. 120

CHAPTER ONE

1 INTRODUCTION

1.1 BACKGROUND INFORMATION

This study integrates the principles of petrophysics and Rock physics with the aim of trying to understand the complex geological challenges in the Bredasdorp Basin at the Upper Shallow Marine (USM) sandstone reservoirs interval in particular. The field of Rock Physics represents the link between qualitative geologic parameters and quantitative geophysical measurements. Increasingly over the last decade, Rock Physics stands out as a key technology in petroleum geophysics, as it has become an integral part of quantitative seismic interpretation (Jensen, 2016). Petrophysics is defined as the study of rock principles and their interactions with fluid (oil, gas or water) (Rider, 2002). Petrophysical interpretation transforms well log measurements into reservoir properties (e.g. porosity, permeability, saturation, mineral component volume and volume of clay) (Bisht, et al., 2013). Petrophysics uses all kind of logs, core and integrates all pertinent information. It is more concerned about using wellbore measurements to contribute to reservoir characterization and less concerned with seismic (Dewar, 2001).

A considerable amount of work has been carried out on the upper shallow marine by PETROSA (South African national oil company); however, the understanding of the acoustic impedance variations on the USM reservoirs has not been well documented.

This study involves reservoir quality prediction and the estimation of the petrophysical and acoustic properties such as porosity, water saturation, volume of clay, acoustic impedance, compressional velocity, bulk density, fluid substitution, diagenesis, mineralogy and 3D models deduced from well logs and core data to understand the variation and distribution of acoustic impedance (AI) of the upper shallow marine sandstones as well as reasons of variations. It is of utmost importance to understand the diagenetic history of potential reservoirs because diagenesis plays an important role in preserving, creating or improving porosity (Fadipe, 2012).

1.2 BASICS

2.1.1 1.2.1 Thesis Outline

This thesis contains a written report of the study carried out to investigate the acoustic impedance variation of the Upper Shallow Marine reservoirs in a spatial content and also to understand the possible causes of this variation. The thesis comprises of three technical work chapters (Four, Five and Six). The format of these chapters includes abstract, introduction, aims and objectives, methodology, results and interpretation, conclusion and references per chapter. The flowchart below (Figure 1-1) illustrates the structure of the thesis.

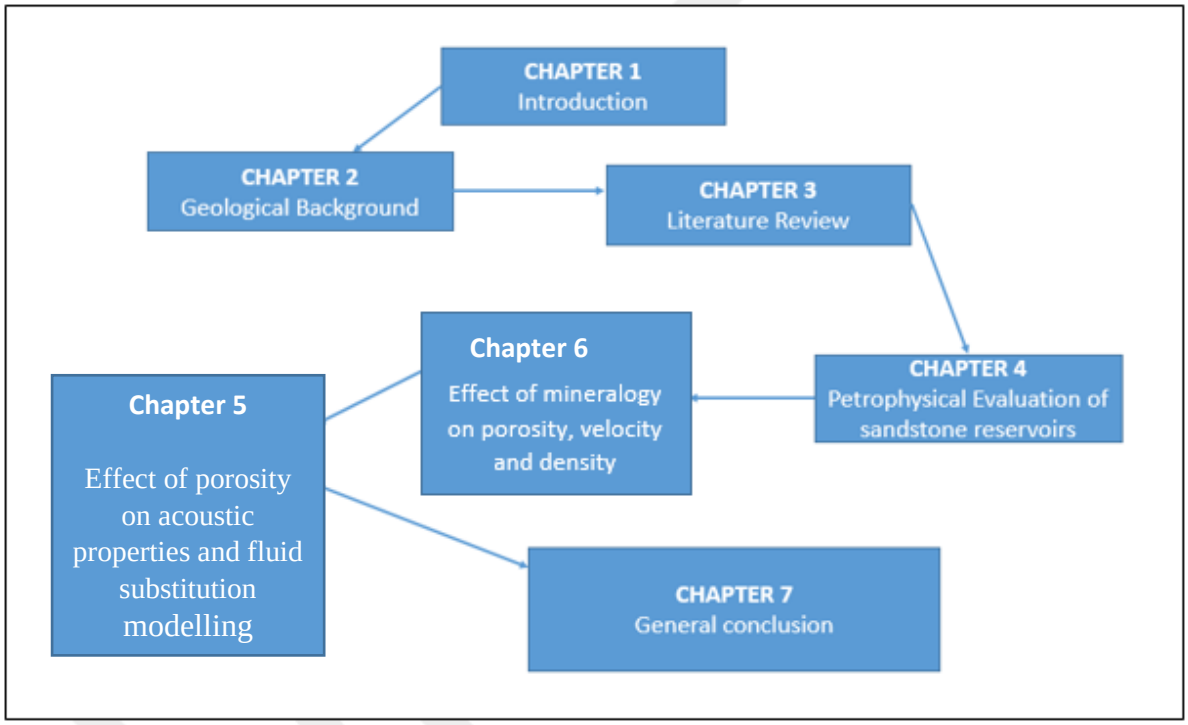

Figure 1-1: Flow chart illustrating the structure of the thesis.

1.2.2 Chapter 1

Chapter one gives a broad overview of the research by means of presenting research background information on the topic of the study, aims and objectives and the location of the study area.

1.2.3 Chapter 2

Chapter two focus on the geology of the Basin which includes the time and events of deposition of sediments. It also zooms into the geology of the study area within the Basin.

1.2.4 Chapter 3

Chapter three presented a literature review of the study area. Consulted publications relating to geology, stratigraphy, reservoir characterization and detailed description of the techniques and methods involved were discussed. This chapter is important because it helps the researcher to be familiarised with the debates going on about the topic of the study and also highlight the areas that need more research. The literature review is not only limited to this chapter but it extends to the technical work chapters.

1.2.5 Chapter 4

This chapter contains the petrophysical evaluation of selected reservoirs in the target area. It only focuses on the petrophysical results that are required to fulfil the aim of the study.

1.2.6 Chapter 5

Chapter five focused on the acoustic properties of the sandstone reservoirs and how they get affected by porosity and pore fluids. Various relationships were observed through the use of cross plotting the parameters against one another.

1.2.7 Chapter 6

Chapter 6 takes a look into the effect of mineralogy on the acoustic properties. Various lab experiments and analysis of mineralogy were performed and detailed interpretation was given to explain the effect of mineralogy on density, velocity, and porosity.

1.2.8 Chapter 7

This chapter gives a general conclusion of the thesis. It summarises the findings of every chapter and draws a broad conclusion.

1.3 LOCATION OF THE STUDY AREA

The Bredasdorp Basin is one of the sub-basins of the greater Outeniqua Basin and is located in the southeast of Cape Town and west south-west of Port Elizabeth, south coast of the Republic of South Africa (Turner, et al., 2000). The basement arches that are aligned parallel to the structural grain of the orogenic Cape Fold Belt (CFB) define the Bredasdorp Basin. It is bounded by the Infanta arch on the northeast and the Agulhus arch in the southeast which

defines a south-easterly elongate basin of approximately 200km long and 80km wide and also 18 000km2 in an area (McMillan, et al., 1997). Figure 1-2 below shows the location of the selected wells in the Bredasdorp Basin. The well location map displays the ten wells selected for the purpose of this study. The selected wells are F-O1, F-O2, E-M4, E-CN1, E-W1, E-G1, F-A10, F-A11, F-A13 and F-L1.

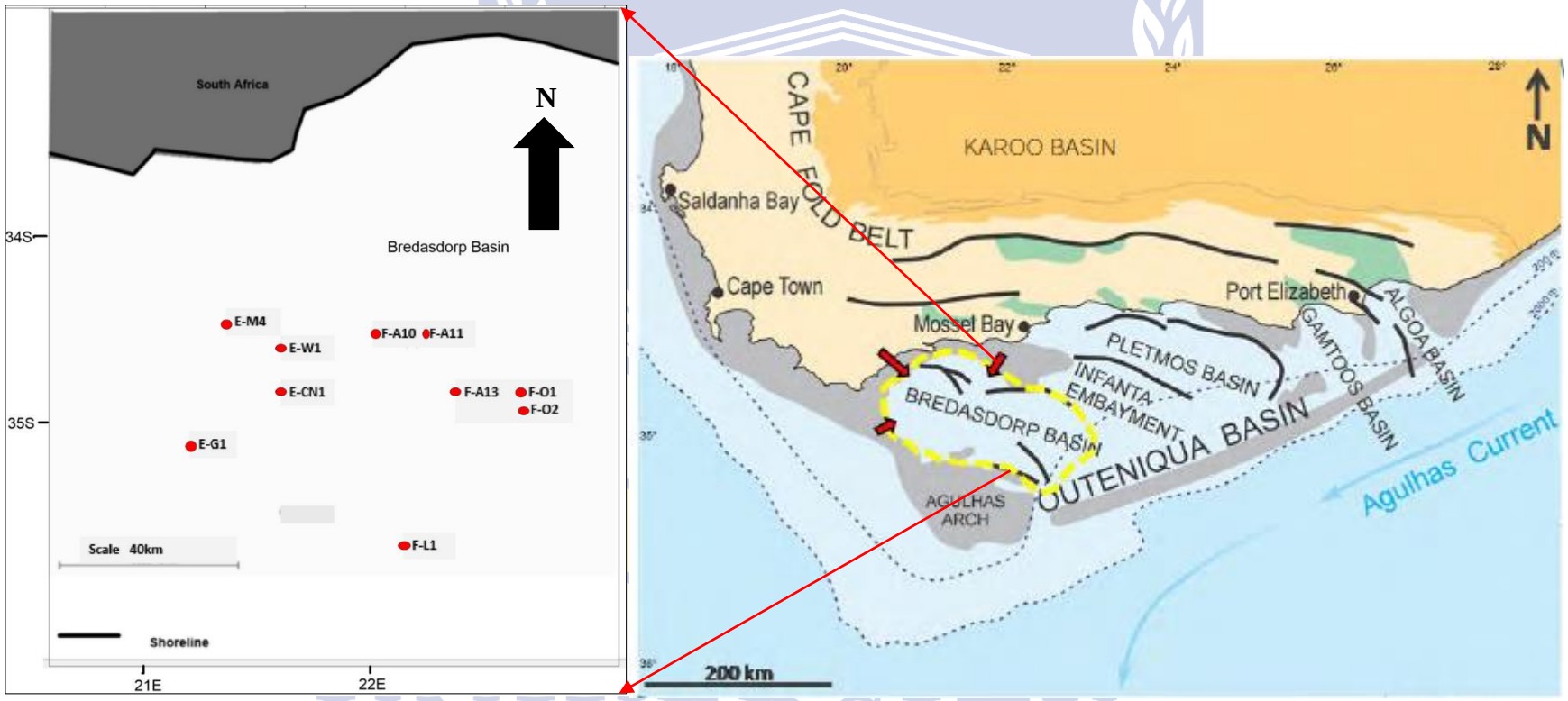

Figure 1-2: Map showing the location of the selected wells in the Bredasdorp Basin (PASA, 2004/2005).

1.4 STATEMENT OF RESEARCH PROBLEM

The complex relationship between acoustic properties and the texture, composition, and facies of sedimentary rocks strongly influences the geological interpretation of wireline logs, seismic reflection and the seismic modelling of the outcrops (Kenter and Ivanov, 1995). To connect rock physics with geology, it is essential to identify and quantify factors influencing the density and acoustic velocity of the sediments. The behaviour of the reflection coefficient is directly influenced by acoustic impedance (product of velocity and density). High acoustic impedance will result in positive reflection coefficient (peak) whereas low acoustic impedance will result in a negative reflection coefficient (trough) under normal polarity condition. It is therefore critical to define acoustic impedance and also understand the factors influencing it.

The response of the top of the Upper Shallow Marine sandstone gas reservoir just below 1At1 unconformity varies between weak negative reflections coefficients in some areas to a positive reflection coefficient in other areas (Fatti, et al., 1994). The causes of these impedance variations and its behaviour across the upper shallow marine wells have not been addressed. Therefore this study aims to answer the following questions by means of using wireline log and core data:

- What is the effect of lithology and thickness variations on the acoustic impedance of the Upper Shallow Marine sandstone reservoirs?
- What is the effect of porosity on the acoustic properties of the studied reservoirs?
- What is the effect of the pore fluids on the acoustic properties and the acoustic impedance of the reservoirs?
- What is the effect of mineralogy on the acoustic properties (density and velocity) and porosity?

1.5 AIMS AND OBJECTIVES

The aim of the study was to identify the variation in acoustic impedances (Al) of the Upper Shallow Marine sandstone reservoirs in a spatial content and also understand why the variation takes place by making use of wireline logs and core data. The following objectives had to be fulfilled in order to achieve the above-mentioned aim:

- Identify the lithology and thickness variation of the Upper Shallow Marine sandstone reservoirs using core and wireline logs.

- Calculate porosity from wireline logs and core plugs using Helium Porosimeter instrument.
- Determine water saturation from the wireline logs.
- Determine the P-wave velocity from the Greenberg and Castagna, 1992 equation for all the selected intervals.
- Calibration of conventional core data with wireline logs generated using Interactive Petrophysics (IP) software.
- Identification of the mineral content from core samples using XRD Diffractometer, EDS and SEM, and thin sections to evaluate the effect of mineralogy on the velocity, density, and Porosity.
- Identifying the relationship between velocity and bulk density, velocity and porosity, porosity and bulk density, and acoustic impedance and porosity from the cross plots.
- Perform a Gassmann fluid substitution modelling to investigate the effect of pore fluid on acoustic properties and acoustic impedance.

REFERENCES

Bisht, B.S. Sas, S.K., Chaudhuri, P.K., Singh, R.B.N and Singh, S.K. (2013). Integration of petrophysics and rock-physics modelling in a single workflow reduces uncertainty in seismic reservoir characterization: a case study. *Geohorizons, 44*(7).

Dewar, J. (2001). Rock Physics for the rest of us- An informal discussion. *Recorder, 26*(5).

Fadipe, O.A. (2012). Facies, depositional environments and reservoir properties of the Albian age gas bearing sandstone of the ibhubesi oil field, orange basin, South Africa . Cape Town: PhD thesis, University of the Western Cape.

Jensen, E.H., Johansen, T.A., Avseth, P and Bredesen, K. (2016). Quantitative interpretation using inverse rock-physics modelling on AVO data. *The leading edge, 35*(8), 677-683.

Kenter, J. A. M., and Ivanov, M. (1995). Parameters controlling acoustic properties of carbonate and volcaniclastic sediments at sites 866 and 869. *Ocean Drilling Program, Scientific Results, 143*, 305-316.

McMilian, I.K., Brink, G.J., Broad, D.S and Maier, J.J. (1997). Late Mesozoic sedimentary basins off The South Coast of South Africa. *Sedimentary Basins of the world, 3*, 319 – 376.

Petroleum Agency of South Africa. (2004/2005). Petroleum Exploration Information and Opportunities. *Petroleum Agency SA Brochure*, pp. 16-18.

Rider, M.H. (2002). The geological interpretation of well logs (2nd ed.). Rider-French Consulting Ltd.

Turner, J.R., Grobbler, N. and Sontudu, S. (2000). Geological modelling of the Aptian and Albian sequences within Block 9, the Bredasdorp Basin, offshore South Africa. *Journal of African sciences, 31(1), 80.*

CHAPTER TWO

2 GEOLOGICAL BACKGROUND OF THE BREDASDORP BASIN

2.1 INTRODUCTION

The Bredasdorp Basin is a sub-basin of the Outeniqua Basin. The Southern Outeniqua Basin is located off the South Coast of South Africa. This basin consists of South Eastern deep-water extensions of Bredasdorp, Gamtoos, Algoa and Pletmos basins (Roux, 1997).

The Bredasdorp Basin covers approximately 18000km^2 beneath the Indian Ocean along the Southern coast of South Africa. The upper Jurassic and lower Cretaceous (lower Cenomanian) synrift continental and marine strata and post-rift Cretaceous and Cenozoic divergent margin rocks are believed to have filled this basin. Bounded on the West and Southeast by the Agulhus Arch and on the Northeast by the Infanta arch the Bredasdorp Basin opens on South-westwards to connect with the Southern Outeniqua basin and is terminated on the Southeast by the Agulhus-Falkland Fracture zone (Figure 2-1) (Dingle, et al., 1983 and Malan and Viljoen, 1990). Agulhus arch is defined by the reactivated rift fault along the margin and the Infanta arch is defined by the minor faults in the North-eastern margin (Brown, et al., 1995).

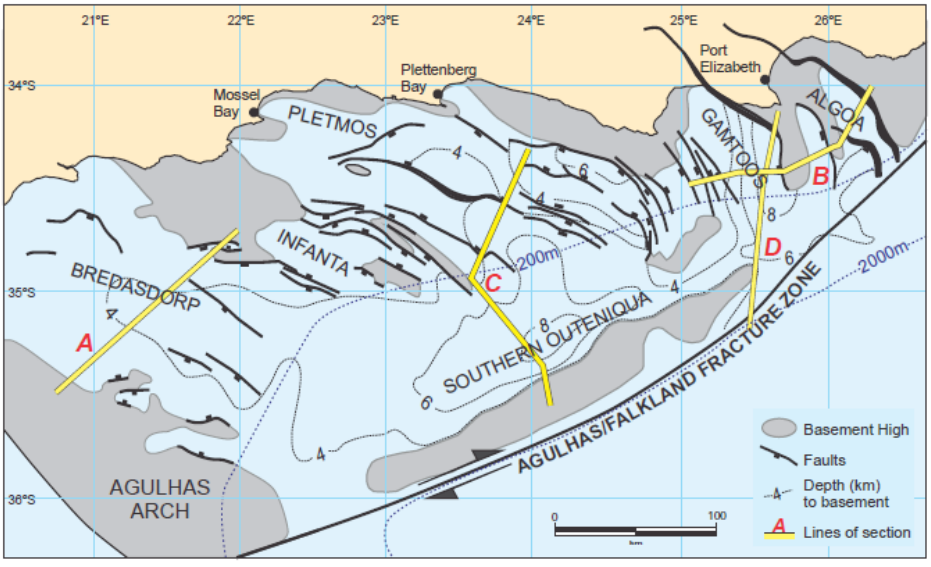

Figure 2-1: Major tectonic elements of the Outeniqua Basin (PASA, 2012).

2.2 BASIN EVOLUTION

The Bredasdorp Basin has undergone four major structural developments as discussed below:

2.2.1 RIFT TECTONICS AND SEDIMENTATION (D TO 1AT1)

This stage marks the initial rifting which is characterized by the development of horst and graben tectonics in an extensional stress regime (Figure 2-2). Lithostratigraphic study of rift sediment conducted along the North-eastern flank of the basin showed that differential subsidence of the basement floor heavily influenced sedimentation rates from horizon D to 1At1. The basement consists of black slates of the Devonian Bokkeveld group and the qualities of the Ordovician-Silurian Table Mountain group have been encountered close to the Infanta embayment. Four lithogenic units of the rift sequence have been identified in the gas field area, namely: (1) a lower fluvial interval, (2) a lower shallow marine interval, (3) an Upper fluvial interval and (4) an Upper shallow marine interval. The sandstones of the Upper shallow marine are regarded as the best reservoirs of the gas field which possess high porosity and permeability (Roux, 1997). The 1At1 unconformity marks the termination of the active rift sedimentation and also records a significant uplift and truncation of the underlying deposits along the basin margins during the late Valanginian.

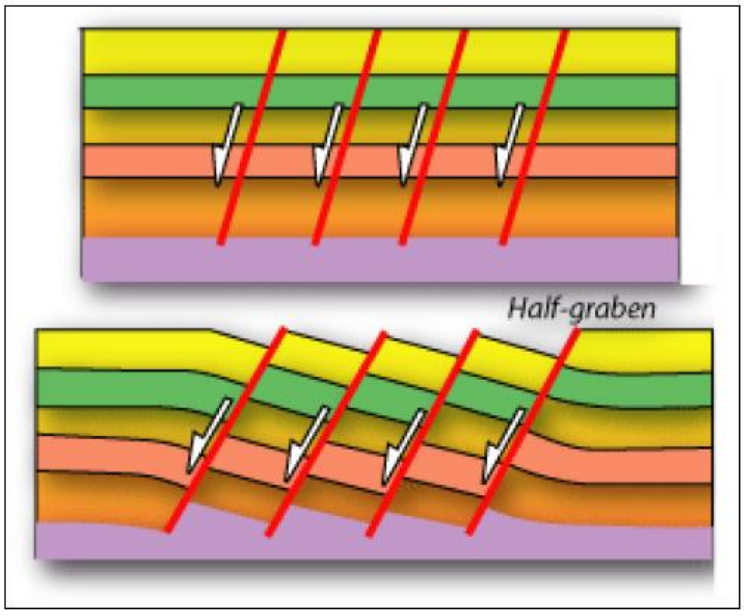

Figure 2-2: Half graben formation from a series of normal faults dipping in the same direction (Modified from Houston, 1986).

2.2.2 TRANSITIONAL –EARLY DRIFT TECTONICS AND SEDIMENTATION STAGE (1AT1 TO 5AT1)

This tectonic stage is divided into sub-stages discussed below: 1At1 to 5At1 (Late valanginian to Hauterivian). During this period the sedimentation starvation and erosion was experienced in the Northern flank of the basin including the gas field area (McMillan, et al., 1997). Argillaceous deposits are deposited distally and are accumulated in poorly oxygenated conditions and locally exhibit source rocks (Davies, 1997). The pre-1At1 upper shallow marine sandstones were subdivided into discrete areas by the channels and canyons and provide part of the trapping mechanisms for gas reservoirs.

2.2.3 5AT1 TO 13AT1 (BARREMIAN TO EARLY APTIAN)

At 5At1 unconformity, several changes occurred in the area of active sedimentation like the effective movement of the bounding Arniston fault in the North, the merging of the depocenter to the South of the fault with the depocenter in the centre of the Sothern Bredasdorp Basin and most importantly the occurrence of the major shoreward advancement of sedimentation throughout the north-eastern flank of the Basin to make way for the deposition to occur over the entire region of the gas field. During this period sedimentation was dominated by turbidity flows into a poor circulating and poor oxygenated deep marine basin. Subsidence rates and faulting show declines towards 13At1 predicting a more stable Bredasdorp Basin. A major change in the direction of the input sediment can be seen in a north-easterly direction where sandstones became widespread throughout the Basin in a distal lowstand turbidites and proximally in highstand tracts.

2.2.4 LATE DRIFT TECTONICS AND SEDIMENTATION (13AT1 TO PRESENT DAY)

The 13At1 unconformity in the early Aptian had ushered in a very different sedimentation regime. The 13At1 and 14At1 is the site of the oil accumulations located in the submarine fan channel and sand basin floor fans respectively. The infamous Oribi/Oryx oil field is located in the 14At1 oil-bearing reservoirs. The claystone overlying the 13At1 are believed to have accumulated severely lowered oxygen conditions. Post 22At1 sedimentation is composed of highstand shelf deposition of glauconitic clay, occasional sands widespread clays exclusively. A major late Oligocene unconformity can be recognized. The biogenic clay of the early

Miocene widely developed throughout the Southern half of the basin and other depositional environments suggest that the Agulhus arch has essentially been founded by this time (McMillan, et al., 1997). The stratigraphy (Figure 2-3) below shows the tectonic events that took place over the years in the Bredasdorp Basin.

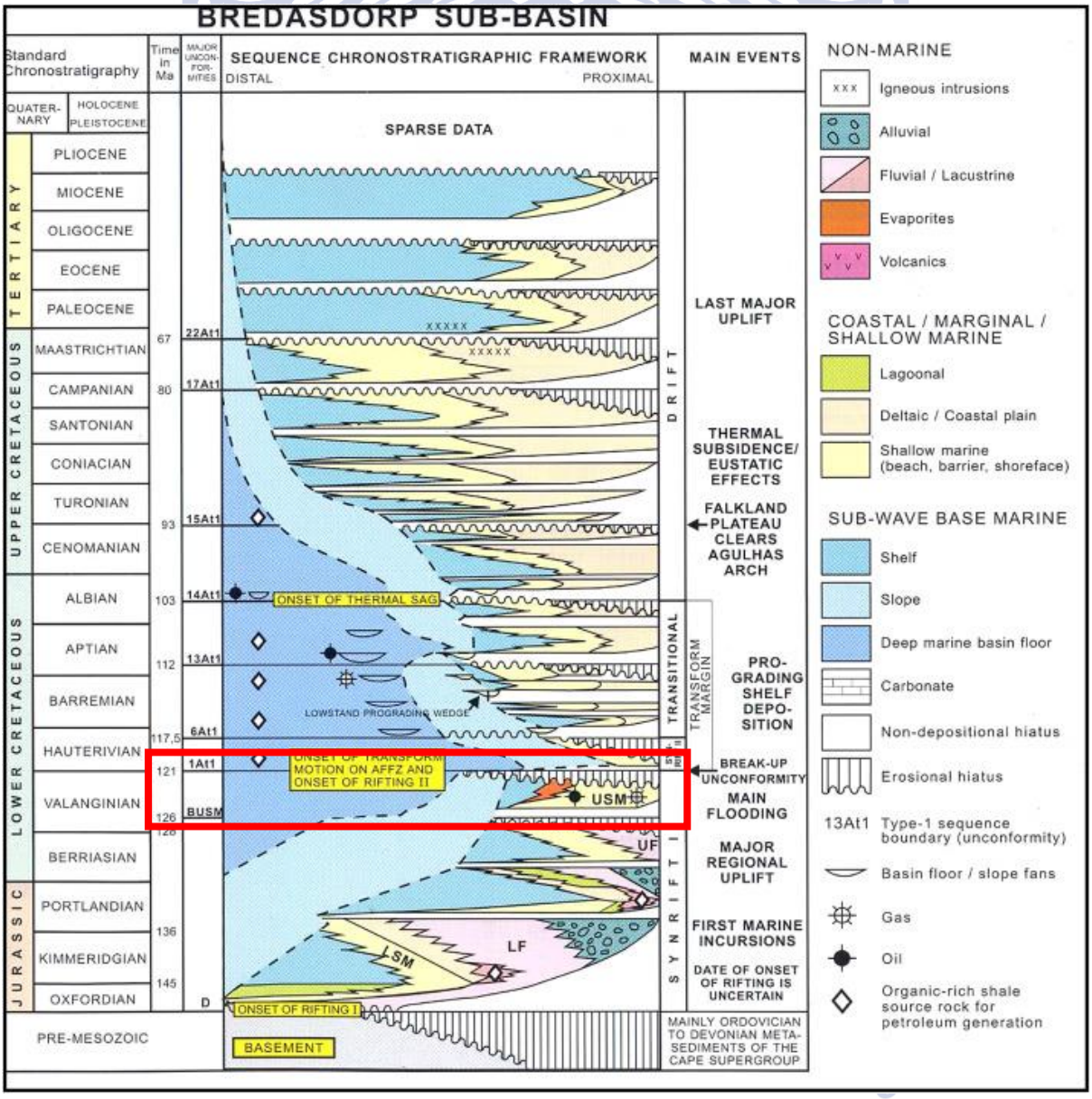

Figure 2-3: General Chronostratigraphy of the Bredasdorp Basin (Mudaly, et al., 2009).

2.3 DEPOSITIONAL SETTING

Bredasdorp Basin developed from fan deltas, river-dominated deltas, and wave-dominated deltas as well as associated coastal systems during its post-rift Cretaceous history (Brown, et

al., 1995). Concurrently, fine-grained density and suspension deposits to leveed slope and basin floor turbidite fans and again to fine-grained turbidite system lead to the evolution of the slope and basin system. These depositional changes were in response to the second-order tectonic episodes, to variations in sediment supply rates and subsidence or accommodation rate, and increasing open process (Brown, et al., 1995). The high gradient fluvial systems supplied the sediments during the supercycle 1-5 (126-117.8Ma) to the four relatively isolated fault-bounded sub-basins. The central restricted sub-basin is dominated by prograding river-deltaic systems in the southward direction across the ramp like and faulted north margin. During the second post-rift supercycle 6-12 (117.5-112Ma), the progradation of the well-developed river-dominated deltaic and it's associated coastal systems took place into the expanded basin predominantly from the north and northwest. Type 1 erosion was developed by the lower subsidence rates and high sediment supply and also developed a well-developed low stand and highstand deltaic systems. The Bredasdorp Basin expanded extensively following the uplift and the second order unconformity 13At1 (112Ma). The Basin become fully open to the Indian Ocean circulation and wave energy which leads to a deltaic and inter-deltaic coastal system to enter the basin from the West to Northwest direction during supercycle 13 and southwest during supercycle 14. During supercycle 14-15 and 17-20 the river shifted from northwest to enter the basin (Brown, et al., 1995).

2.4 THE GEOLOGY OF THE UPPER SHALLOW MARINE SANDSTONES

The upper glauconitic sandstone developed above an unconformity taking after a second major marine transgression into the Bredasdorp Basin. This was trailed by an overall regressive phase which was dominated by recurrent progradation. The western and eastern areas of the gas field region were subjected to essentially diverse subsidence rates and depositional styles at this time (Mcmillan, et, al., 1997). The uniformly thick upper shallow marine unit in the east gives way to interbedded marine and non-marine intervals in the west. Discontinuous reactivation of faulting records for exceptionally thick stacked cycles and synsedimentary tectonic settings which were prevalently vertical in the east and predominantly tilted in the west (Mcmillan, et al., 1997). It is understood that the reactivation of the basin margin normal faulting at the time may have been responsible for the second marine transgression. The upper glauconitic sandstones in the eastern area of the gas field achieved a thickness of up to 237 meters. The glauconitic sandstone sequence is generally composed of blocky or recurrent upward coarsening and cleaning units that are commonly cross-bedded. These sandstones are generally

rich in quartz grains, poor in lithic, and variably glauconitic (Mcmillan, et al., 1997). The exact age of these sandstones interval is not clearly defined because identifying macrofaunal and microfaunal proved difficult to find and hence the age is estimated to be anywhere between Portland and late valanginian (Figure 2-4 and 2-5). The Western gas fields consist of the marine components which are characterized by a huge abundance of the coarse-grained sandstones and conglomerates and carboniferous detritus corresponding with the disappearance of merge shell debris, compared with eastern sandstones (Mcmillan, et al., 1997). The upper shallow marines are the best reservoirs of the gas field area and possess significant porosities and permeability.

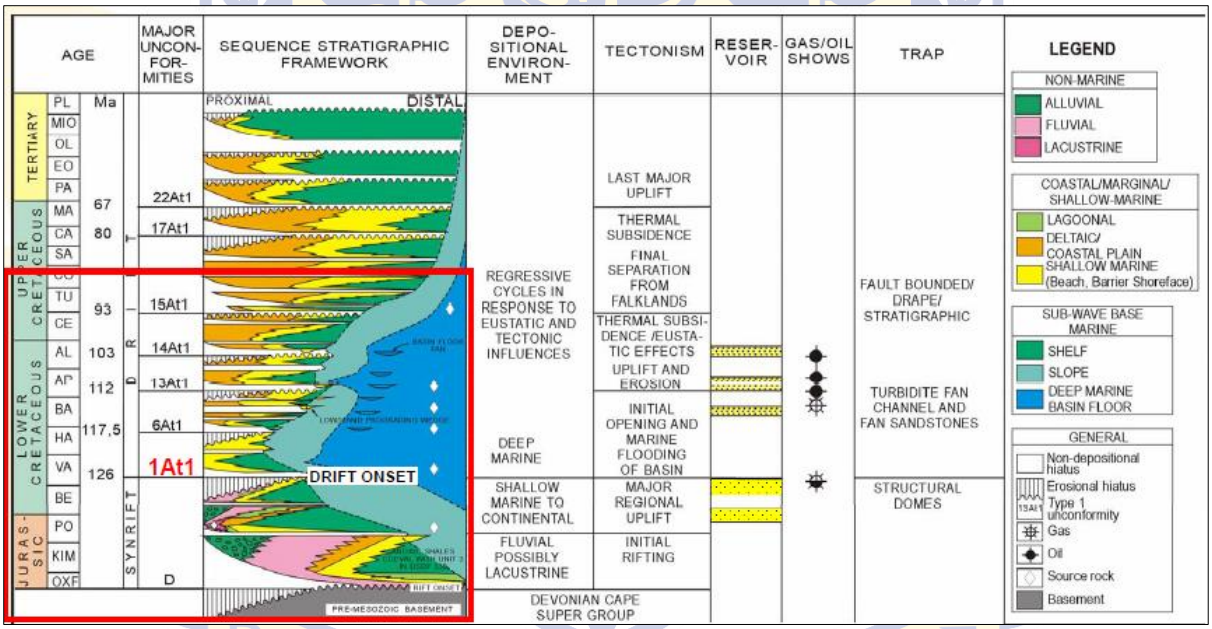

Figure 2-4: Generalised chronostratigraphy of the Bredasdorp Basin (Mudaly, et al., 2009).

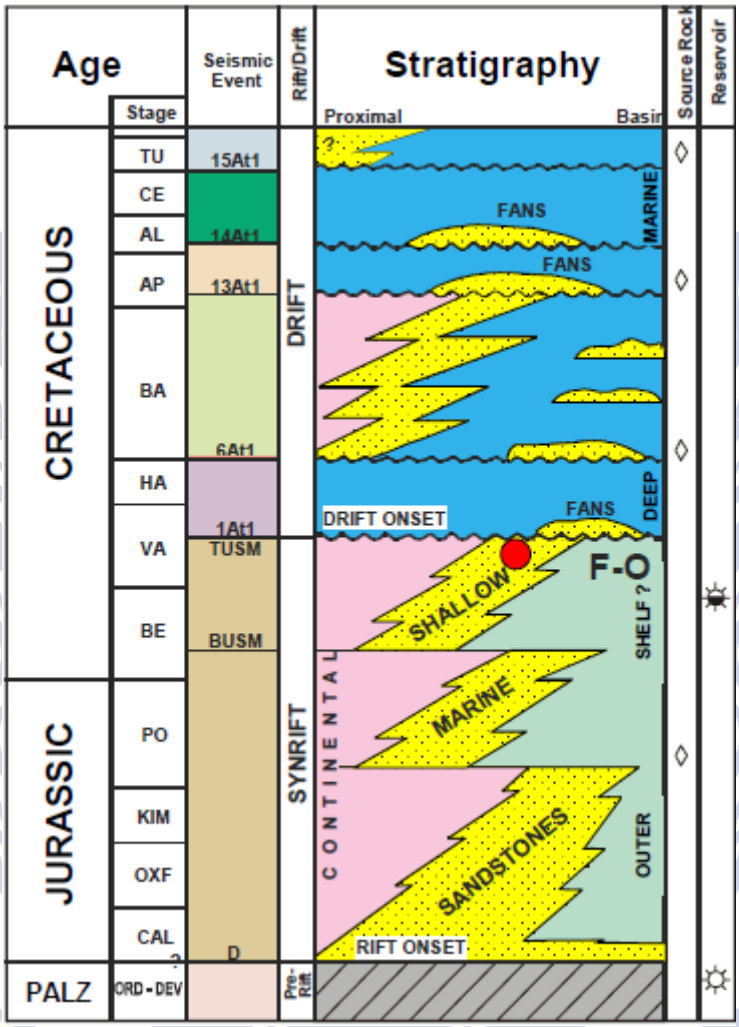

Figure 2-5: Simplified chronostratigraphy of the Bredasdorp Basin (Mudaly, et al., 2009).

The principal reservoirs of the Valanginian shallow marine sandstones are overpressured, tight and highly faulted located beneath the 1At1 drift onset unconformity (Mudaly, et al., 2009). These sandstones were deposited within a tidal dunefield setting as an extensive "sheet". The top of the upper shallow marine (TUSM) is a diachronous flooding surface overlain by a low-velocity shale (LVS) (Higgs, 2009).

REFERENCES

Brown, L.F., Brown Jr., L.F., Benson, J.M., Brink, G.J., Doherty, S., Jollands, A., Jungslager, E.H.A., Keenan, J.H.G., Muntingh, A and Van Wyk, N.J.S. (1995). Sequence stratigraphy in offshore South African divergent basins: an Atlas on Exploration for Cretaceous Lowstand Traps by SOEKOR Limited. AAPG Studies. Geol. 41, p 83–137 (SOEKOR (Pty) Ltd.).

Davies, C.P.N. (1997). Hydrocarbon evolution of the Bredasdorp Basin, offshore South Africa: From source rocks to reservoir. PhD thesis, University of Stellenbosch, South Africa.

Dingle, R.V., Siesser, W.G and Newton, A.R. (1983). Mesozoic and Tertiary Geology of Southern Africa: A Global Approach to Geology. s.l.: Taylor and Francis.

Higgs, R. (2009). Cretaceous 'USM' Reservoir, FO Gas Field, Offshore South Africa: Sedimentological factors affecting economic viability. Cape Town South Africa, AAPG International Conference and Exhibition Search and Discovery article #20072.

Malan, J.A and Viljoen, J.H.A. (1990). Mesozoic and Cenozoic geology of the Cape South Coast. Guidebook Congress '90, *Geological Society of South Africa*, 1-81.

McMilian, I.K., Brink, G.J., Broad, D.S and Maier, J.J. (1997). Late Mesozoic sedimentary basins off The South Coast of South Africa. *Sedimentary Basins of the world*, Volume 3, p. 319 – 376.

Mudaly, K., Turner, J., Escorcia, F and Higgs, R. (2009). F-O gas field, Offshore South Africa - From Integrated approach to field development. *American Association of Petroleum Geologist (AAPG) Search and Discovery article*, Issue 20070.

Petroleum Agency South Africa. (2012). Petroleum Exploration in South Africa.

Roux, J. (1997). Potential outlined in Southern Outeniqua Basin off South Africa. Oil & Gas Journal. July 21, 87-91.

CHAPTER THREE

3 LITERATURE REVIEW

3.1 INTRODUCTION

The Bredasdorp basin is well known because of its wide accumulation and production of oil and gas but mostly gas. A large number of work undertaken by Soeker (now PETROSA) and other petroleum companies on the Southern offshore basins (Bredasdorp in particular) remains internal reports, and only a few components are essentially published. Published information dealing with Geology, Stratigraphy, tectonic history and depositional environment include those of (Mcmillan, et al., 1997), Du Toit (1976, 1979), Leith and Rowsel (1979), (Mclachlan, et al., 1976), Marot and Mclachlan (1982) and Dingle et al., (1983). (Mudaly, et al., 2009) and Higgs (2009) also conducted a study focusing on the geology, depositional environment, and economic potential of the upper shallow marine (USM) wells (F-O) gas field.

The succession of shales and siltstones of lower Cretaceous age and younger are overlying the reservoir interval and covering the horizon 1At1 unconformity which was deposited during the drift phase in open marine conditions (Fatti, et al., 1994).

Fatti, et al., 1994 studied the variation of acoustic impedance across the upper shallow marine (USM) gas sandstone reservoirs. They observed that in some wells (F-O2 and F-A10), low-velocity shale and the underlying gas reservoir have low acoustic impedance with little contrast between them and in some area gas sandstones have a high velocity and therefore higher acoustic impedance. The studies conducted in the upper shallow marine interval highlighted the effect of low-velocity shale overlying the gas sandstone reservoirs on the 1At1 and the acoustic impedance variations at the top of the gas sandstone reservoirs (Base of low-velocity shale). However, the cause of the acoustic impedance variations across the USM has not been understood and therefore this research aims to investigate the cause of these variations.

3.2 CORING

The best way to obtain more detailed information about the formation is through coring. The core sample results are unequivocal (Rider, 2002). Two techniques are commonly used to obtain the core from the well. The first one is a “whole core”; this technique is very expensive

and slow. It involves a cylinder of rock, usually about 7.62cm to 10.16cm in diameter and up to 15m to 18m long. It is obtained by core barrel, a hollow pipe tipped with a ring-shaped diamond chip-studded bit which cut the core and bring it to the surface. The second and the cheaper technique to get a core sample of the formation is "sidewall coring". This technique is subdivided into two methods, percussion cores and rotary sidewall cores with the latter being the more expensive of the two and yield better results. The percussion method involves steel cylinder-coring gun-hollow point steel bullets mounted along its sides and moored to the gun by short steel cables. This method can be performed after the formation has been drilled by means of lowering the coring gun to the bottom of the area of interest and firing the gun individually as the guns are pulled up the hole. The cables pull the hollow bullets and the plug of the formation loses and carries them to the surface. The second method involves the lowering of a circular-saw assembly to the area of interest on wireline and the core is pulled out. There is a serious problem with cores and is usually neglected. The change the core undergoes as they are pulled to the surface, they always degrade to some degree during the process of cutting, handling and studying it. A non-destructive technique is being used commonly when studying the cores nowadays such as MRI scanning to characterize grain size, porosity, permeability and the type of fluid present within the pore space. More attention is paid and care is being taken when dealing with cores to minimize the damage on the cores especially during transportation from the drilling site to the laboratory. The most common way to do this is to completely freeze the using liquid nitrogen and in some cases, a special polymer is used to preserve the core from the damage.

3.3 WELL LOGS

The continuous recording of the geophysical parameter along a borehole/well produces a geophysical wireline log (Rider, 2002). This geophysical well log is obtained by plotting the value of measurement continuously against depth in the well. This continuous recording can go as deep as 6km or more. The appropriate name given for this application is a wireline geophysical well log, shortened to well log. Different geophysical logs exist nowadays which records the geophysical measurement along the borehole. The characteristics of geophysical well logs such as gamma-ray logs, which measure the radioactivity of the elements within the formation or sonic log which measures the time taken for the sound to reach the receiver at a distance along a tool, and many others, will be discussed later. The process of well logging is necessary because geological sampling during drilling leaves a very imprecise record of the

formations encountered (Rider, 2002). The results of cores are unequivocal but taking the whole core to the surface by mechanical coring is both slow and expensive. Geophysical well logging can be used because it fills the gap between cuttings and core but greater care needs to be taken because even though this process is precise but it is equivocal which means it needs interpretation to bring a log to the level of petrophysical and geological experience.

3.4 CHARACTERISTICS OF THE SELECTED WIRELINE LOGS

3.4.1 GAMMA RAY

The gamma-ray log is a measurement of the formations of natural radioactivity. Gamma-ray emissions are produced by three radioactive series found on the earth crust (1) potassium K_{40}) series (2) Uranium-series (3) Thorium series (Rider, 2002). Gamma-ray emissions passing through rocks are slowed and absorbed at a rate which depends on the formation. The gamma-ray log can be used to identify lithologies and for correlating zones. Clean sandstones (shale-free) and carbonates have a low concentration of radioactive elements and therefore give low gamma-ray log readings. In shale formations, a gamma-ray logs response increase because of the high concentration of radioactive in the shale formations. However, a shale free formation may also a high gamma-ray response if the formation contains potassium feldspar, glauconite, uranium-rich water, and micas because these minerals have high radioactive concentration. Besides the use of gamma-ray for identifying lithologies and correlating zones, it can also be used for the volume of shale calculation in the porous reservoirs because shale is more radioactive than sands or shale.

3.4.2 RESISTIVITY LOG

Resistivity is the rock property on which the entire concept of logging first existed. The first electric log was run in 1927 by the Schlumberger brothers Marcel and Conrad (Asquith and Gibson, 1982). Resistance is the property of any material irrespective of their size and shape to resist the flow of electricity. Resistivity is the measurement of resistance, the opposite of resistivity is conductivity. Hydrocarbons, rock and freshwater in log interpretation all act as an insulator and are non- conductive and therefore have lower resistivity. The principal use of resistivity log is to detect hydrocarbons within a reservoir, it can also be used estimate porosity and water-bearing zones, and this is because, during drilling, borehole fluids (water, oil or gas) move into porous and permeable zones surrounding the borehole.

The rock matrix or grain ore non-conductive and therefore the ability of the rock to transmit current is almost entirely a function of water in the pores. Resistivity response is high if there is a presence of hydrocarbons in the formation because hydrocarbons like the matrix are non-conductive. The resistivity response is low if there is a presence of water in the pore spaces. Resistivity is also very important for water saturation calculation. There are two types of logs today which measure formation resistivity, an induction and electrode logs with the former as the most common type of logging tool (Atlas, 1975). Induction tools consist of one or more transmitting coils emitting a high-frequency alternating current at a constant intensity and should be used in non-salt saturated drilling mud to obtain an accurate value of formation true resistivity. The two types of induction devices are induction electrode log and Dual induction focused log. The second is the electrode device. In the borehole, the electrodes are connected to the power source which allows the current to flow from the electron passing through the borehole fluids into the formation (Figure 3-1). The electrode resistivity logs include the following (1) normal (2) lateral (3) laterolog (4) microlog (5) microlaterolog (6) Spherically focused log and these logs are used in a borehole filled with salt-saturated drilling muds to obtain a more accurate value of formation true resistivity.

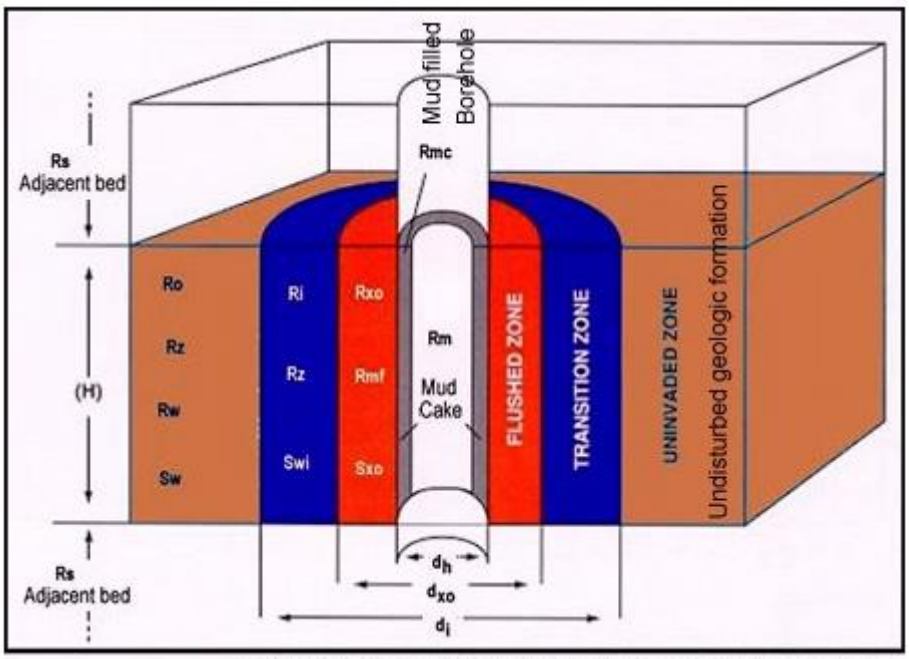

Figure 3-1: Illustration of the borehole formation and resistivity measurements (https://www.eoas.ubc.ca/~fjones/aglosite/objects/meth_10c/boreholes.htm) August 2019.

During the drilling process, the mud is kept at a higher pressure than the formation fluid to avoid blowouts. As a result of the higher pressure, the mud is forced to invade the rock formation leaving a mud cake along the borehole. The invasion of mud fluid produces artificial resistivity readings. Logs typically give three measures of resistivities, shallow, medium and deep corresponding to the three zones around the borehole as illustrated in Figure 3-1 above.

3.4.3 SONIC LOG

The sonic log is a porosity log that measures the interval transit time of a compressional sound wave travelling through one foot of formation. The sonic device consists of one or more sound transmitters (sound source) and two or more receivers. The most recent sonic logs are Compensated Borehole device (BHC). These devices are mostly preferred because they reduce the borehole irregularities (Kobesh and Blizard, 1959) as well as errors caused by the tilting on the sonic device (Schlumberger, 1972). BHC tool (Figure 3-2) has two transmitter and four receivers which are arranged in two dual receiver sets. BHC typically has a pulse of 100 ≠s to 200 ≠s with a gap of about 50ms, giving about 20 pulses per second. There are four individual Tx-Rx recordings needed per measurements, therefore 5 measurements can be made per second. A sonic logging speed of 1500m/h gives one reading per 8/cm of the borehole. The Tx-Rx difference is usually 0.9m and 1.5m and the Rx-Rx distance between pairs is usually 0.6m. The sonic velocity can be determined from a chart or by following the formula (Wyllie, et al., 1958). This formula can be used to determine sonic porosity only in consolidated sandstones and carbonates with intergranular or intercrystalline porosities. However, it cannot be used in vuggy or fracture porosity because the calculated porosity will be too low. This is due to sonic porosity only recording matrix porosity rather than vuggy or fracture secondary porosity. The vuggy or fracture porosity vuggy or fracture porosity can be obtained by subtracting sonic porosity from the total porosity. This porosity can be very useful in carbonate exploration as a mapping parameter. The sonic log response increase due to the presence of hydrocarbons (hydrocarbon effect) in the formation. The sonic derived porosity needs to be corrected from the hydrogen effect or otherwise, it will be too high. Hilchie (1978) suggest the following the empirical corrections for hydrocarbons effect

Φ=Φsonic X 0.7 (Gas)

Φ=Φsonic X 0.9 (Oil)

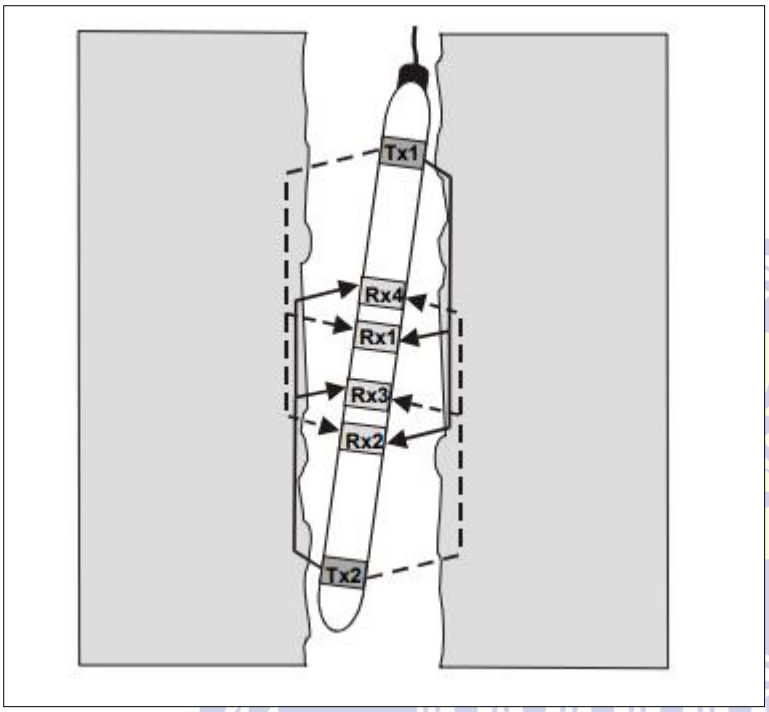

Figure 3-2: Borehole compensated sonic tools (Glover, 2009)

3.4.4 DENSITY LOG

The formation density log is a porosity log that measures the electron density of the formation (Serra, 1984). A density logging tool (Figure 3-3) is a contact tool which consists of a medium gamma-ray source that emits gamma rays into a formation (Serra, 1984). The source of the gamma-ray emissions is either Cobalt-60 or Cesium-137. The gamma-ray emissions collide with the electrons in the formations which results in a loss of energy from gamma ray particles. The interactions process between gamma-ray emissions and electrons was described by (Tittman and Wahl, 1965) as Compton scattering. The formation density indicator is counted as those scattered gamma rays which reach the detector located at a fixed point from the gamma-ray source (Asquith and Gibson, 1982). The number of electrons in formations (electron density) is directly proportional to the number of Compton scattering collisions. Because of that, we can relate electron density to bulk density of the formation in gm/cc. The density log can be used to (1) detect gas bearing zones (2) identify evaporate minerals (3) determine hydrocarbon density and (4) evaluate shaly sand reservoirs and complex lithologies (Schlumberger, 1972). The density log is also easily affected by borehole invasion. If the formation invasion is shallow then the low density of the formation's hydrocarbons will increase density-porosity. Gas affects the density logs significantly as opposed to oil. A fluid

density of 0.7 gm/cc has been suggested to be used if the true gas density is unknown (Hilchie, 1978).

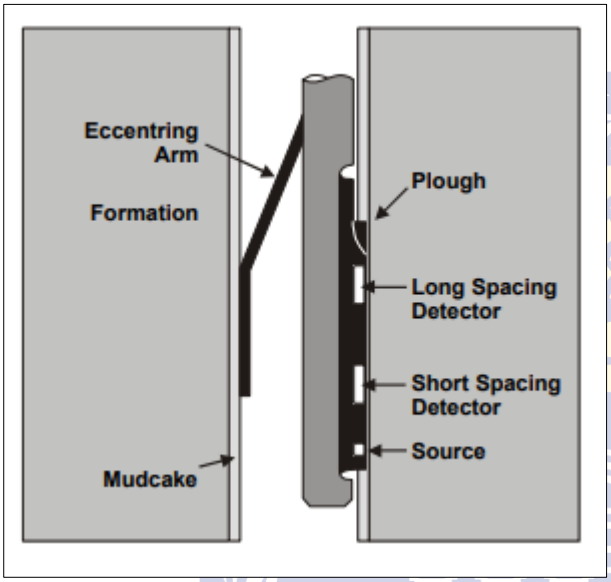

Figure 3-3: Schematic diagram of a formation density tool (Glover, 2009)

3.4.5 NEUTRON LOG

Neutron logs are porosity logs that measure the hydrogen ion concentration in a formation (Rider, 2002). The chemical source in the neutron logging tool produces neutrons. This chemical source may be a mixture of americium and beryllium which will continuously emit neutrons. The collision of neutrons with the nucleus in the formation results in some neutron losing energy (Rider, 2002). The maximum energy loss of the neutron occurs during the collision with hydrogen atoms because the mass of the hydrogen atom and nucleus is almost equal. The amount of energy lost during collisions can be related to porosity because, in porous formations, hydrogen in a porous formation is concentrated in the fluid-filled pores. This lowering of neutron reading by the presence of gas is called the gas effect (Asquith and Gibson, 1982). The neutron log response is controlled by various things like the difference in detector types, spacing between source and detector and lastly by lithology, sandstone, limestone or dolomite (Rider, 2002). There are two types of neutron log tool. The first one was the sidewall neutron log. This neutron device has both the source and the detector in a pad which is pushed against the borehole wall. The second one is the compensated neutron log (Figure 3-4) which has a neutron source and two detectors. The latter is the most preferred one because it is less

affected by borehole irregularities. However, both these tools can be recorded in limestone, sandstone and dolomite units.

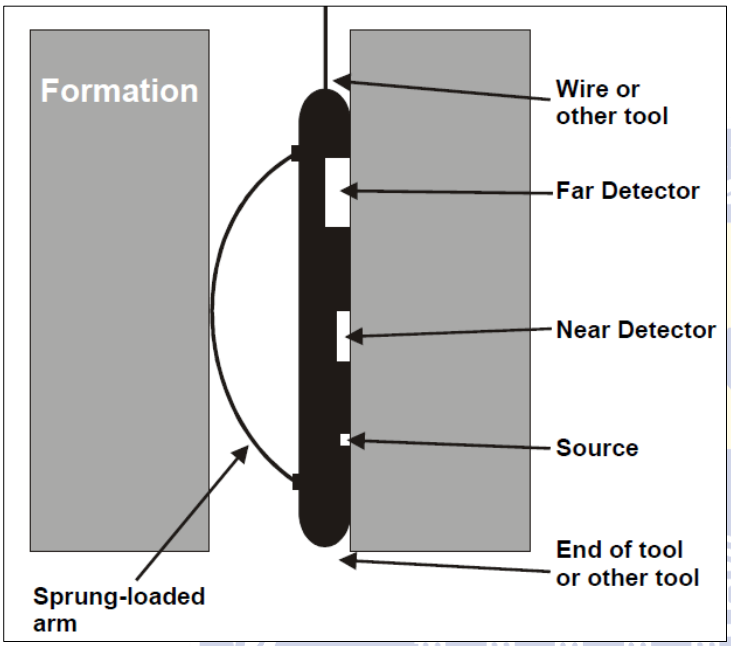

Figure 3-4: The Compensated Neutron Log (CNL) tool (Glover, 2009)

3.4.6 CALIPER LOG

Caliper logs measure the diameter (size and shape) of the recently drilled borehole. Mechanical arms (Figure 3-5) record the borehole size. The measured borehole size can be used to correct other logs, predict borehole volume for cementing and also gives an indication about the condition of the lithology such as washouts of formation properties (Schroeder, 2004).

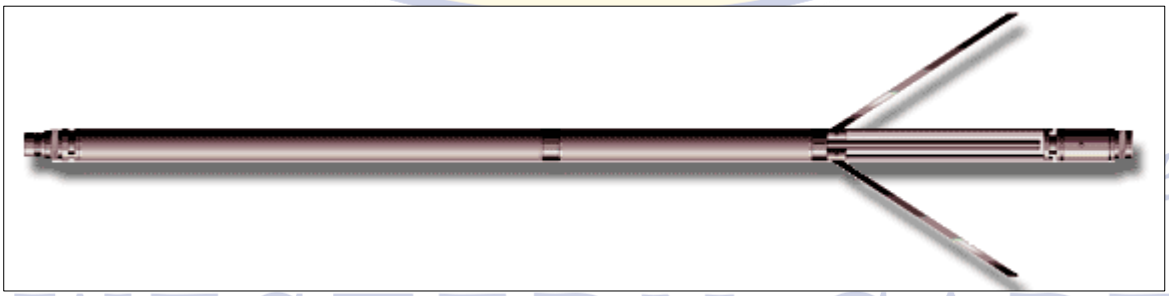

Figure 3-5: Two arm caliper instrument (http://www.geologging.com/wp-content/uploads/2017/04/3-arm-Caliper.pdf) February 2019.

REFERENCES

Asquith, G.B and Gibson, G. (1982). Basic well log analysis for Geologists. Tulsa, Oklahoma, USA: The American Association of Petroleum Geologists.

Atlas, D. (1975). Log Interpretation fundamentals. s.l.:Dresser Atlas.

Dingle, R.V., Siesser, W.G and Newton, A.R. (1983). Mesozoic and Tertiary Geology of Southern Africa: *A Global Approach to Geology.* s.l.: Taylor and Francis.

Du Toit, S.R. (1976). Mesozoic Geology of the Agulhas Bank, South Africa, Cape Town: PhD thesis (Unpublished). University of Cape Town.160 pp.

Du Toit, S.R. (1979). The Mesozoic history of the Agulhas Bank in terms of the plate tectonic theory. *Geokongress 77. Geological Society of South Africa,* Volume 6, pp. 197-203.

E.H., Johansen, T.A., Avseth, P and Bredesen, K. (2016). Quantitative interpretation using inverse rock-physics modelling on AVO data. *The leading edge,* pp. 677-683.

Fatti, J.L., Smith, G.C., Vail, P, J., Strauss, P, J and Levitt, P.R. (1994). Detection of gas in sandstone reservoirs using AVO analysis: A 3-D seismic case history using the Geostack technique. *Geophysics,* 59(9), pp. 1362-1376.

Higgs, R. (2009). Cretaceous 'USM' Reservoir, FO Gas Field, Offshore South Africa: Sedimentological factors affecting economic viability. Cape Town South Africa, AAPG International Conference and Exhibition Search and Discovery article #20072.

Hilchie, D.W. (1978). *Applied open-hole log interpretation.* Golden, Colorado: D.W. Hilchie. Inc.

Glover, P. (2009). Petrophysics course notes, University of the Aberdeen, Scotland

Kobesh, F.P and Blizard, R.B. (1959.) Geometric factors in sonic logging. *Geophysics,* Volume 24, pp. 64-76.

Leith, M.J and Rowsel, D.M. (1979). Burial history and temperature-depth conditions for hydrocarbon generation and migration on the Agulhas Bank, South Africa. *Geokongress, Geological Society of South Africa,* Volume 6, pp. 205-217.

Marot, J.E.B and McLachlan, I.R. (1982). Petrography of the reservoir sandstones of the gas-bearing F-A structure, Offshore South Africa. *Abstract, 3rd. Symp. Sediment. Div., Geological Society of South Africa,* pp. 74-78.

McLachlan, I.R., Brenner, P.W. and McMillan, I.K. (1976). The stratigraphy and micropaleontology of the Cretaceous Benton Formation and the PB-A/1 well, near Knysna, Cape Province Trans. *Geological Society of South Africa abstract,* pp. 60-63.

McMilian, I.K., Brink, G.J., Broad, D.S and Maier, J.J. (1997). Late Mesozoic sedimentary basins off The South Coast of South Africa. *Sedimentary Basins of the world,* Volume 3, p. 319 – 376.

Mudaly, K., Turner, J., Escorcia, F and Higgs, R. (2009). F-O gas field, Offshore South Africa - From Integrated approach to field development. *American Association of Petroleum Geologist (AAPG) Search and Discovery article,* Issue 20070.

Rider, M.H. (2002). *The geological interpretation of well logs.* 2nd ed. s.l.: Rider-French Consulting Ltd.

Schlumbeger, (1972). *Log interpretation/charts.* Houston: Schlumberger well services.

Schroeder, F. (2004). *Well Log Data,* s.l.: American Association of Petroleum Geologists.

Serra, O. (1984). *Fundamentals of Well-Log Interpretation: The acquisition of logging data.* Vol.1 ed. Amsterdam: Elsevier.

Tittman, J. and Wahl, J. S. (1965). The physical foundations of formation density logging (Gamma-Gamma). *Geophysics*, 30(2), pp. 284-294.
Wyllie, M.R.J., Gregory, A.R and Gardner, G.H.F. (1958). An experimental investigation of factors affecting elastic wave velocities in porous media. *Geophysics*, Volume 23, pp. 459-493.
http://www.geologging.com/wp-content/uploads/2017/04/3-arm-Caliper.pdf

https://www.eoas.ubc.ca/~fjones/aglosite/objects/meth_10c/boreholes.htm

CHAPTER FOUR

4 PETROPHYSICAL INTERPRETATION OF SHALLOW MARINE SANDSTONE RESERVOIRS

ABSTRACT

This chapter focused on the study carried out to assess the Petrophysical evaluation of Upper Shallow Marine (1AT1 formation) sandstone reservoirs of 10 selected wells (F-O1, F-O2, E-M4, E-CN1, E-G1, E-W1, F-A10, F-A11, F-A13 and F-L1) in the Bredasdorp Basin, offshore, South Africa. The studied wells were selected randomly across the upper shallow marine interval with the purpose of conducting a regional study to assess the difference in reservoir properties across the formation. The datasets used in this study were geophysical wireline logs, conventional core analysis, and geological well completion report. The physical rock properties, such as lithology, fluid type, and hydrocarbon bearing zone were qualitatively characterized while different parameters like the volume of clay, porosity, and water saturation and were quantitatively estimated. The upper shallow marine reservoirs were penetrated in different depth ranging from a shallow depth of 2442m at well F-L1 to a deeper depth of 4256.7m at well E-CN1. The average volume of clay, average effective porosity, and average water saturation ranged from 8.6%- 43%, 9%- 16% and 12%- 68%, respectively. Porosity distribution is fairly equal across the field from east to west except in well F-A10, F-A13 and F-A11 which shows a much higher porosity and E-CN1, F-O1 and F-O2 which shows lower porosity.

4.1 INTRODUCTION

Acoustic impedance is the product of density and velocity. These two parameters are influenced by many factors such as porosity, water saturation and volume of clay amongst others. It is then of utmost importance to determine those Petrophysical properties to understand the extent at which they are affecting acoustic impedance. The understanding of the distribution of these parameters will also play a vital role in understanding the variations in acoustic impedance across the study area. This chapter focused on the study carried out to assess the Petrophysical evaluation of Upper Shallow Marine sandstone reservoir of 10 selected wells (F-O1, F-O2, E-M4, E-CN1, E-G1, E-W1, F-A10, F-A11, F-A13 and F-L1) in the Bredasdorp Basin, offshore, South Africa. The studied wells were selected randomly across the Upper Shallow Marine interval with the purpose of doing a regional study to assess the difference in reservoir properties across the formation of the study area. Petrophysical evaluation is regarded as the process of characterizing the physical and chemical properties of the rock-pore-fluid system through the integration of geological environment, geophysical well logs, reservoir rock, and fluid sample analyses. Geophysical well logs are a continuous recording of a geophysical parameter along a well/borehole (Rider, 2002). A reservoir rock is a porous and permeable rock that contains interconnected pores or holes that occupy the areas between the mineral grains of the rock (Rider, 2002). Geophysical logs are used for the calculation of the volume of clay, porosity, water saturation, moveable hydrocarbon, hydrocarbon density and other factors related to quantification of the amount of hydrocarbons in a reservoir for the estimation of reserves (Rider, 2002).

The sandstone reservoirs of the Bredasdorp Basin are characterized by a range of stacked and amalgamated channels (McMillan, et al., 1997). The upper glauconitic sandstone developed above an unconformity taking after a second major marine transgression into the Bredasdorp Basin. This was trailed by an overall regressive phase which was dominated by recurrent progradation. The western and eastern areas of the gas field region were subjected to essentially diverse subsidence rates and depositional styles at this time (McMillan, et al., 1997). The uniformly thick upper shallow marine unit in the east gives way to interbedded marine and non-marine intervals in the west. The discontinuous reactivation of faulting, records for exceptionally thick stacked cycles and synsedimentary tectonic settings which were prevalently vertical in the east and predominantly tilted in the west (McMillan, et al., 1997). It is understood that the reactivation of the Basin margin normal faulting at the time may have been responsible for the second marine transgression. The upper glauconitic sandstones in the eastern area of

the gas field achieved a thickness of up to 237 meters. The glauconitic sandstone sequence is generally composed of blocky or recurrent upward coarsening and cleaning units that are commonly cross-bedded. These sandstones are generally rich in quartz grains, poor in lithic, and variably glauconitic (McMillan, et al., 1997).

The Western gas fields consist of the marine components which are characterized by a huge abundance of the coarse-grained sandstones and conglomerates and carboniferous detritus corresponding with the disappearance of merge shell debris, compared with Eastern sandstones (McMillan, et al., 1997). The upper shallow marines are the best reservoirs of the gas field area and possess significant porosities and permeability.

4.2 AIMS AND OBJECTIVES

The study was aimed at applying the expansive use of petrophysical analysis in the evaluation of the selected USM sandstone reservoirs. The physical rock properties, such as lithology, fluid type, and hydrocarbon bearing zone are qualitatively characterized while different parameters, such as the volume of clay, porosity, water saturation, and gas saturation have been assessed for selected reservoir intervals.

The strategic aims of this research were to:

- Identify sandstone reservoirs from the gamma-ray logs in the upper shallow marine interval (1AT1 unconformity).
- Calculate the volume of clay from gamma-ray log within the identified reservoirs.
- Calculate porosity and water saturation of the identified reservoirs and calibrate core data with the wireline logs to validate the results.
- Create a 3D parameter viewer TVD model from Interactive Petrophysics (IP) software to show the distribution of the calculated reservoir parameters across the study area.

4.3 MATERIALS AND METHODS

4.3.1 DATA ANALYSIS

The data was collected by Schlumberger Service Company and was provided for this study by the Petroleum Agency of South Africa (PASA). The data provided was as follows: geophysical wireline logs (LAS format) for 10 wells, 177 core plugs, conventional core analysis reports, and geological well completion reports. Geophysical wireline log data was arranged carefully, sorted, and prepared for easy access and quality controlled (QC) before being loaded into Interactive Petrophysics (IP) 4.2 software to be displayed as log Curves. IP software was used extensively throughout this study for interpretation, and analysis of the available digitized wireline logs (LAS format) data (Figure 4-1). The wireline log interpretation includes identification of sandstone reservoirs from gamma-ray and density/ neutron logs, calculation of clay volume, porosity and water saturation.

Table 4-1: Characteristics of wireline logs

Name	Uses
Gamma Ray (GR)	Lithology interpretation, shale volume calculation, calculate clay volume, porosity calculation, etc.
Calliper (CALI)	Detect permeable zone, locate a bad hole
Shallow Resistivity (LLS,ILS, MSFL)	Lithology interpretation, finding hydrocarbon bearing zone, calculate water saturation, etc.
Deep Resistivity (LLD and ILD)	Lithology interpretation, finding hydrocarbon bearing zone, calculate water saturation, etc.
Density (RHOB)	Lithology interpretation, identifying hydrocarbon bearing zone, porosity calculation, etc.
Neutron Porosity (NPHI)	Finding hydrocarbon bearing zone, porosity calculation, etc.
Sonic (DT)	Porosity calculation, wave velocity calculation, etc.

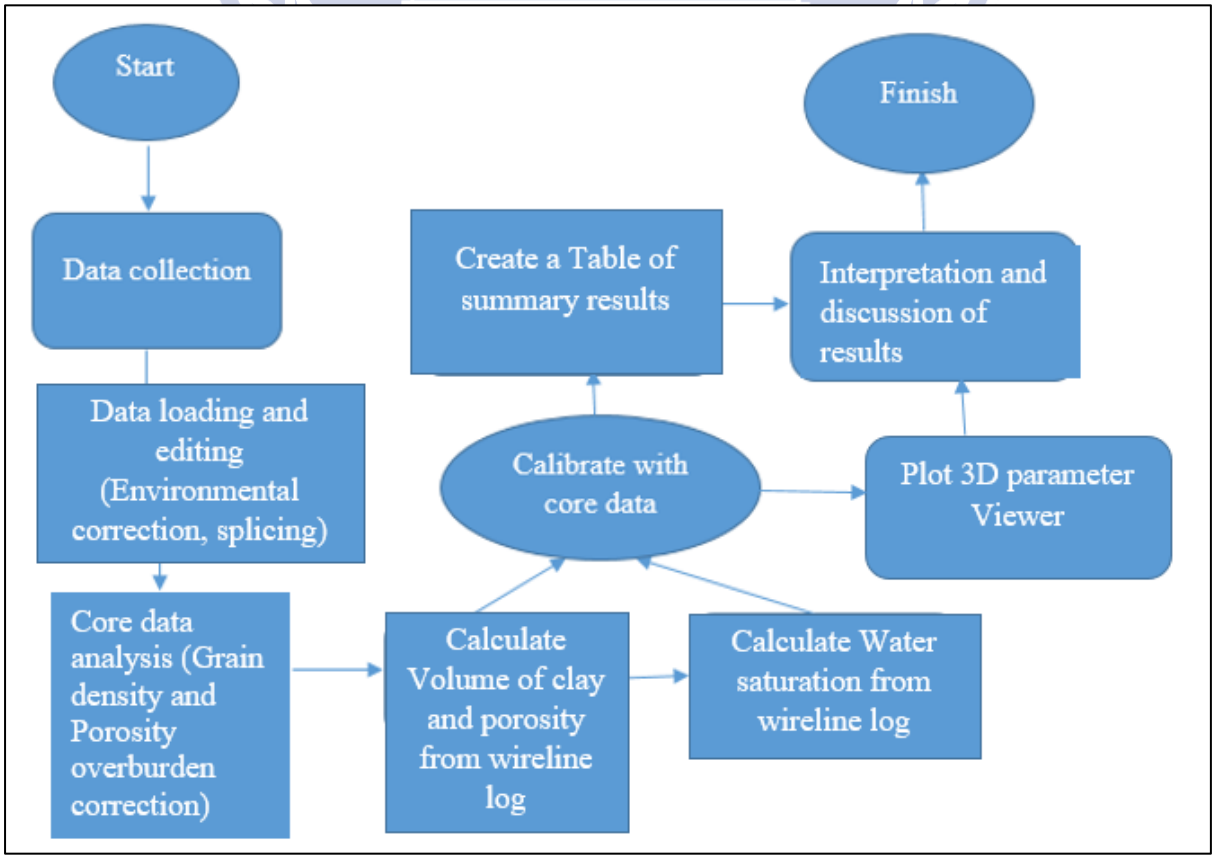

Figure 4-1: Flowchart illustrating a sequence of steps taken during petrophysical analysis.

4.3.2 CLAY VOLUME ESTIMATION

The first step in a Petrophysical analysis is to identify potential sandstone reservoirs or zone of interest (clean zones, free from shale with hydrocarbon) by defining a baseline on the gamma-ray (GR) logs to distinguish between sandstone and clay lithology. This is achieved by observing the behaviour of the gamma-ray log, maximum deflection to the right indicate a shale formation and maximum deflection to the left indicate clean sandstone (Jensen, et al., 2013). The gamma-ray baseline value is taken as the mean value obtained from the gamma-ray histogram plot (Figure 4-2). After identifying zones of interest or potential sandstone reservoirs, the next step is to calculate the volume of Clay (Vcl). The volume of clay (Vcl) quantity is defined as the volume of the wetted shale per unit volume of the reservoir rock (Jensen, et al., 2013. Clay volume is generally determined from the gamma-ray log in a porous reservoir because clay is usually more radioactive than sand or carbonate (Jensen, et al., 2013).

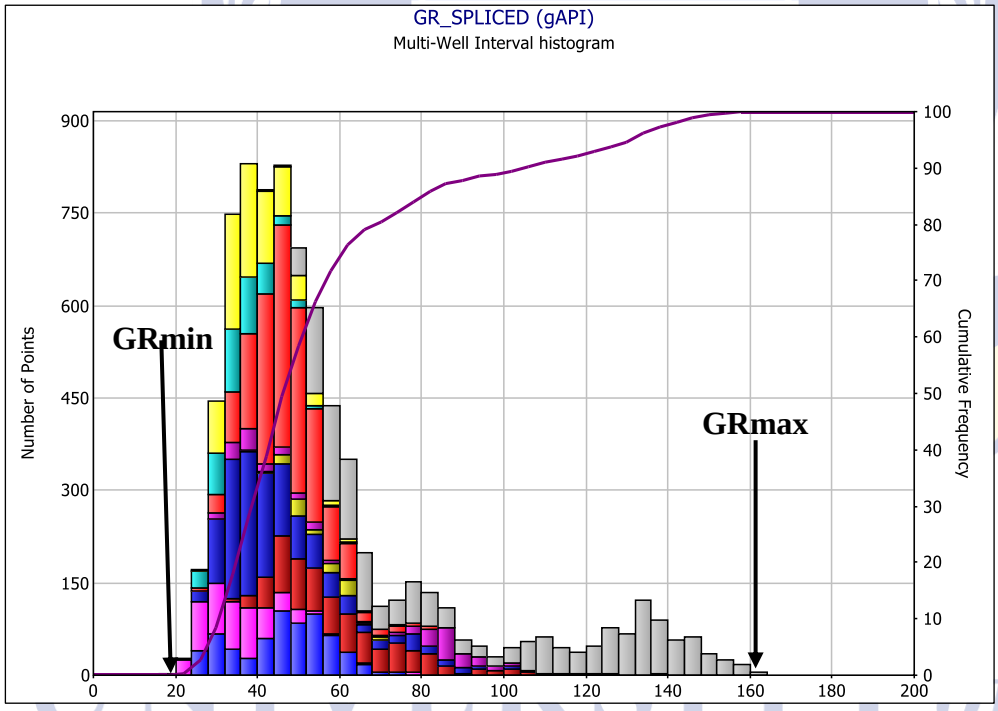

Figure 4-2: Multi-well histogram plot displaying the minimum and maximum gamma ray values.

The amount of volume of clay can be expressed as decimal fraction or percentage. The first step required to determine the volume of clay was to calculate the gamma-ray index (IGR). The linear equation explained below was used to determine the gamma-ray index:

$$IGR = \frac{GRlog - GRmin}{GRmax - GRmin} \quad \text{(1)}$$

Where:

IGR= Gamma-Ray Index

GRlog= Gamma-ray reading for each zone

GRmin and GRmax are the minimum (Clean sand) and maximum Gamma-ray value (shale). The minimum and maximum values used in the equation were obtained from the gamma-ray histogram plots (Appendix A) of which one example of the multi-well histogram plot is presented in Figure 4.2 above. The value of IGR obtained have to be corrected by a valid formula to obtain the optimum value usable for interpretation. Various non-linear (correction) equations and models used to calculate the volume of shale are presented below.

Larinov (1969) for tertiary rocks

$$Vsh = 0.083(2^{3.7IGR}-1) \quad \text{(2)}$$

Steiber (1970) $$Vsh = \frac{IGR}{3 - 2 * IGR} \quad \text{(3)}$$

Clavier (1971) $$Vsh = 1.7-[(3.38-(IGR+0.7)^2]^{1/2} \quad \text{(4)}$$

Larinov for older rocks $$Vsh = 0.33*(2^{2IGR}-1) \quad \text{(5)}$$

4.3.3 POROSITY DETERMINATION FROM WIRELINE LOGS

Porosity is the ability of the rock to store fluid within the pore spaces. Porosity was calculated from all three porosity logs (density, neutron and sonic). The following formulas were used to calculate porosity:

Density log porosity

$$\Phi = P_{ma}-P_b/P_{ma}-P_f \quad \text{(6)}$$

Where: P_b= fluid density of the mud filtrate (g/cc)

P_{ma}= matrix density (g/cc)

P_f= fluid density (g/cc); salt mud=1 and fresh water= 1 (Crain, 2014).

Neutron log porosity:

PhiN= Pe x Sxo x PhiNw…….. (7)

Where: PhiN= log reading, Phie= effective porosity, Sxo= water saturation in invaded zone and PhiNw= log reading in 100% water (Crain, 2014)

Sonic log porosity:

The porosity from the sonic slowness is different from the density or neutron tool. It reacts to primary porosity only (it does not react to fractures or vugs) (Crain, 2014). The basic equation for sonic porosity is the Wyllie Time Average

$\Phi=\Delta tl_{og}-\Delta t_{ma}/\Delta t_f-\Delta t_{ma}$..... (8)

Where Δt_f= time taken to travel through the pore space

Δt_{ma}= time taken to travel through the matrix (Crain, 2014).

The interval transit time of a formation is increased in the presence of hydrocarbons; this effect is known as the hydrocarbon effect. If this effect is not corrected, the porosity calculated from the sonic will be too high. Hilchie (1978) suggested the following empirical formulas to correct the hydrocarbon effect:

$\Phi= \Phi_{sonic}$ X 0.7 (Gas)……9

$\Phi=\Phi_{sonic}$ X 0.9 (Oil)……..10

The gas empirical correction was used for this study.

The core data was only available for eight wells (E-G1, E-W1, F-A10, F-A13 E-M4, E-CN1 F-O1, and F-O2) and therefore, calibration of core and well log data was only performed within those eight wells to validate the accuracy of the calculated logs. The conventional core analysis data used in combination with laboratory measured data for calibration is presented in Appendix B.

4.3.4 POROSITY DETERMINATION FROM LABORATORY MEASUREMENTS

The porosity laboratory measurements were conducted on the 177 core plugs from 8 out of 10 studied wells. The core porosity of the remaining two wells could not be determined from the laboratory because of the unavailability of core plugs in those wells. The core porosity was measured from the Helium porosimeter instrument (Figure 4-5) from the state of the art Petrophysics and Basin analysis laboratory (PETROLAB) at the School of Marine Geosciences, University of Haifa, Israel. Helium porosity is dedicated to determining grain

volume (solid volume) of the core plug this principle is based on Boyle-Marriotte's law. An XLS (Excel) report template was provided ready to calculate grain volume and pore volume based on the input of sample diameter (Figure 4-3), weight (Figure 4-4) and pressure read at the nanometer. All the input parameters are presented in the results of each well (Table 4-6 to 4-13). Nitrogen gas was used as a gas supply for these measurements. The core porosity measurements were calculated from the following equation:

$$\text{Porosity} = \frac{\text{Pore Volume}}{\text{Bulk Volume}} \quad \text{.....11}$$

$$\text{Pore Volume= Bulk Volume- Grain volume} \quad \text{.....12}$$

$$\text{Porosity} = \frac{\text{Bulk Volume} - \text{Grain Volume}}{\text{Bulk volume}} \quad \text{.....13}$$

Where:

Bulk volume = geometric volume calculated from diameter and length.

Grain volume= volume of the solid sample.

Pore volume= volume of connected pores that can be invaded by gas.

Porosity= the ratio of pore volume to sample bulk volume.

Boyle- Marriotte's law is used to calculate grain and pore volume from two measures of a known mass of Nitrogen gas. The gas is initially held in a reference pressure and then expanded into a matrix cup (core holder)

$$\frac{Pref * Vref}{\text{Tref}} = \frac{\text{Pexp} * \text{Vexp}}{\text{Texp}} \quad \text{.....14}$$

Where:

Pref= reference pressure (initial pressure)

Vref= reference volume

Tref- reference temperature

Pexp= expanded pressure (final pressure)

Vexp-expanded volume

Texp= expanded absolute temperature

During the experiment, it was assumed that the temperature remains constant during a series of measurements. The measurements were run twice on each core sample to increase the accuracy of the results and the average values were taken as the final measurements.

Figure 4-3: Calliper scale measuring the length and the diameter of the core plug.

Figure 4-4: Scale measuring the dry weight of the core plug.

Figure 4-5: Porosimeter instrument used to measure the porosity of the core plugs.

4.3.5 WATER SATURATION DETERMINATION

Water saturation is the ratio of water volume to pore volume (Crain, 2014.) The determination of water saturation from log curves can be grouped into two models namely, clean sand (shale free) and shaly sand models. The formation of the area of interest for this study is a shaly-sand formation; therefore water saturation models suitable for shaly-sand were used to determine the water saturation. Water saturation models used were simandoux, and Indonesia models. The models used the effective porosity as the input porosity in the water saturation model.

Simandoux (1963) proposed the following relationship:

$$\mathbf{Sw = aRw / 2\Phi m - Vsh/Rsh + \sqrt{(Vsh/Rsh)\,2 + 4/F * Rw * Rt}} \quad \ldots\ldots\ldots\ldots\ldots\ldots\ldots\ldots\ldots\ldots (9)$$

Where: Sw = water saturation, a= equation coefficient, Rw = resistivity of water, Rsh = resistivity of shale, Vsh = volume of shale, F = formation resistivity factor, Rt = true formation resistivity from corrected deep resistivity log, Φ = effective porosity fraction and m= cementation exponent

And the Indonesian formula was proposed in 1971 by Puopon and Leveaux. The relationship can be written as follows:

$$1/ \surd Rt = \surd \Phi e^{m}/ a*Rw + Vcl^{(1-Vcl/2}/\surd Rcl) * Swn^{/2} \ldots\ldots (10)$$

Where: Rt = resistivity curve from deep log reading, Rcl = resistivity of wet clay, Φe = effective porosity, Sw= water saturation fraction, Vcl = volume of clay fraction, Rw= formation water resistivity, m= cementation exponent, a=tortuosity factor and n= saturation exponent.

Calculated water saturation logs of the 10 studied wells were calibrated with the conventional core data presented in Appendix B to validate the accuracy of the calculated logs.

4.4 RESULTS AND INTERPRETATION

Two approaches (qualitative and quantitative) were taken to interpret the results obtained from the software modelling.

4.4.1 ANALYSIS AND INTERPRETATION OF CONVENTIONAL CORE RESULTS

4.4.1.1 GRAIN DENSITY

The grain density is defined as all the solid material in the rock because when interpreting the measurements, no effort is made to distinguish grains from any other solid mineral (Schlumberger, 2018). The grain density values of core samples were calculated in the laboratory using porosimeter analysis by dividing the dry measured weight with the grain volume. Grain density can also be determined from the density log using an estimate of porosity and the knowledge of the fluid content within the formation of interest.

The matrix densities of some common lithology are presented in Table 4-2 below.

Table 4-2: Matrix densities of common lithology (Schlumberger, 2018).

Lithology	Matrix value (g/cm^3)
Clay minerals	2.02-2.81
Chlorite	2.81
Illite	2.61
Kaolinite	2.55
Smectite	2.02
Coal	1.19
Halite	2.04
Sandstones (quartz)	2.65
Limestones	2.71
Dolomites	2.85
Orthoclase	2.57
Plagioclase	2.59
Anhydrite	2.98
Siderite	3.88
Pyrite	4.99
Glauconite	2.96
muscovite	3.88
albite	2.6
calcite	2.71

4.4.1.2 WELL F-O1 GRAIN DENSITY

The grain density of well F-O1 determined from the conventional core analysis measurements ranges from 2.55 g/cc to 2.67g/cc (Figure 4-6).

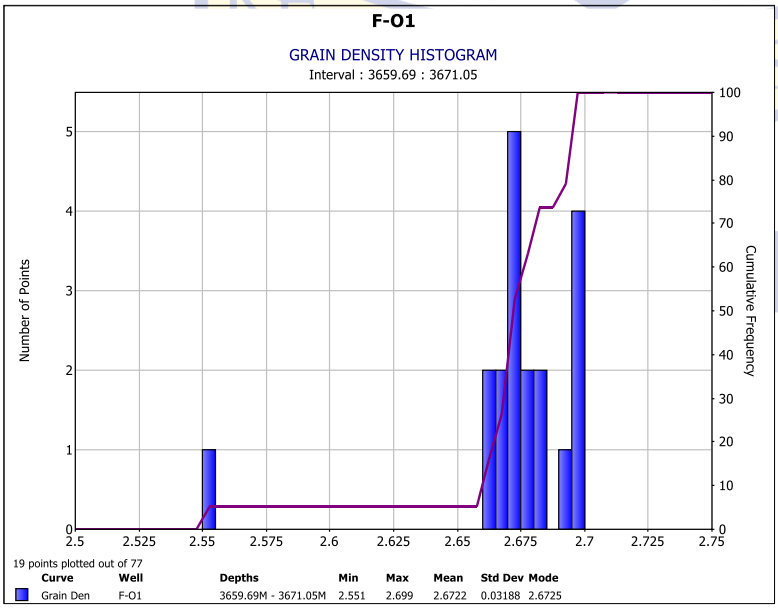

Figure 4-6: Histogram of well F-O1 grain densities.

A grain density value of about 2.551 g/cc in the histogram is due to the presence of Kaolinite. The presence of calcite and dolomite is in a small percentage in most of the core plugs. The standard deviation which is the number that shows approximately how far the values in the data set deviate from the mean value is 0.03 g/cc, which implies that the values vary from 2.64 g/cc to 2.7 g/cc.

4.4.1.3 WELL F-O2 GRAIN DENSITY

The grain density of well F-O2 ranges from 2.64 g/cc to 3.69 g/cc with a mean value of 2.67 g/cc as shown in Figure 4-7 below.

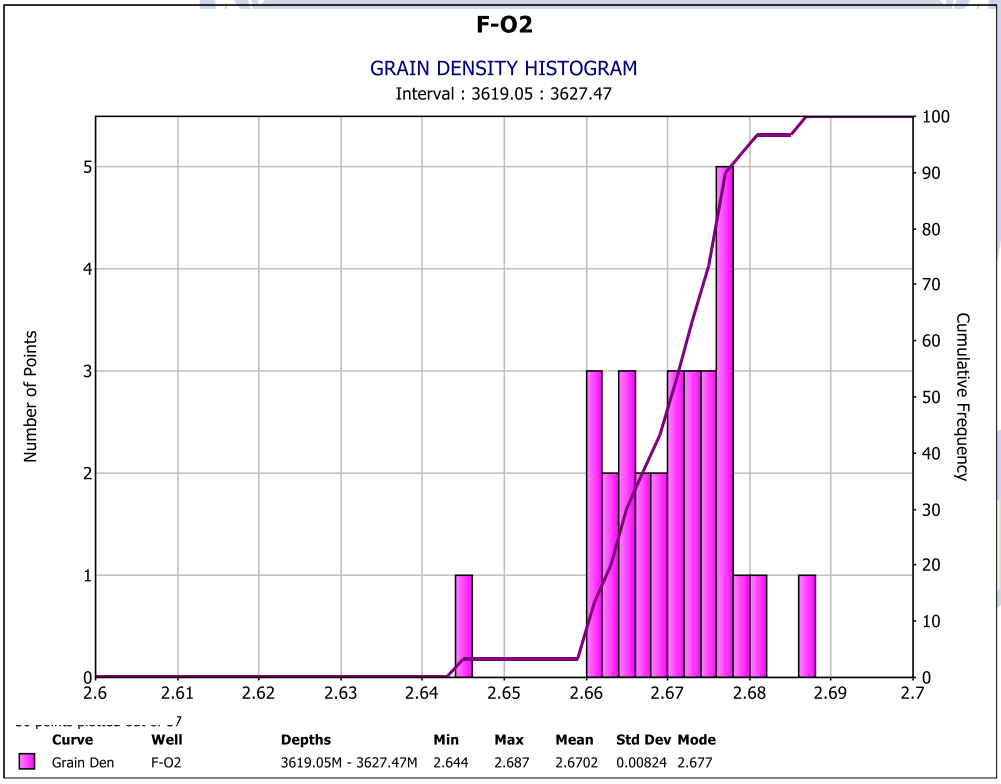

Figure 4-7: Histogram of well F-O2 grain densities.

Core results do not indicate persistence carbonate cement (calcite and dolomite) because of their insignificant presence except for 3677m and 3626m depth where the percentage of carbonate cement is between 3%-6% which was also confirmed by the thin section analysis. A standard deviation of 0.01 g/cc was recorded in the histogram plot which implies a mean distribution of 2.6565 g/cc to 2.68 g/cc. In order to get the correct mean value of grain density for sandstones, the calcite grain density values had to be excluded.

4.4.1.4 WELL E-M4 GRAIN DENSITY

The grain density of well E-M4 from the core plugs measurements ranges from 2.65 g/cc to 2.688 g/cc with a mean value of 2.66 g/cc (Figure 4-8).

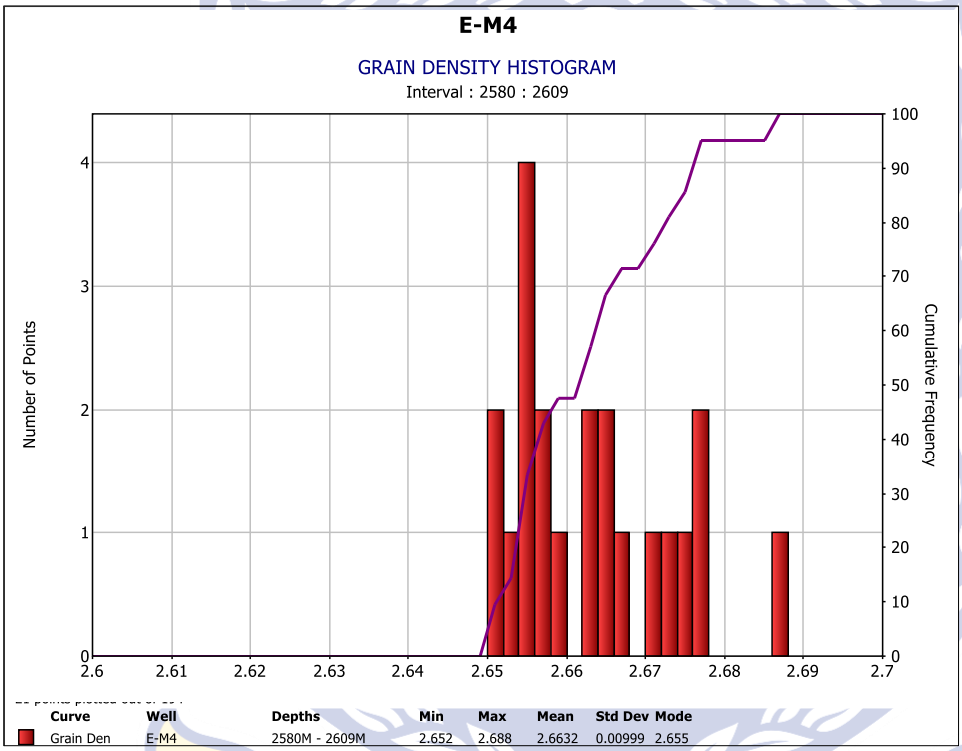

Figure 4-8: Histogram of well E-M4 grain densities.

In a clean quartz sandstone interval, a grain density of 2.65 g/cc is expected. The grain density of 2.72 g/cc at depth 2601m indicates the presence of a very thin presence of calcite. A standard deviation of 0.009 g/cc was recorded in the histogram plot which indicates that the mean distribution ranges from 2.651 g/cc to 2.669 g/cc.

4.4.1.5 WELL E-CN1 GRAIN DENSITY

The grain density of well E-CN1 determined from the routine core analysis measurements ranges from 2.664 g/cc to 2.699 g/cc with a mean value of 2.68 g/cc (Figure 4-9).

The dominant grain matrix of around 2.67 g/cc to 2.69/ g/cc is caused by the presence of carbonates and other heavy minerals like barite and possibly Ca- feldspar. The standard

deviation which is a number that shows approximately how far the values in the data set deviate from the mean value is 0.09 g/cc, which implies that the values vary from 2.67 g/cc to 2.689 g/cc.

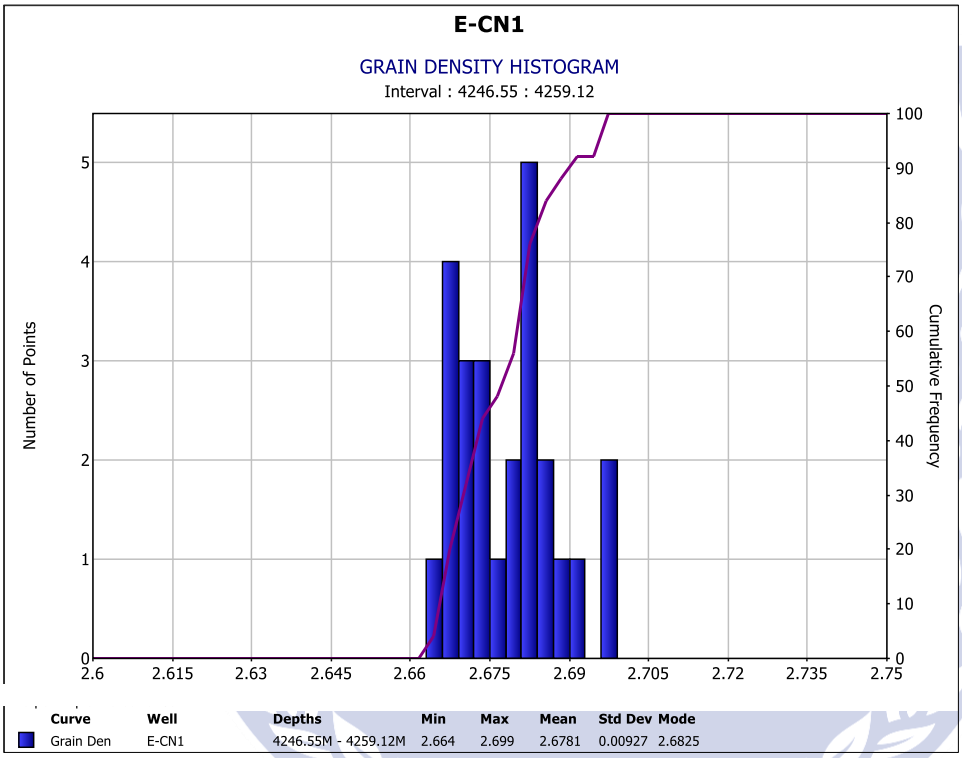

Figure 4-9: Histogram of well E-CN1 grain densities.

4.4.1.6 WELL E-W1 GRAIN DENSITY

The grain density of well E-W1 range from 2.664g/cc to 2.862g/cc with a mean value of 2.75 g/cc (Figure 4-10).

The dominant grain density value between 2.71g/cc and 2.75g/cc indicates the presence of calcite. The standard deviation value of 0.03 g/cc was recorded in the histogram plot, which implies a mean distribution of 2.72g/cc to 2.78g/cc

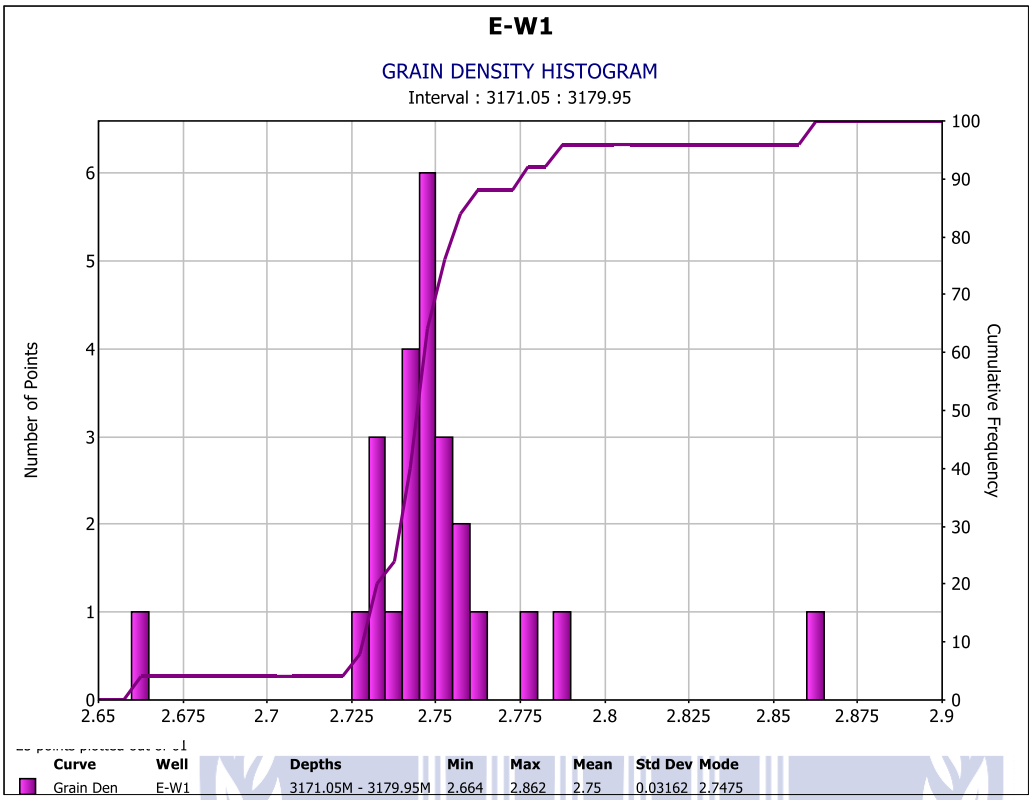

Figure 4-10: Histogram of E-W1 grain densities.

4.4.1.7 WELL F-A10 GRAIN DENSITY

The Grain density of well F-A10 determined from the routine core analysis ranges from 2.757g/cc to 3.813g/cc with a mean value of 2.953g/cc (Figure 4-11).

The grain density value of 2.966g/cc at 2722.25g/cc indicate the presence of Glauconite in the formation which is also confirmed by the petrography analysis (presented in chapter 5). The standard deviation of 0.12g/cc implies that the mean distribution ranges from 2.833g/cc to 3.073g/cc.

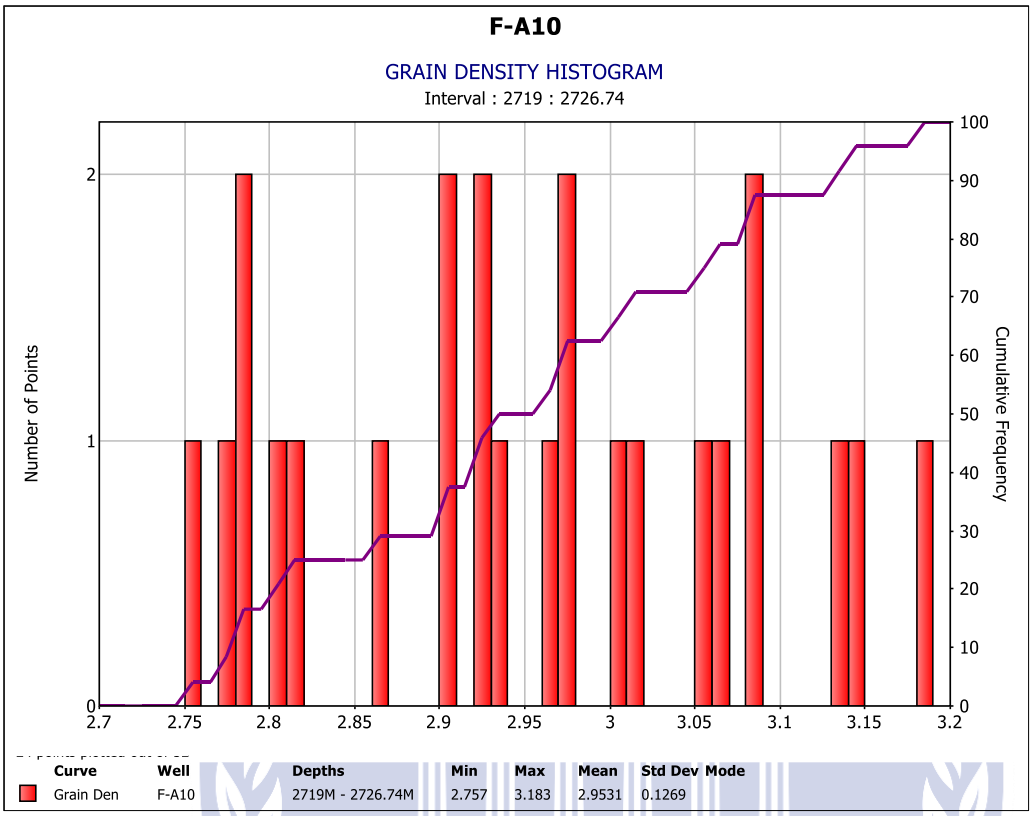

Figure 4-11: Histogram of well F-A10 grain densities.

4.4.1.8 WELL F-A13 HISTOGRAM GRAIN DENSITIES

The grain density of well F-A13 ranges from 2.659g/cc to 2.697g/cc with a mean value of 2.6792g/cc (Figure 4-12).

In a clean sandstone reservoir interval, a grain density of 2.65g/cc (2619.5m) is expected. A standard deviation value of 0.01g/cc was recorded on the histogram which implies a mean distribution of 2.6692g/cc to 2.689g/cc.

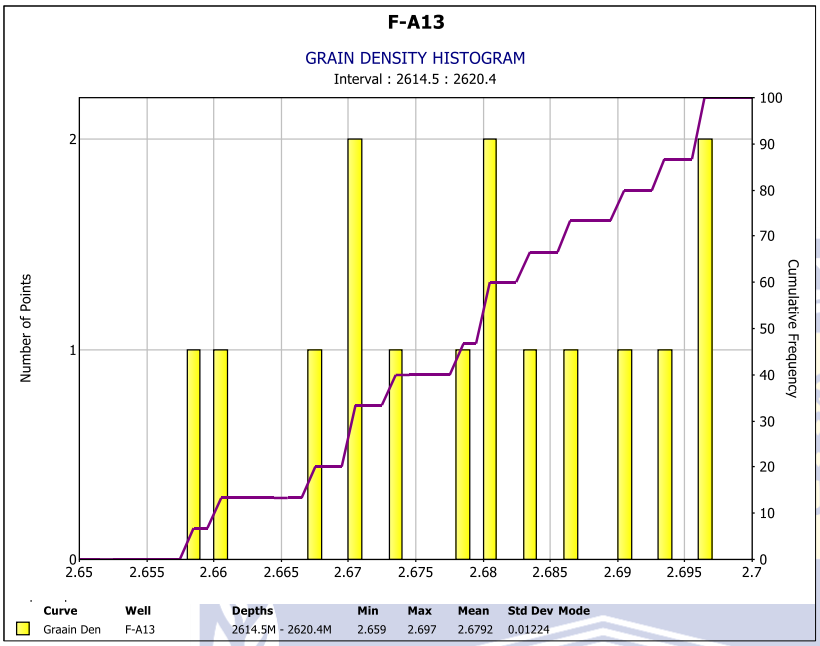

Figure 4-12: Histogram of F-A13 grain densities.

4.4.2 INTERPRETATION OF CORE POROSITY

4.4.2.1 WELL F-O1 CORE POROSITY

The core porosity of well F-O1 ranged from 1.6% to 15.5% with a mean value of 9.8% within the cored interval. The porosity histogram showed three (3) different porosity zones (Figure 4-13). One zone showed porosity values of less than 4% which is comprised of clay/shale. Another zone showed porosity values ranging from 5% to 10% and is predominantly silt. A zone of porosity values between 10% and 16% which is comprised of massive clean sandstone was also observed in the histogram plot.

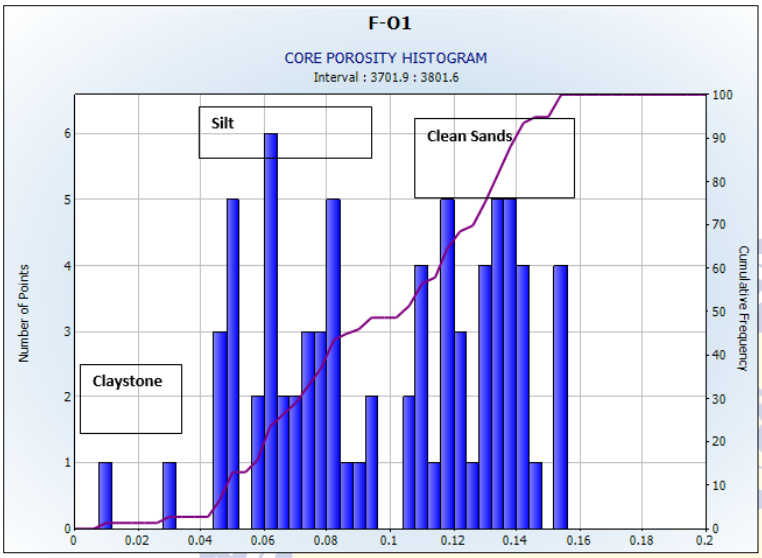

Figure 4-13: F-O1 core porosity histogram plot.

4.4.2.2 WELL F-O2 CORE POROSITY

The core porosity values of F-O2 ranges from 0%/negligible to 27% at the cored interval. The low porosity values of less than 5% were observed in intervals associated with claystone. Intermediate values between 5% and 9% were associated with siltstone. The relatively highest porosity values between 10% and 27% were associated with sandstone interval. The core porosity histogram of well F-O2 is given in figure 4-14 below.

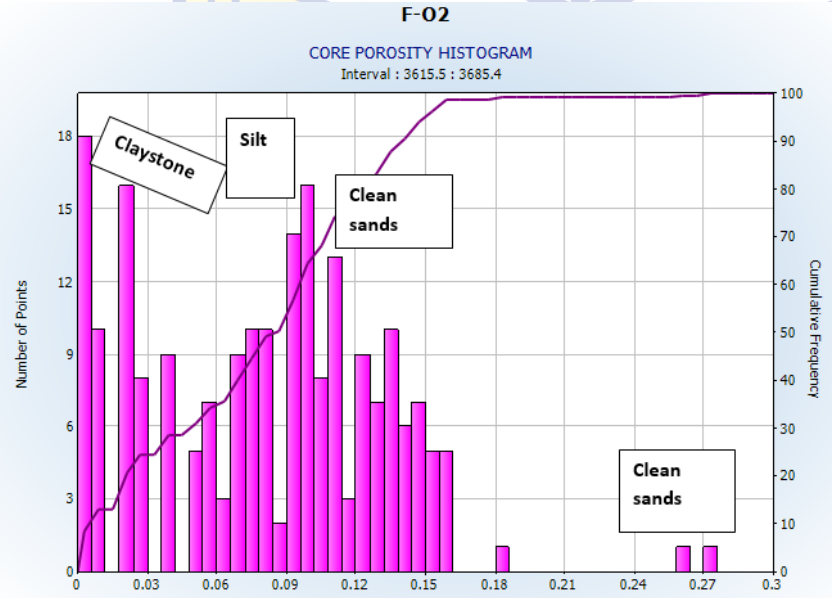

Figure 4-14: F-O2 core porosity histogram plot.

4.4.2.3 WELL E-M4 CORE POROSITY

Core porosity ranges from 6.75% to 16.6% with a standard deviation of 0.02892 and a mean value 12.9%. The distribution of core porosity values on histogram plot (Figure 4-15) shows two zones. One zone is comprised of porosity between 6.75% and 9% and can be classified as siltstone. The second zone is comprised of porosity above 10% and can be classified as sandstone.

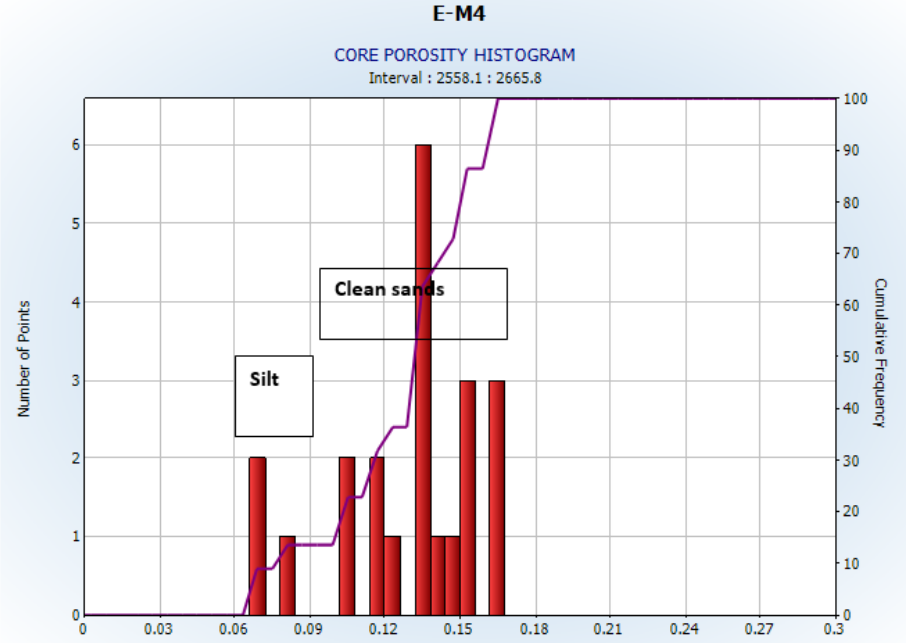

Figure 4-15: E-M4 core porosity histogram plot.

4.4.2.4 WELL E-CN1 CORE POROSITY

The core porosity values of E-CN1 ranges from 2.2% to 12.6% with a mean value of 4.5% and a standard deviation of 0.019. The histogram plot (Figure 4-16) shows predominantly low porosity values between 2% and 6% which shows that the E-CN1 reservoir is a relatively tight sandstone reservoir. The nature of this tight sandstone reservoir is described in details in chapter 5.

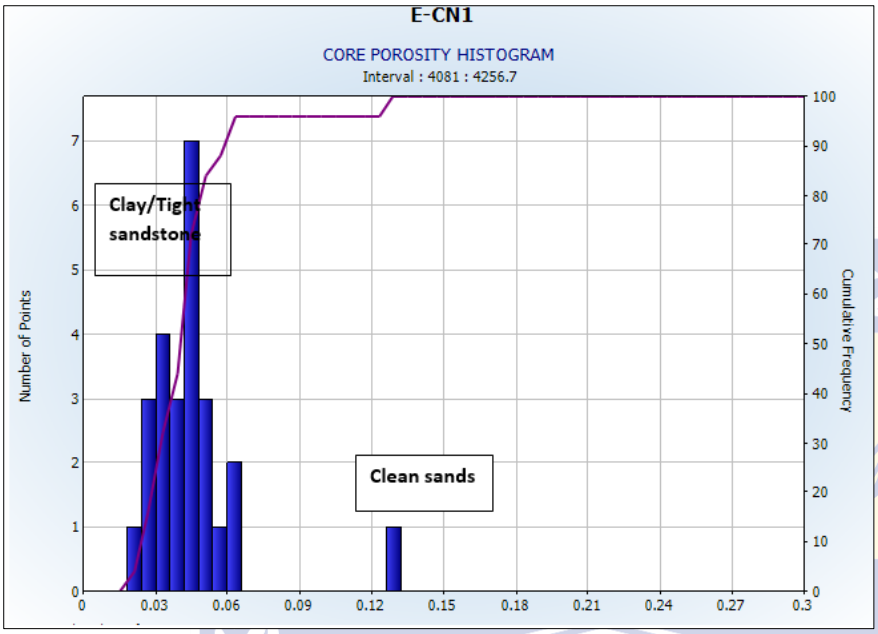

Figure 4-16: E-CN1 core porosity histogram plot.

4.4.2.5 WELL E-G1 CORE POROSITY

The E-G1 core porosity values range from 1.2% to 12.1% with a mean value of 9.1% and the standard deviation of 0.034. The distribution of porosity values from the histogram plot (Figure 4-17) shows two zones within the cored reservoir interval. Zone with a porosity of less than 4% can be classified as claystone and the zone with a porosity between 9% and 12% can be classified as sandstone.

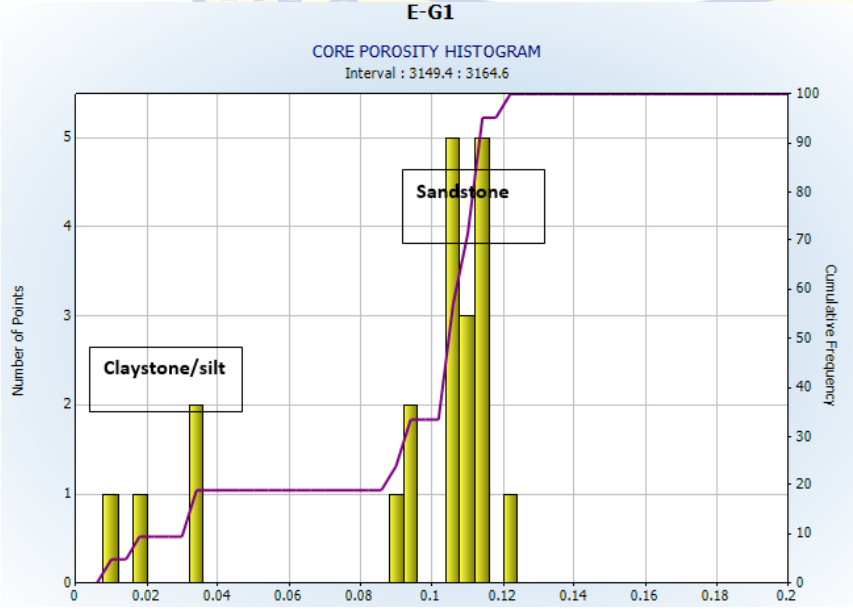

Figure 4-17: E-G1 core porosity histogram plot.

4.4.2.6 WELL E-W1 CORE POROSITY

The E-W1 core porosity values range from 1.65 to 14.3% with a mean value of 7.7% and a standard deviation of 0.031. The distribution of core porosity values on the histogram plot (Figure 4-18) shows three zones within the cored reservoir interval. Porosity values below 4% were classified as claystone, between 6% and 9% as siltstone and above 10% as sandstone.

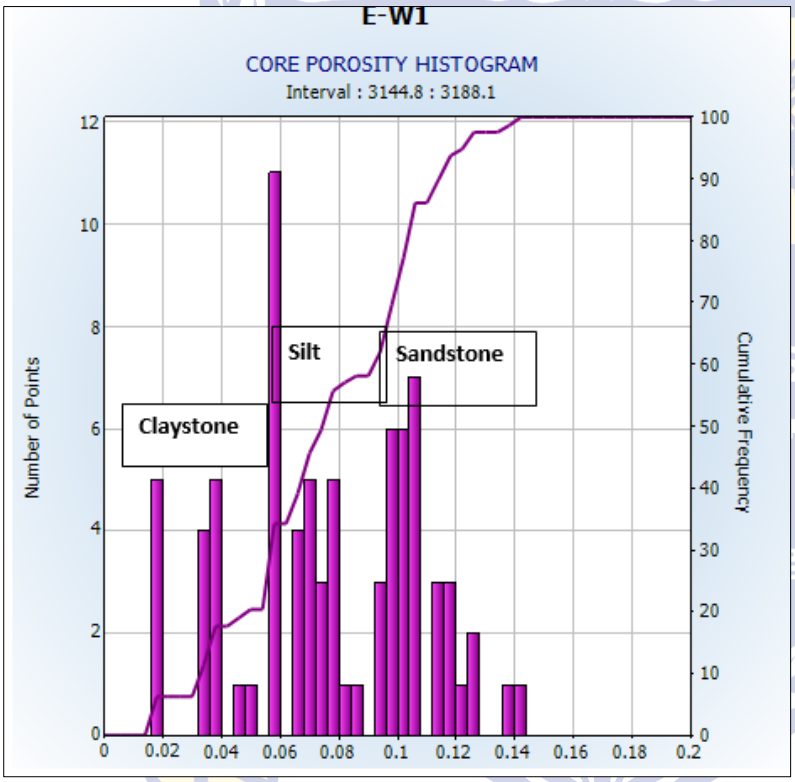

Figure 4-18: E-W1 core porosity histogram plot.

4.4.2.7 WELL F-A10 CORE POROSITY

Core porosity ranges from 1.4% to 19.7% with a mean value of 14% and a standard deviation of 0.034 in the cored interval. The distribution of core porosity in the histogram plot (Figure 4-19) shows high distribution values between 9% and 19%. This high distribution can be associated with a massive sandstone.

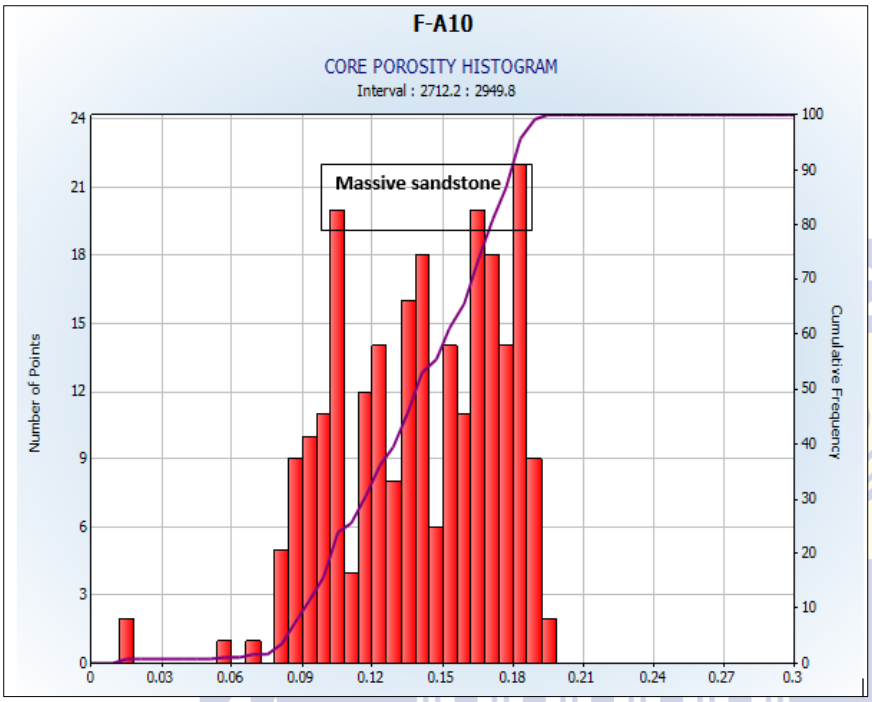

Figure 4-19: F-A10 core porosity histogram plot.

4.4.2.8 WELL F-A13 CORE POROSITY

The core porosity values of F-A13 ranges from 3.8% to 23.1% with a mean value of 15.2% and a standard deviation of 0.043. The core porosity distribution from the histogram plot (Figure 4-20) shows two porosity zone within the cored reservoir interval. The zone between 3% and 9% can be classified as claystone/ siltstone and the high distribution between 10% and 23.1% can be classified as a massive sandstone which predominates the reservoir interval.

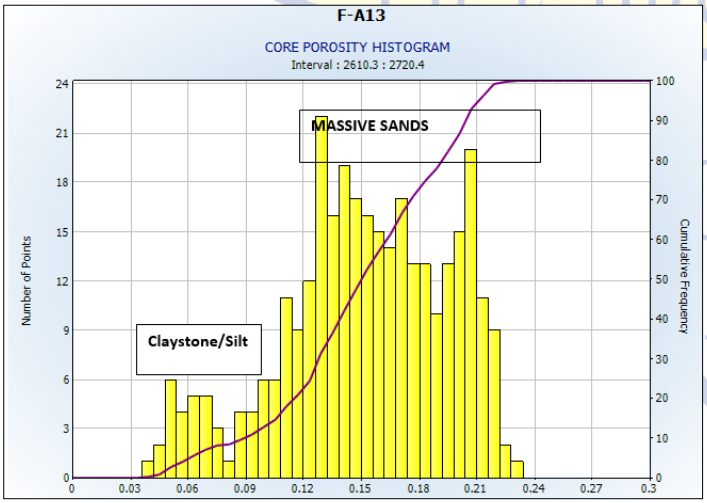

Figure 4-20: F-A13 core porosity histogram plot.

4.4.3 SPECIAL CORE ANALYSIS (SCAL)

The special core analyses are measurements made on core plugs to complement conventional core analysis measurements which are concerned with measurements of reservoir properties that allows calculation of static fluid distribution and dynamic flow performances of a reservoir (Opuwari, 2010).

In this section, the discussion will be focused on the results of special core analysis measurements on the core plug samples from well F-O1, F-O2 and F-A13. The discussion will only be focused on the additional routine core analysis of helium injection porosity at room and overburden conditions. Special core analysis measurements are performed on a relatively small number of core plug samples and analyses can be performed at reservoir conditions using fluid samples.

4.4.3.1 POROSITY OVERBURDEN CORRECTION

Overburden correction is defined as the correction from laboratory condition measurements to net effective overburden stress at in situ reservoir conditions (Opuwari, 2010). The overburden correction is mainly carried out because routine core analysis measurements may show some errors because these measurements are performed at a low-pressure condition and may lead to an overestimation of results.

When the core is brought to the surface, all conforming forces are removed and the rock can expand in all directions. The expansion of the core will result in the change of pre geometry which may impact the rock porosity depending on the clay content, the consolidation state of the rock and pressure differential. The differences between laboratory and in situ measurements are caused by the increase in volume that occurs when the core is brought to a lower temperature and pressure at the surface because of the removal of overlying sediments (Moran, 1995). This correction should always be applied to the routine core analysis if the overburden measurements are available.

In this study, the overburden corrections were applied to routine core porosity values because of the availability of core porosity data at overburden pressure. The empirical relationship between porosity at overburden and room conditions was established for porosity overburden corrections.

The special core analysis data for F-O1, F-O2 and F-A13 at room and overburden pressure conditions provide for this corrections. No special core analysis measurements were recorded for the remaining wells (E-W1, E-M4, E-G1, E-CN1, F-A10, F-A11 and F-L1); therefore no

porosity overburden correction was applied to routine core analysis. The overburden corrected porosity values will be used to calibrate wireline log porosity measurements.

The porosity at overburden pressure (4000 psi, 3900 psi, and 5000 psi) was plotted against porosity values at room conditions on a linear scale for well F-O1, F-O2 and F-A13 as shown in figure 4-21, 4-22 and 4-23 respectively.

To obtain an empirical linear relationship for the application of porosity overburden correction, the regression equation was obtained from the plot of porosity at overburden pressure against porosity at room conditions and was used as presented in the equations below for each well:

F-O1: $\Phi_{Correct} = -0.196272+0.987906*\Phi_{room\ conditions}$

F-O2: $\Phi_{Correct} = -0.338603+0.98828*\Phi_{room\ conditions}$

F-A13: $\Phi_{Correct} = -0.539309+0.9833*\Phi_{room\ conditions}$

Where

$\Phi_{Correct=}$ Overburden corrected porosity and $\Phi_{room\ conditions}$= Porosity at room conditions

Table 4.3-5 present core data used for the porosity overburden correction and Table 4.6 shows the results of the overburden corrected porosities.

Table 4-3: Well F-O1 core data used for porosity overburden correction.

	Room conditions	Overburden pressure (4000psi)
Depth (m)	Porosity (%)	Porosity (%)
3370,4	11,2	10,9
3704,63	11,2	10,8
3705,03	10,4	10,2
3712,35	8,2	7,9
3712,63	10,4	9,9
3713,86	14,2	13,6
3714,51	15,4	14,7
3716,91	9,1	8,6
3717,62	8,2	7,7
3717,92	8,1	7,8
3718,91	9,6	9,2
3719,71	8,5	8,2
3720,88	11,9	11,5
3722,69	11,6	11,1
3723,35	15,3	14,7
3724,75	13,9	13,5
3725,63	12,5	12
3725,89	12	11,5
3726,8	11,7	7,8

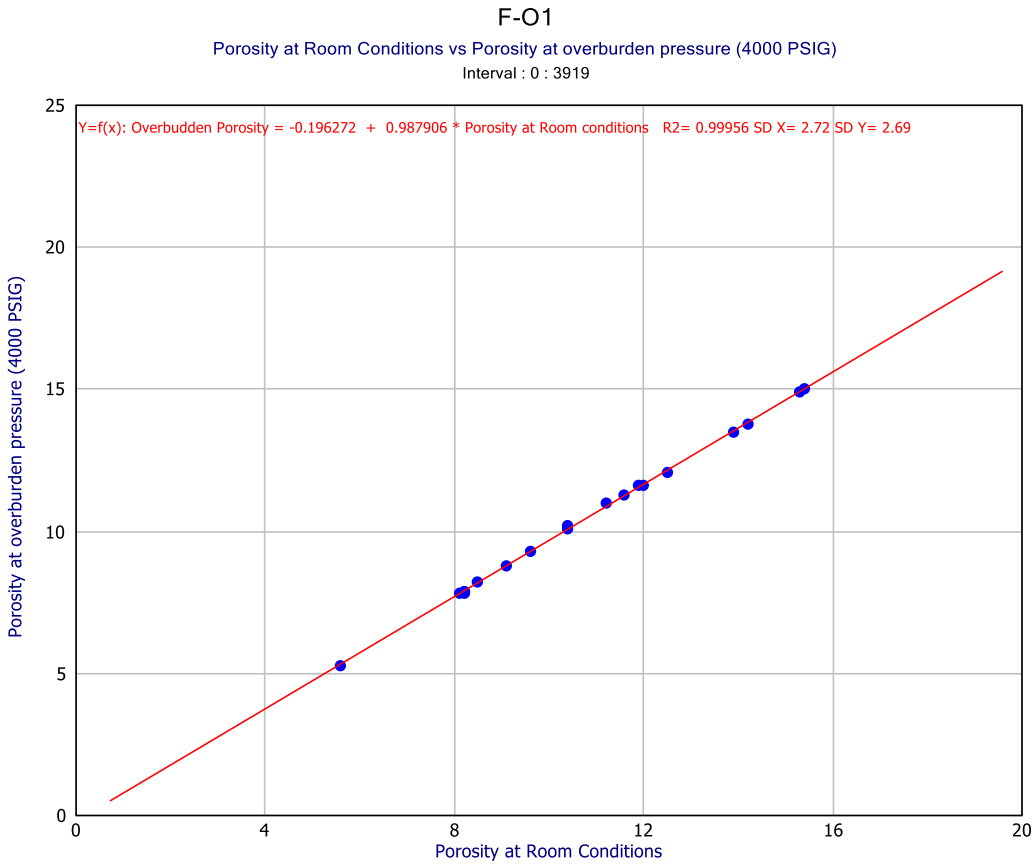

Figure 4-21: Well F-O1 porosity at overburden pressure versus porosity at room conditions.

Table 4-4: Well F-O2 core data used for porosity overburden correction.

Depth (m)	Room condition Porosity (%)	Overburden pressure (3900psi) Porosity (%)
3617,2	10,8	10,3
3625,21	10,8	10,3
3630,26	15,7	15,1
3632,23	14	13,4
3636,18	13,3	12,8
3641,2	9,3	8,9
3646,11	15,8	15,2
3648,21	12,9	12,4
3649,2	13,5	13
3651,09	12,4	11,9
3653,94	13,7	13
3667,9	13,9	13,2
3669,95	13,6	13,1
3670,89	15,5	15,1
3674,81	12,7	12,3
3675,83	12,1	11,6
3728,12	12,6	12
3736,79	12,3	11,9

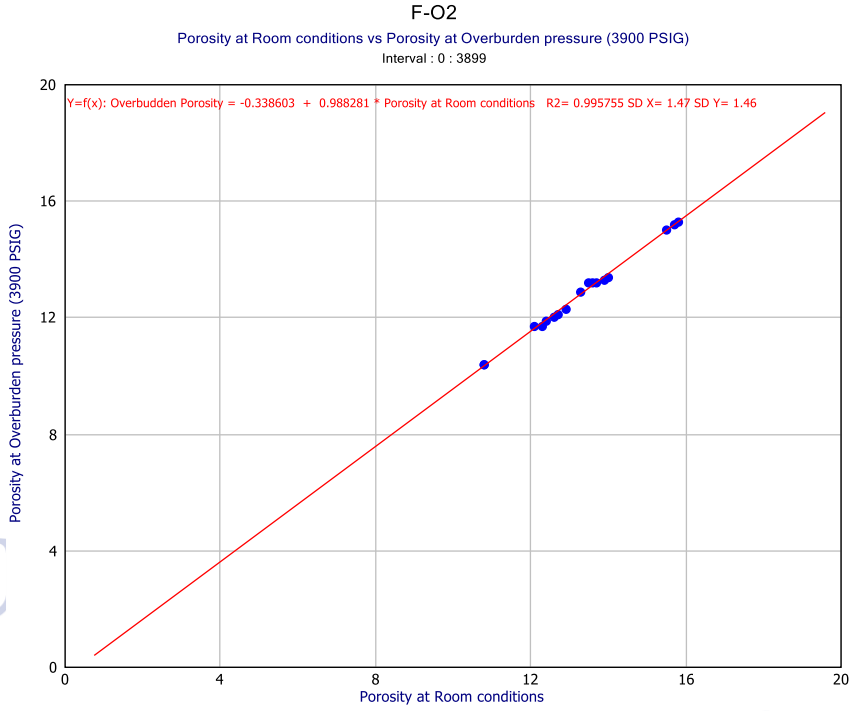

Figure 4-22: Well F-O2 porosity at overburden pressure versus porosity at room conditions.

Table 4-5: Well F-A13 core data used for porosity overburden correction.

	Room conditions	Overburden pressure (5000psi)
Depth (m)	**Porosity (%)**	**Porosity (%)**
2616,7	18,5	17,6
2617,65	20,2	19,3
2622,73	20,1	19,3
2627,69	20,3	19,5
2631,99	15,6	14,7
2634,32	16,3	15,4
2635,97	13,5	12,6
2641,75	15,5	15
2650,45	16,6	15,7
2657,28	19,4	18,5
2658,34	17,1	16,2
2669,57	12,8	12,1
2672,44	15,9	15,1
2682,53	12,9	12,1
2689,18	12,9	12,1
2695,35	10,4	9,7
2703,22	13,6	12,9
2705,8	14,2	13,5
2708,67	10,8	10,1
2711,68	5,9	5,2

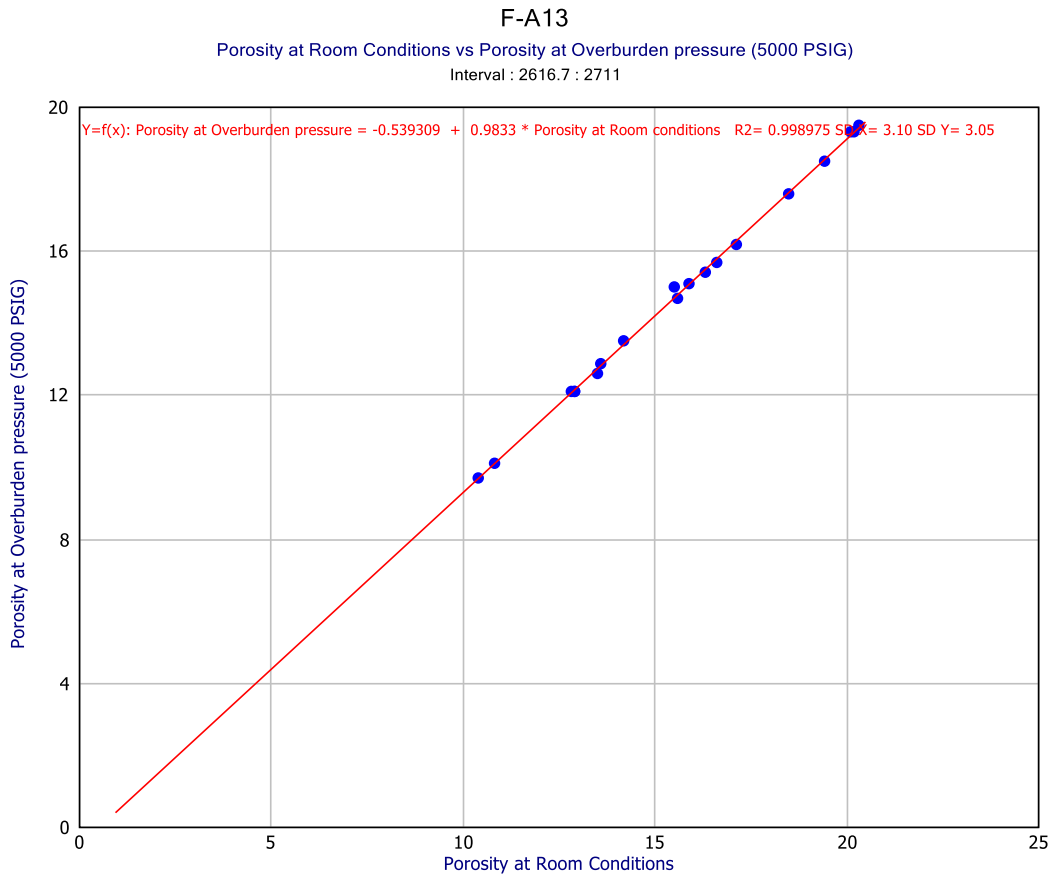

Figure 4-23: Well F-A13 porosity at overburden pressure versus porosity at room conditions.

Table 4-6: Wells F-O1, F-O2 and F-O3 calculated overburden corrected porosities.

F-O1			F-O2			F-A13		
Depth (m)	**Routine porosity (%)**	**Corrected Porosity (%)**	**Depth (m)**	**Routine Porosity (%)**	**Corrected Porosity (%)**	**Depth (m)**	**Routine Porosity (%)**	**Corrected Porosity (%)**
3370.4	10.9	10.57	3617.2	10.3	9.84	2616.7	17.6	16.77
3704.63	10.8	10.47	3625.21	10.3	9.84	2617.65	19.3	18.44
3705.03	10.2	9.88	3630.26	15.1	14.58	2622.73	19.3	18.44
3712.35	7.9	7.61	3632.23	13.4	12.90	2627.69	19.5	18.64
3712.63	9.9	9.58	3636.18	12.8	12.31	2631.99	14.7	13.92
3713.86	13.6	13.24	3641.2	8.9	8.46	2634.32	15.4	14.60
3714.51	14.7	14.33	3646.11	15.2	14.68	2635.97	12.6	11.85
3716.91	8.6	8.30	3648.21	12.4	11.92	2641.75	15	14.21
3717.62	7.7	7.41	3649.2	13	12.51	2650.45	15.7	14.90
3717.92	7.8	7.51	3651.09	11.9	11.42	2657.28	18.5	17.65
3718.91	9.2	8.89	3653.94	13	12.51	2658.34	16.2	15.69
3719.71	8.2	7.90	3667.9	13.2	12.71	2669.57	12.1	11.36
3720.88	11.5	11.16	3669.95	13.1	12.61	2672.44	15.1	14.31
3722.69	11.1	10.77	3670.89	15.1	14.58	2682.53	12.1	11.36
3723.35	14.7	14.33	3674.81	12.3	11.82	2689.18	12.1	11.36
3724.75	13.5	13.14	3675.83	11.6	11.13	2695.35	9.7	9.00
3725.63	12	11.66	3728.12	12	11.52	2703.22	12.9	12.15
3725.89	11.5	11.16	3736.79	11.9	11.42	2705.8	13.5	12.74
3726.8	7.8	7.51				2708.67	10.1	9.39
						2711.68	5.2	4.57

4.4.4 QUALITATIVE INTERPRETATION

A qualitative approach involved the interpretation of wireline log curves. Gamma-ray log curves together with well formation tops were used to identify the Upper Shallow Marine sandstone reservoirs (1AT1 formation). A Gamma-ray log reading is low in sandstone intervals and high is shales. Resistivity logs were used to identify and detect the presence of hydrocarbons in the formation. Resistivity reading is generally high in the presence of hydrocarbons and low in the presence of water in the formation. The combination of density and neutron logs were used to identify the presence of gas in the formation. The logs will

crossover each other, with density reflecting high readings and neutron reflecting low reading in the presence of gas. Sonic log measures the time taken to travel through the formation and it is also a good indicator of porosity. The sonic reading is low when passing through the pore spaces and high when passing through tight formation with little or no pore spaces. Calliper log was used to evaluate the condition of the borehole to determine whether the sidewall was washed out which may result in drilling mud invading the formation. Figure 4-24 to 4-33 below represents the petrophysical logs interpretation of Upper Shallow Marine sandstone of all the studied wells.

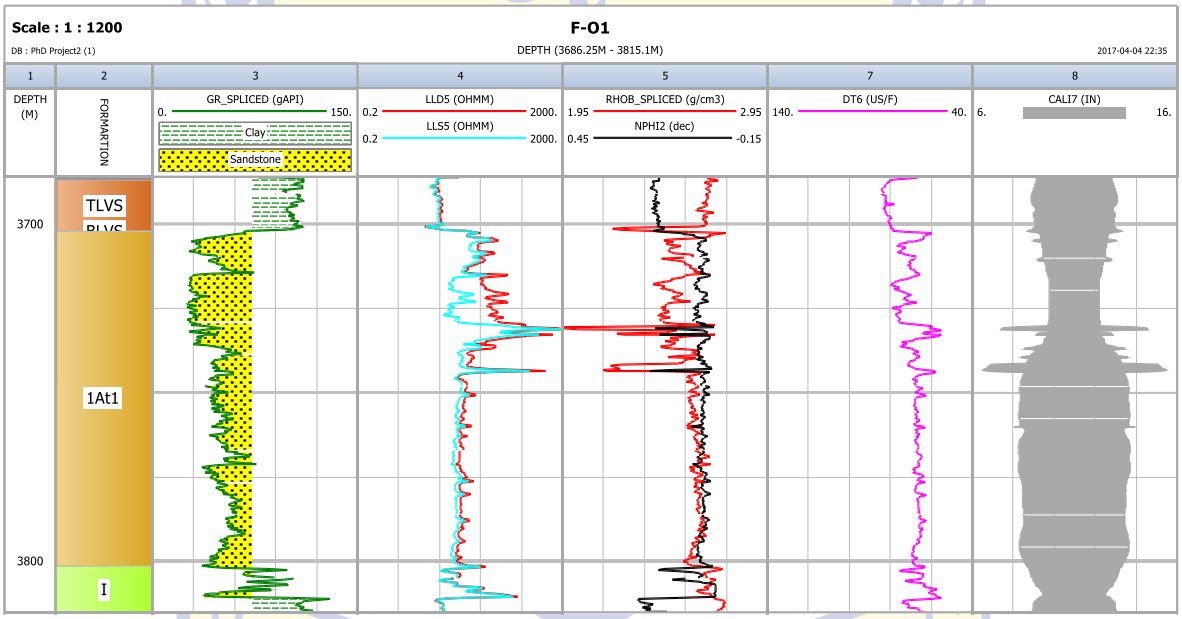

Figure 4-24: The petrophysical logs interpretation of Upper Shallow Marine sandstone (3701.9-3810.6m), a 1AT1 formation of well F-O1.

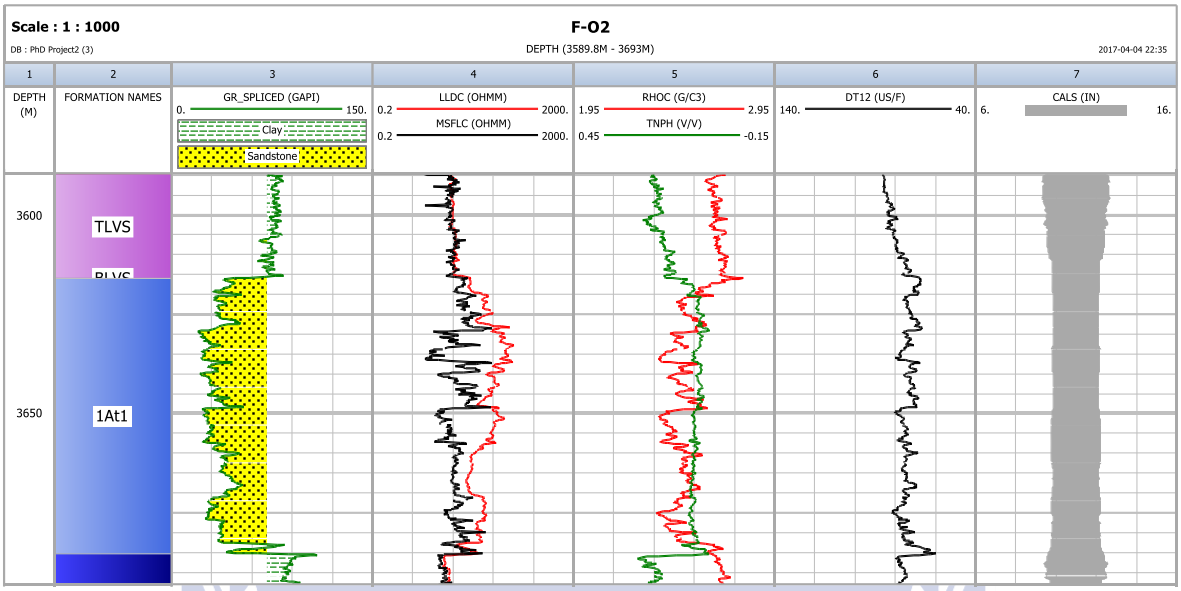

Figure 4-25: The petrophysical logs interpretation of Upper Shallow Marine sandstone (3615.5-3685.4m), a 1AT1 formation of well F-O2.

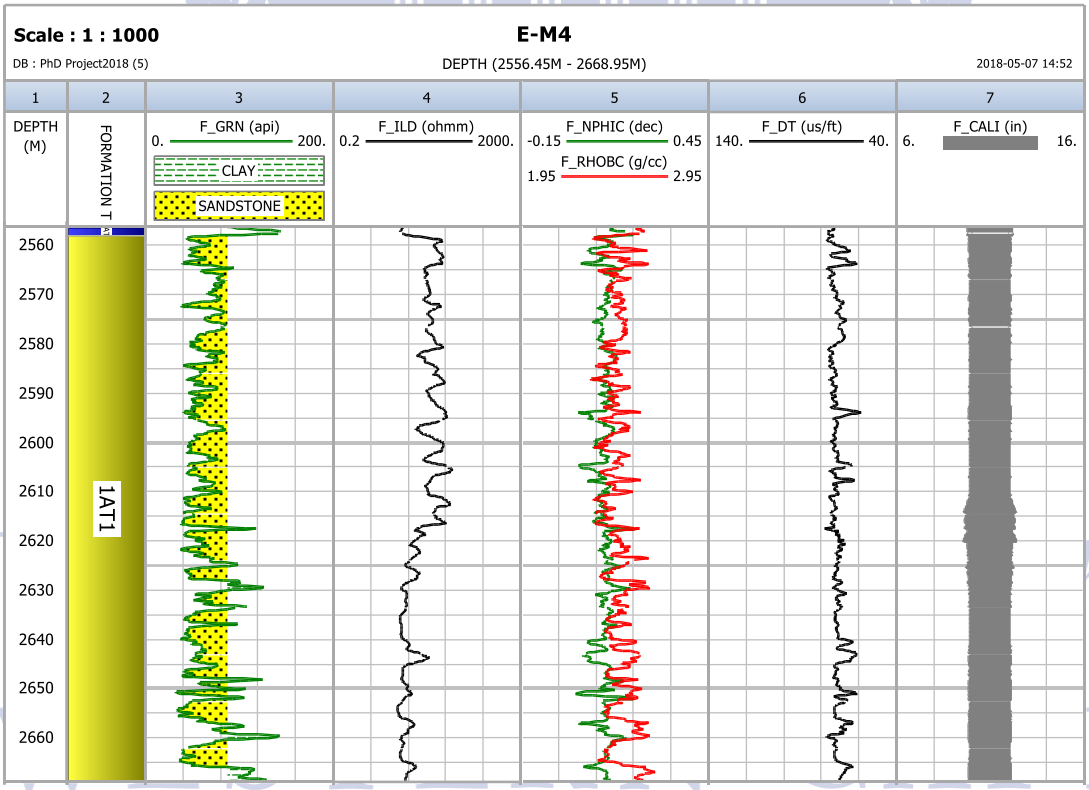

Figure 4-26: The petrophysical logs interpretation of Upper Shallow Marine sandstone (2558.1m-2665.8m), a 1AT1 formation of well E-M4.

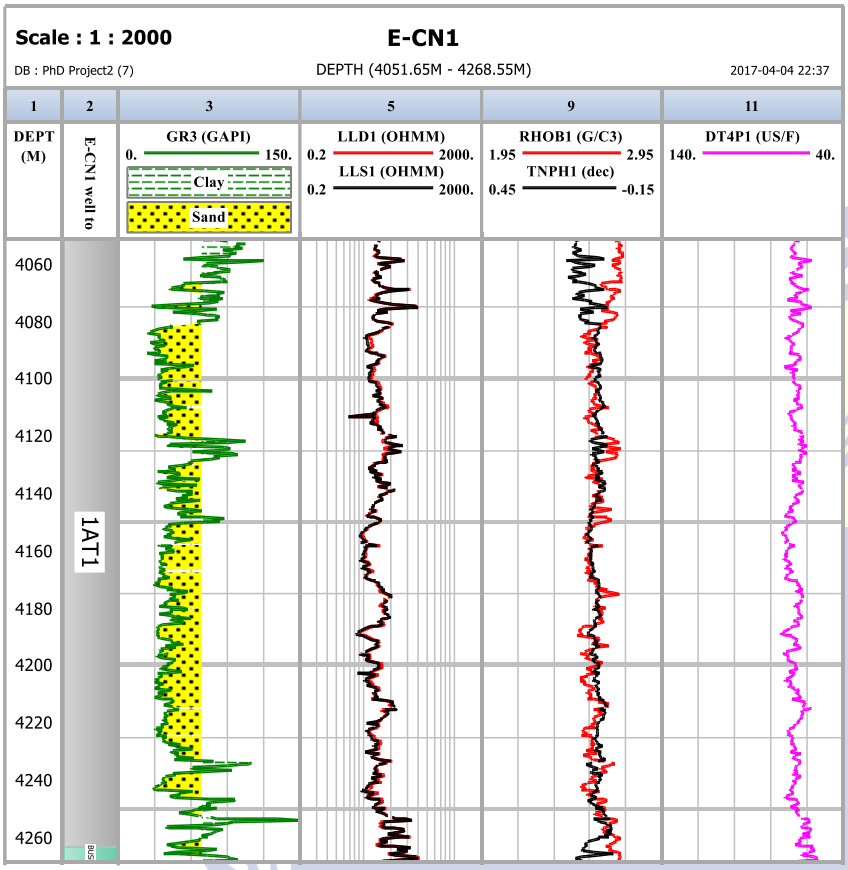

Figure 4-27: The petrophysical logs interpretation of Upper Shallow Marine sandstone (4081-4246.7m), a 1AT1 formation of well E-CN1.

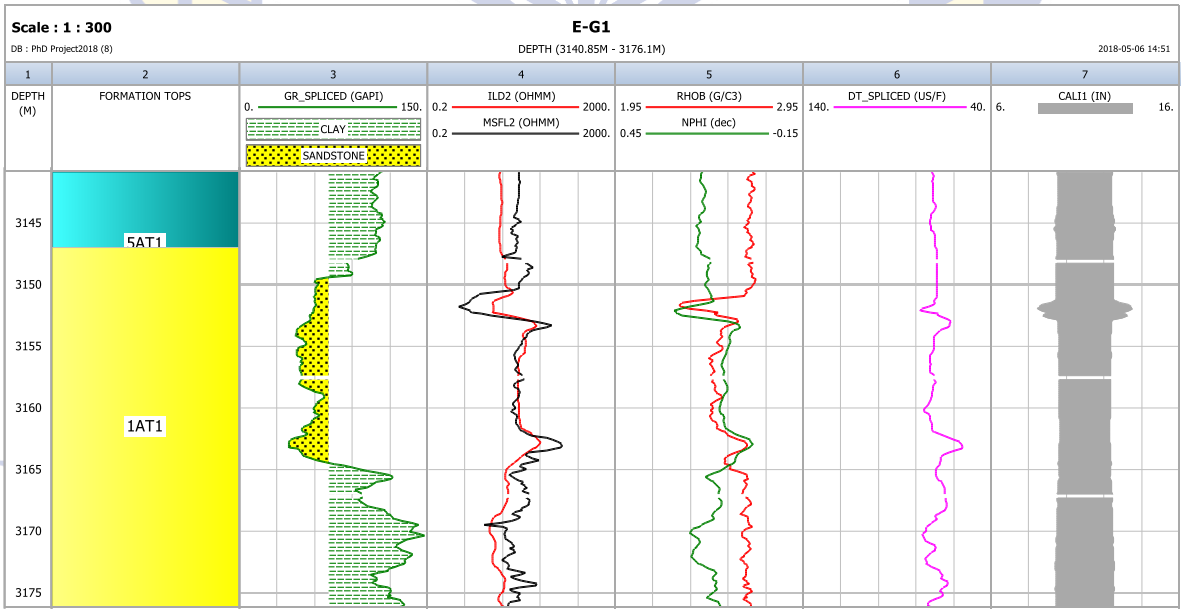

Figure 4-28: The petrophysical logs interpretation of upper Shallow Marine Sandstone (3149.4-3164.6m), a 1AT1 formation of well E-G1.

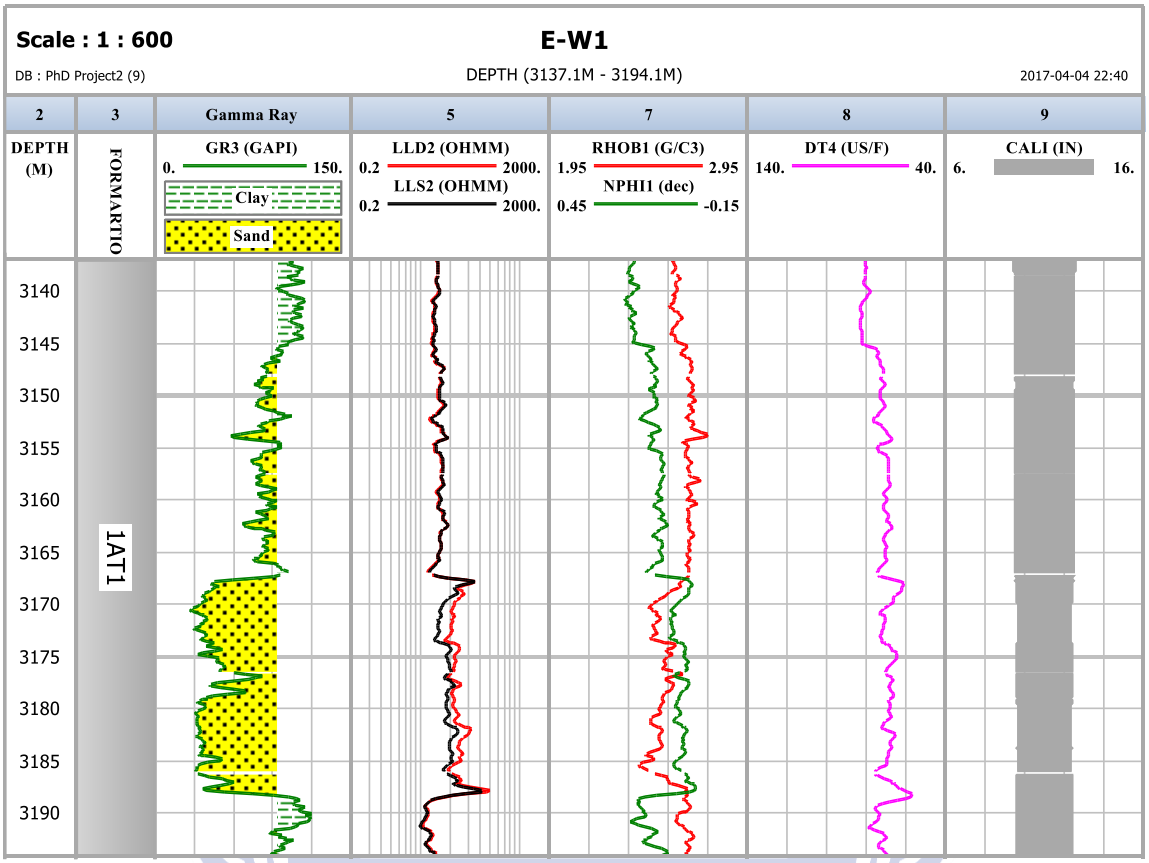

Figure 4-29: The petrophysical logs interpretation of Upper Shallow Marine sandstone (3144.8-3188.1m), a 1AT1 formation of well E-W1.

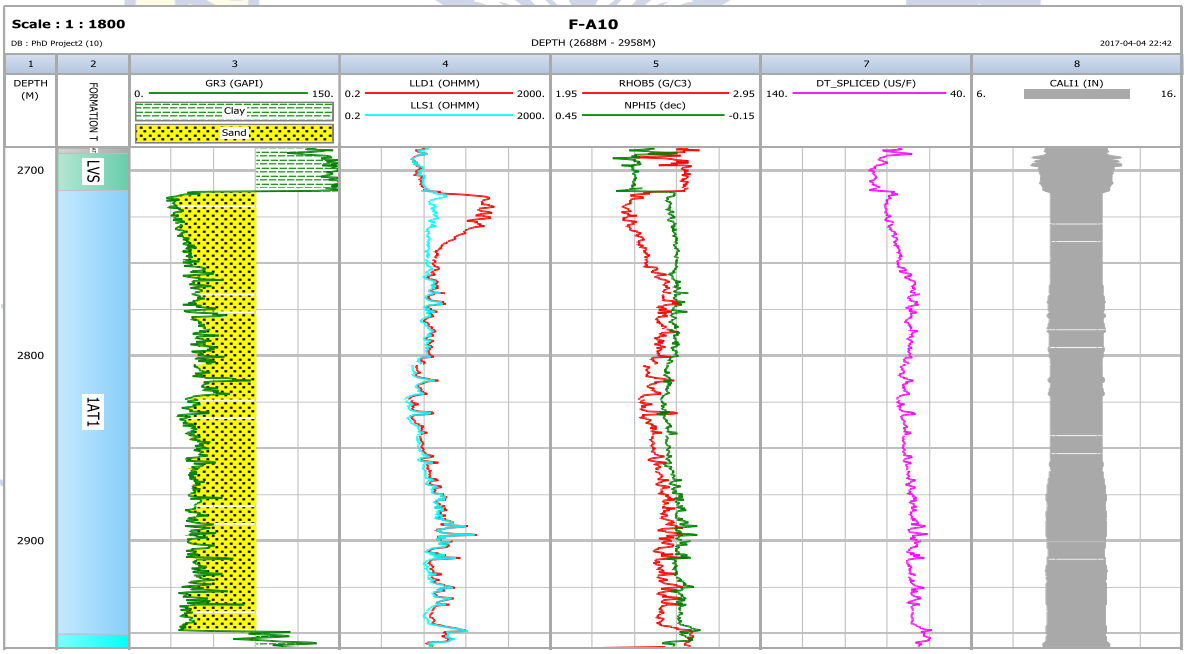

Figure 4-30: The petrophysical logs interpretation of Upper Shallow Marine sandstone (2712.2-2949.6m), a 1AT1 formation of well F-A10.

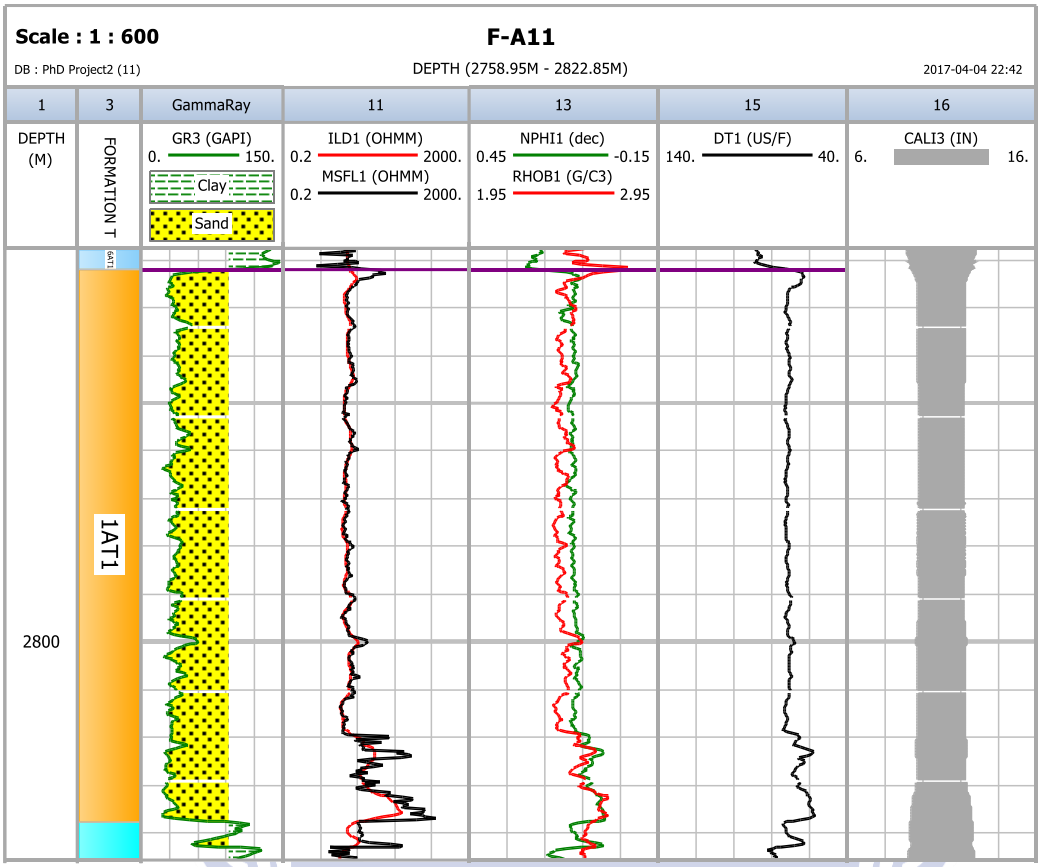

Figure 4-31: The petrophysical logs interpretation of Upper Shallow Marine sandstone (2761.1-2818.8m), a 1AT1 formation of well F-A11.

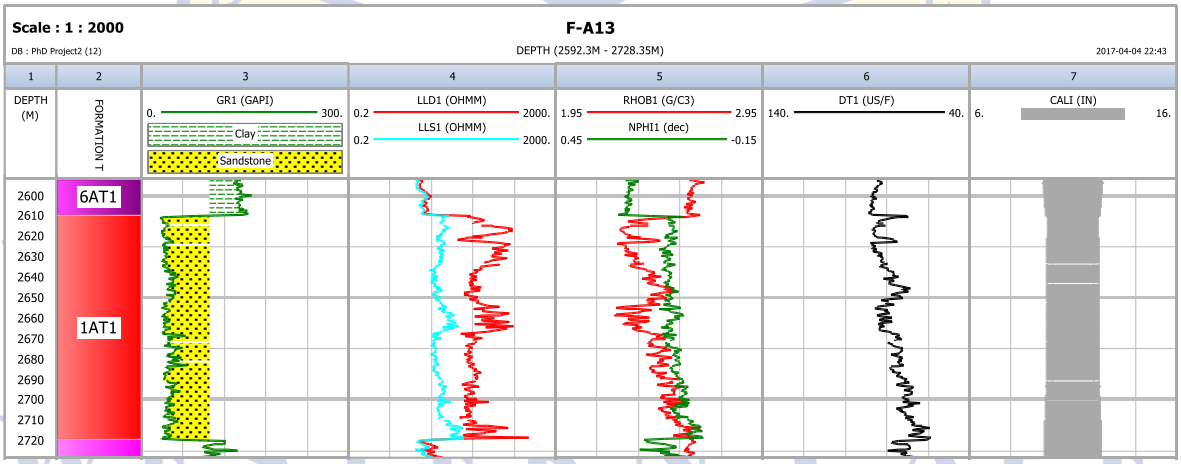

Figure 4-32: The petrophysical logs interpretation of Upper Shallow Marine sandstone (2610.3-2720.4m), a 1AT1 formation of well F-A13.

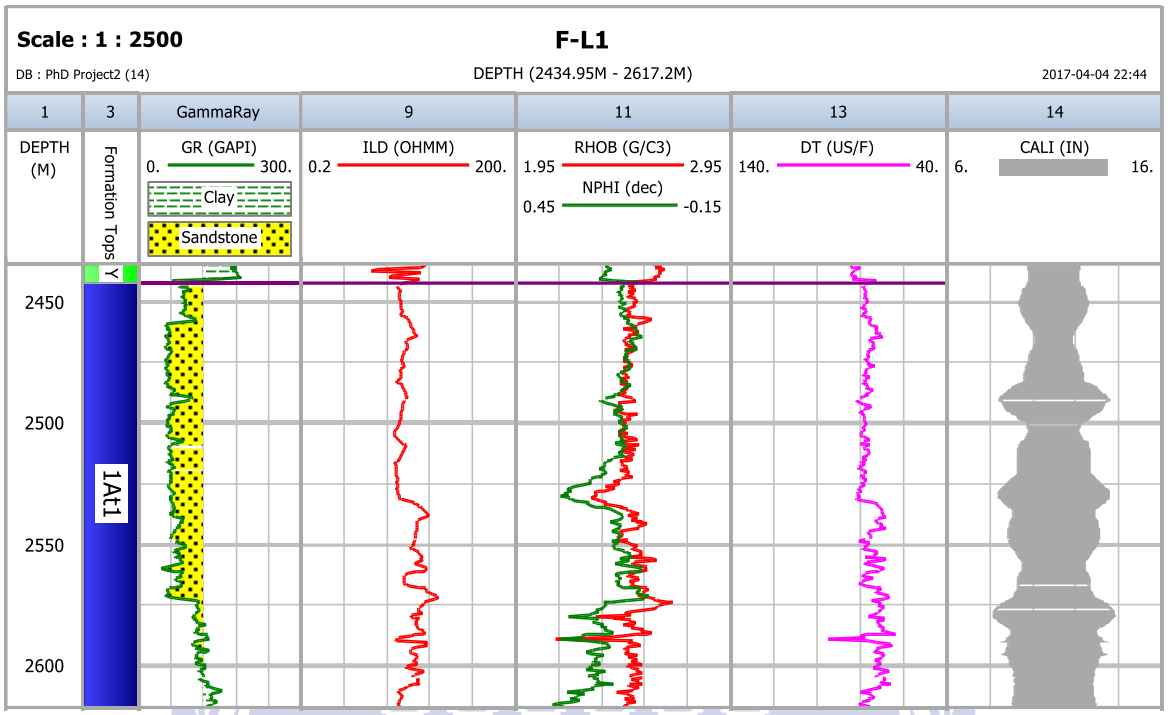

Figure 4-33: The petrophysical logs interpretation of Upper Shallow Marine sandstone (2442-2606.3m), a 1AT1 formation of well F-L1.

4.4.5 QUANTITATIVE INTERPRETATION

A quantitative approach was chosen to interpret the results of the delineated reservoirs in each well. The summary results of the computed petrophysical parameters of reservoir sands are presented in Table 4-14.

4.4.5.1 F-O1 QUANTITATIVE RESULTS

The F-O1 reservoir interval ranged between 3710.9m-3810.6m with a gross thickness of 108.7m. The average clay volume of 19.8% indicates that the reservoir is a shaly sand reservoir. The average water saturation value was 18.9%. Twenty core plugs were used for porosity measurement (Table 4-6). Core porosity measurement ranged between 2.8%- 12.61% with an average porosity of 9.1%. Core porosity and log porosity were calibrated (Figure 4-34) and showed a good calibration between the two measurements.

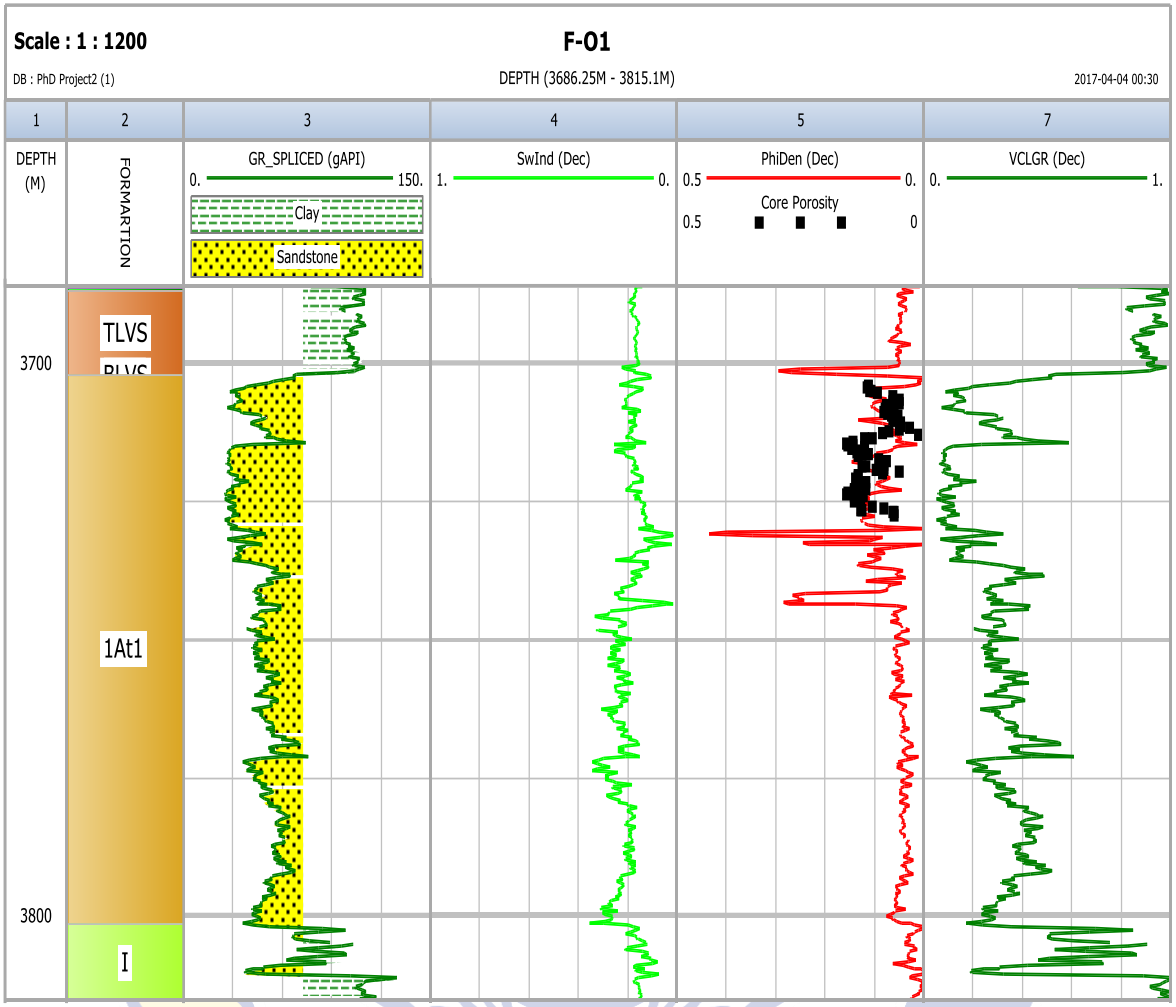

Figure 4-34: Calculated reservoir results of well F-O1.

Table 4-6: F-O1 core porosity results obtained from Helium porosimeter.

Sample No	Sample name	Depth (M)	Sample dia (mm)	Sample length (mm)	Bulk Vol (ml)	Dry Weight (g)	Grain Vol. (ml)	Grain density (g/ml)	Pore Volume (ml)	Porosity (%)	Billets loaded (1 to 6)	Patm recorded (psia)	P_{ref} (psia)	P_{exp} (psia)	P_{ref}/P_{exp}	V. billets loaded (ml)
1	BJ 31	3659,69	37,97	50,24	56,89	134,19	49,72	2,699	7,17	12,61%	235	13,98	170,13	114,40	1,55	29,880
2	BJ 37	3661,39	37,95	49,79	56,32	139,51	49,38	2,825	6,94	12,33%	1235	13,98	169,74	118,48	1,49	32,602
3	BJ 38	3661,6	37,96	44,77	50,67	123,66	46,35	2,668	4,33	8,54%	245	13,98	169,34	117,58	1,50	35,298
4	BJ 39	3661,89	37,98	55,37	62,73	153,10	57,33	2,671	5,40	8,61%	15	13,98	169,52	117,96	1,50	24,451
5	BJ 40	3662,14	38,07	55,81	63,53	157,97	59,12	2,672	4,41	6,95%	25	13,98	170,02	121,75	1,45	24,438
6	BJ 41	3662,39	38,05	53,1	60,38	149,70	55,90	2,678	4,48	7,42%	35	13,98	169,86	120,67	1,46	27,170
7	BJ 42	3662,55	38,02	56,27	63,88	160,08	59,73	2,680	4,15	6,49%	15	13,98	169,29	122,52	1,43	24,451
8	BJ 43	3662,85	38,07	52,1	59,31	145,00	54,38	2,667	4,93	8,32%	35	13,98	169,55	117,54	1,50	27,170
9	BJ 46	3663,62	38,14	51,11	58,39	133,99	50,12	2,673	8,27	14,16%	135	13,98	168,65	114,18	1,54	29,892
10	BJ 60	3667,58	38,12	49,15	56,09	140,53	52,76	2,664	3,33	5,94%	45	13,98	169,42	125,08	1,40	32,588
11	BJ 61	3668,03	38,05	46,18	52,51	130,21	51,04	2,551	1,47	2,80%	45	13,98	169,44	121,50	1,45	32,588
12	BJ 62	3668,53	37,99	48,52	55,00	129,64	48,07	2,697	6,93	12,61%	45	13,98	170,31	116,40	1,53	32,588
13	BJ 65	3669,34	38,07	41,85	47,64	113,15	42,35	2,672	5,29	11,11%	1345	13,98	168,60	119,87	1,46	40,752
14	BJ 66	3669,59	37,92	37,7	42,58	107,19	39,75	2,697	2,83	6,65%	6	13,98	169,96	121,00	1,46	43,453
15	BJ 67	3669,78	38,02	48,36	54,90	138,82	51,54	2,694	3,37	6,13%	45	13,98	169,75	122,72	1,43	32,588
16	BJ 68	3670,1	37,99	49,69	56,32	140,20	52,33	2,679	3,99	7,09%	235	13,98	169,33	118,64	1,48	29,880
17	BJ 69	3670,33	37,99	47,12	53,41	135,56	50,25	2,698	3,16	5,91%	45	13,98	169,42	119,92	1,47	32,588
18	BJ 70	3670,47	38,03	49,92	56,70	139,52	52,46	2,660	4,24	7,49%	235	13,98	169,81	119,21	1,48	29,880
19	BJ 71	3670,75	38,02	42,63	48,40	118,28	44,30	2,670	4,10	8,47%	345	13,98	168,32	118,19	1,48	38,029
20	BJ 72	3671,05	38	45,39	51,48	126,32	47,09	2,683	4,39	8,53%	245	13,98	168,40	118,35	1,48	35,298

4.4.5.2 F-O2 QUANTITATIVE RESULTS

The F-O2 reservoir interval ranged between 3615.5m-3685.4m with a gross thickness of 69.9m. The average clay volume of 23.3% indicates that the reservoir is a shaly sand reservoir. The average water saturation value was 12.2%. Thirty core plugs were used for porosity measurement (Table 4-7). Core porosity measurement ranged between 7.42%- 12.29% with an average porosity of 10.8%. Core porosity and log porosity were calibrated (Figure 4-35) and showed a good calibration between the two except for a few anomalies towards the bottom of the reservoir.

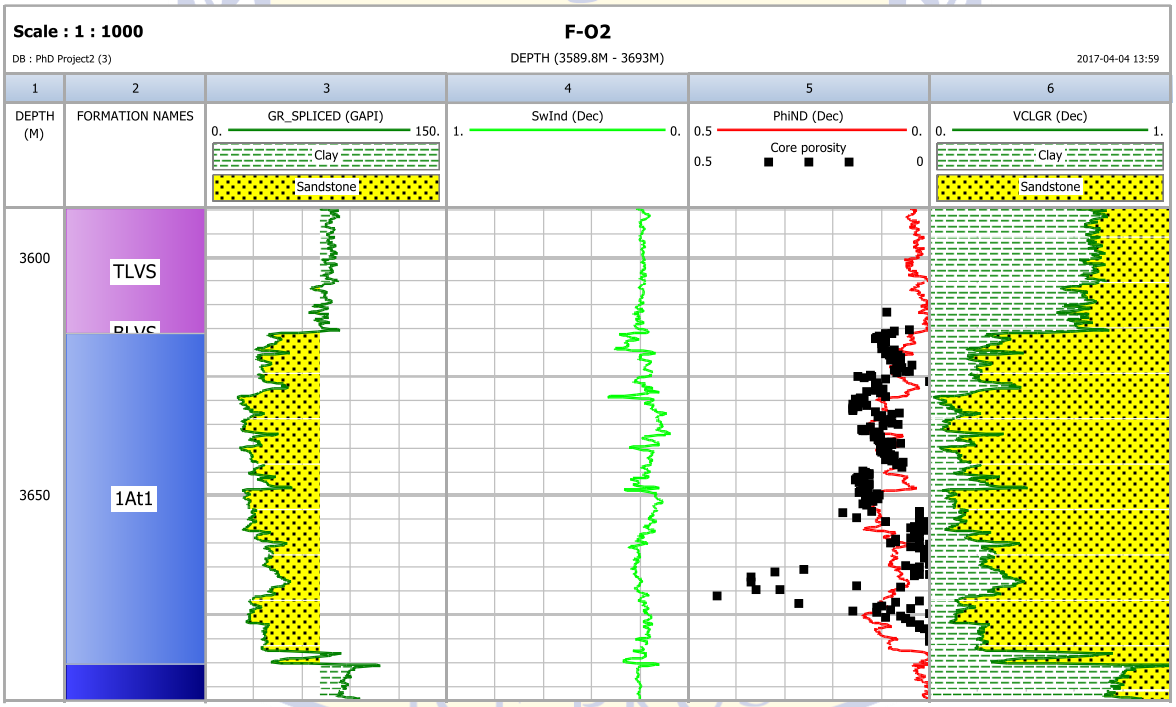

Figure 4-35: Calculated reservoir results of well F-O2.

Table 4-7: F-O2 core porosity results obtained from Helium porosimeter.

Sample No	Sample name	Depth (m)	Sample dia (mm)	Sample length (mm)	Bulk Vol (ml)	Dry Weight (g)	Grain Vol. (ml)	Grain density (g/ml)	Pore Volume (ml)	Porosity (%)	Billets loaded (1 to 6)	Patm recorded (psia)	Pref (psia)	Pexp (psia)	Pref/Pexp	V. billets loaded (ml)
1	CF16	3619.05	38,16	38,27	43,77	106,80	39,88	2,678	3,90	8,90%	6	14,01	169,33	120,83	1,45	43,453
2	CF17	3619.35	38,21	39,37	45,14	109,23	41,31	2,644	3,83	8,48%	6	14,01	169,45	123,85	1,42	43,453
3	CF19	3619.61	38,2	38,23	43,81	102,58	38,34	2,675	5,47	12,48%	6	14,01	170,21	118,46	1,50	43,453
4	CF20	3619.86	38,31	31,67	36,51	84,97	31,84	2,669	4,67	12,79%	136	14,01	169,67	121,32	1,45	51,616
5	CF21	3620.04	38,26	39,37	45,26	106,12	39,75	2,670	5,51	12,17%	6	14,01	170,01	121,05	1,46	43,453
6	CF22	3620.37	38,2	39,46	45,22	106,69	40,04	2,665	5,18	11,46%	6	14,01	170,34	121,85	1,45	43,453
7	CF23	3620.56	38,28	40,04	46,08	108,74	40,74	2,669	5,34	11,58%	6	14,01	170,74	123,57	1,43	43,453
8	CF25	3620.81	38,21	39,64	45,45	107,76	40,33	2,672	5,12	11,27%	6	14,01	170,46	122,52	1,44	43,453
9	CF26	3621.03	38,16	39,89	45,62	107,95	40,54	2,663	5,09	11,15%	6	14,01	171,27	123,51	1,44	43,453
10	CF27	3621.35	38,74	38,77	45,70	108,66	40,66	2,673	5,04	11,04%	6	14,01	170,88	123,49	1,43	43,453
11	CF28	3621.6	38,16	39,38	45,04	108,73	40,64	2,675	4,40	9,76%	6	14,01	170,18	122,97	1,43	43,453
12	CF29	3621.85	38,74	39,22	46,23	108,17	40,47	2,673	5,76	12,46%	6	14,01	170,28	122,69	1,44	43,453
13	CF30	3622.35	38,1	40	45,60	109,32	40,94	2,670	4,66	10,21%	6	14,01	170,16	123,58	1,43	43,453
14	CF31	3622.6	38,43	38,4	44,54	107,75	40,40	2,667	4,14	9,29%	6	14,01	170,53	122,72	1,44	43,453
15	CF32	3623.03	38,21	39,05	44,78	109,25	40,82	2,676	3,96	8,84%	6	14,01	170,77	123,75	1,43	43,453
16	CF67	3623.33	38,31	38,88	44,82	106,32	39,90	2,665	4,92	10,97%	6	14,01	170,21	121,49	1,45	43,453
17	CF68	3623.6	38,18	39,05	44,71	107,39	40,36	2,661	4,35	9,72%	6	14,01	170,35	122,52	1,44	43,453
18	CF69	3623.83	38,2	40,16	46,03	112,09	41,89	2,676	4,14	9,00%	2345	14,01	170,47	120,23	1,47	40,739
19	CF70	3624.07	38,15	40,19	45,94	109,38	40,71	2,687	5,23	11,38%	6	14,01	168,69	122,07	1,43	43,453
20	CF71	3624.36	38,6	39,87	46,66	104,99	39,45	2,661	7,21	15,45%	6	14,01	168,36	119,33	1,47	43,453
21	CF75	3624.62	38,16	39,3	44,95	106,17	39,87	2,663	5,08	11,31%	6	14,01	170,02	121,29	1,45	43,453
22	CF76	3624.87	38,14	36,67	41,89	99,69	37,37	2,668	4,52	10,80%	16	14,01	170,03	121,74	1,45	46,175
23	CF79	3625.07	38,12	40,05	45,71	108,77	40,82	2,664	4,89	10,69%	6	14,01	170,72	123,72	1,43	43,453
24	CF88	3625.35	38,1	39,89	45,48	111,85	41,79	2,676	3,69	8,11%	6	14,01	170,44	125,57	1,40	43,453
25	CF90	3625.64	38,12	40,11	45,78	111,72	41,70	2,679	4,09	8,92%	6	14,01	169,97	125,03	1,40	43,453
26	CF91	3626.3	38,23	39,94	45,85	109,58	41,00	2,673	4,85	10,59%	6	14,01	170,36	123,83	1,42	43,453
27	CF92	3626.77	38,17	39,75	45,49	110,66	41,37	2,675	4,12	9,05%	6	14,01	170,25	124,54	1,41	43,453
28	CF93	3626.98	38,11	40,62	46,33	113,42	42,30	2,681	4,03	8,69%	2345	14,01	170,33	120,95	1,46	40,739
29	CF94	3627.14	38,12	39,19	44,73	111,12	41,49	2,678	3,24	7,24%	6	14,01	169,66	124,38	1,41	43,453
30	CF96	3627.47	38,13	40,4	46,13	110,50	41,53	2,660	4,60	9,96%	2345	14,01	167,38	117,46	1,48	40,739

4.4.5.3 E-M4 QUANTITATIVE RESULTS

The E-M4 reservoir interval ranged between 2558.1m-2665.8m with a gross thickness of 107.7m. The average volume of clay value of 29.8% indicates that the reservoir is a shaly sand reservoir. The average water saturation value was calculated to be 18.7%. Twenty three (23) core plugs were used for porosity measurement (Table 4-8). Core porosity measurement ranged between 3.56%- 16.45% with an average porosity of 10.2%. Core porosity and log porosity were calibrated (Figure 4-36) and showed a very good calibration between the two.

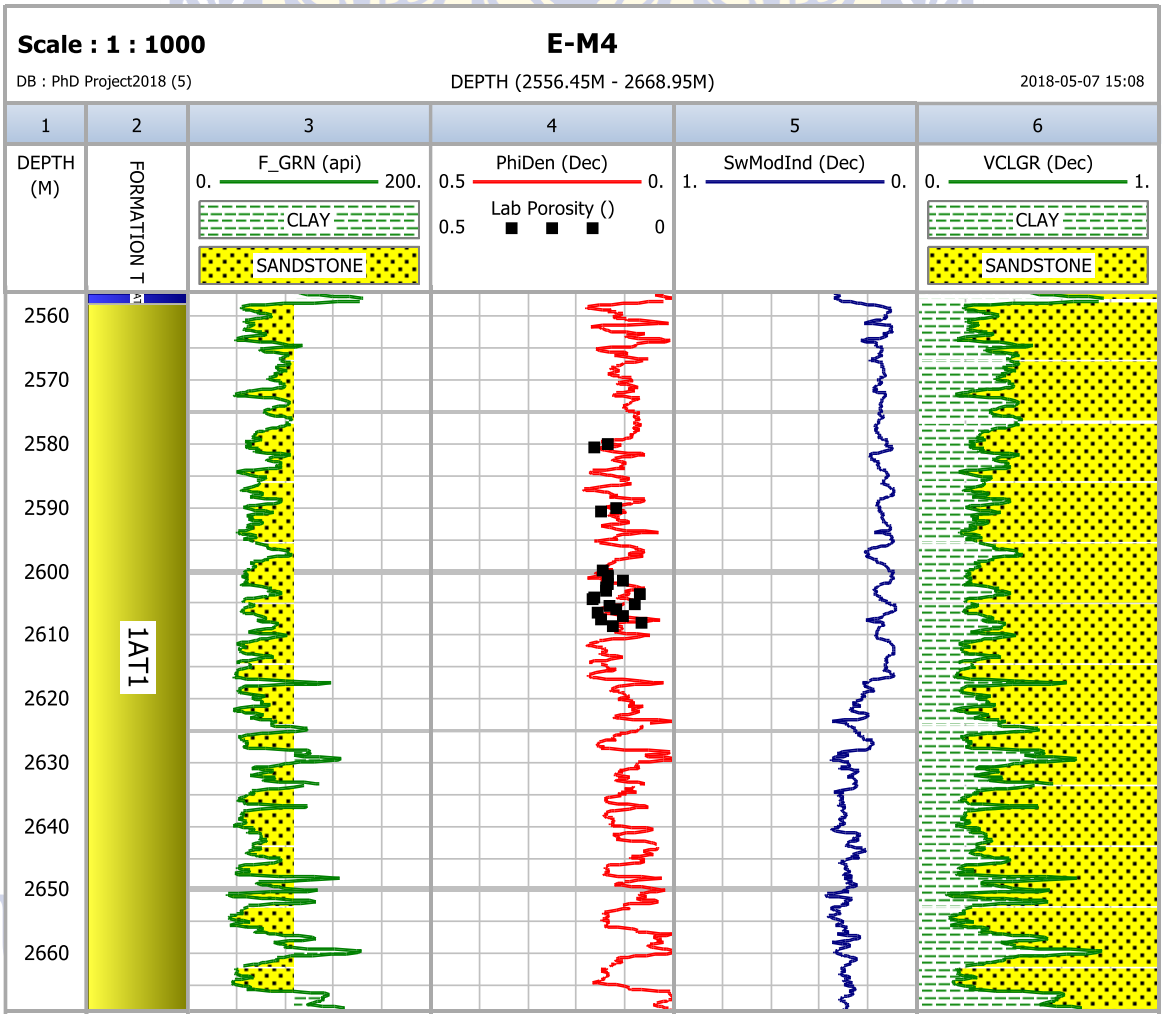

Figure 4-36: Calculated reservoir results of well E-M4.

Table 4-8: E-M4 core porosity results obtained from Helium porosimeter.

Sample No	Sample name	Depth (M)	Sample dia (mm)	Sample length (mm)	Bulk Vol (ml)	Dry Weight (g)	Grain Vol (ml)	Grain density (g/ml)	Pore Volume (ml)	Porosity (%)	Billets loaded (1 to 6)	Patm recorded (psia)	P_{ref} (psia)	P_{exp} (psia)	P_{ref}/P_{exp}	V. billets loaded (ml)
1	1	2580	37,97	52,28	59,20	135,98	51,22	2,655	7,98	13,47%	35	13,90	170,33	112,44	1,59	27,170
2	1A	2580.5	37,08	48,61	52,49	116,35	43,86	2,653	8,63	16,45%	45	13,90	169,98	109,06	1,64	32,588
3	2	2590	38,07	54,49	62,03	146,21	54,64	2,676	7,39	11,92%	25	13,90	169,96	113,36	1,57	24,438
4	2A	2590.5	37,14	49,64	53,78	121,67	45,69	2,663	8,09	15,05%	45	13,90	170,12	112,11	1,59	32,588
5	3	2600	38	56,49	64,07	145,02	54,63	2,654	9,44	14,73%	15	13,90	170,11	113,47	1,57	24,451
6	3B	2600.5	37,07	49,68	53,62	122,86	46,32	2,652	7,30	13,61%	235	13,90	170,43	108,95	1,65	29,880
7	4	2601	38	49,99	56,69	133,22	48,99	2,720	7,71	13,59%	235	13,90	169,88	112,95	1,57	29,880
8	4B	2601.5	37,17	49,34	53,54	128,33	47,98	2,675	5,56	10,38%	45	13,90	169,99	116,01	1,53	32,588
9	5	2602	37,98	49,58	56,17	129,26	48,52	2,664	7,65	13,62%	235	13,90	170,30	112,43	1,59	29,880
10	5B	2602.5	37,1	46,59	50,37	115,74	43,40	2,667	6,97	13,84%	145	13,90	170,16	112,86	1,58	35,310
11	6	2603	38,16	50,04	57,23	139,41	59,27	2,352	-2,04	-3,56%	235	13,90	170,33	134,54	1,30	29,880
12	6A	2603.5	37,13	50,89	55,10	126,17	47,50	2,656	7,60	13,79%	235	13,90	169,96	110,54	1,61	29,880
13	7	2604	38,1	36,02	41,07	102,66	38,20	2,688	2,87	7,00%	16	13,90	170,25	123,56	1,43	46,175
14	7B	2604.5	37,17	47,95	52,03	115,52	43,47	2,657	8,56	16,45%	45	13,90	170,22	108,60	1,65	32,588
15	8A	2605	37,18	36,53	39,66	87,83	33,05	2,657	6,61	16,66%	16	13,90	170,19	113,77	1,56	46,175
16	9	2605.5	38,08	51,11	58,21	143,58	53,64	2,677	4,57	7,85%	135	13,90	169,99	121,66	1,45	29,892
17	9B	2606	37,19	49,96	54,27	125,27	47,03	2,664	7,24	13,35%	235	13,90	170,05	109,83	1,63	29,880
18	10	2606.5	38,09	56,65	64,55	150,84	56,88	2,652	7,67	11,88%	5	13,90	170,13	112,68	1,58	21,729
19	10B	2607	37,08	48,03	51,87	116,24	43,78	2,655	8,09	15,60%	45	13,90	170,28	109,12	1,64	32,588
20	11A	2607.5	37,11	43,95	47,54	113,69	42,58	2,670	4,96	10,43%	345	13,90	170,09	116,15	1,53	38,029
21	12	2608	37,16	46,56	50,50	114,04	42,91	2,658	7,59	15,03%	45	13,90	169,96	107,58	1,67	32,588
22	13A	2608.5	37,13	49,89	54,02	134,65	50,37	2,673	3,65	6,75%	235	13,90	170,07	115,49	1,54	29,880
23	15	2609	37,3	49,34	53,91	125,75	47,23	2,663	6,68	12,39%	45	13,90	170,07	114,72	1,55	32,588

4.4.5.4 E-CN1 QUANTITATIVE RESULTS

The E-CN1 reservoir interval ranged between 4081m-4246.7m with a gross thickness of 167.7m. The average volume of clay value of 8.6% indicates that the reservoir is more of a clean sandstone reservoir. The average water saturation value was calculated to be 25.5%. Twenty-six core plugs were used for porosity measurement (Table 4-9). Core porosity measurement ranged between 2.19%- 12.68% with an average poor porosity of 8.7%. Core porosity and log porosity were calibrated (Figure 4-37) and showed a good agreement between the two.

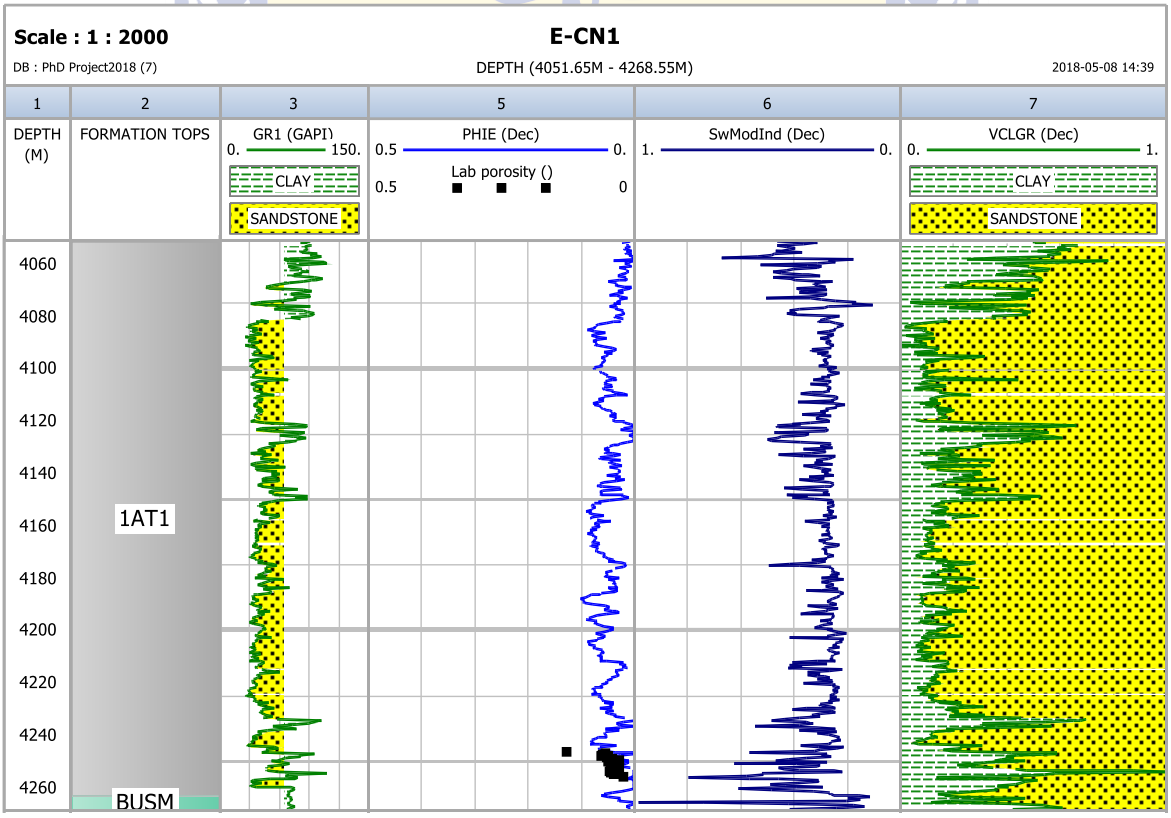

Figure 4-37: Calculated reservoir results for well E-CN1.

Table 4-9: E-CN1 core porosity results obtained from Helium porosimeter.

Sample N+A2:X29o	Sample name	Depth (m)	Sample dia (mm)	Sample length (mm)	Bulk Vol (ml)	Dry Weight (g)	Grain Vol. (ml)	Grain density (g/ml)	Pore Volume (ml)	Porosity (%)	Billets loaded (1 to 6)	Patm recorded (psia)	P_{ref} (psia)	P_{exp} (psia)	P_{ref}/P_{exp}	V. billets loaded (ml)
1	HAA64	4246.55	37,23	51,82	56,41	143,20	53,26	2,689	3,15	5,58%	35	13,89	170,18	115,88	1,53	27,170
2	HAA65	4246.8	37,53	51,62	57,10	133,60	49,86	2,679	7,24	12,68%	135	13,89	170,06	114,60	1,55	29,892
3	HAA66	4247.45	37,26	51,92	56,61	143,70	53,55	2,684	3,06	5,41%	35	13,89	170,12	116,36	1,52	27,170
4	HAA67	4247.70	37,27	52,01	56,74	61,49	53,31	1,153	3,43	6,04%	35	13,89	170,25	116,02	1,53	27,170
5	HAA68	4247.95	37,27	52,12	56,86	143,10	53,38	2,681	3,48	6,13%	35	13,89	170,06	116,01	1,53	27,170
6	HAA69	4248.48	37,25	51,6	56,23	143,00	53,46	2,675	2,77	4,92%	135	13,89	169,90	121,24	1,45	29,892
7	HAA70	4248.72	37,27	52,55	57,33	145,20	54,39	2,669	2,94	5,12%	35	13,89	170,01	117,85	1,50	27,170
8	HAA71	4248.97	37,31	52,5	57,40	147,00	54,80	2,682	2,60	4,53%	35	13,89	170,12	118,69	1,49	27,170
9	HAA72	4249.43	37,3	52,06	56,89	145,50	54,48	2,671	2,41	4,24%	35	13,89	170,11	118,07	1,50	27,170
10	HAA73	4249.7	37,4	51,91	57,03	146,00	54,42	2,683	2,61	4,58%	135	13,89	170,31	123,47	1,43	29,892
11	HAA74	4249.95	37,32	52,8	57,76	149,70	56,05	2,671	1,71	2,97%	35	13,89	170,26	121,21	1,46	27,170
12	HAA75	4250.19	37,4	52,03	57,16	148,30	78,86	1,880	-21,70	-37,97%	35	13,89	170,01	199,79	0,84	27,170
13	HAA76	4251.28	37,51	51,57	56,99	146,10	54,19	2,696	2,80	4,91%	135	13,89	170,17	122,91	1,43	29,892
14	HAA77	4251.5	37,29	50,55	55,21	144,10	53,55	2,691	1,66	3,01%	235	13,89	170,27	121,64	1,45	29,880
15	HAA78	4252.3	37,35	51,98	56,95	148,50	55,02	2,699	1,93	3,40%	35	13,89	169,85	118,92	1,48	27,170
16	HAA79	4252.55	37,35	50,18	54,98	141,90	52,97	2,679	2,02	3,66%	235	13,89	170,15	120,40	1,47	29,880
17	HAA80	4252.79	37,43	52,77	58,07	151,40	56,43	2,683	1,64	2,82%	35	13,89	171,11	122,57	1,45	27,170
18	HAA81	4253.33	37,39	51,47	56,51	145,30	54,48	2,667	2,03	3,59%	135	13,89	170,04	123,41	1,43	29,892
19	HAA82	4253.58	37,58	51,67	57,31	146,40	54,77	2,673	2,54	4,43%	135	13,89	169,50	123,64	1,42	29,892
20	HAA83	4253.83	37,41	52,24	57,42	147,60	55,05	2,681	2,37	4,12%	135	13,89	169,98	124,57	1,41	29,892
21	HAA84	4254.37	37,41	51,26	56,34	143,90	53,86	2,672	2,48	4,40%	235	13,89	169,95	122,05	1,44	29,880
22	HAA85	4254.67	37,36	51,22	56,15	143,00	53,48	2,674	2,67	4,75%	235	13,89	170,14	121,42	1,45	29,880
22	HAA86	4254.93	37,56	49,83	55,21	140,60	52,73	2,667	2,48	4,50%	235	13,89	170,14	119,93	1,47	29,880
23	HAA87	4255.07	37,4	51,32	56,38	145,85	54,69	2,667	1,69	3,00%	135	13,89	170,22	123,97	1,42	29,892
24	HAA88	4255.72	37,33	51,53	56,40	144,47	54,24	2,664	2,17	3,84%	235	13,89	170,00	122,85	1,43	29,880
25	HAA89	4258.87	37,45	52,04	57,32	148,87	55,47	2,684	1,85	3,23%	135	13,89	169,67	125,24	1,40	29,892
26	HAA90	4259.12	37,42	52,39	57,62	150,63	56,36	2,673	1,26	2,19%	35	13,89	170,25	121,83	1,45	27,170

4.4.5.5 E-G1 QUANTITATIVE RESULTS

The E-G1 reservoir interval ranged between 3149.4m-3164.6m with a gross thickness of 15.2m. The average volume of clay value of 813.8% indicates that the reservoir is a shaly sand reservoir. Thirty-five core plugs were used for porosity and 8 for water saturation measurement (Appendix B). Core porosity measurement ranged between 3.6%- 12.7% with average log porosity of 8.7%. Core water saturation ranged between 36.6%- 67% with an average log water saturation of 33.9%. The discrepancies between log water saturation average value and core water saturation reading may be caused by the fact that only 8 core plugs were used for core water saturation whereas log water saturation covers a large interval with a reading every recorded every 15 cm. The core measurements of porosity and water saturation were calibrated (Figure 4-38). Porosity showed a fairly poor agreement and water saturation showed good calibration.

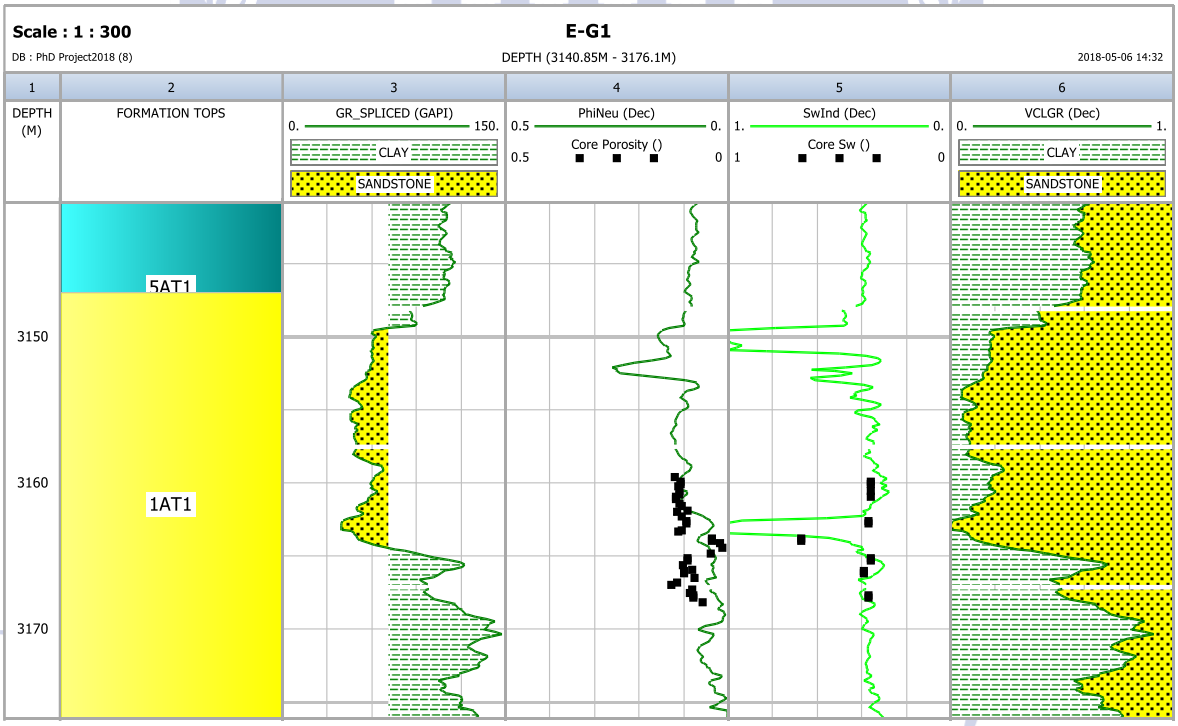

Figure 4-38: Calculated reservoir results of E-G1 well.

4.4.5.6 E-W1 QUANTITATIVE RESULTS

The E-W1 reservoir interval ranged between 3144.8m-3188.1m with a gross thickness of 43.3m. The average volume of clay value of 17.4% indicates that the reservoir is a shaly sand reservoir. The average water saturation value was calculated to be 44.8%. Thirty core plugs

were used for porosity measurement in the laboratory (Table 4-10) and 106 core plugs for core water saturation (Appendix B). Core porosity measurement ranged between 13.42- 22.37% with an average log porosity of 9.5%. Core water saturation ranged between 21%-83% with an average log water saturation of 44.8%. Core porosity and core water saturation were calibrated with log measurements (Figure 4-39). Porosity measurements showed fairly poor calibration whereas water saturation showed a better calibration.

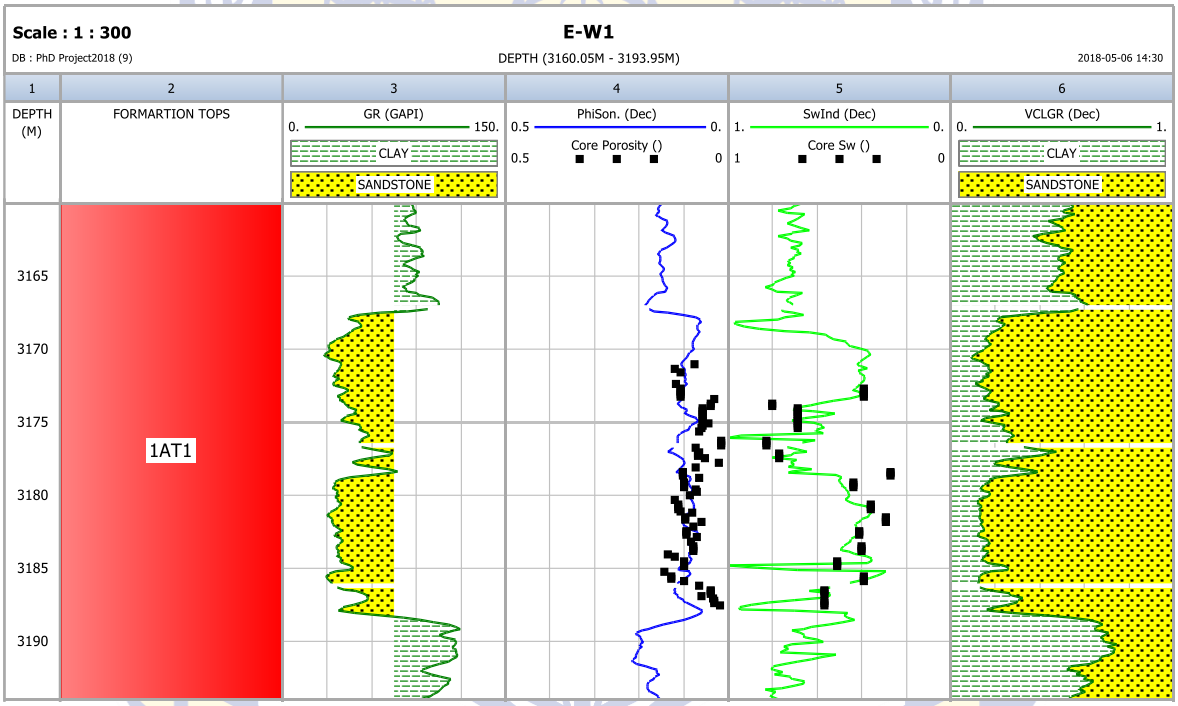

Figure 4-39: Calculated reservoir results of well E-W1.

Table 4-10: E-W1 core porosity results obtained from Helium porosimeter.

Sample No	Sample name	Depth (m)	Sample dia (mm)	Sample length (mm)	Bulk Vol (ml)	Dry Weight (g)	Grain Vol. (ml)	Grain density (g/ml)	Pore Volume (ml)	Porosity (%)	Billets loaded (1 to 6)	Patm recorded (psia)	P_{ref} (psia)	P_{exp} (psia)	P_{ref}/P_{exp}
1	1	3171.05	26,5	31	17,10	40,32	14,09	2,862	3,01	17,61%	46	14,83	169,57	98,12	1,86
2	2	3171.3	26	30	15,93	34,55	12,53	2,758	3,40	21,36%	46	14,83	170,35	96,68	1,90
3	3	3171.55	26	26	13,80	29,54	10,71	2,757	3,09	22,37%	346	14,83	169,85	100,86	1,80
4	4	3171.55	26	26,1	13,86	30,40	11,01	2,762	2,85	20,58%	246	14,83	170,48	98,16	1,87
5	5	3172.35	26	29	15,40	33,80	12,28	2,753	3,12	20,29%	46	14,83	169,82	96,11	1,91
6	6	3172.6	26	29,5	15,66	34,56	12,49	2,767	3,17	20,23%	46	14,83	170,01	96,46	1,90
7	7	3172.69	26	29	15,40	36,16	13,17	2,745	2,23	14,47%	46	14,83	170,11	97,31	1,88
8	8	3173.35	26,1	30	16,05	38,53	13,83	2,787	2,22	13,86%	46	14,83	170,44	98,27	1,86
9	9	3173.73	26	28	14,87	33,98	12,45	2,728	2,42	16,25%	246	14,83	169,87	99,61	1,83
10	10	3174.05	26	30	15,93	37,53	13,79	2,721	2,14	13,42%	46	14,83	170,18	98,09	1,87
11	11	3174.3	26	30	15,93	36,59	13,32	2,747	2,61	16,39%	46	14,83	170,25	97,56	1,88
12	12	3174.55	26	30	15,93	36,86	13,44	2,743	2,49	15,63%	46	14,83	170,43	97,80	1,88
13	13	3174.04	26	30,5	16,19	37,70	13,72	2,747	2,47	15,23%	46	14,83	170,52	98,19	1,87
14	14	3175.4	26	31	16,46	37,21	13,52	2,752	2,94	17,87%	46	14,83	169,82	97,57	1,87
15	15	3175.65	26	31	16,46	37,27	13,63	2,735	2,83	17,21%	46	14,83	170,01	97,80	1,87
16	16	3175.03	26	30	15,93	37,48	13,65	2,746	2,28	14,33%	46	14,83	170,00	97,82	1,87
18	18	3176.24	26	28,5	15,13	34,58	12,58	2,749	2,55	16,85%	46	14,83	169,68	96,39	1,90
19	19	3176.67	26	30	15,93	36,84	13,42	2,745	2,51	15,76%	46	14,83	170,23	97,67	1,88
20	20	3176.93	26	29,5	15,66	35,39	12,94	2,735	2,72	17,38%	46	14,83	169,91	96,93	1,89
21	21	3177.14	26	30	15,93	36,77	13,46	2,732	2,47	15,52%	46	14,83	169,96	97,57	1,87
22	22	3177.5	26	30	15,93	35,53	12,99	2,736	2,94	18,47%	46	14,83	170,01	97,04	1,89
23	23	3177.75	26	30	15,93	33,99	12,38	2,746	3,55	22,28%	46	14,83	169,78	96,21	1,90
24	24	3178	26	24	12,74	27,64	10,02	2,758	2,72	21,35%	346	14,83	170,08	100,10	1,82
25	25	3178.39	26	27	14,34	31,96	11,65	2,743	2,69	18,76%	246	14,83	169,92	98,64	1,85
26	26	3178.8	26	30	15,93	36,62	13,30	2,754	2,63	16,52%	46	14,83	170,24	97,53	1,88
27	27	3179.09	26	23	12,21	27,38	9,86	2,777	2,35	19,25%	1346	14,83	170,02	103,44	1,75
28	28	3179.5	26	28	14,87	34,38	12,52	2,746	2,35	15,82%	146	14,83	169,75	99,64	1,83
27	27	3179.7	26	28	14,87	32,24	12,10	2,664	2,77	18,62%	46	14,83	170,09	96,05	1,91

4.4.5.7 F-A10 QUANTITATIVE RESULTS

The F-A10 reservoir interval ranged between 2721.2m-2949.6m with a gross thickness of 237.4m. The average volume of clay value of 22.3% indicates that the reservoir is a shaly sand reservoir. The core porosity measurements (Table 4-11 and Appendix B) ranged between 19.43%- 27.65% with average log porosity of 15.8%. Core water saturation (Appendix B) ranged between 30%-71% with an average log water saturation of 41.6%. Core porosity and core water saturation were calibrated with log measurements (Figure 4-40). Porosity measurements showed fairly good calibration whereas water saturation showed a fairly poor calibration.

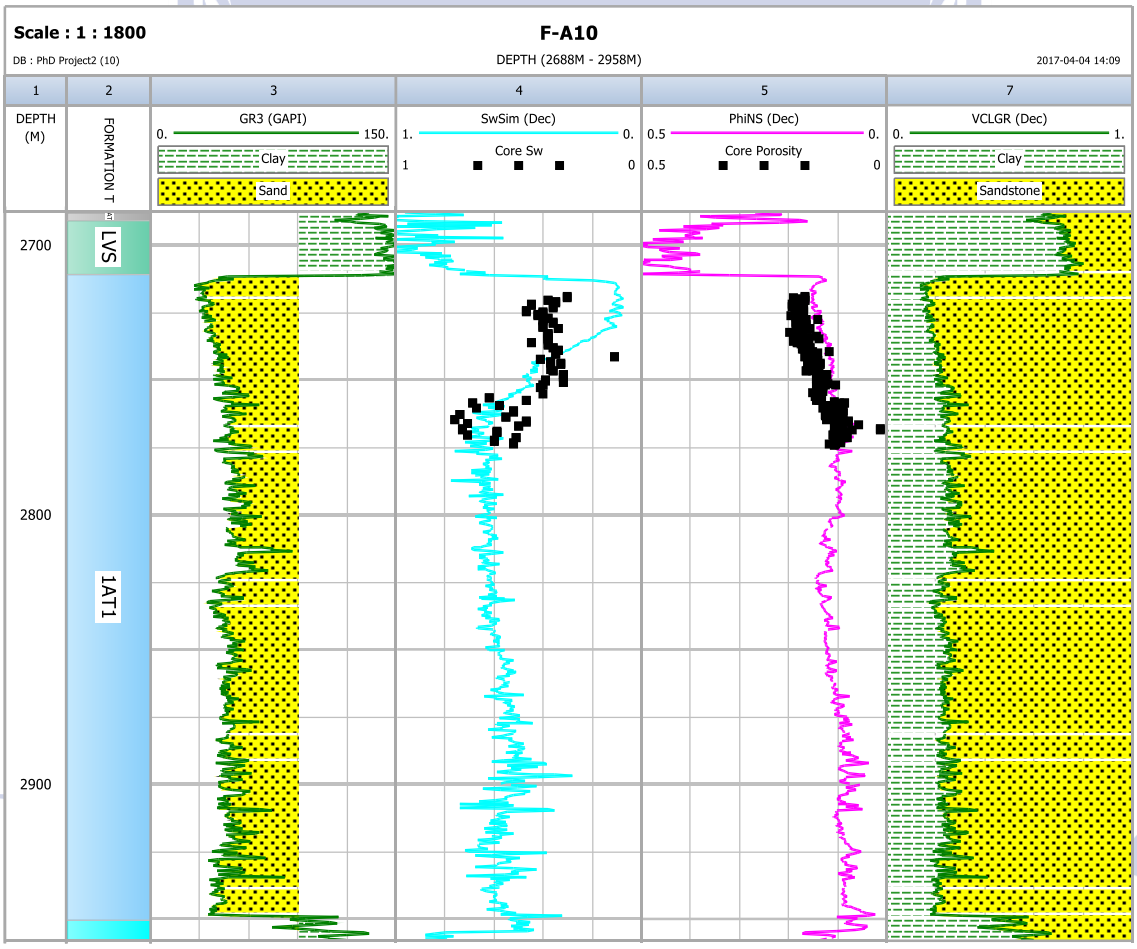

Figure 4-40: Calculated reservoir results of well F-A10.

Table 4-11: F-A10 core porosity results obtained from Helium porosimeter.

Sample No	Sample name	Depth (m)	Sample dia (mm)	Sample length (mm)	Bulk Vol (ml)	Dry Weight (g)	Grain Vol. (ml)	Grain density (g/ml)	Pore Volume (ml)	Porosity (%)	Billets loaded (1 to 6)	Patm recorded (psia)	P_{ref} (psia)	P_{exp} (psia)	P_{ref}/P_{exp}	V. billets loaded (ml)
1	1	2719	25	27	13,25	27,88	9,59	2,908	3,66	27,65%	246	13,98	170,20	95,93	1,91	57,022
2	2	2719.55	24,5	27	12,73	30,93	9,85	3,141	2,88	22,64%	246	13,98	169,87	96,06	1,90	57,022
3	3	2719.85	24,9	27,1	13,20	27,04	9,65	2,801	3,55	26,88%	246	13,98	170,19	96,00	1,90	57,022
4	4	2720.12	24,5	27,9	13,15	30,79	9,97	3,088	3,18	24,17%	146	13,98	170,25	96,42	1,90	57,034
5	5	2720.24	24,5	27,5	12,96	30,11	9,83	3,062	3,13	24,13%	246	13,98	169,94	96,08	1,90	57,022
6	6	2720.64	24,5	27,1	12,78	29,20	9,67	3,018	3,11	24,30%	246	13,98	170,18	96,02	1,90	57,022
7	7	2720.94	25	27,9	13,70	32,01	9,93	3,224	3,77	27,53%	246	13,98	170,03	96,24	1,90	57,022
8	8	2721.03	24,5	27,9	13,15	28,73	9,82	2,927	3,33	25,35%	246	13,98	170,26	96,23	1,90	57,022
9	9	2721.49	24,5	27	12,73	27,77	9,69	2,866	3,04	23,88%	246	13,98	170,24	96,07	1,90	57,022
10	10	2721.79	24,1	27	12,32	29,77	9,74	3,058	2,59	20,98%	246	13,98	170,50	96,26	1,90	57,022
11	11	2721.83	25	24,5	12,03	24,31	8,77	2,771	3,26	27,07%	346	13,98	170,12	98,18	1,85	59,754
12	12	2722.35	24,9	27	13,15	28,82	9,72	2,966	3,43	26,11%	246	13,98	170,20	96,08	1,90	57,022
13	13	2722.65	24,1	27	12,32	31,59	9,93	3,183	2,39	19,43%	246	13,98	170,00	96,22	1,90	57,022
14	14	2722.93	24,5	27,5	12,96	27,78	9,79	2,838	3,17	24,46%	246	13,98	170,15	96,14	1,90	57,022
15	15	2722.94	24,2	27	12,42	26,10	9,73	2,684	2,70	21,70%	246	13,98	170,01	95,99	1,90	57,022
16	16	2723.3	24,9	26	12,66	25,86	9,65	2,680	3,01	23,78%	346	13,98	170,01	99,21	1,83	59,754
17	17	2723.64	24,2	27,1	12,46	27,09	9,73	2,783	2,73	21,89%	246	13,98	170,22	96,11	1,90	57,022
18	18	2723.95	24,2	27,5	12,65	30,93	10,03	3,084	2,62	20,73%	246	13,98	169,98	96,33	1,89	57,022
19	19	2724.22	24,3	28	12,99	32,12	9,95	3,229	3,04	23,42%	246	13,98	170,16	96,33	1,90	57,022
20	20	2724.23	24,5	26,5	12,49	27,85	9,51	2,930	2,98	23,89%	246	13,98	169,96	95,71	1,91	57,022
21	21	2724.44	24,5	28	13,20	27,59	10,01	2,757	3,19	24,20%	146	13,98	169,85	96,25	1,89	57,034
22	22	2724.65	24,5	28,5	13,44	28,61	10,16	2,816	3,28	24,40%	246	13,98	170,48	96,75	1,89	57,022
23	23	2724.95	24,5	28	13,20	27,82	10,09	2,758	3,11	23,58%	146	13,98	170,35	96,61	1,89	57,034
24	24	2724.97	24,5	28,5	13,44	31,55	10,49	3,006	2,95	21,92%	246	13,98	170,88	97,36	1,88	57,022
25	25	2725.37	24,5	29	13,67	30,05	10,34	2,906	3,33	24,35%	1236	13,98	169,53	93,39	1,96	54,326
26	26	2725.67	24,5	28	13,20	27,81	9,97	2,788	3,23	24,44%	246	13,98	170,50	96,54	1,90	57,022
27	27	2725.8	24,5	28,2	13,29	32,15	10,26	3,133	3,03	22,78%	246	13,98	169,80	96,51	1,89	57,022
28	28	2726.14	24,5	28,9	13,62	30,63	10,28	2,980	3,34	24,52%	46	13,98	169,77	93,43	1,96	54,312
29	29	2726.44	24,5	28	13,20	29,71	10,14	2,929	3,06	23,15%	146	13,98	170,11	96,55	1,89	57,034
30	30	2726.74	24,5	28,5	13,44	30,99	10,42	2,974	3,02	22,46%	46	13,98	169,64	93,52	1,96	54,312

4.4.5.8 F-A11 QUANTITATIVE INTERPRETATION

The F-A11 reservoir interval ranged between 2761.1m-2818.8m with a gross thickness of 57.7m. The average volume of clay value of 14.3% indicates that the reservoir is a shaly sand reservoir. The average water saturation and porosity log (Figure 4-41) was 45.5% and 12.9%. No core plugs were available to perform the core measurements.

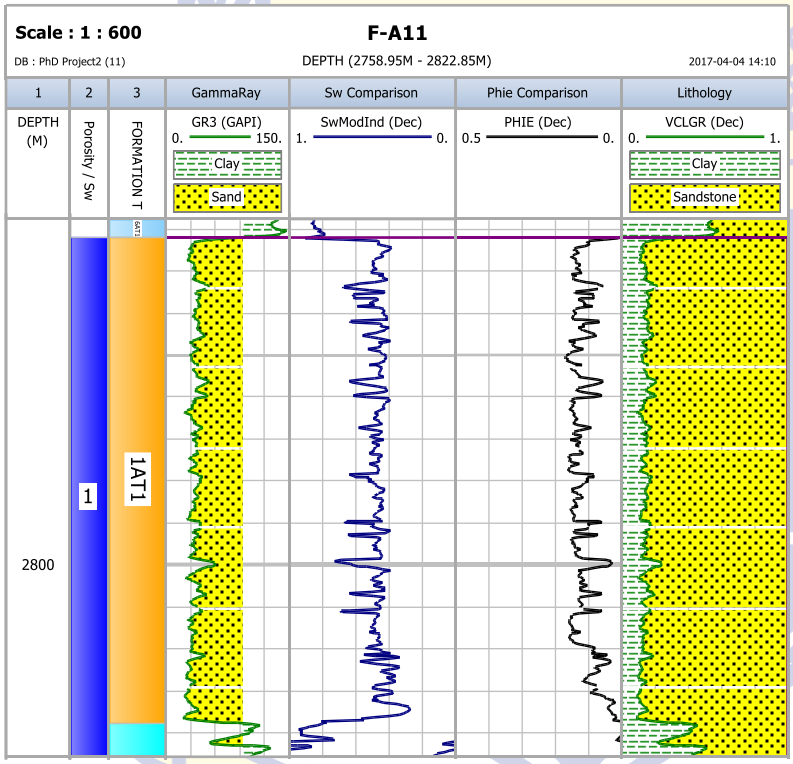

Figure 4-41: Calculated reservoir results of well F-A11.

4.4.5.9 F-A13 QUANTITATIVE RESULTS

The F-A13 reservoir interval ranged between 2610.3 m-2720.4m with a gross thickness of 110.1m. The average volume of clay value of 17.4% indicates that the reservoir is a shaly sand reservoir. The average water saturation value was calculated to be 30.4%. Eighteen core plugs were used for laboratory porosity measurement (Table 4-12) and 120 conventional core analyses (Appendix B). Core porosity measurement ranged between 11.71%- 22.91% with an average porosity of 16.6%. Core porosity and log porosity were calibrated (Figure 4-42) and showed a very good agreement between the two.

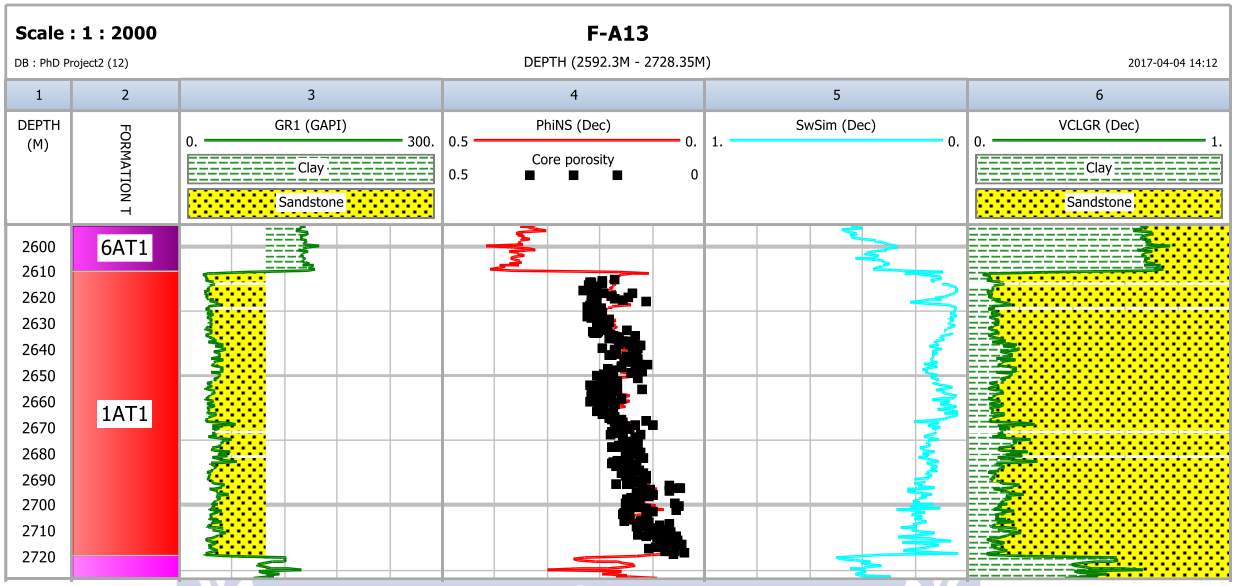

Figure 4-42: Calculated reservoir results of well F-A13.

Table 4-12: F-A13 core porosity results obtained from Helium porosimeter.

Sample No	Sample name	Depth (m)	Sample dia (mm)	Sample length (mm)	Bulk Vol (ml)	Dry Weight (g)	Grain Vol, (ml)	Grain density (g/ml)	Pore Volume (ml)	Porosity (%)	Billets loaded (1 to 6)	Patm recorded (psia)	P_{ref} (psia)	P_{exp} (psia)	P_{ref}/P_{exp}	V, billets loaded (ml)
1	AE9	2615,4	37,89	40,37	45,52	94,83	35,61	2,663	9,91	21,77%	2345	13,89	170,63	109,30	1,64	40,739
2	AE10	2615,43	37,9	40,18	45,33	95,70	35,94	2,66	9,39	20,71%	6	13,89	169,29	113,48	1,56	43,453
3	AE11	2615,94	37,96	40,06	45,34	94,45	35,25	2,679	10,09	22,25%	6	13,89	170,42	113,02	1,58	43,453
4	AE12	2616,19	37,81	40,47	45,44	97,92	36,70	2,668	8,74	19,24%	2345	13,89	170,19	110,77	1,61	40,739
5	AE13	2616,38	37,84	40,55	45,60	101,47	35,15	2,886	10,45	22,91%	6	13,89	169,66	112,37	1,58	43,453
6	AE14	2616,93	37,9	40,19	45,34	99,52	36,96	2,693	8,38	18,48%	6	13,89	169,43	115,36	1,53	43,453
7	AE15	2617,18	38,02	39,9	45,30	105,29	39,06	2,696	6,24	13,78%	6	13,89	168,62	118,71	1,48	43,453
8	AE16	2617,33	38,18	40,26	46,09	108,31	40,53	2,672	5,56	12,05%	2345	13,89	169,68	117,09	1,51	40,739
9	AE17	2617,39	37,92	40,24	45,44	107,54	40,12	2,681	5,32	11,71%	2345	13,89	169,90	116,47	1,52	40,739
10	AE18	2618,14	37,92	40,15	45,34	97,93	36,50	2,683	8,84	19,49%	6	13,89	169,03	114,29	1,55	43,453
11	AE19	2618,3	37,96	40,1	45,38	102,43	38,23	2,680	7,16	15,77%	6	13,89	169,30	117,59	1,50	43,453
12	AE20	2618,77	37,84	39,96	44,94	100,27	37,51	2,673	7,43	16,53%	6	13,89	169,80	116,60	1,52	43,453
13	AE21	2619,04	37,98	40,15	45,49	105,28	39,12	2,691	6,37	13,99%	6	13,89	170,79	120,31	1,47	43,453
14	AE22	2619,29	37,89	40,16	45,28	106,20	39,77	2,671	5,51	12,18%	2345	13,89	169,48	115,56	1,53	40,739
15	AE23	2619,46	37,97	39,72	44,98	101,78	38,11	2,670	6,87	15,27%	6	13,89	170,08	117,90	1,50	43,453
16	AE24	2619,8	37,98	39,77	45,06	104,40	39,27	2,659	5,79	12,85%	6	13,89	169,39	119,64	1,47	43,453
17	AE25	2620,1	38,03	39,67	45,06	102,85	38,13	2,697	6,93	15,38%	6	13,89	169,66	117,65	1,50	43,453
18	AE26	2620,4	38,01	39,77	45,13	103,42	38,49	2,687	6,64	14,72%	6	13,89	170,29	118,75	1,49	43,453

4.4.5.10 F-L1 QUANTITATIVE RESULTS

The F-L1 reservoir interval ranged between 2442m-2606.3m with a gross thickness of 164.3m. The average volume of clay value of 42.8% indicates that the reservoir is shaly sand to shaley. The average water saturation and porosity log (Figure 4-43) was 68.18% and 8.77%. No core plugs were available to perform the core measurements.

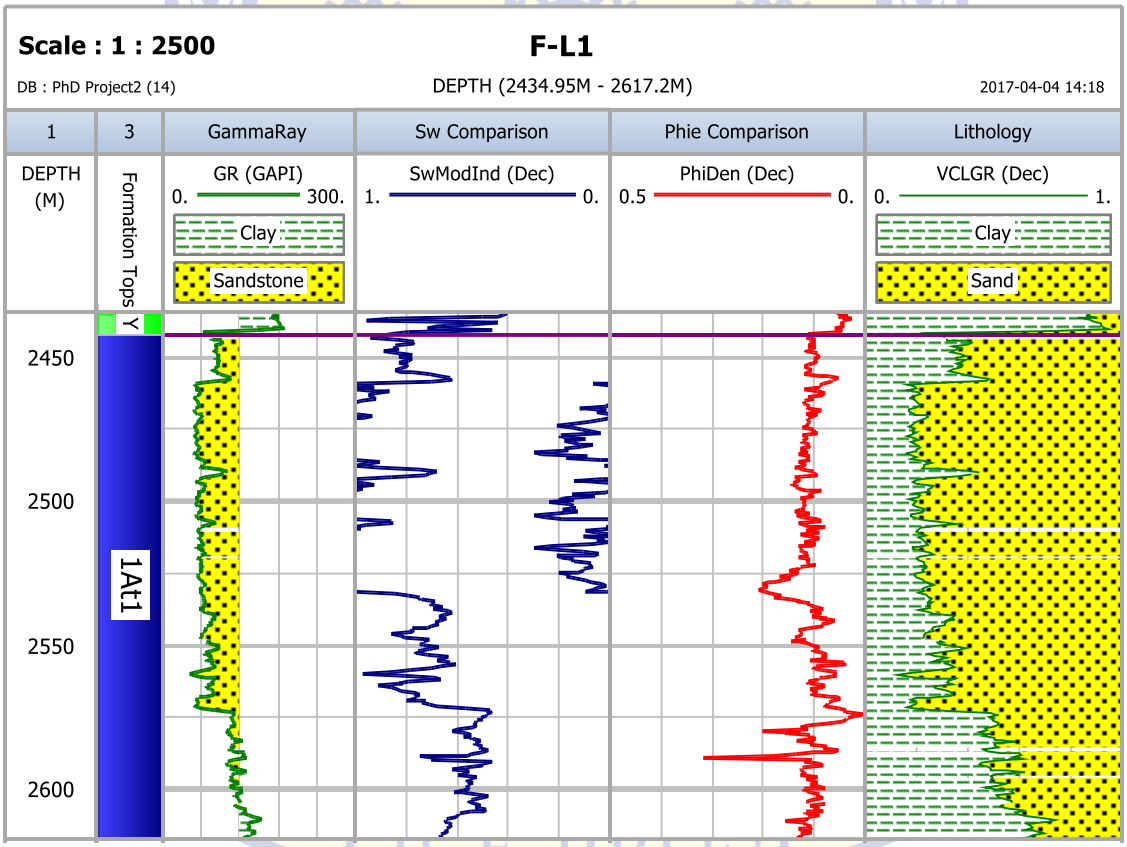

Figure 4-43: Calculated reservoir results of well F-L1.

Table 4-13: Porosity values for reservoir characterization (Modified from Rider, 1986).

Porosity Description	
Percentage porosity (%)	**Description**
0-5	**Negligible**
5-10	**Poor**
10-20	**Good**
20-30	**Very Good**
>30	**Excellent**

Table 4-14: Reservoir summary results of all the studied wells

Well Name	Zone Name	Top (m)	Bottom (m)	Gross (m)	AvPhi (%)	AvSw (%)	Av Vcl(%)
F-O1	1At1	3701.9	3810.6	108.7	9.1	18.9	19.8
F-O2	1At1	3615.5	3685.4	69.9	10.8	12.2	23.3
E-M4	1At1	2558.1	2665.8	107.7	10.2	18.7	29.5
E-CN1	1At1	4081	4246.7	165.7	8.7	25.5	8.6
E-G1	1At1	3149.4	3164.6	15.2	9.2	33.9	13.8
E-W1	1At1	3144.8	3188.1	43.3	9.5	44.8	17.4
F-A10	1At1	2712.2	2949.6	237.4	15.8	41.6	22.3
F-A11	1At1	2761.1	2818.8	57.7	12.9	45.5	14.3
F-A13	1At1	2610.3	2720.4	110.1	16.6	30.4	17.4
F-L1	1At1	2442	2606.3	164.3	8.7	68.2	42.8

4.4.6 GENERAL DISTRIBUTION OF PETROPHYSICAL PROPERTIES ACROSS THE FIELD IN 3D VIEW

The 3-D parameter viewer was used to demonstrate the general trend of petrophysical properties within the studied field. Three parameters (average porosity, average water saturation and the average volume of clay) were displayed within the view. These parameters were determined within the reservoir interval of the evaluated reservoirs. The parameters were plotted against True Vertical Depth (TVD). The legend bar was used to distinguish different values of the parameters using different colours based on the scale. All ten studied wells (F-O1, F-O2, E-M4, E-CN1, E-G1, E-W1, F-A10, F-A11, F-A13 and F-L1) were displayed together with their average reservoir values.

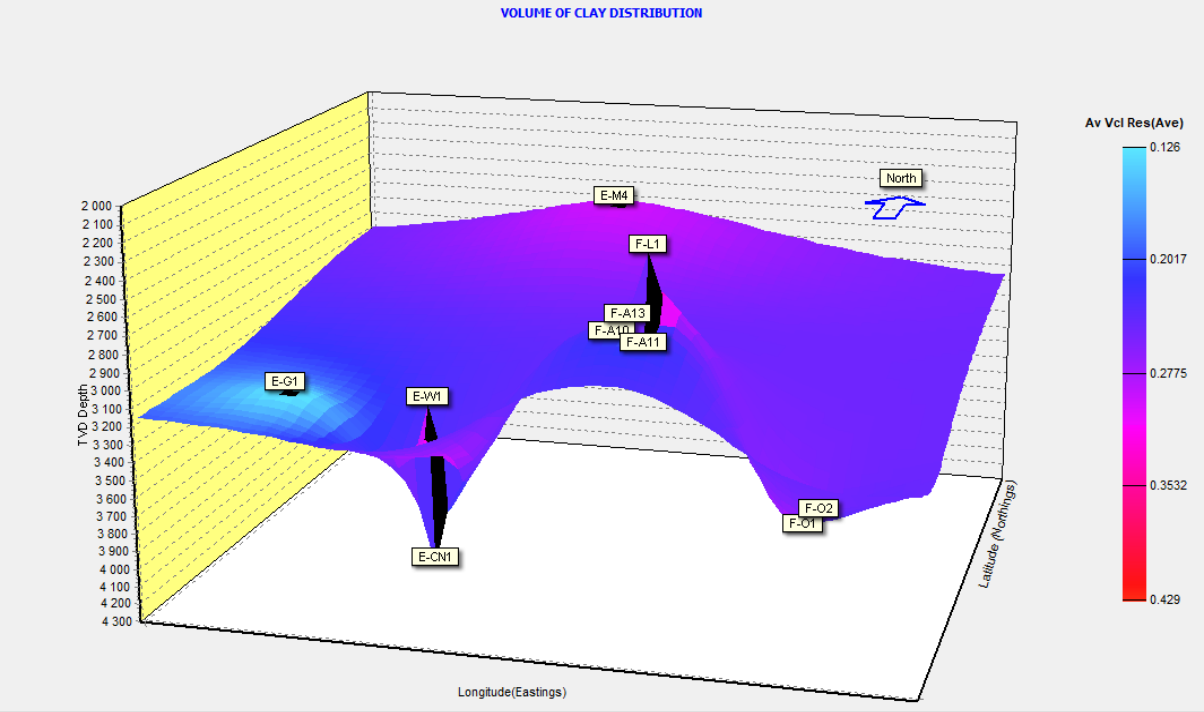

Figure 4-44: 3D parameter view showing the volume of clay content across the field.

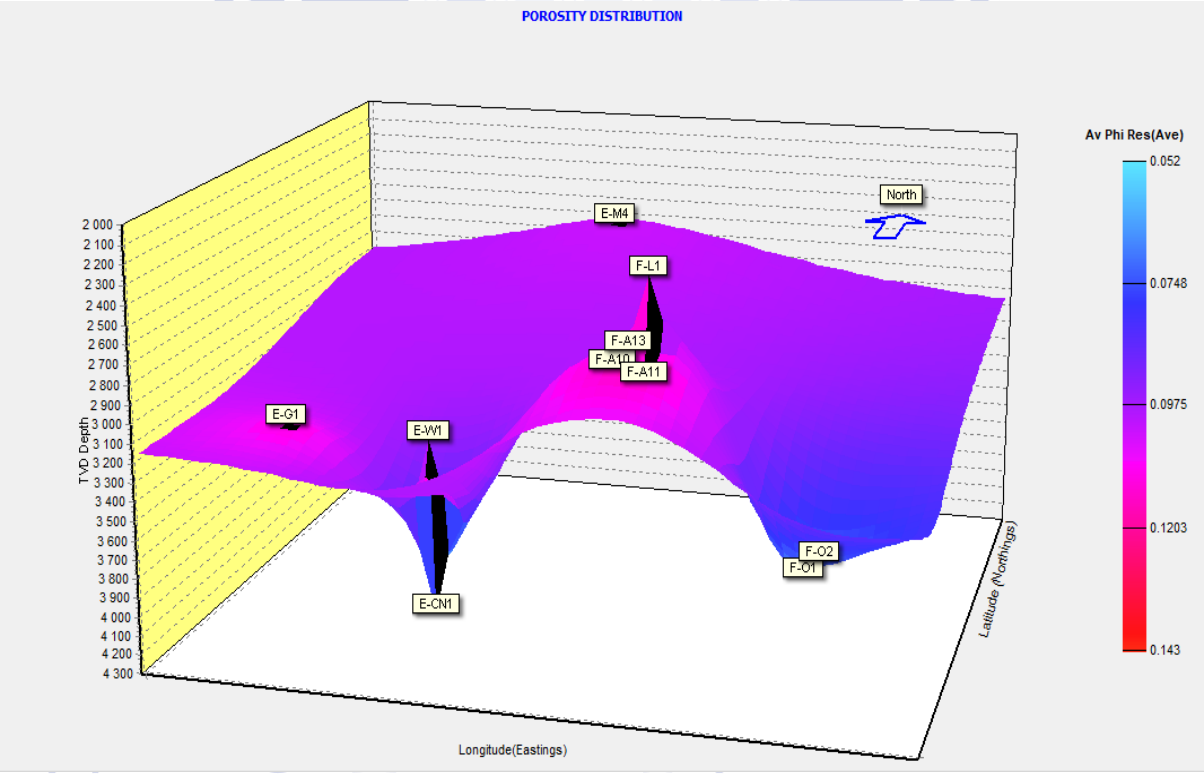

Figure 4-45: 3D parameter view showing porosity distribution across the field.

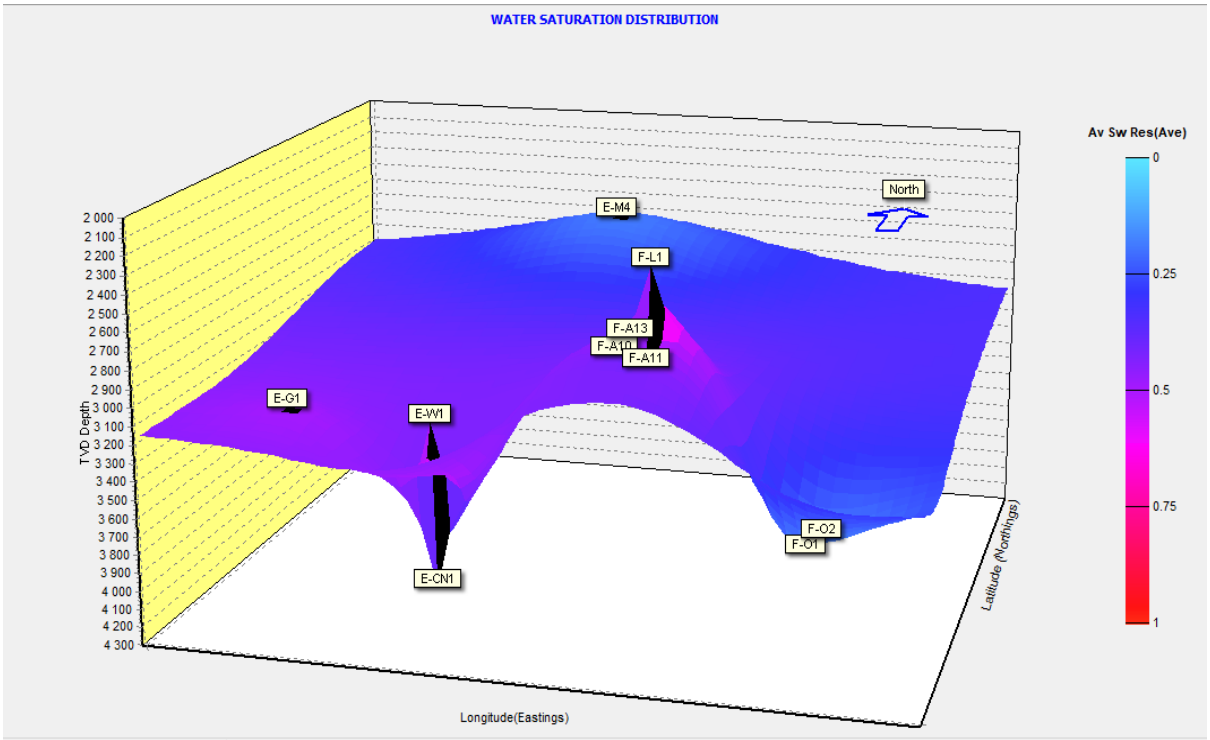

Figure 4-46: 3D parameter view showing water saturation distribution across the field.

The distribution of volume of clay across the field was clearly illustrated in Figure 4-44. The trend can be seen from the eastern side decreasing towards southern direction (E-G1) and increases again going further north-west. This indicates that a low volume of clay is expected in well E-G1 whereas a high volume of clay is expected in E-M4. Porosity distribution in Figure 4-45 was fairly equal across the field from east to west except in well F-A10, F-A13 and F-A11 which showed a much higher porosity and in well E-CN1 which showed a much lower porosity. Water saturation is very low in the eastern and western side of the field. Figure 4-46 showed that low water saturation was expected in well F-O1, F-O2 and E-M4 whereas the rest of the wells showed slightly higher water saturation content.

4.5 CONCLUSION

The investigation of petrophysical properties of the upper shallow marine sandstone reservoir units encountered by ten wells was made possible by detailed analysis and interpretation of well logs and core data within the limits of the quality and amount of data available. The gamma-ray log was used to delineate ten potential reservoirs, one reservoir per well. The results showed the delineated reservoir intervals having average effective porosity ranging from 9% to 16% indicating a good quality reservoir. The average volume of clay, porosity and water saturation values ranged from 8.6%-43%, 9%-16%, and 12%-68% respectively. The distribution of the petrophysical properties across the field was clearly defined with F-A10, F-A13 and F-A13 showing good porosity and E-C1, F-O1 and F-O2 showing poor porosity. E-G1 showed the lowest volume of clay whereas E-M4 showed the highest volume of clay. F-L1 showed the highest water saturation with the value of 68.2% whereas F-O2 showed the lowest value of 12.2%.

4.6 REFERENCES

Broad, (2004). South Africa Activities and Opportunities. An Unpublished PowerPoint Presentation to PetroChina.

Clavier, C., Hoyle, W.R and Meunier, D. (1971). Quantitative interpretation of TDT logs: Parts I and II. J. Pet. Technol. 23, 743 – 763.

Crain, 2014. www.spec2000.net/14-swbasics.htm

Hilchie, D.W. (1978). Applied open hole log interpretation. Colorado: D.W Hilchie Inc.

Houston, J.E. (1986). Dynamic core-hole screening effects in the C-KVV Auger line shape of graphite.

Jensen, J.L., Ayers, W.B. and Blasingane, T.A. (2013). Introduction to shally sand analysis. Department of Petroleum Engineering. Texas A and M University.

Larionov, V. (1969). Radioactivity by Well Log. *Nedra, Moscow (in Russian)*.

Opuwari, M. (2010). Petrophysical evaluation of the Albian age gas bearing sandstone reservoir of the O-M field, Orange Basin, South Africa, PhD thesis, University of the Western Cape, South Africa.

Petroleum Agency of South Africa. (2004/005). Petroleum Exploration Information and Opportunities: *Petroleum Agency SA Brochure*, 2004/2005, 16-18.

Poupon, A. and Leveaux, J. (1971). Evaluation of water saturation in shaly formations; Trans. SPWLA 12th Annual Logging Symposium; 2.

Rider, M. (2002). The Geological interpretation of well logs. Second edition, p1

Schlumberger. (2018). *Schlumberger oilfield glossary*

Simandoux, P. (1963). Dielectric Measurements on Porous Media: Application to measurement of water saturation. Study of the behaviour of argillaceous formation. SPWLA, Houston, vol; 97-124.

Stieber, S. J. (1970, January). Pulsed neutron capture log evaluation-Louisiana gulf coast. In *Fall Meeting of the Society of Petroleum Engineers of AIME*. Society of Petroleum Engineers.

Suzanne, G.C. and Robert, M.C. (2004). Petrophysics of the Lance Sandstone Reservoirs in Jonah Field, Sublette County, Wyoming. AAPG Studies in Geology 52 and Rocky Mountain Association of Geologists 2004 Guidebook; 226-227.

Turner, J.R., Grobbler, N and Sontundu, S. (2000). Geological modelling of the Aptian and Albian sequences within Block 9, the Bredasdorp Basin, Offshore South Africa: *Journal of African sciences*, 31 (1), 80.

Worthington, P.F and Cosentino, L. (2005). The role of Cut-Offs in Integrated Reservoir studies. SPE Reservoir Evaluation and Engineering (4). SPE 84387.

Worthington, P.F. (2008). The Application of Cut-Offs in Integrated Reservoir Studies. SPE Reservoir Evaluation and Engineering (SPE 95428)

CHAPTER FIVE

5 EFFECT OF POROSITY ON ACOUSTIC PROPERTIES AND FLUID SUBSTITUTION MODELLING

ABSTRACT

Acoustic impedance is the product of velocity and density. It gives important information about the nature of the rock and changes in lithology. It is controlled by many factors such as porosity variations, lithological conditions, changes in pore fluid and cementation. To connect rock physics with geology, it is essential to identify and quantify factors influencing density and the acoustic velocity of the sediments that generate seismic reflections patterns. The aim of this chapter was to determine acoustic properties of the Upper Shallow Marine sandstone reservoirs from geophysical wireline logs and core laboratory measurements in order to calculate acoustic impedance and also investigate factors controlling density and acoustic velocities of these sediments. Bulk density and compressional velocity were thoroughly utilized to predict acoustic impedance within the studied reservoirs. The acoustic impedance proved to be highest on the central to the western side of the field at E-CN1well with an average value of 11832 g/cm3s whereas, well F-A13 reservoir in the eastern side of the field proved to have the lowest average acoustic impedance of 9821 g/cm3s. There was a good linear negative relationship between acoustic impedance and porosity, compressional velocity vs porosity and porosity vs bulk density. A good linear negative relationship between acoustic impedance and porosity was obtained where the reservoir was homogenous, thick sandstone. However, interbedded shale units within the reservoir appear to hinder a reliable correlation between acoustic impedance and porosity. The Gassmann equation was used for the calculation of the effects of fluid substitution on acoustic properties using rock frame properties. Three fluid substitution models (brine, oil, and gas) were determined for pure sandstones and were used to measure the behaviour of the different sandstone saturations. A significant decrease was observed in Vp when the initial water saturation was substituted with a hydrocarbon (oil or gas) in all the wells. The value of density decreased quite visibly in all the wells when the brine (100% water saturation) was substituted with gas or oil. The fluid substitution affected the rock property significantly. The Vp slightly decreased when brine was substituted with water in well F-A13, F-A10, F-O2, F-O1 F-A11, F-L1 and E-CN1. Wells E-G1, E-W1 and E-M4 contain both oil and gas and therefore showed a notable decrease from brine to oil and from oil to gas

respectively. Shear velocity (Vs) remained unaffected in all the wells. The acoustic impedance logs showed a decrease when 100% water saturation was replaced with a hydrocarbon (Oil or Gas) in all the wells.

The results showed that porosity and pore fluids are some of the major factors controlling bulk density, compressional and acoustic impedance.

5.1 INTRODUCTION

Acoustic impedance, the product of density and velocity is a basic physical rock property of rocks (Becquey, Lavergne and Willm, 1979). It gives important information about the nature of the rock and changes in lithology. Acoustic impedance is influenced by many geological factors such as lithology interfaces, porosity variations, and changes in pore fluid, overpressure and cementation. Lithology interfaces is a common cause of impedance contrasts. Density and velocity changes whenever lithology changes. Measurement of the acoustic properties of the sandstone reservoirs is of considerable interest in both marine acoustics and geophysics applications (Dunlop and Whichello, 1981). Acoustic velocity is defined as the rate at which a seismic wave travels through a medium, that is, distance divided by travel time (Schlumberger, 2015). It can be determined from vertical seismic profiles, velocity analysis of seismic data or from a sonic log. It can differ laterally, vertically or azimuthally in anisotropic media and increase with depth because compaction reduces porosity (Schlumberger, 2015).

Bulk density is referred to as the density of the grains in a formation or core samples. The term grain refers to all the solid material in the rock because when interpreting the measurements, grains and other solid materials are not distinguished (Schlumberger, 2015). The grain density of the core samples is determined from the measured dry weight divided by the grain volume. It can also be determined by geophysical logs from the density log with known porosity and knowledge of the fluid content present in the formation (Schlumberger, 2015). It is common in units of g/cm3.

These acoustic properties may be measured in-situ during the drilling process or in the laboratory. The preferred measurement technique is always an in-situ measurement through wireline logs as it gives more reliable information. The laboratory measurements with the new technology such as Multi-Sensor Core Log (MSCL) instrument is easily accomplished, but the credibility of the samples/core may be compromised by its removal from the subsurface to the laboratory hence the accuracy of the results obtained from the lab may be questionable. Porosity variation affects acoustic impedance because density and velocity are porosity dependent. Generally, porosity is inversely proportional to acoustic impedance. If there is a slight change in porosity it will generate modest impedance contrast, whereas a rapid change in porosity can result in a large reflection coefficient. Pore fluid changes affect density and velocity. A change in pore fluid from water to oil will result in small impedance contrast that can be detected seismically only in ideal signal-to-noise conditions whereas a change in pore

fluid from the liquid (oil or water) to gas can produce a large impedance contrast and massive seismic reflections. Acoustic impedance is also affected by overpressure because of density and velocity decrease in overpressure zones. Cementation affects the mechanical strength of rock properties. Generally, velocity increases with increasing mechanic strength. The effect of some of these geological factors on acoustic impedance will be investigated in this chapter. The results reported in this chapter are those measured from the in-situ (Sonic (transit time), bulk density) and those computed from the IP 4.2 software.

5.2 AIMS AND OBJECTIVES

The aim of this chapter was to determine the acoustic properties (Bulk density and acoustic velocities) of the shallow marine gas sandstone reservoirs from wireline logs in order to calculate acoustic impedance and investigate factors affecting density and acoustic velocities of these sediments. The effect of the pore fluid on acoustic impedance was also thoroughly investigated. The objective was to create a 3D parameter viewer model to illustrate the distribution of acoustic impedance across all the studied wells and also to identify and model parameters affecting acoustic velocity and density. Gassmann fluid substitution model was used to model the effect of pore fluid on the acoustic properties. The effect of porosity on acoustic impedance, bulk density and velocity was thoroughly studied using cross-plots.

5.3 MATERIALS AND METHOD

5.3.1 DATA SET

A suite of wireline logs (LAS format) was provided by the Petroleum Agency of South Africa (PASA). The wireline logs used in this study were bulk density (RHOB), Sonic (DT) and Gamma Ray (GR). Interactive Petrophysics version 4.2 software was used extensively throughout this chapter to display, calculate and model all the parameters from the logs.

5.3.2 ESTIMATION OF COMPRESSIONAL VELOCITY AND ACOUSTIC IMPEDANCE FROM WIRELINE LOGS

Acoustic velocities (Vp and Vs) were calculated from Shear sonic QC/create model under the Rock Physics module on IP software. This method requires Sonic log (DT) as an input log. The

output curve is a shear sonic log (DTS). The DT shear curve is calculated using the Greenberg-Castagna (1992) empirical relations (Figure 5-1).

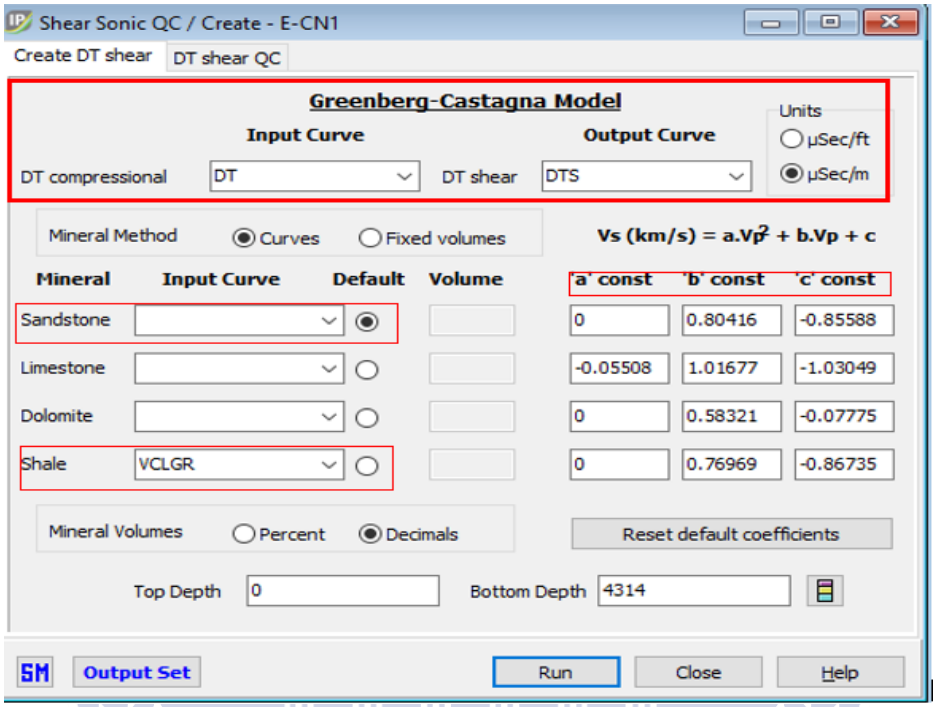

Figure 5-1: Illustration of steps followed for the Vp and Vs calculations.

The defaults constant are those defined by Greenberg-Castagna (1992) for 100% brine saturated rocks. These constants can be modified. The mineral method was used to select the mineral input curve to the computation. The mineral method specifies which mineral is used as the default when the other mineral does not add up to 100%. In this calculation, only shale input mineral curve (VCLGR) has been entered and the default mineral has been set to sandstone. Therefore, the mineral mixture will be the shale volume specified by the VCLGR with the sandstone volume being 1-VCLGR. The resulting DT shear output curve is calculated by first computing the equivalent velocities for all the pre-defined minerals and then averaging the results using a Voigt-Reuss-Hill averaging technique. This technique creates mineral volume weighted arithmetic- and weighted harmonic-averages and then takes the average of these results. The Following equation is used:

$$V_S = \frac{1}{2}\left\{\left(\sum_{i=1}^{4} X_i \times Vs_i\right) + \left(\sum_{i=1}^{4} X_i / Vs_i\right)^{-1}\right\}$$

Where

Xi = Volume of ith mineral

Vsi = Shear velocity of ith mineral

Vs = Shear Velocity

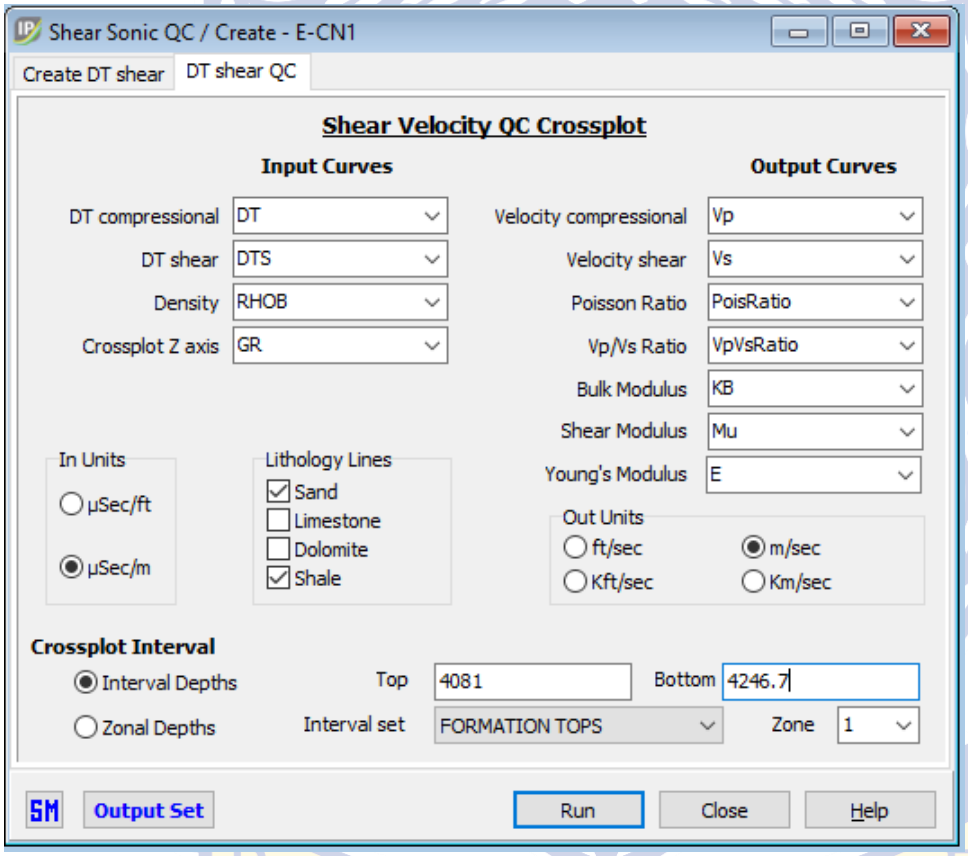

Figure 5-2: Shear velocity QC cross-plot calculation.

The shear velocity cross-plot is generated by this module using Greenberg-Castagna (1992) empirical relationship to verify that the calculated Shear sonic curve is a good shear wave curve and not a mud-wave or Stoneley-wave velocity produced by poor processing of the sonic waveform data. DT compressional sonic, calculated DT shear, Density (RHOB) and Gamma-ray (GR) were used as an input log. The module generates the equivalent compressional and shear velocity curves (Vp and Vs) plus the Poissons ratio (PoisRatio), Vp/Vs Ratio, Bulk Modulus (KB) and Shear Modulus (Mu) curves (Figure 5-2).

Velocity was also calculated from Petrel Schlumberger software 2015 using the following formula:

Vint= deltaZ/deltaT

Where Vint= Interval velocity, detltaT is the OWT (Checkshots data) over the interval in seconds and deltaZ is the depth over the interval in meters. Interval velocity is the average velocity over a given interval.

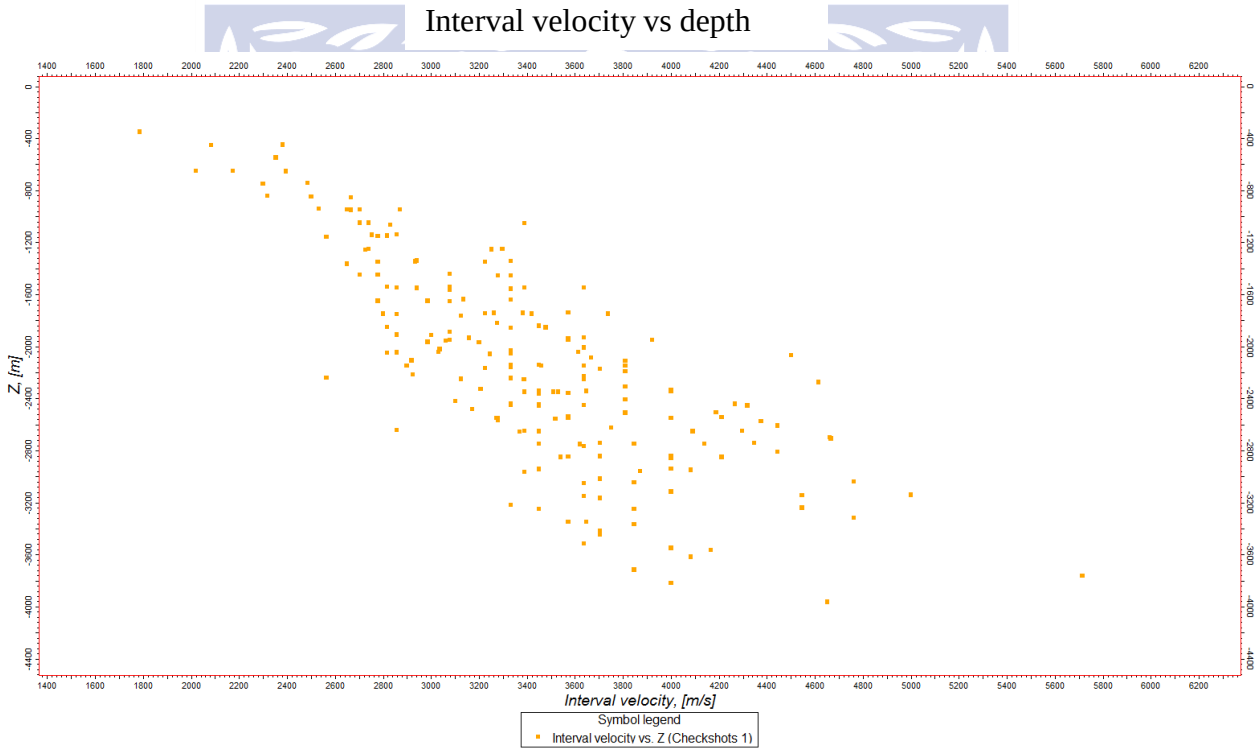

Figure 5-3: Relationship between velocity and depth in well F-A13.

The relationship between velocity and depth is illustrated in Figure 5-3 to verify the reliability of the calculated velocity log. Both compressional velocity log estimated from Greenberg and Castagna on IP 4.2 software and interval velocity log calculated from petrel agreed with each other.

Acoustic impedance is the product of velocity and density. The following equation was used to calculate a continuous acoustic impedance log for all 10 wells:

Al= Vp*RHOB

Where:

Al= Acoustic impedance

Vp= Compressional velocity

RHOB= Bulk density

5.4 WELL LOG RESULTS AND INTERPRETATION

5.4.1 INTRODUCTION TO WELL LOG ANALYSIS

Acoustic impedance is defined as "the product of density and seismic velocity which varies among different rock layers and is commonly symbolized as Z" (but in this study it will be symbolized as Al). The variations in acoustic impedance between rock layers affect the reflection coefficient. Acoustic impedance is represented by the formula as:

Al= Vp* RHOB

Where Vp is compressional velocity and RHOB is the bulk density.

The acoustic impedance of the studied sandstone reservoirs was calculated for each well to understand the variation across the field. Gamma-ray and bulk density logs from the LAS file and the calculated compressional velocity and acoustic impedance logs are displayed in Figure 5-4 to 5-13 below.

5.4.2 F-O2 WELL LOG INTERPRETATION

The zone of interest in the 1At1 formation falls within the range of 3615.5m-3685.4m with a thickness of 69m (Figure 5-4). Gamma-ray log reveals a thick sandstone unit within this interval. Track 4 and 5 shows a continuous density (RHOB) and compressional velocity (Vp) logs used to predict acoustic impedance (Al) log displayed in track 6. Notice the change in velocity (Vp) from Top and Bottom of the Low-Velocity Shale (TLVS and BLVS) to the top of the gas sandstone interval. It is important to note that there is a little or no reflection on the acoustic impedance log at the top of the gas sandstone reservoir. This lack of reflection in acoustic impedance will result in the lack of reflection coefficient on the seismic data. This makes it difficult for seismic interpreters to pick up the top of the gas sandstone on the seismic data. The average reading of RHOB, Vp and Al (Table 5-1) within the zone of interest is 2.5g/cm^3, 4126.5m/s and 10316g/cm^{3}s respectively.

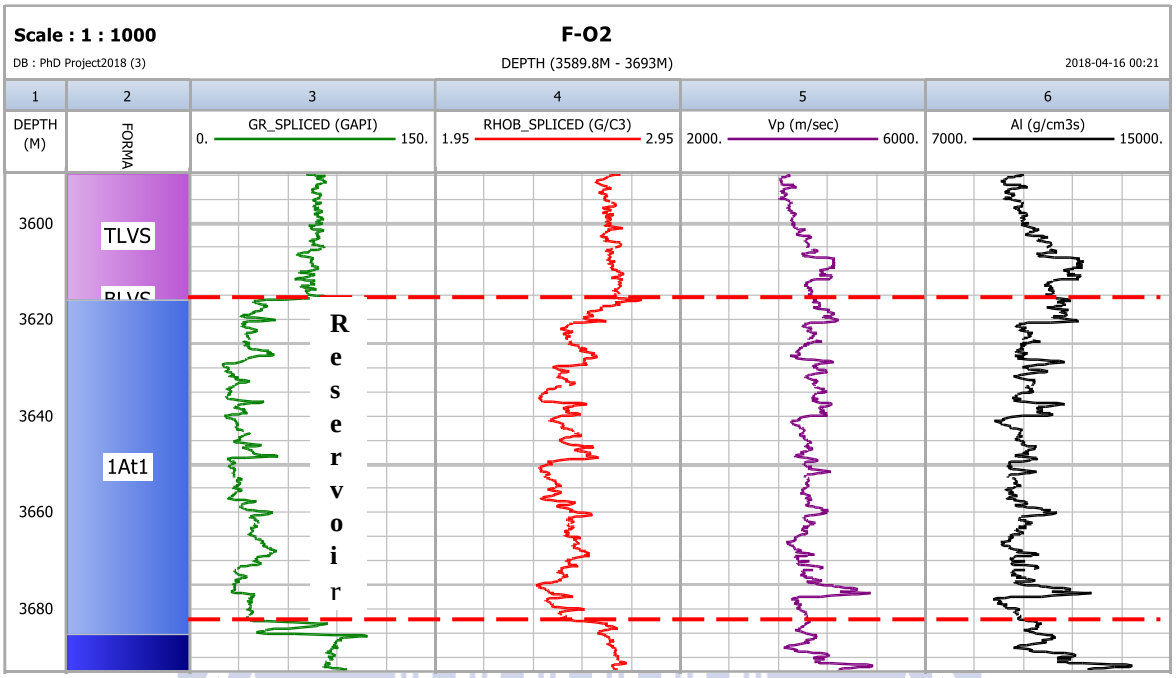

Figure 5-4: Gamma-ray, Bulk density, Compressional velocity and acoustic impedance logs of well F-O2.

5.4.3 E-M4 WELL LOG INTERPRETATION

The zone of interest in the 1At1 formation falls within 2558.1m-2665.8 (Figure 5-5). Gamma-ray log (Track 3) reveals a 107.1m thickness of sandstone reservoir. Track 4 and 5 shows a density (F_RHOC) and compressional velocity (Vp) which was used to predict the acoustic impedance (Al) log. The average reading of RHOB, Vp and Al recorded (Table 5.1) was 2.472g/cm^3, 4296.16m/s and 10594g/cm^{3}s respectively.

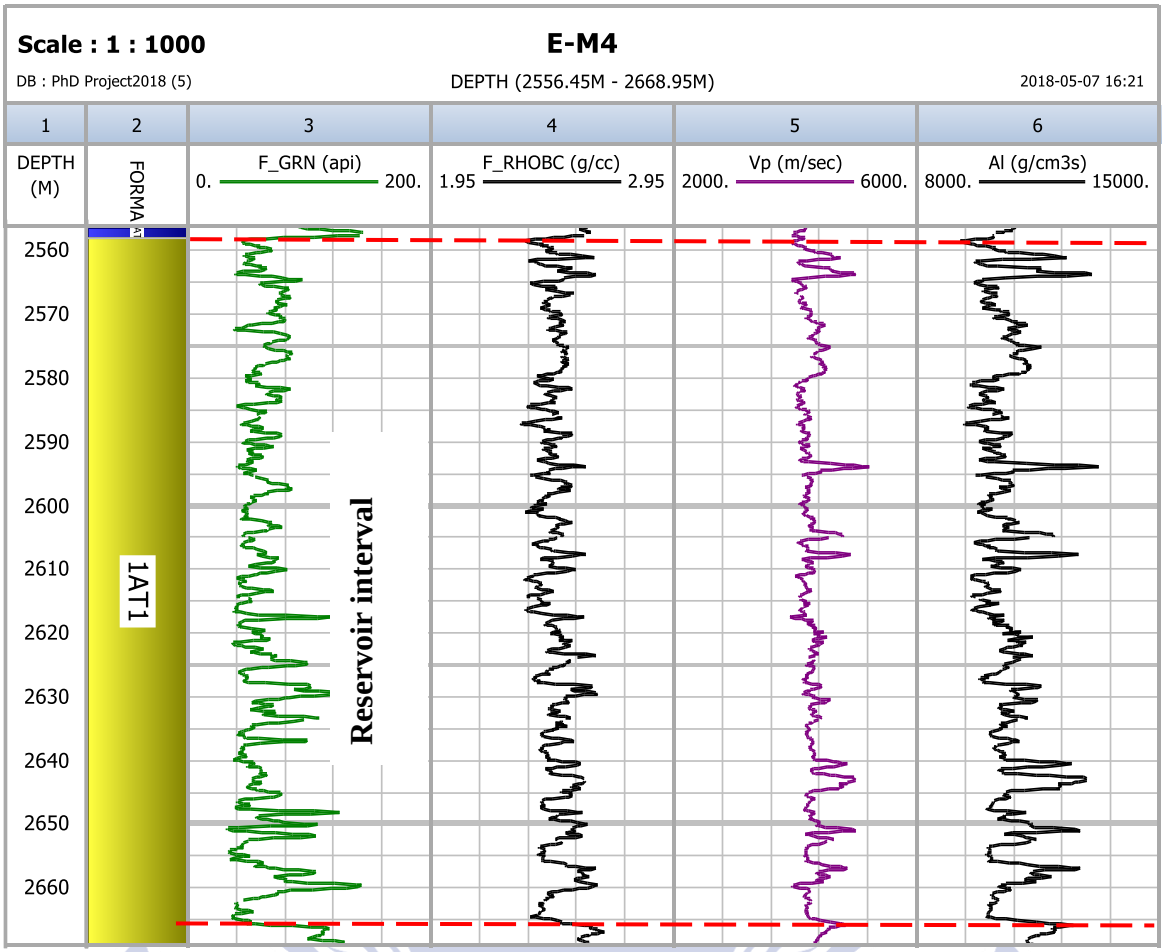

Figure 5-5: Gamma-ray, Bulk density, Compressional velocity and acoustic impedance logs of well E-M4.

5.4.4 E-CN1 WELL LOG INTERPRETATION

The zone of interest was identified within the 1At1 formation using the gamma-ray log (track 1) with a thickness of 165.7m (Figure 5-6). The behaviour of Vp and Al within the zone of interest does not show a clear trend with depth because there are a continuous increase and decrease in both logs. The average reading of RHOB, Vp and Al recorded (Table 5.1) was 2.578g/cm^{3}s, 4587m/s and 11832g/cm^{3}s respectively.

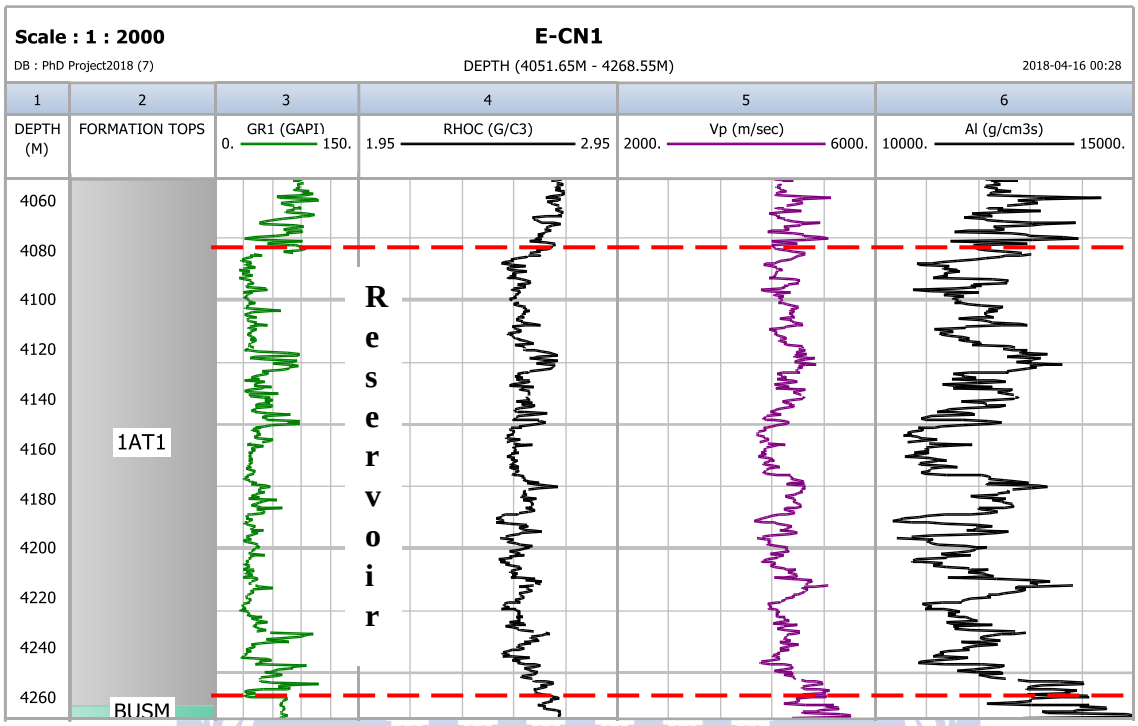

Figure 5-6: Gamma-ray, Bulk density, Compressional velocity and acoustic impedance logs of well E-CN1.

5.4.5 E-G1 WELL LOG INTERPRETATION

The gas sandstone reservoir of E-G1 identified from the gamma-ray log in 1At1 formation ranges between 3149m-3616.6m with a thickness of 15.2m (Fig 5-7). A quick look at Vp and Al logs show a trough just below the top of the gas sandstone reservoir which might be an indication of high porosity interval, both logs also shows a peak just above the bottom of the reservoir which might also indicate either a low porosity zone or the presence of dense clay minerals. The average readings of RHOB, Vp and Al recorded (Table 5.1) was 2.566g/cm^3, 4442m/s and 11121g/cm^{3}s respectively.

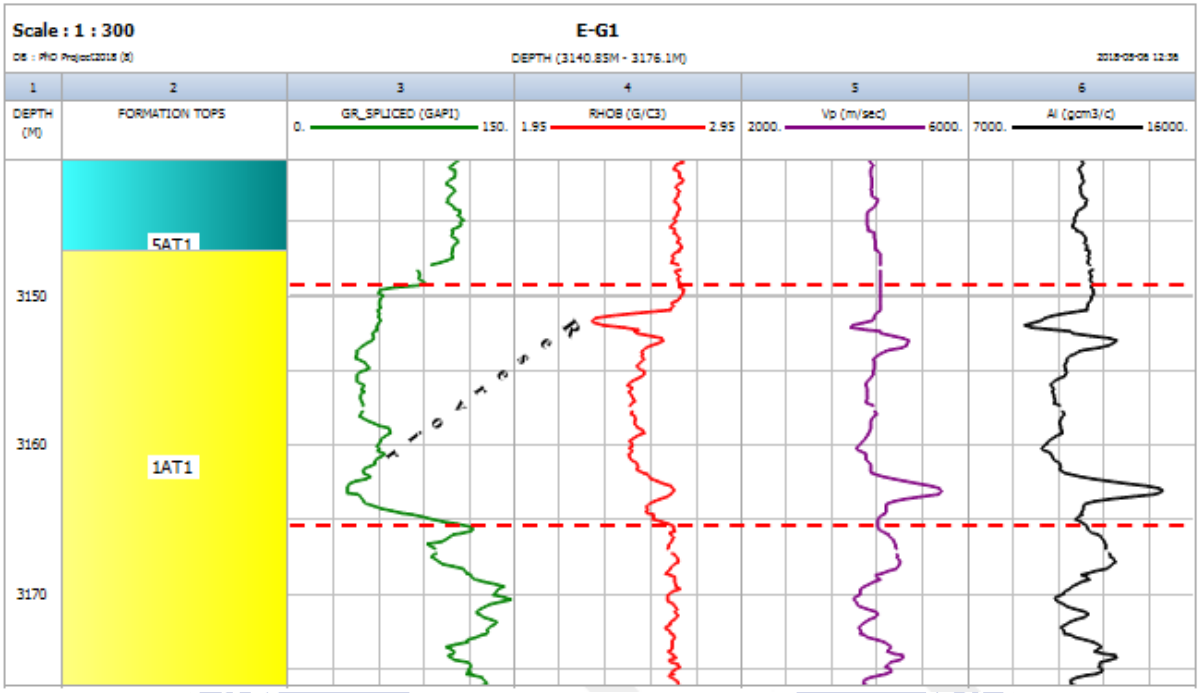

Figure 5-7: Gamma-ray, Bulk density, Compressional velocity and acoustic impedance logs of well E-G1.

5.4.6 E-W1 WELL LOG INTERPRETATION

The zone of interest in the 1At1 formation identified using the gamma-ray log (track 3) revealed a thickness of 43.3m between 3144m-3188m (Fig 5-8). There is a sharp increase in both Vp and Al at the top of gas sandstone which indicates a change in lithology from shale to sandstone. There is intercalation of clay/shale within the reservoir zone which explains the increase and decrease of Vp and Al logs with depth. The average readings of RHOB, Vp and Al was 2.596g/cm3, 4394m/s and 11405g/cm3s (Table 5-1).

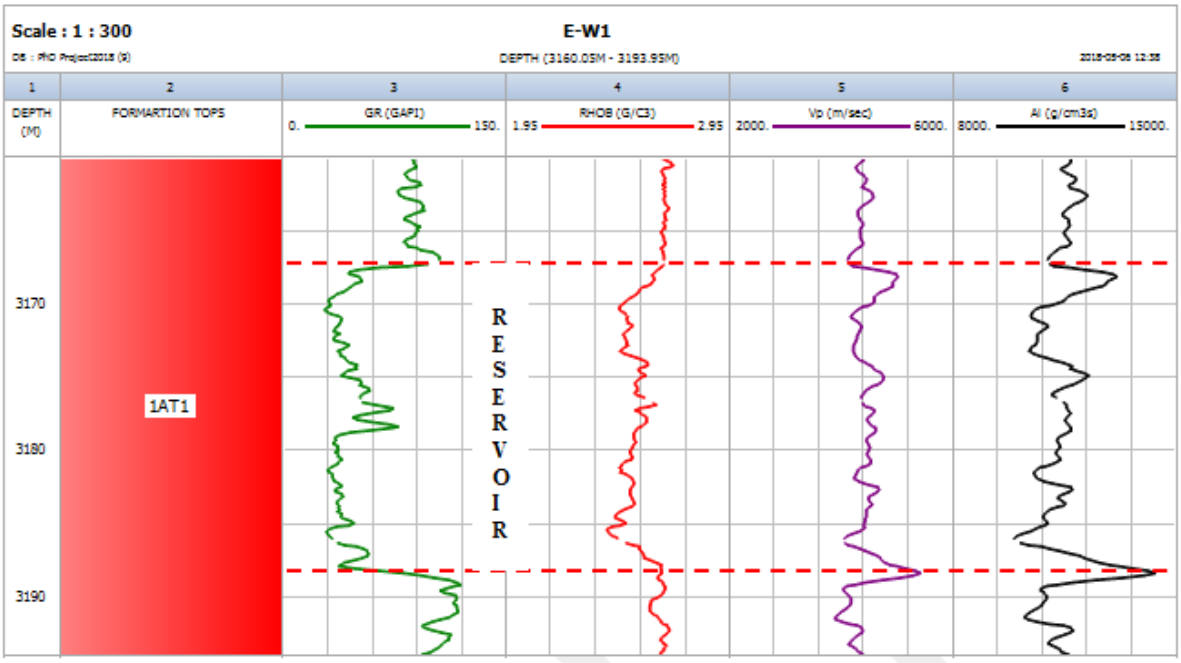

Figure 5-8: Gamma-ray, Bulk density, Compressional velocity and acoustic impedance logs of well E-W1.

5.4.7 F-A10 WELL LOG INTERPRETATION

The gamma-ray log (track 3) identified a very thick gas sandstone interval between 2712m-2949m with a thickness of 237m (Figure 5-9). Track 4 and 5 shows density and compressional velocity logs which were used to predict the acoustic impedance log. The behaviour of F-A10 acoustic impedance log is almost similar to that of F-O2 whereby there is a little or no reflection at the top of the gas sandstone reservoir just below the Low-Velocity Shale (LVS). This is also an indication that the Low-Velocity Shale overlying the top of the gas sandstone reservoir is also playing a role in affecting the acoustic impedance because of the similar velocity readings between LVS and gas sandstone. The average reading of RHOB, Vp and Al logs recorded (Table 5-1) was 2.455g/cm3, 4334m/s, and 10656g/cm3s.

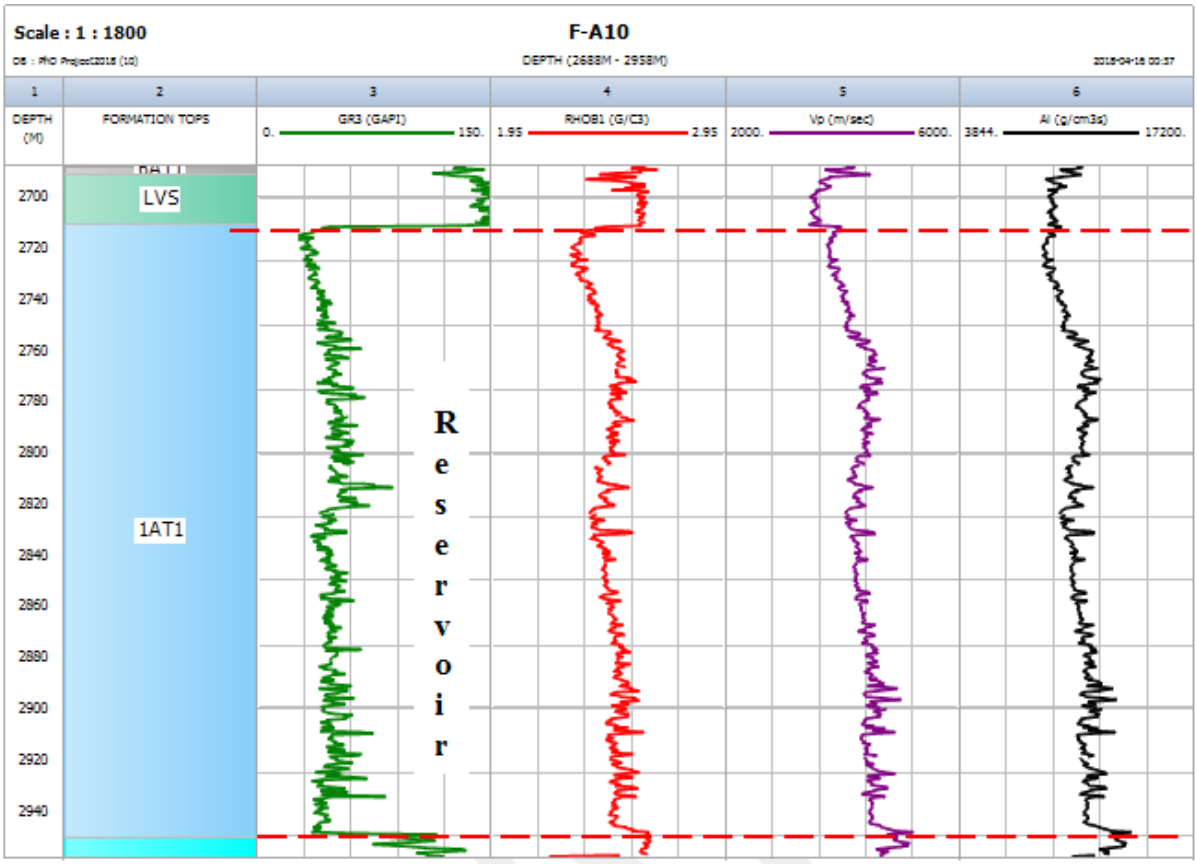

Figure 5-9: Gamma-ray, Bulk density, Compressional velocity and acoustic impedance logs of well F-10.

5.4.8 F-O1 WELL LOG INTERPRETATION

The zone of interest in the 1At1 formation falls within the range of 3710.9m- 3810.6m with a thickness of 108.7m. A quick look at the section (Figure 5-10) reveals a thick pack of sandstone unit identified from Gamma-ray log (Track 3). Track 4 and 5 display the density (RHOB) and compressional velocity (Vp) log used to predict acoustic impedance (Al) log displayed in track 6. The trend of RHOB, Vp and Al can be seen increasing with depth. At depth 3720m-3740, Vp and Al logs show a peak and RHOB shows a trough which might be an indication of low porosity zone. The average reading of RHOB, Vp and Al recorded (Table 5-1) within the zone of interest was 2.573 g/cm3, 4530m/s and 11610g/cm3s respectively.

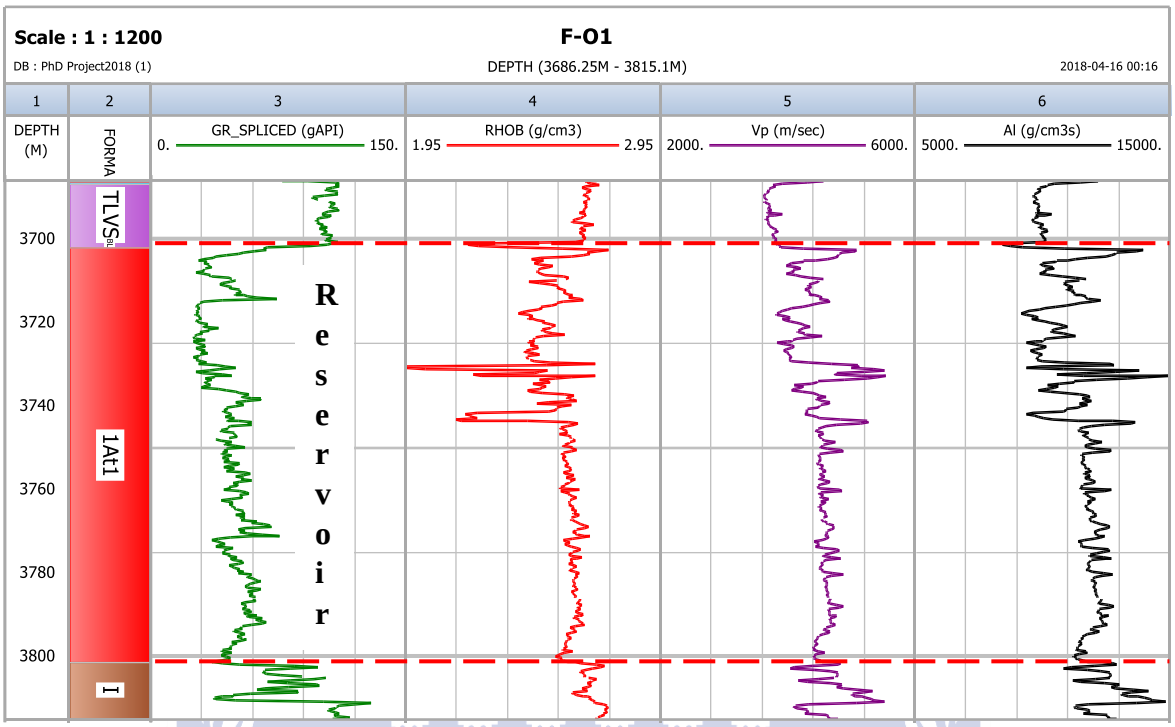

Figure 5-10: Gamma-ray, Bulk density, Compressional velocity and acoustic impedance logs of well F-O1.

5.4.9 F-A11 WELL LOG INTERPRETATION

The zone of interest of 1At1formation falls within 2761.1m-2818.8m with a thickness of 57.7m. A quick look at the log section (Figure 5-11) reveals a thick pack of sandstone reservoir interval identified from the gamma-ray log (track 3). The density and compressional velocity log used to predict acoustic impedance log (track 6) were displayed in track 4 and 5 respectively. The RHOB, Vp and Al logs show a rapid increase at about 2810m. This rapid change can be attributed to either a change in mineralogy at the bottom of the reservoir or a decrease in porosity. The average readings of RHOB, Vp and Al recorded (Table 5-1) was 2.471g/cm3, 4391.8m/s, and 10866g/cm3s.

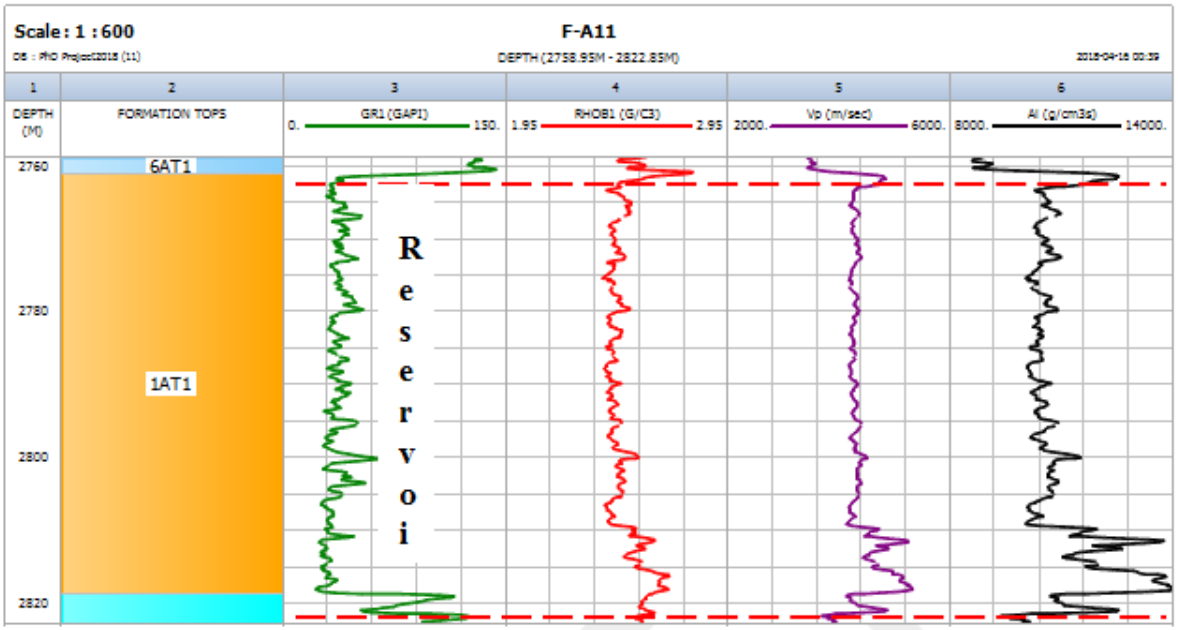

Figure 5-11: Gamma ray, Bulk density, Compressional velocity and acoustic impedance logs of well F-A11.

5.4.10 F-A13 WELL LOG INTERPRETATION

The gas sandstone reservoirs in the 1At1 formation identified from the gamma-ray log fall within 2610.3m-2720.4m depth with a thickness of 110.1m (Figure 5-12). The density and compressional velocity log displayed in track 4 and 5 were used to predict the acoustic impedance log displayed in track 6. The three mentioned logs show a rapid decrease at 2650m-2660m before a continued increase with depth. This decrease might be an indication of high

porosity section. The average readings of RHOB, Vp and Al recorded (Table 5-1) was 2.427g/cm3, 4038m/s and 9821m respectively.

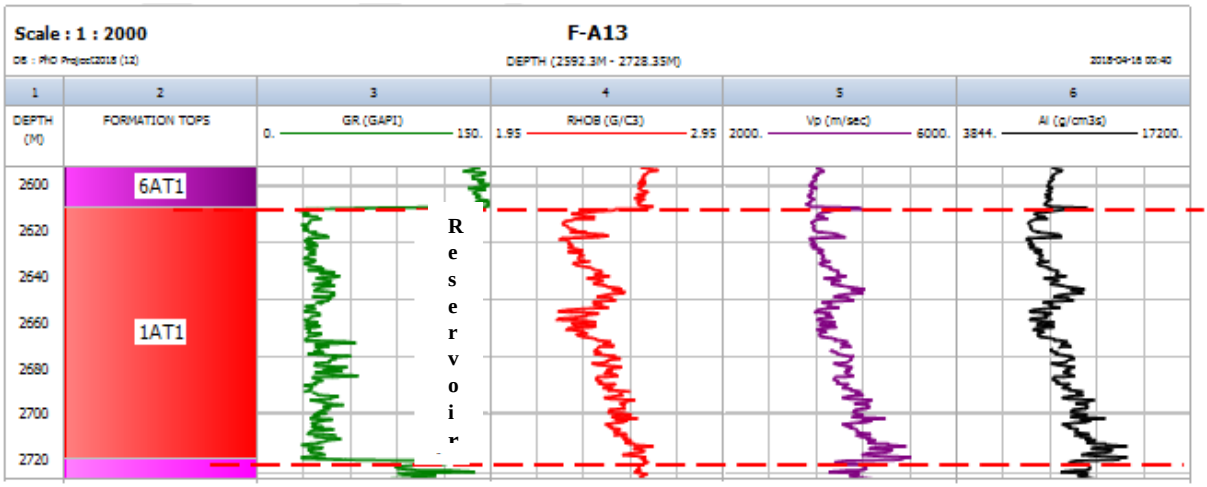

Figure 5-12: Gamma-ray, Bulk density, Compressional velocity and acoustic impedance logs of well F-13.

5.4.11 F-L1 WELL LOG INTERPRETATION

The gamma-ray log identified a pack of sandstone reservoir with intercalation of clay in 1At1 formation between 2442m-2695m with a thickness of 253m (Figure 5-13). Track 4 and 5 shows a density and compressional velocity logs used to predict the acoustic impedance (track 6). All three logs seem to follow the same trend with relation depth. The average RHOB, Vp and Al recorded (Table 5-1) was 2.529g/cm3, 4056.9m/s and 10264g/cm3s.

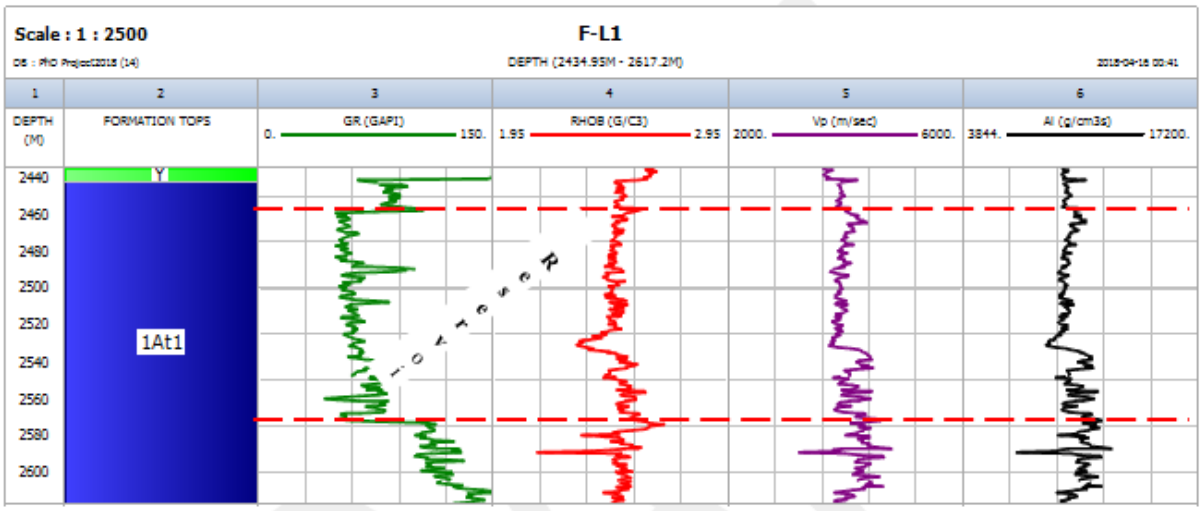

Figure 5-13: Gamma-ray, Bulk density, Compressional velocity and acoustic impedance logs of well F-L1.

Table 5-1: Average values of bulk density, compressional velocity, and acoustic impedance.

Well name	(Depth) From (M)	(Depth) To (M)	Thickness (M)	RHOB (g/cm3)	Vp (m/s)	AI (g/cm3s)
E-M4	2558.1	2665.8	107.70	2,472	4296.15	10594
F-A13	2610,3	2720,4	110,1	2,427	4038	9821
F-A11	2761,1	2818,8	57,7	2,471	4391,8	10866
F-O1	3701,9	3810,6	108,7	2,573	4530,4	11610
F-L1	2442	2695	253	2,529	4056,9	10264
E-W1	3144	3188	43,3	2,596	4394	11405
E-CN1	4081	4246,7	165,7	2,578	4587	11832
F-A10	2712	2949,6	237,6	2,455	4334	10656
E-G1	3149	3616,6	15,2	2,566	4442	11211
F-O2	3615,5	3685,4	69,9	2,5	4126,5	10316

5.4.12 BULK DENSITY, COMPRESSIONAL VELOCITY, AND ACOUSTIC IMPEDANCE DISTRIBUTION PATTERN

The distribution of bulk density, compressional velocity and the acoustic impedance of all the studied wells was clearly defined from the 3D parameters viewer models presented below. The average bulk density distribution displayed in Figure 5-14 revealed E-M4, F-A10, F-A11 and F-A13 as wells with the least bulk density and well E-CN1 with the highest bulk density based on the average bulk density scale displayed on the right side of the model. The average compressional velocity distribution was displayed in Figure 5-15. Well F-L1, F-A10, F-A11 and F-A13 showed the lowest average compressional velocity value whereas well E-CN1 showed the highest average value. The distribution of acoustic impedance was displayed in Figure 6-16 where well F-L1, F-A10, F-A11 and F-A13 showed the lowest average acoustic impedance and well E-CN1 showed the highest average acoustic impedance. The three models showed a similar trend of distribution for F-L1, F-A10, F-A1 and F-A13 wells in particular. Figure 5.16 confirmed that the Upper Shallow Marine sandstone reservoirs show different acoustic impedance from one well to another across the field. The variations in acoustic impedance can be attributed to the porosity variations within the reservoirs. Wells F-A13, F-A10 and F-A11 showed high porosity values and E-CN1 showed the lowest porosity values as indicated in Figure 4-45 in chapter 4. Generally, porosity is inversely proportional to the

acoustic impedance hence all the wells with high porosity showed a low acoustic impedance. The effect of porosity on acoustic impedance will be discussed in details in the next section. The acoustic impedance distribution model also agreed with the mineralogy distribution within the reservoirs. Well E-CN1 reservoir quality was very poor due to the destruction of intergranular porosity by extensive quartz and illite cementation, and compaction which caused high velocity and density (acoustic impedance) whereas well F- A13 showed a highly porous sandstone reservoir with rounded monocrystalline quartz grain and only clusters of elongate to disc-like, authigenic chlorite crystals partly filling a depression within altered detrital grains. There was no evidence of the effect of reservoir thickness on the acoustic impedance as there was no clear trend that can be observed when matching the thickness with acoustic impedance values in Table 5-1.

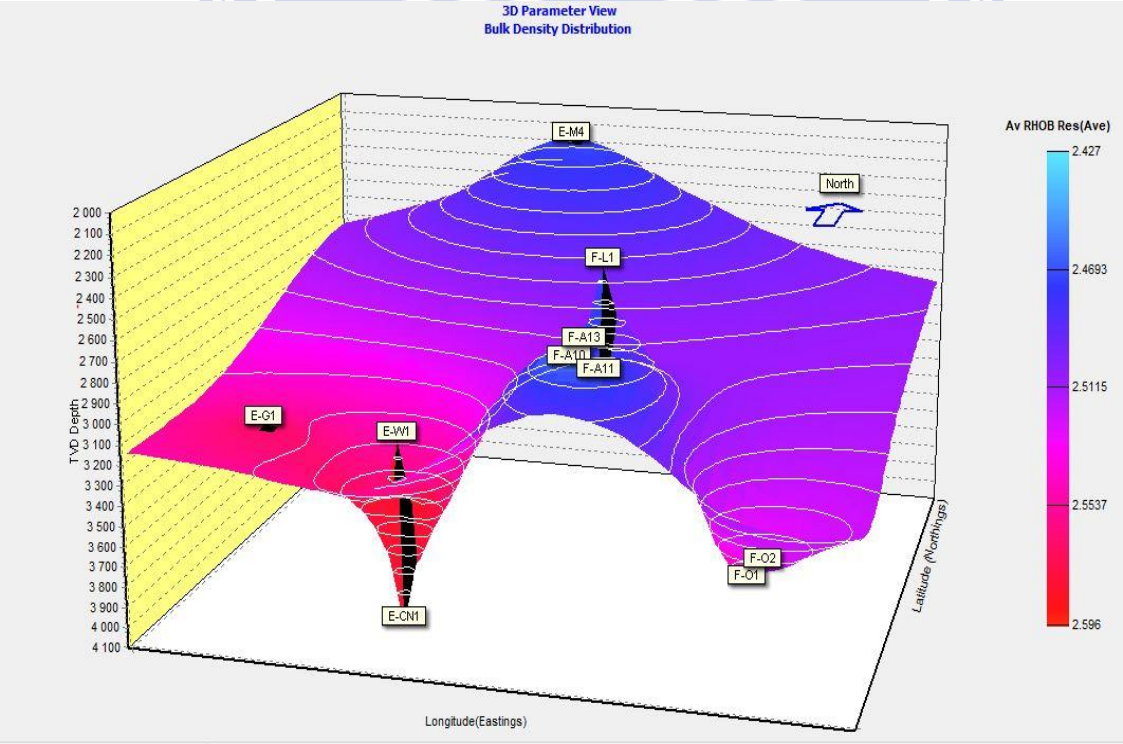

Figure 5-14: Average bulk density distribution.

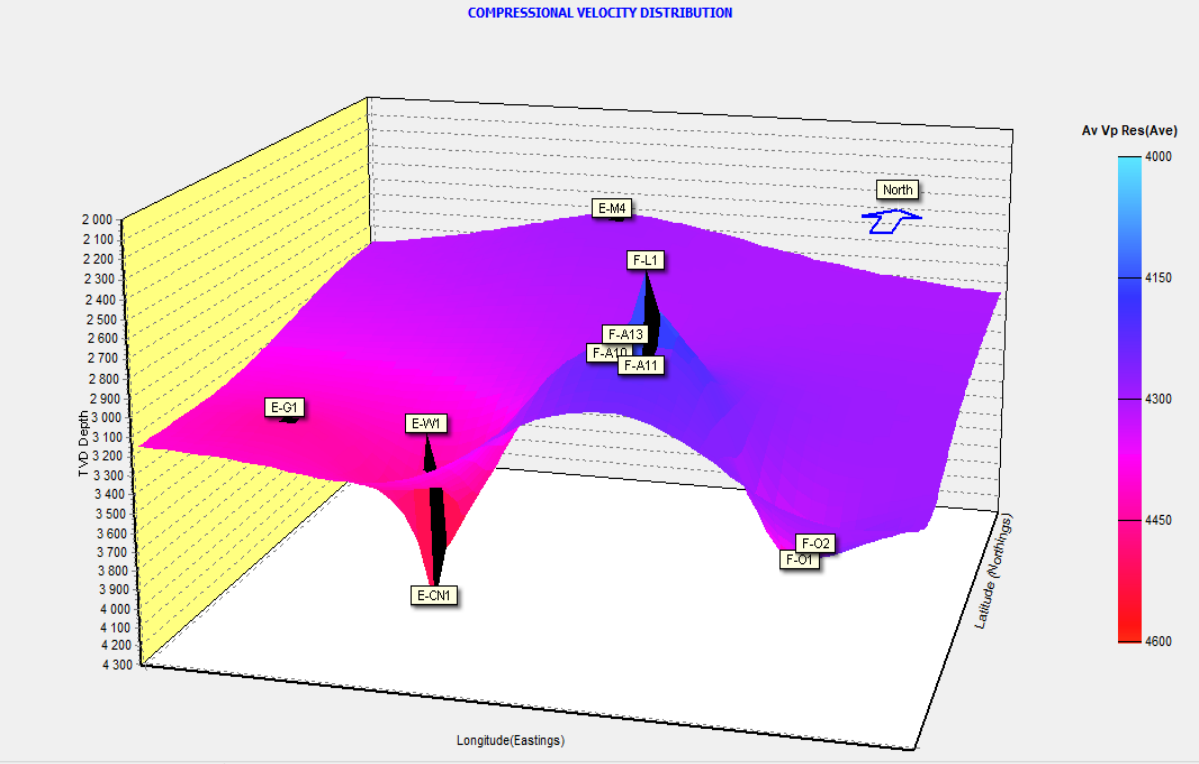

Figure 5-15: Compressional velocity distribution.

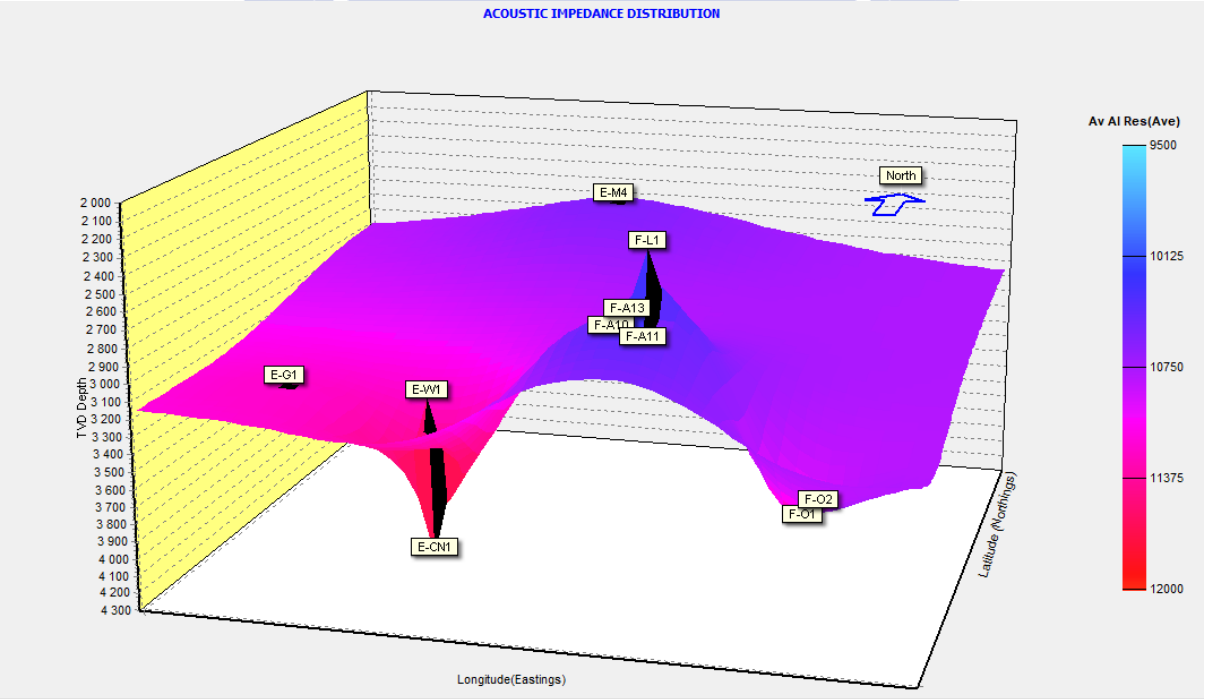

Figure 5-16: Average Acoustic impedance distribution

5.5 CROSS-PLOTS RESULTS AND INTERPRETATION

Cross-plots of compressional velocity versus bulk density was plotted to help identify the lithology within the reservoir interval. The gamma-ray log was used to discriminate the lithology. The lithology with API values of less or equal to 70 was classified as sandstone and those above 70 as shale. A cross-plot of porosity vs bulk density was used to identify the influence of porosity on bulk density. In general, the presence of pore space reduces the bulk density of the rock (Kassab and Weller, 2015). A cross-plot of compressional velocity and porosity can be used to determine the relationship between the two. The relationship between these two parameters has been documented by many authors (Han, Nur, and Morgani, 1986; Kenter, 1997; Knackstedt, Arns and Pinczewski, 2005; Kassab and Weller, 2015). Generally, porosity is inversely proportional to velocity, that is, when porosity increases, velocity decreases, and vice versa. The effect of a general decrease in compressional velocity with increasing porosity is due to the increase in porosity reducing the rigidity of the rock that decreases both P-wave and S-wave. The pore structure of the rock has an effect on both bulk and shear modulus. The cross-plot of porosity versus acoustic impedance can be used to determine the effect of porosity on acoustic impedance by determining the strength of the relationship between those parameters through regression correlation coefficient R^2 obtained from the regression equation.

5.5.1 F-O1 CROSS-PLOTS INTERPRETATION

Cross-plot in Figure 5-17A revealed that the lithology within the reservoir interval is sandstone dominated with a little intercalation of shale. Figure 5-17B showed a strong inverse relationship between porosity and bulk density for porosity lower than 20% and then a constant increase in porosity above 20% with constant bulk density. Figure 5-17C showed the strength of the relationship between porosity and acoustic impedance. The negative correlation of 0.44 showed that there was a fair effect of porosity on the acoustic impedance in this interval. The inverse relationship between Vp and Porosity can be observed in Figure 5-17D even though there was a lot of anomalous points away from the expected trend.

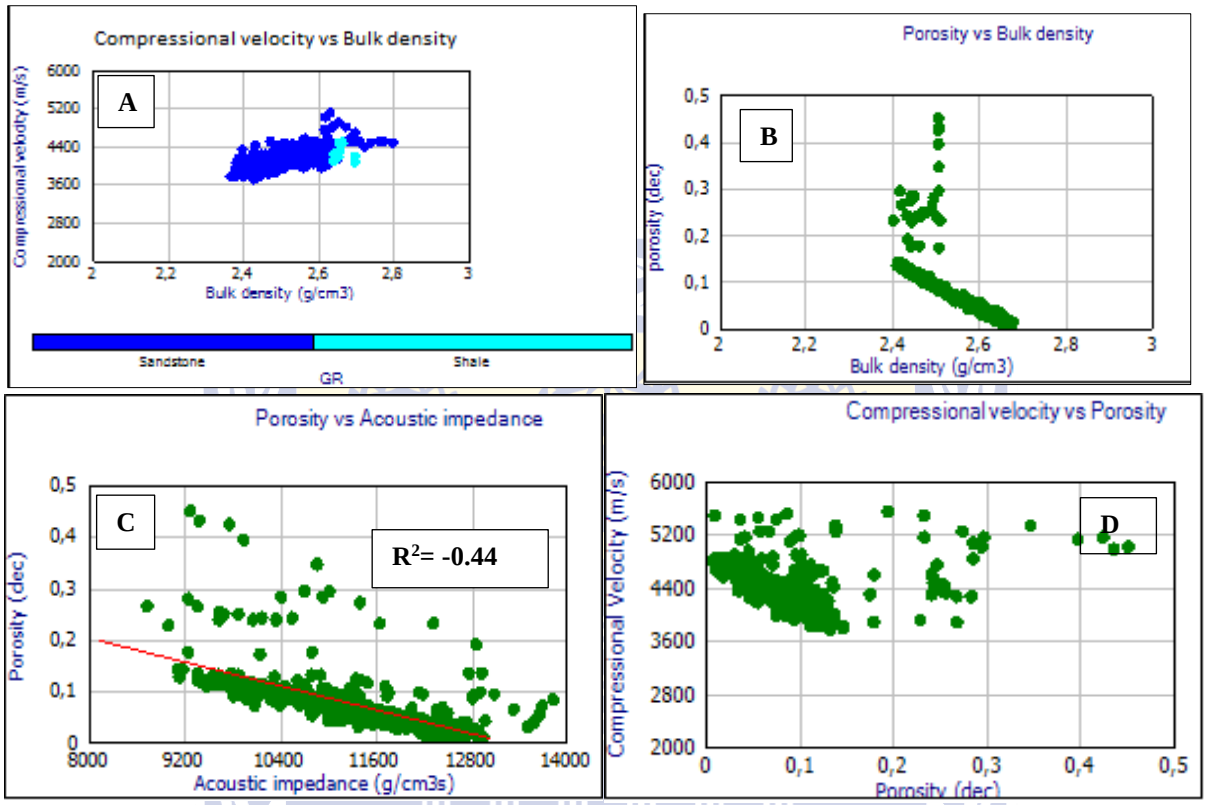

Figure 5-17: Cross-plots of (A) Compressional velocity vs bulk density (B) Porosity vs bulk density (C) Porosity vs acoustic impedance and (D) Compressional velocity vs Porosity.

5.5.2 F-O2 CROSS-PLOTS INTERPRETATION

Figure 5-18A revealed that the reservoir interval was almost clean sandstone with a very little presence of shale. There was a very good inverse relationship between bulk density and porosity (Figure 5-18B). The data points in Figure 5-18C do not follow the general trend of the inverse relationship between Vp and porosity. The data points result in a cloud of points with no clear trend. This is an indication that there are other factors such as clay content influencing velocity instead of porosity alone. There was a poor correlation between porosity and acoustic impedance (Figure 5-18D). The weak negative correlation of 0.16 is a clear indication that there is a very little or no influence of porosity on acoustic impedance at this interval.

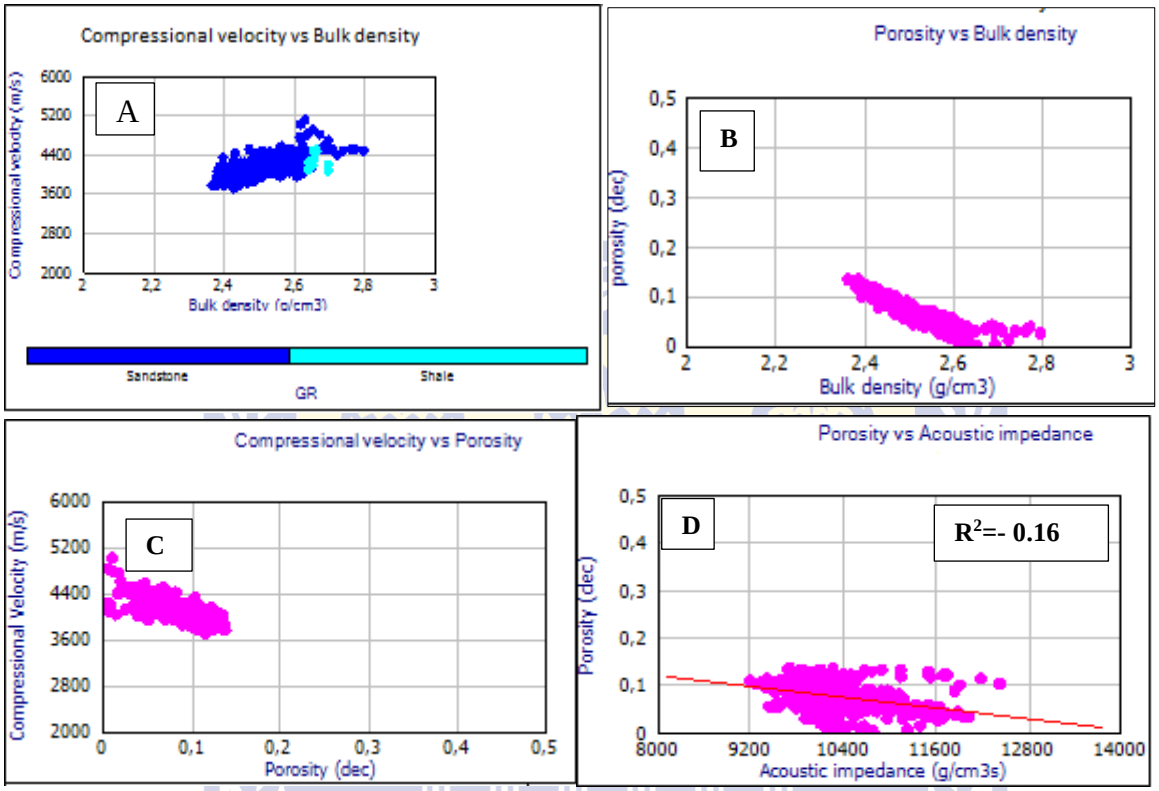

Figure 5-18: Cross-plots of (A) Compressional velocity vs bulk density (B) Porosity vs bulk density (C) Compressional velocity vs Porosity and (D) Porosity vs acoustic impedance.

5.5.3 E-G1 CROSSPLOTS INTERPRETATION

Figure 5-19A showed that the porosity increases with decreasing Vp which confirms the effect of porosity on Vp at this interval. There was a poor correlation between porosity and acoustic impedance (Figure 5-19B) which showed a regression coefficient correlation of negative 0.23. Figure 5-19C revealed that the reservoir interval is a clean sandstone lithology. The data points of Figure 5-19D showed no trend between porosity and bulk density. The bulk density ranged between 2.59g/cm^3 and 2.8 g/cm^3 which indicate mostly a sandstone lithology. Porosity increased with decreasing bulk density within this interval.

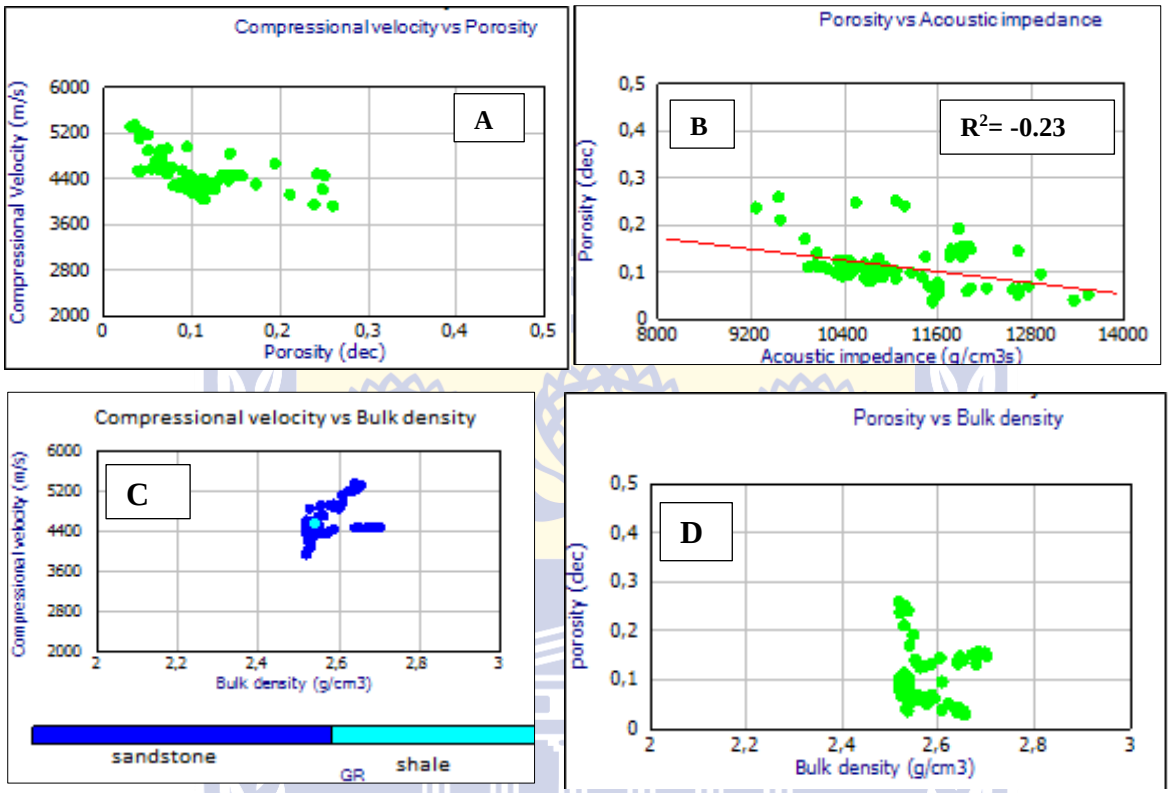

Figure 5-19: Cross-plots of (A) Compressional velocity vs Porosity, (B) Porosity vs acoustic impedance, (C) Compressional velocity vs bulk density (D) Porosity vs bulk density.

5.5.4 E-M4 CROSS-PLOTS INTERPRETATION

A cross-plot in Figure 5-20A revealed that the reservoir interval is a sandstone reservoir with intercalation of shale. There was a strong correlation between porosity and bulk density (Figure 5-20C) as expected. Figure 5-20B also showed a good inverse relationship between compressional velocity and porosity. There was a good negative correlation of 0.59 between porosity and acoustic impedance (Figure 5-20D). This is a clear indication that in this interval porosity was the major factor controlling acoustic impedance.

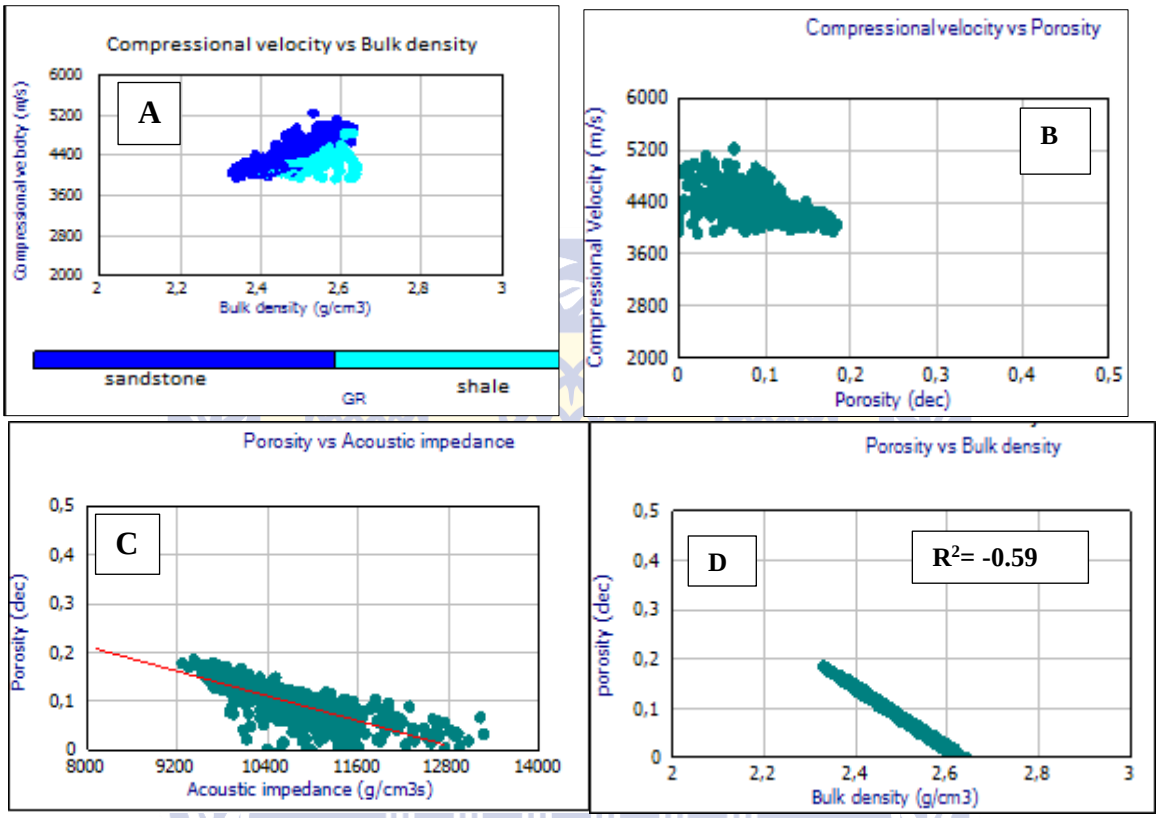

Figure 5-20: Cross-plots of (A) Compressional velocity vs bulk density, (B) Compressional velocity vs porosity, (C) Porosity vs acoustic impedance and (D) Porosity vs bulk density.

5.5.5 E-W1 CROSSPLOTS INTERPRETATION

A cross-plot in Figure 5-21A showed a good inverse relationship between Vp and porosity. There was a clear separation between sandstone and shale lithology (Figure 5-21B) within the reservoir interval, with sandstone as the most dominant lithology. The data points result in clouds of points with no clear data trend (Figure 5-21C), however, there is an indication of the unusual direct relationship between porosity and bulk density which goes against the general trend. This is an indication that there are other factors affecting bulk density. There was a very poor negative correlation of 0.09 between porosity and acoustic impedance (Figure 5-21D). This is due to the interbedded shale unit within the reservoir which appear to inhibit a reliable correlation between acoustic impedance and porosity. This observation also agrees with (Cemen, 2014), where he concluded that reliable good correlation can only be obtained in a homogenous thick sandstone interval. The low porosity values below the regression line are shale and high porosity values above the regression line are sandstone unit.

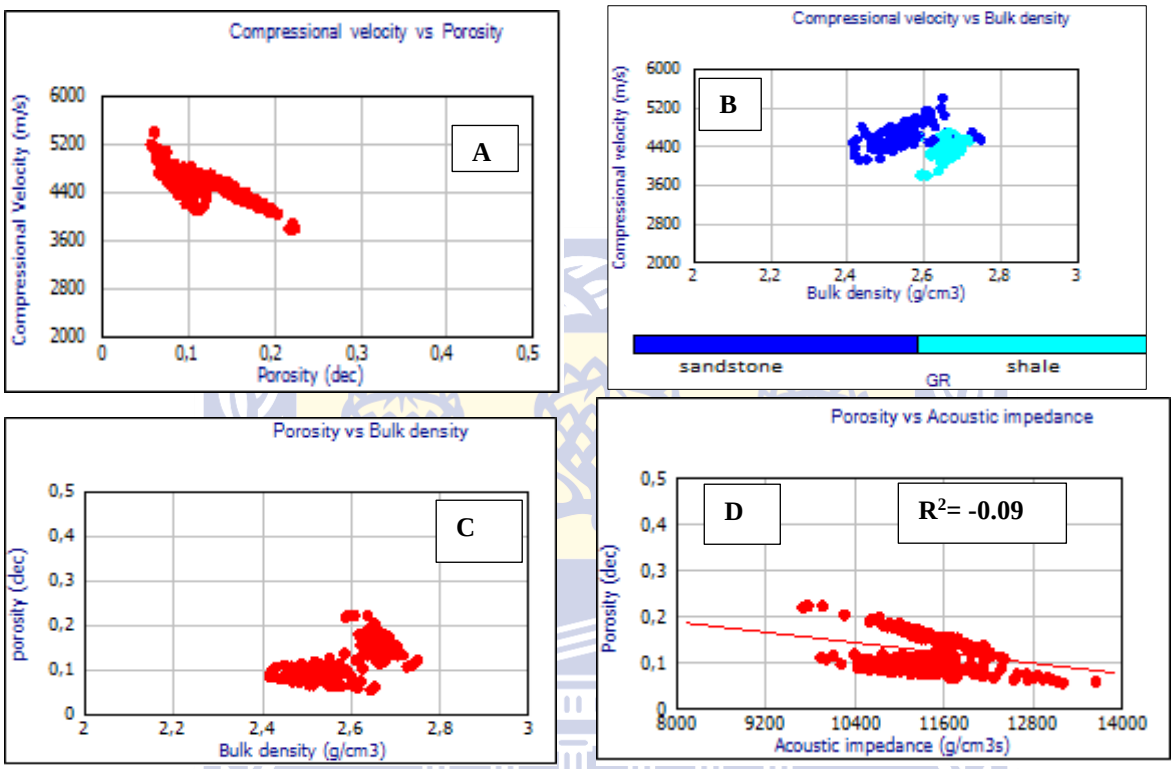

Figure 5-21: Cross-plots of (A) Compressional velocity vs Porosity, (B) Compressional velocity vs bulk density, (C) Porosity vs bulk density and (D) Porosity vs acoustic impedance.

5.5.6 E-CN1 CROSS-PLOTS INTERPRETATION

A cross-plot in Figure 5-22A revealed that the reservoir interval is a sandstone dominated with little intercalation of shale. There was a very good negative correlation between porosity and bulk density (Figure 5-22B) and also compressional velocity and porosity (Figure 5-22C). There was a strong negative correlation of 0.74 between porosity and acoustic impedance (Figure 5-22D). This is a definite indication that porosity was a major factor controlling acoustic impedance within this reservoir interval.

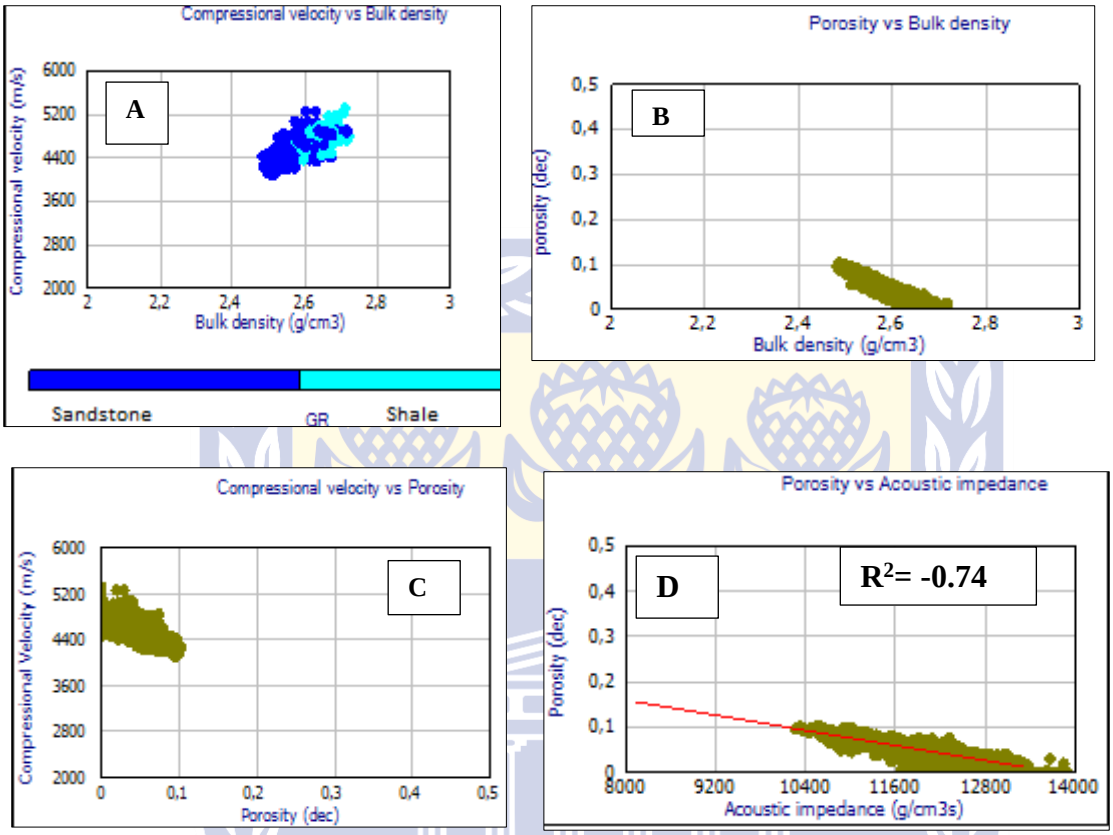

Figure 5-22: Cross-plots of (A) Compressional velocity vs bulk density, (B) Porosity vs bulk density, (C) Compressional velocity vs Porosity and (D) Porosity vs acoustic impedance.

5.5.7 F-A10 CROSSPLOTS INTERPRETATION

A cross-plot in Figure 5-23A revealed that the lithology is more of clean sandstone with negligible shale content. There was a good inverse relationship between porosity and bulk density, which indicates that porosity was influencing bulk density in this interval (Figure 5-23B). Compressional velocity also showed a good relationship with porosity (Figure 5-23C). There was a very good negative correlation of 0.84 between porosity and acoustic impedance (Figure 5-23D). This excellent correlation confirms that porosity was the major factor controlling the acoustic impedance of F-A10.

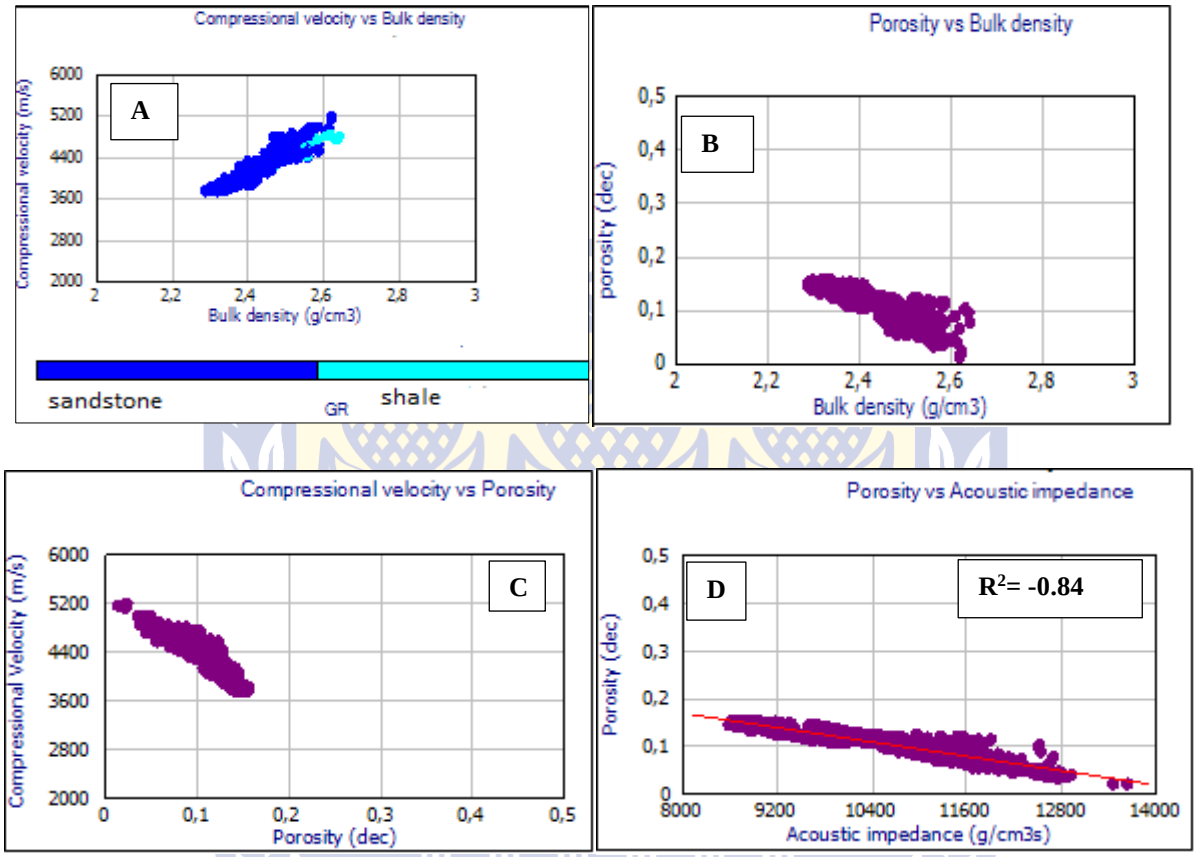

Figure 5-23: Cross-plots of (A) Compressional velocity vs bulk density, (B) Porosity vs bulk density, (C) Compressional velocity vs Porosity and (D) Porosity vs acoustic impedance.

5.5.8 F-A11 CROSS-PLOTS INTERPRETATION

A cross-plot in Figure 5-24A showed a good inverse relationship between compressional velocity and porosity as expected. The lithology of the reservoir interval is clean sandstone with sparse negligible data points of shale (Figure 5-24B). Bulk density decrease with increasing porosity in Figure 5-24C. The negative correlation of 0.61 (Figure 5-24D) is a good indication of the influence of porosity on the acoustic impedance.

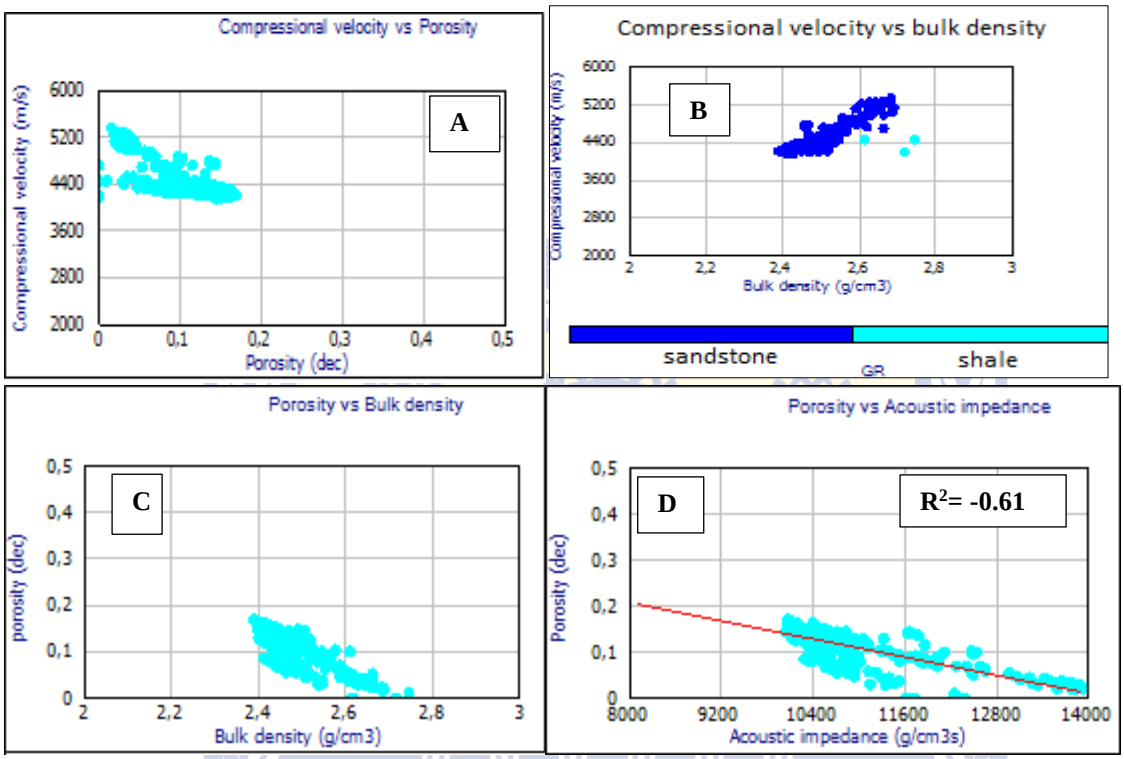

Figure 5-24: Cross-plots of (A) Compressional velocity vs porosity, (B) Compressional velocity vs bulk density, (C) Porosity vs bulk density and (D) Porosity vs acoustic impedance.

5.5.9 F-A13 CROSSPLOTS INTERPRETATION

A cross-plot in Figure 5-25A revealed that the lithology within the reservoir interval is a clean sandstone with negligible shale content. There was a good trend of a negative correlation between porosity and bulk density (Figure 5-25B) and also between Vp and porosity (Figure 5-25C). There was a very strong negative correlation of 0.86 between porosity and acoustic impedance (Figure 5-25D). This was a clear indication of the strong influence of porosity on acoustic impedance.

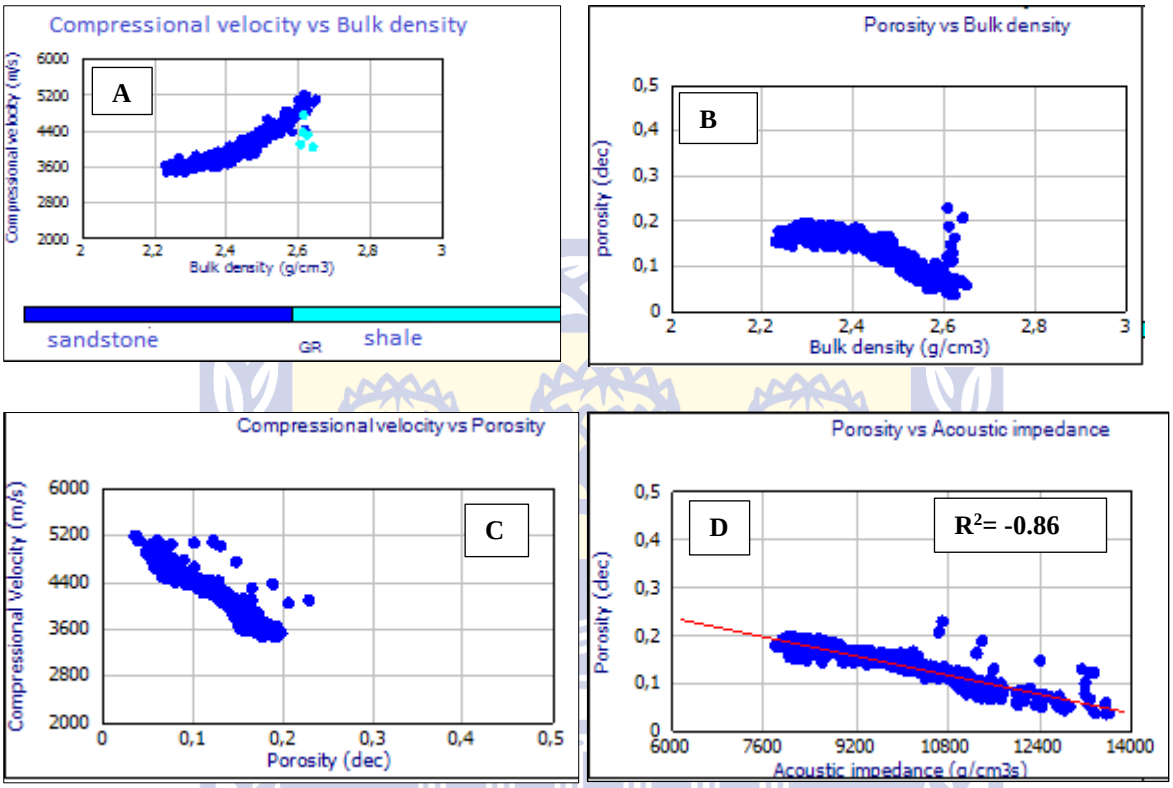

Figure 5-25: Cross-plots of (A) Compressional velocity vs bulk density, (B) Porosity vs bulk density, (C) Compressional velocity vs Porosity and (D) Porosity vs acoustic impedance.

5.5.10 F-L1 CROSSPLOTS INTERPRETATION

A cross-plot in Figure 5-26A revealed that the lithology of reservoir interval is dominated by both sandstone and shale units. There was a very good negative correlation between porosity and bulk density (Figure 5.26B). There was no clear relationship between Vp and porosity because data points result in clouds of points with no clear trend (Figure 5-26C). The strength of a negative correlation between porosity and acoustic impedance (Figure 5-26D) can be classified as fair with a value of 0.48. This showed that the porosity was not the only factor controlling acoustic impedance. There are other factors such as mineralogy.

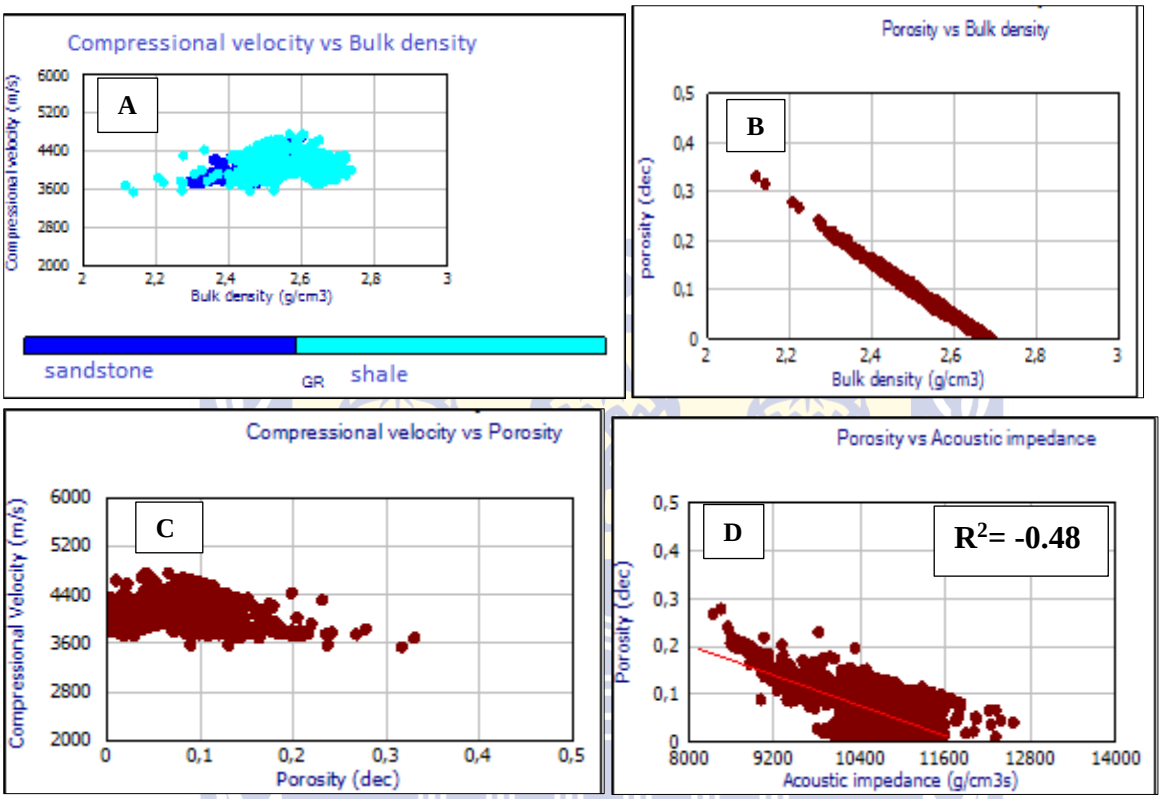

Figure 5-26: Cross-plots of (A) Compressional velocity vs bulk density, (B) Porosity vs bulk density, (C) Compressional velocity vs Porosity and (D) Porosity vs acoustic impedance.

5.5.11 MULTI-WELL CROSSPLOT OF POROSITY VS ACOUSTIC IMPEDANCE

There is a fair linear negative correlation between the calculated acoustic impedance and porosity within the sandstone reservoir interval. Higher porosity values were correlated with lower acoustic impedance values within the sandstone interval. The negative regression correlation coefficient of 0.48 in Figure 5-27 clearly indicates that when you combine the 10 studied wells/reservoirs porosity is one of the major factors controlling the acoustic impedance.

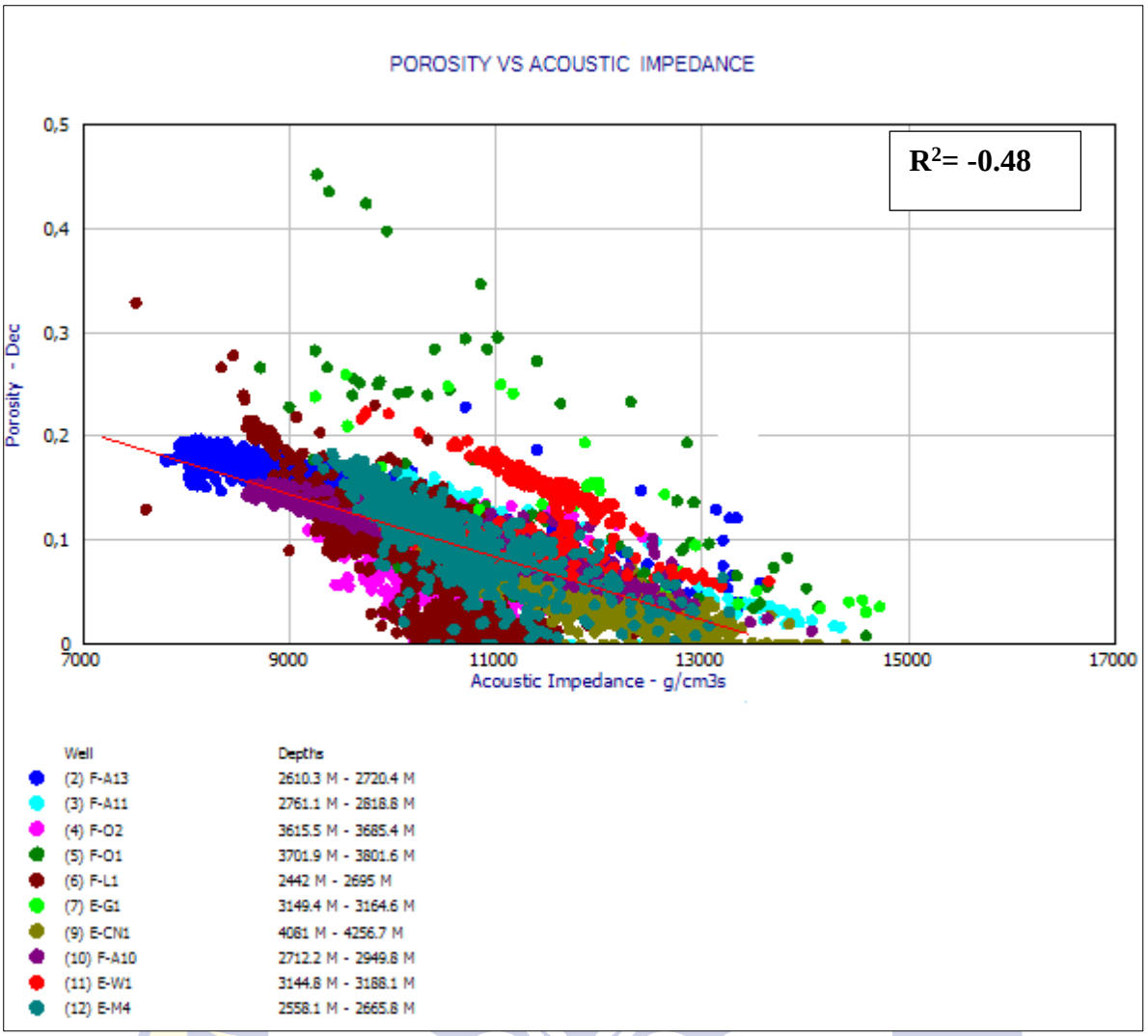

Figure 5-27: A multi-well cross-plot of porosity versus acoustic impedance.

5.6 EFFECT OF PORE FLUID ON ACOUSTIC IMPEDANCE

Changes in pore fluids affect acoustic impedance because pore fluid density affects both density and velocity. A change in pore fluid from water to oil creates a small impedance contrast that can only be detected seismically ideal signal to noise ratio conditions. However, a change from a liquid (either water or oil) to gas can create a larger acoustic impedance contrast and strong seismic reflections. The effect of pore fluid was investigated using gasman fluid substitution modelling.

5.6.1 GASSMANN FLUID SUBSTITUTION MODELLING

Fluid substitution is an important part of the rock physics because it provides a valuable tool for modelling various pore fluid scenarios which might explain the changes in amplitude variation with offset (Smith, et al., 2003). The most common method used in performing fluid substitution is based on the work of Gassmann (1951). This method relates the saturated bulk modulus of the rock to its porosity, the bulk modulus of the porous rock frame, the bulk modulus of the mineral matrix and the bulk modulus of the pore-filling fluids. This method depends on changing the type of pore fluids in the reservoir interval to study the AVO response caused by the new fluid type (El-Bahiry, et al., 2016). Gassmann relations reflect variations in Vp and Vs velocities with changes in fluid saturations with simple input parameters. The primary inputs are Vp, Vs and bulk density while the matrix bulk modulus (K_o), frame or dry rock modulus (K^*), porosity and the rock shear modulus remains constant during the substitution modelling (Smith, et al., 2003 and Khan, 2018).

The Gassmann fluid substitution was performed on the upper shallow marine sandstone reservoirs in the 10 studied wells to model the seismic velocity and density at different water saturation levels (Figure 5-29 to 5-38). Before performing the fluid substitution modelling using Gassmann equation, the following input parameters were determined : (1) The porosity of the rock, (2) the properties of the pore fluids ($K_{fl,}$ fluid density), (3) the bulk modulus of the mineral matrix (K_o) and (4) the bulk modulus of the porous rock frame (K^*). The Gassmann equation is presented as follows:

$$K_{sat} = K^* + \frac{\left(1 - \frac{K^*}{K_o}\right)^2}{\frac{\phi}{K_{fl}} + \frac{(1-\phi)}{K_o} - \frac{K^*}{K_o^2}},$$

Where *Ksat* = the saturated bulk modulus (undrained of pore fluids), *Ko* =the bulk modulus of the mineral matrix, *Kfl* =the bulk modulus of the pore fluid, *K* =the bulk modulus of the porous rock frame, (drained of any pore-filling fluid), and ø=porosity.

All the parameters were determined from the analysis of the wireline log data while porosity was determined by both wireline log data and routine core data. Table 5-2 presented the temperature, pressure, and salinity of the studied reservoirs.

The Gassmann equation was used for the calculation of the effects of fluid substitution on acoustic properties using rock frame properties in this study. This procedure required that the effect of the initial fluid be removed before modelling the new fluid. The input data (density, Sw, Sxo and Vclay) were obtained from the petrophysical analyses of the reservoirs whereas Vp and Vs were obtained from the Greenberg and Castagna (1992). The example of the shear velocity vs compressional velocity quality control cross-plot from one well is presented in Figure 5-28 and the rest of the plots are presented in appendix G. Three fluid substitution models (Brine, Oil and Gas) were determined for pure sandstones and were used to measure the behaviour of the different sandstone saturations. The fluid substitution cross plots (Figure 5-37A-J) gives a clear indication of the change in Vp with water saturation within the reservoir intervals of 10 wells. The Vp in E-G1 (Figure 5-27A) shows a drastic increase of velocity with water saturation displaying a steep slope from 0% to 100% water saturation. E-M4, F-A10, F-A13, and F-A13 shows a gradual decrease in Vp below 70% water saturation before increasing drastically from 80% water saturation onwards. F-O1, F-O2, F-L1, E-W1 and E-CN1 shows a Vp that is almost uniform below 75% water saturation and then a rapid increase was observed above 80% water saturation.

A significant decrease was observed in Vp when the initial water saturation was substituted with the hydrocarbon (oil or gas) in all the wells. The value of density decreased quite visibly in all the wells when the brine (100% water saturation) was substituted with gas or oil.

The fluid substitution affected the rock property significantly. The rock physical properties (Vp, Vs, and density) change depending on the level and type of pore fluid saturations. The average Gassmann results are listed in appendix C1-C10. The Poisson ratio ranged from 0.167 to 0.226 as indicated in Figure 5-29 to 5-38 and Table 5-3 to 5-12. The Poisson ratio is an elastic constant which measures the compressibility of the material perpendicular to the applied stress. Generally, the Poisson ratio range between 0 and 0.5. Poisson ratio for sandstone is approximately 0.2, for carbonate is approximately 0.3 and for shale is greater than 3. The range of Poisson ratio in this study agrees with the typical values for sandstone. The dry rock properties (Bulk modulus, shear modulus, poison ratio, and modulus) for the 10 wells shows different values indicating the difference in compaction level of clastic rocks in the study area. Table 5-2 shows the reservoir input parameters used to determine the fluid substitution model.

The Vp slightly decreases when brine was substituted with water in well F-A13, F-A10, F-O2 and E-CN1. E-G1 contains both oil and gas and therefore showed a notable decrease from brine to oil and from oil to gas respectively. The Vs remained unaffected in all the wells. The acoustic impedance logs showed a decrease when 100% water saturation was replaced with the hydrocarbon (Oil or Gas) in all the wells. The change in the Al variation contrast is caused by the change in density and Vp (Al being the product of Vp and Density).

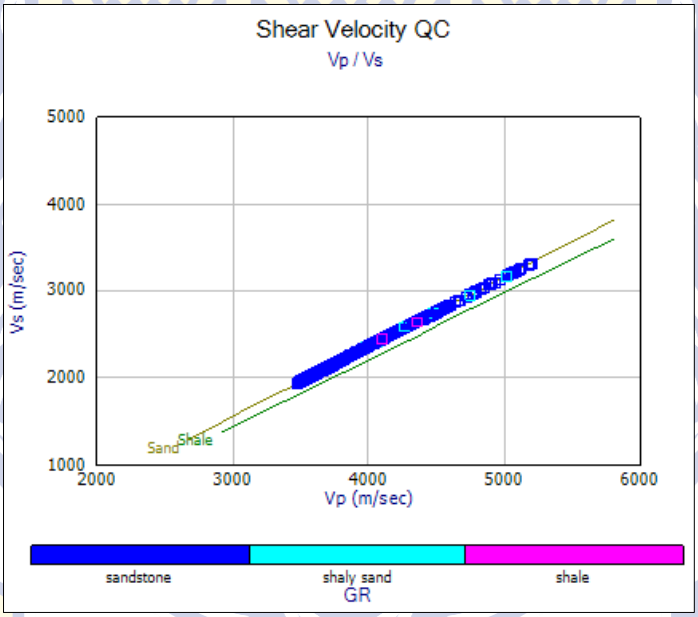

Figure 5-28: Shear velocity QC cross plots showing the relationship between Vp and Vs calculated using the Greenberg and Castagna (1992) relationship.

Table 5-2: Reservoir temperature, pressure and salinity used in the substitution model.

Well name	Temperature (^{0}C)	Pressure (PSI)	Salinity (ppm NACl)
F-01	152	4000	32000
F-02	153	3900	32000
E-CN1	164	3800	43500
E-G1	137.65	6639	32000
E-M4	115.03	4000	38000
E-W1	121.61	5000	32000
F-A10	116.47	4000	32000
F-A11	114.62	5000	32000
F-A13	109.6	5000	32000
F-L1	86.66	3900	32000

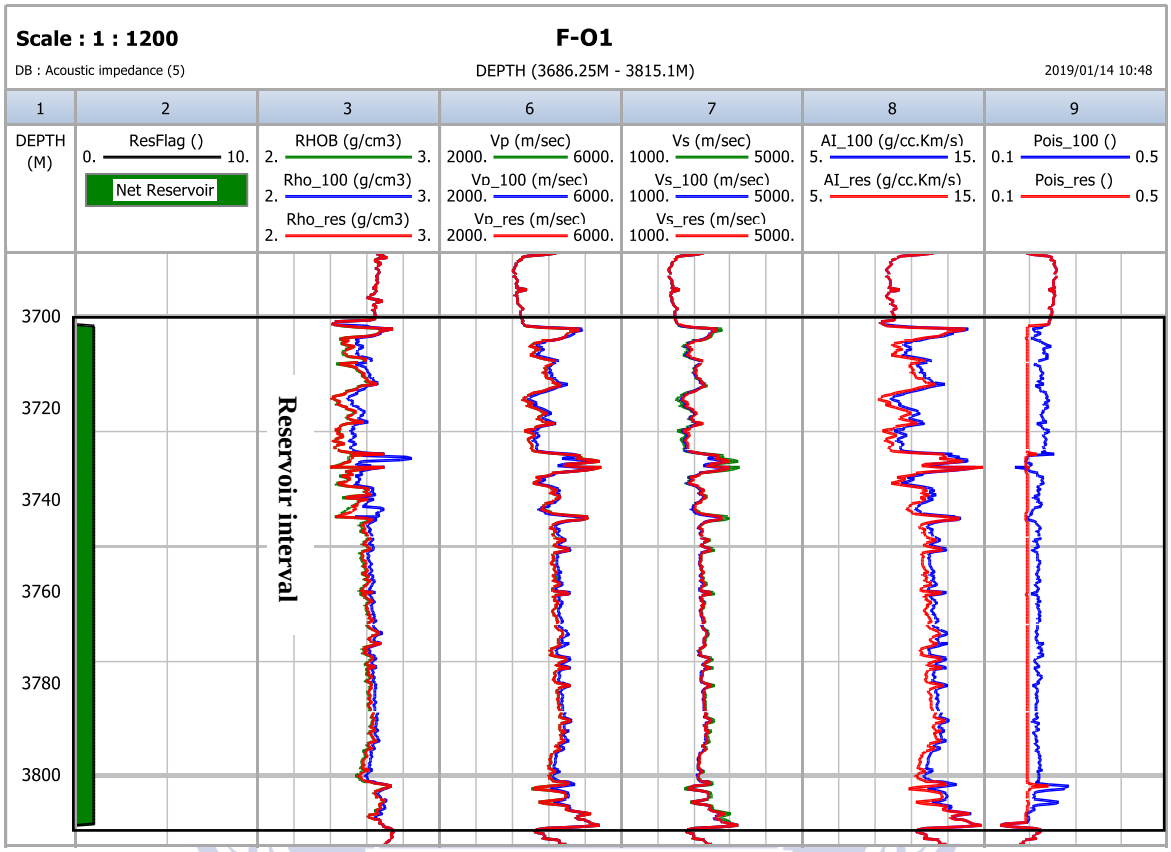

Figure 5-29: Elastic impedance logs for F-O1 well showing the calculated parameters (Vp, Vs, Al and Poison ratio) at different saturation levels (100% water saturation and gas) in reservoir interval.

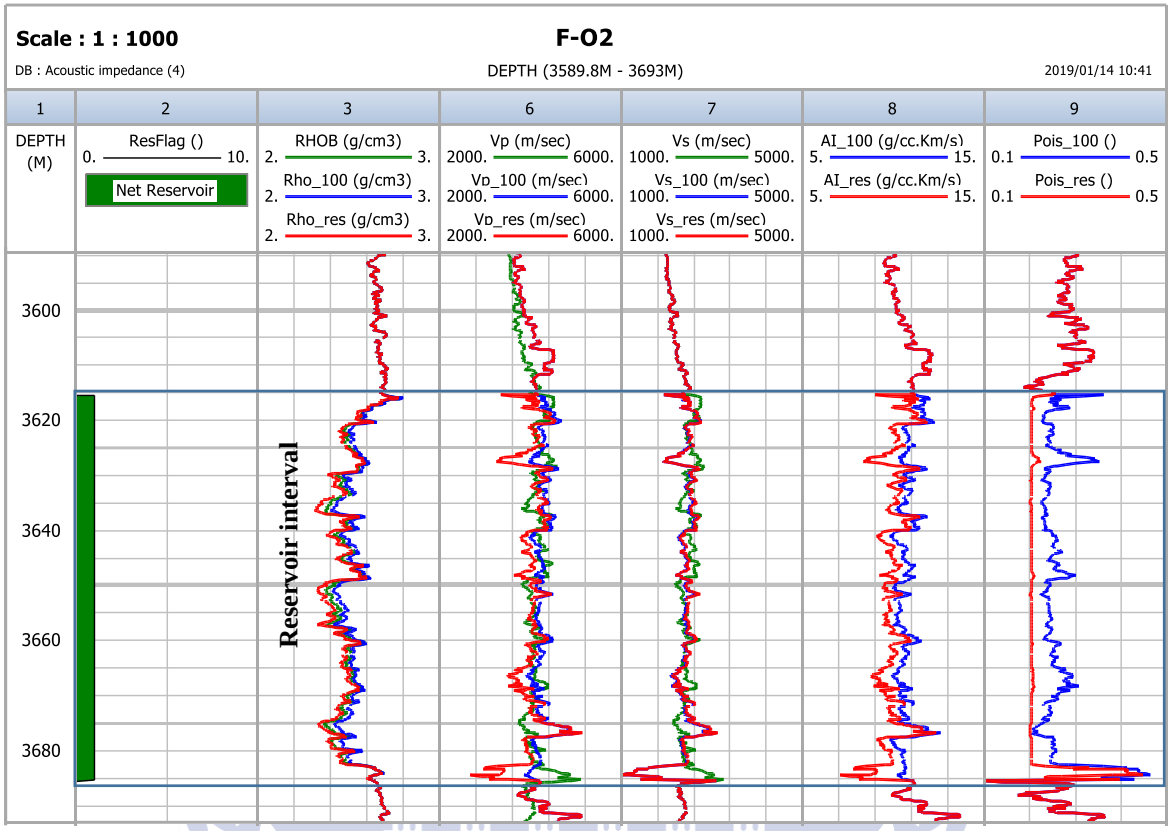

Figure 5-30: Elastic impedance logs for F-O2 well showing the calculated parameters (Vp, Vs, Al and Poison ratio) at different saturation levels (100% water saturation and gas) in reservoir interval.

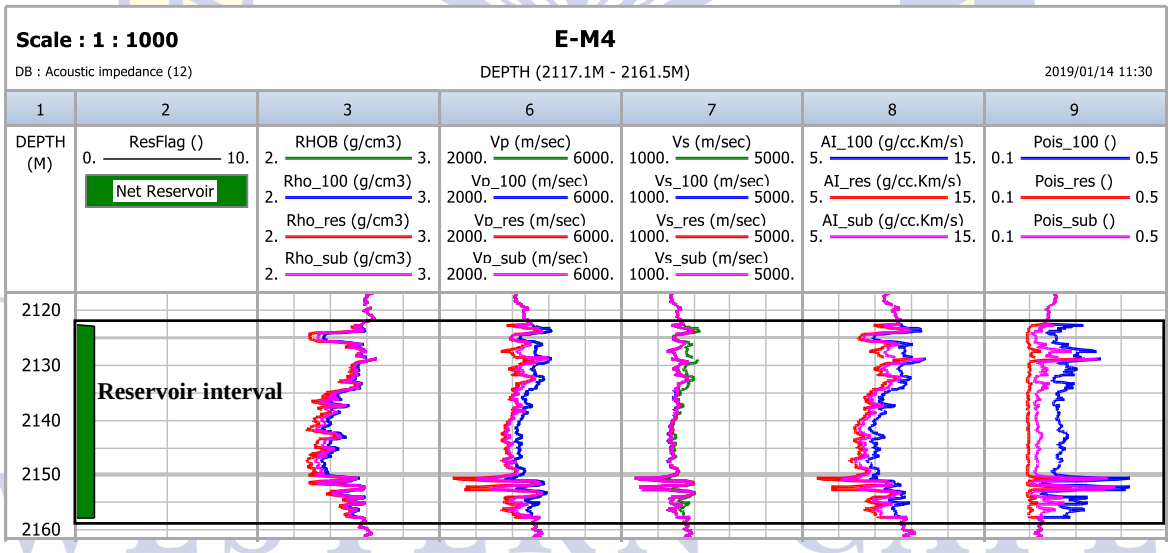

Figure 5-31: Elastic impedance logs for E-M4 well showing the calculated parameters (Vp, Vs, Al and Poison ratio) at different saturation levels (100% water saturation and gas and oil) in reservoir interval.

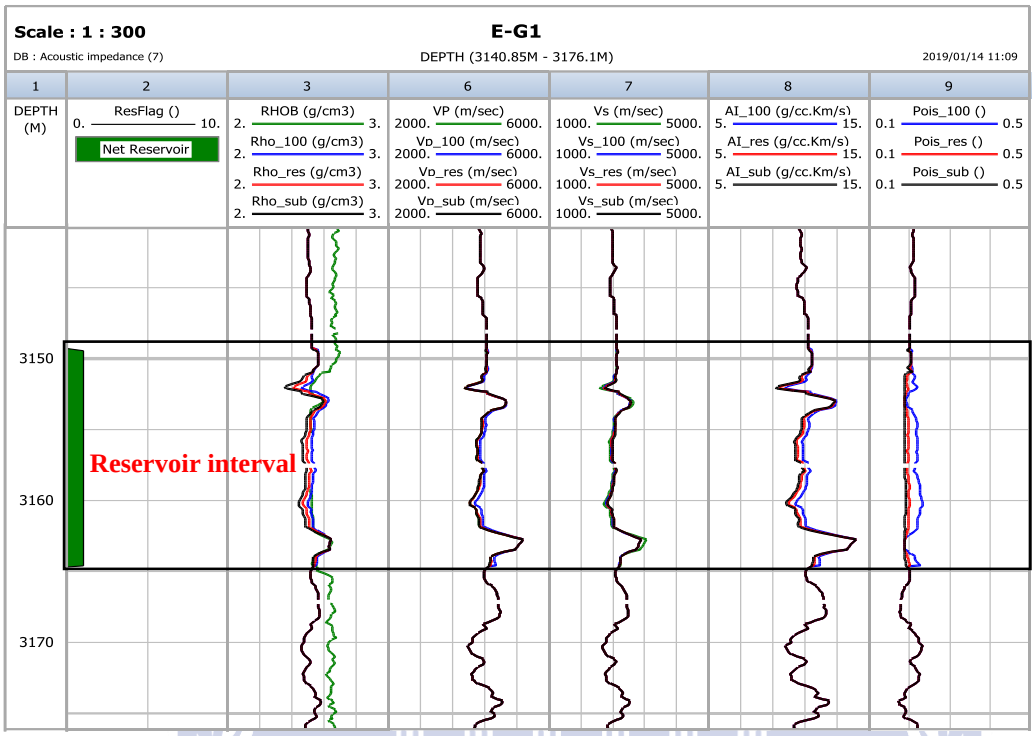

Figure 5-32: Elastic impedance logs for E-G1 well showing the calculated parameters (Vp, Vs, Al and Poison ratio) at different saturation levels (100% water saturation and gas and oil) in reservoir interval.

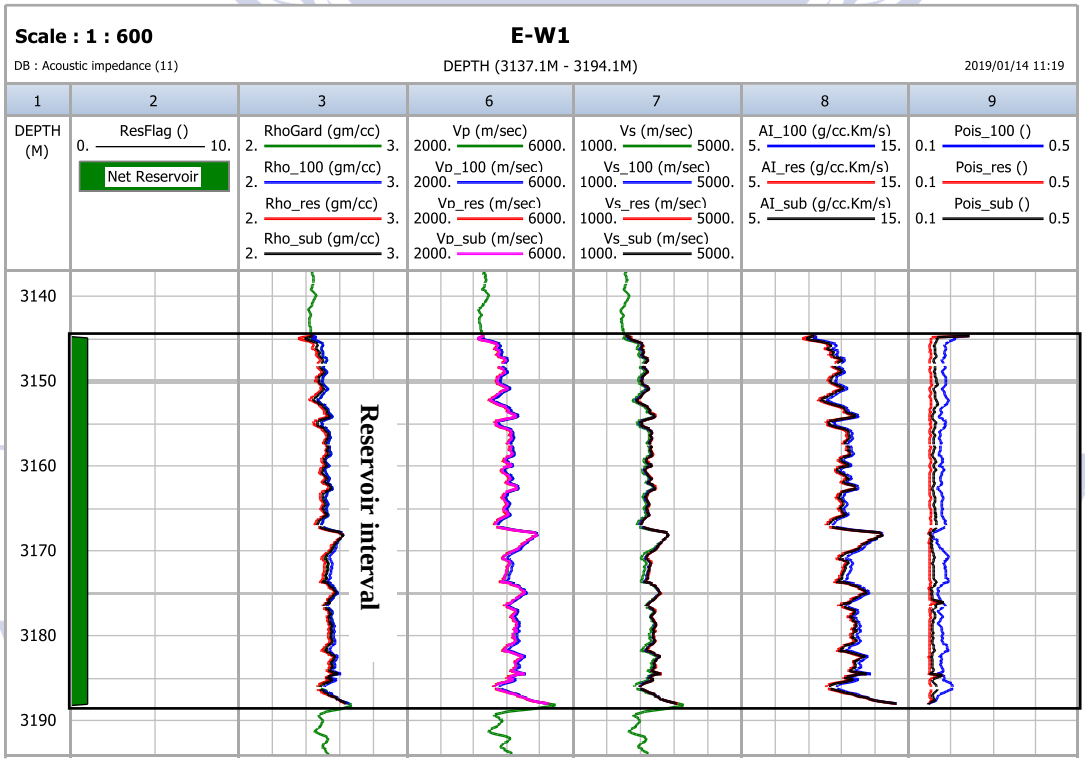

Figure 5-33: Elastic impedance logs for E-W1 well showing the calculated parameters (Vp, Vs, Al and Poison ratio) at different saturation levels (100% water saturation and gas and oil) in reservoir interval.

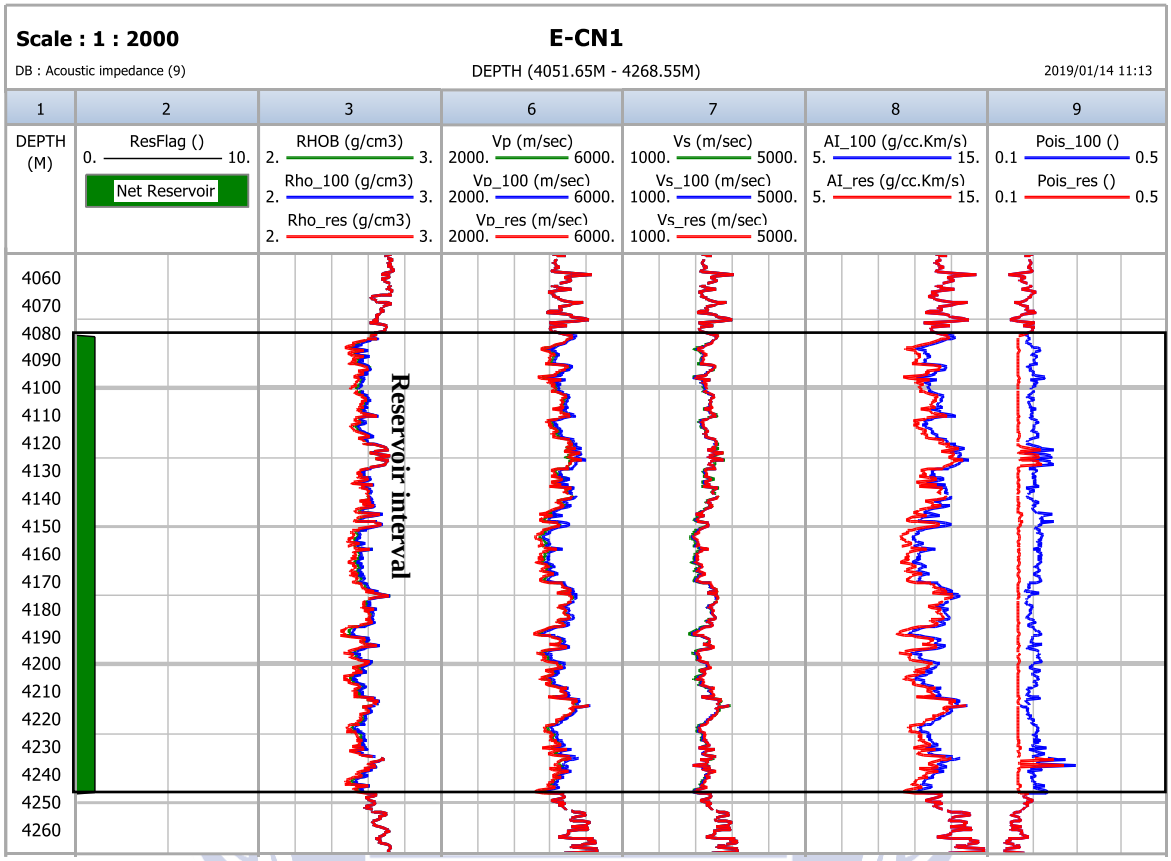

Figure 5-34: Elastic impedance logs for E-CN1 well showing the calculated parameters (Vp, Vs, Al and Poison ratio) at different saturation levels (100% water saturation and gas) in reservoir interval.

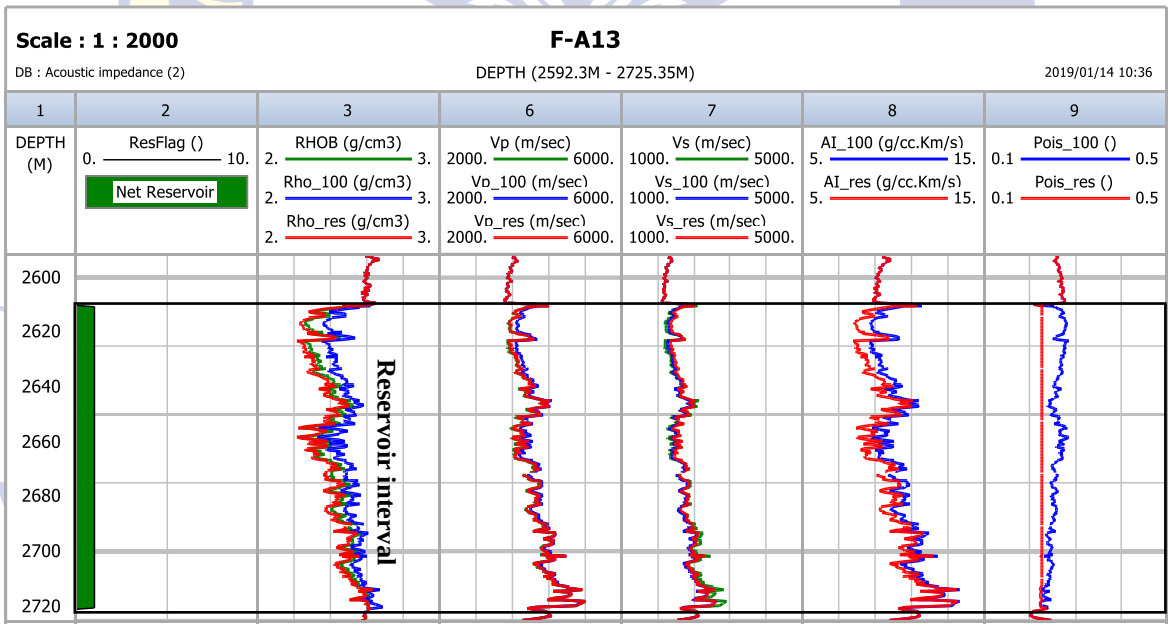

Figure 5-35: Elastic impedance logs for F-A13 well showing the calculated parameters (Vp, Vs, Al and Poison ratio) at different saturation levels (100% water saturation and gas) in reservoir interval.

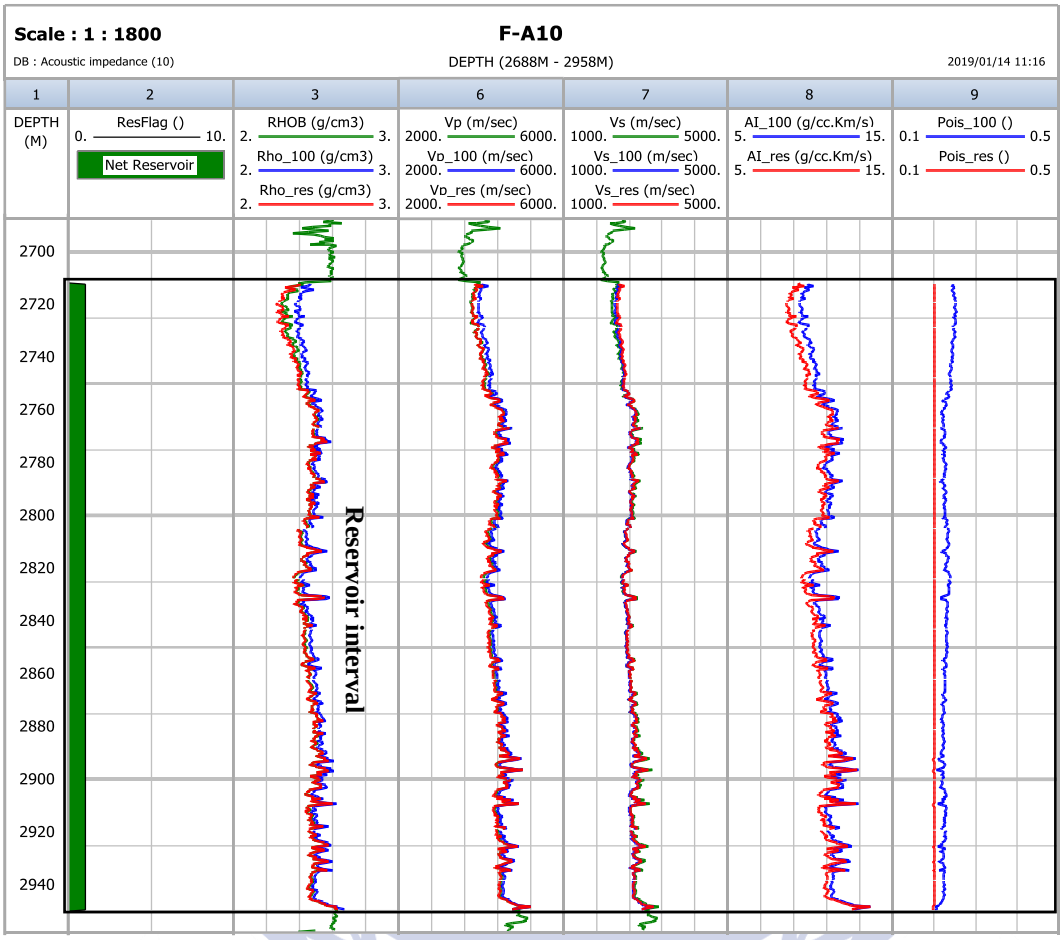

Figure 5-36: Elastic impedance logs for F-A10 well showing the calculated parameters (Vp, Vs, Al and Poison ratio) at different saturation levels (100% water saturation and gas) in reservoir interval.

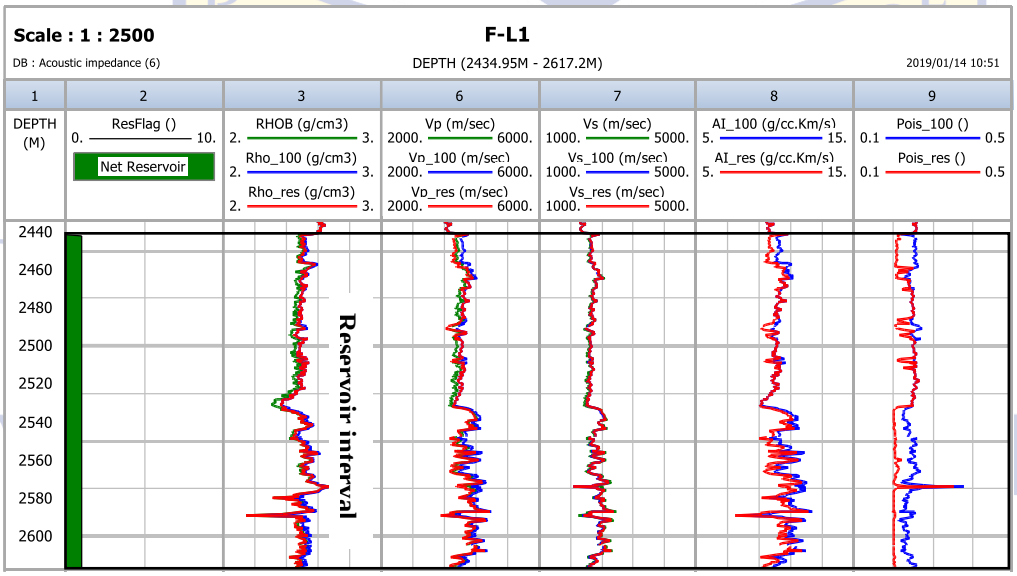

Figure 5-37: Elastic impedance logs for F-L1 well showing the calculated parameters (Vp, Vs, Al and Poison ratio) at different saturation levels (100% water saturation and gas) in reservoir interval.

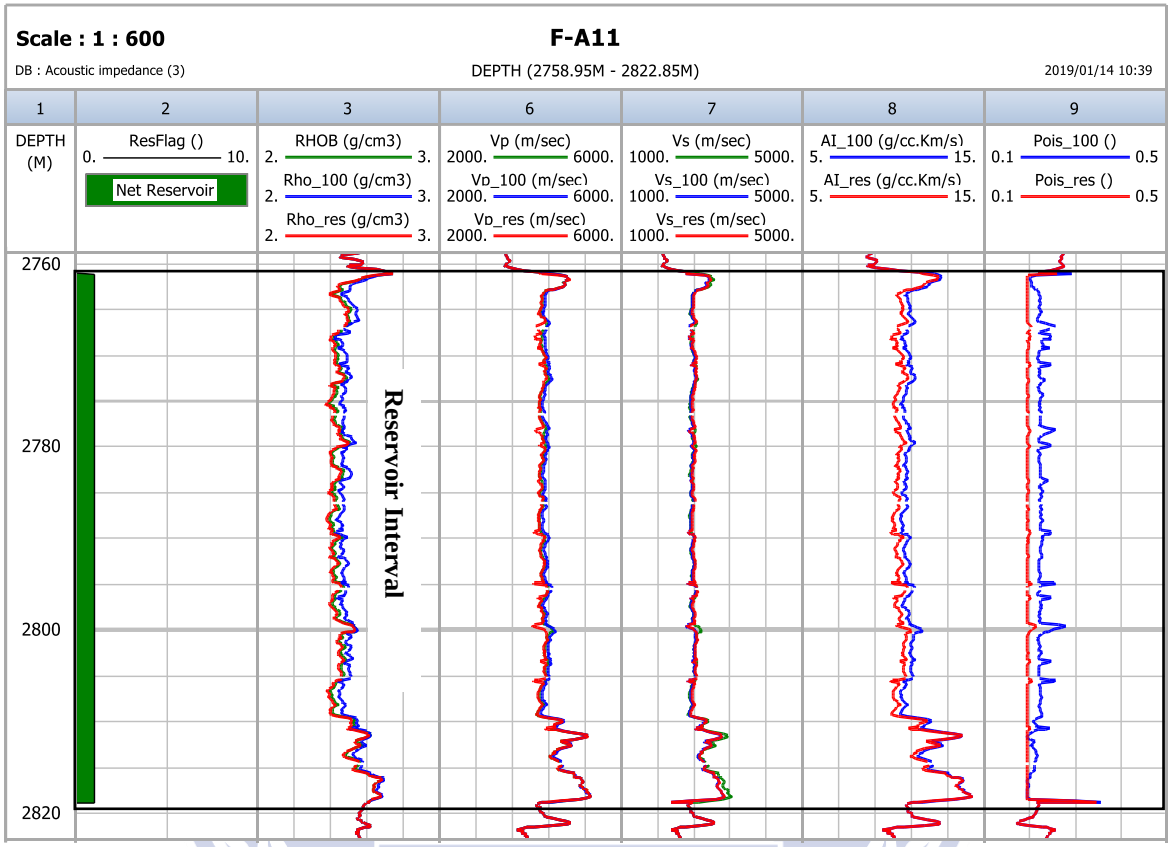

Figure 5-38: Elastic impedance logs for F-A11 well showing the calculated parameters (Vp, Vs, Al and Poison ratio) at different saturation levels (100% water saturation and gas) in reservoir interval.

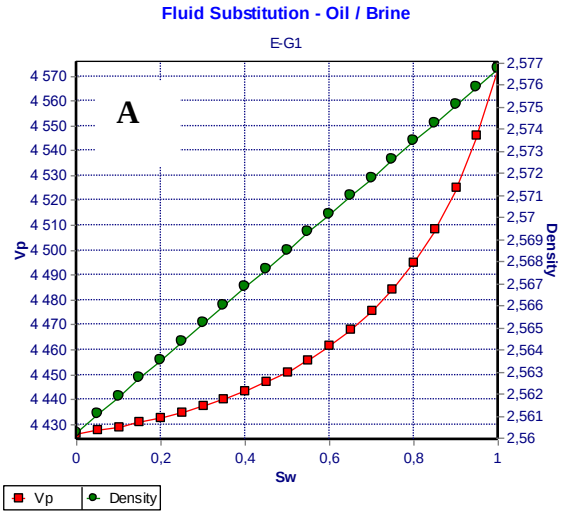

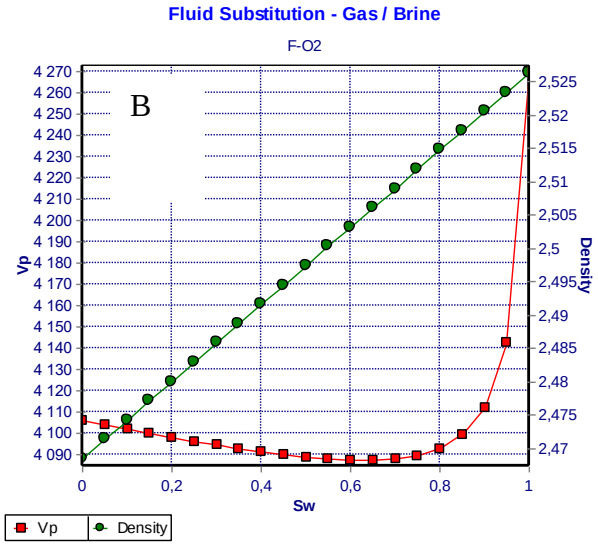

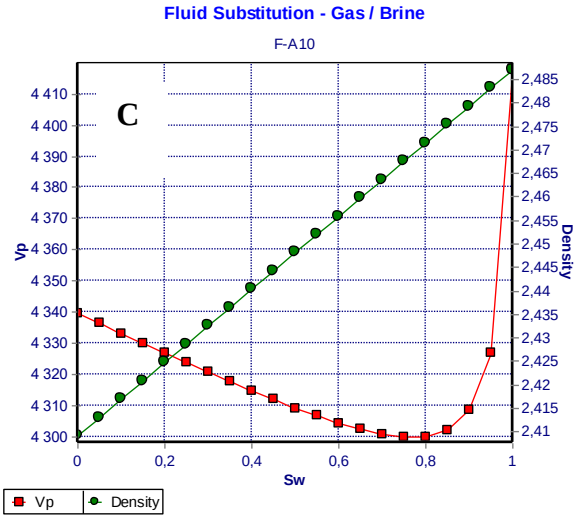

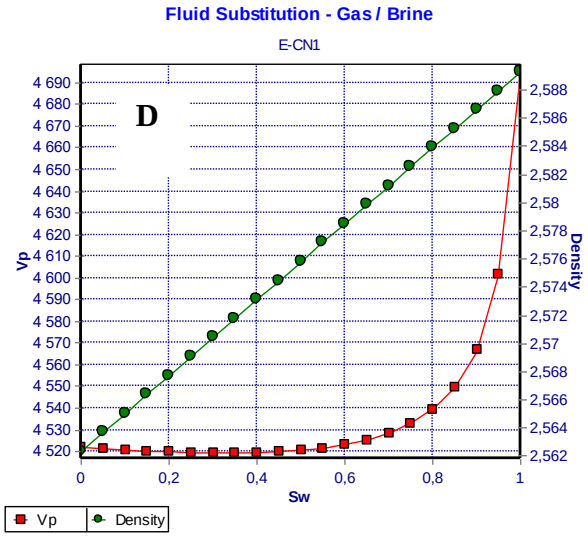

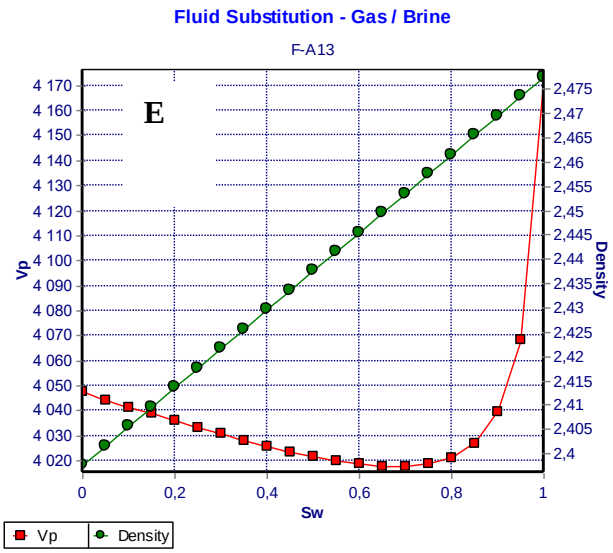

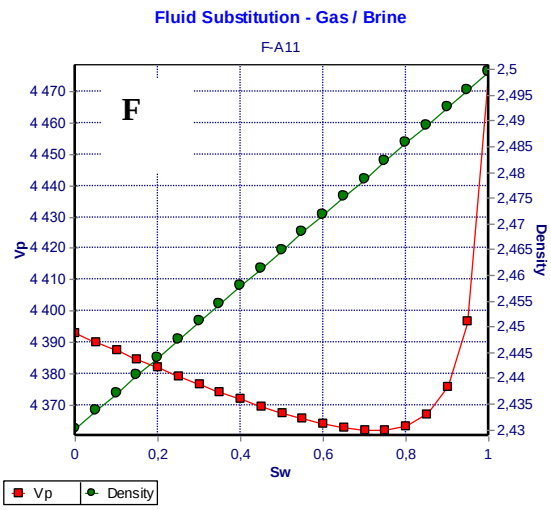

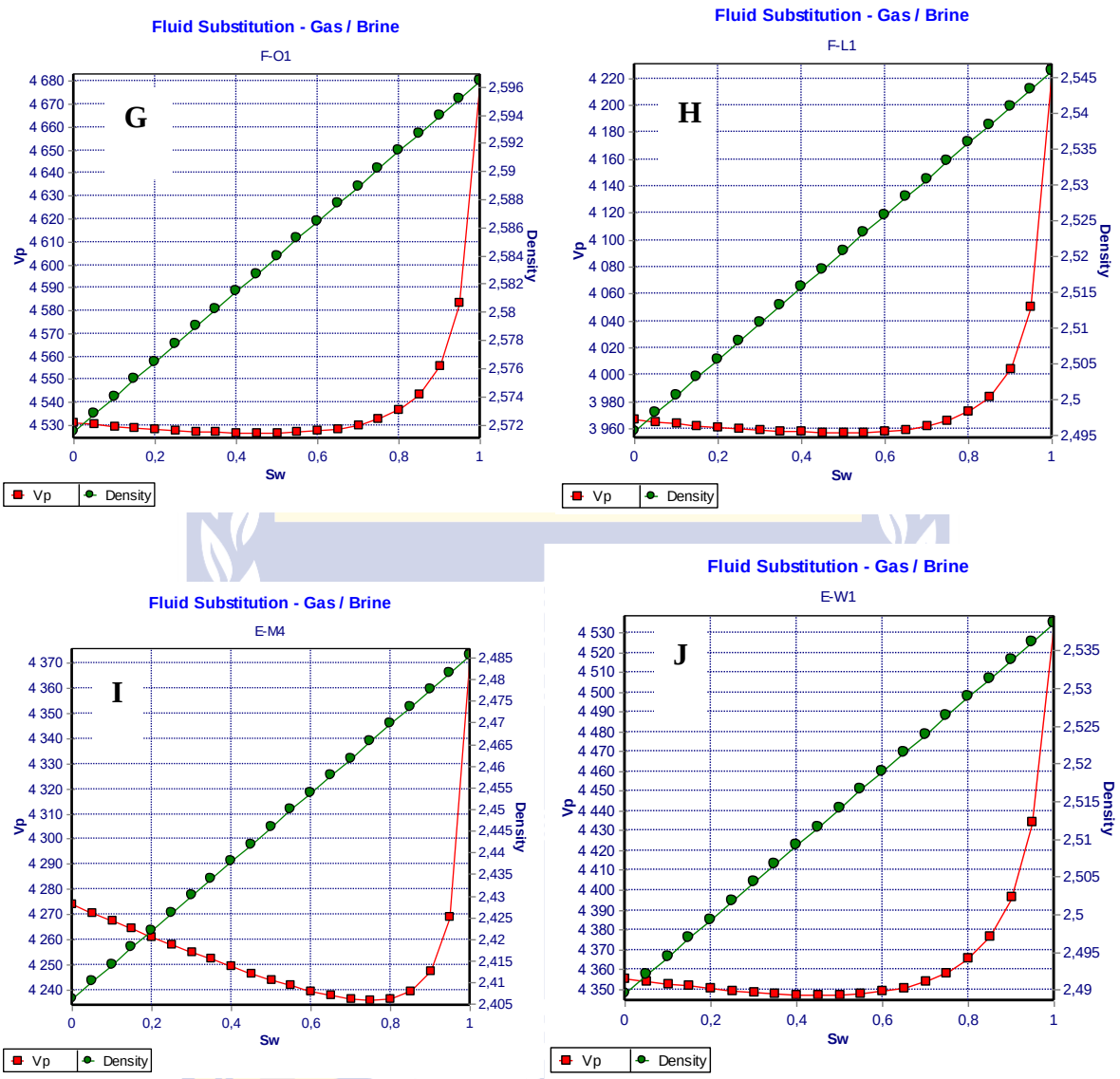

Figure 5-37: Fluid substitution cross-plots of E-G1 (A), F-O2 (B), F-A10 (C), E-CN1 (D), F-A13 (E)), F-A11 (F), F-O1 (G), F-L1 (H), E-M4 (I) and E-W1 (J) showing change in Vp for the reservoir intervals in 10 wells.

5.7 CONCLUSION

The bulk density and compressional velocity were thoroughly utilized to predict the acoustic impedance within the 10 studied reservoirs of the Upper Shallow Marine sandstones.

The 3D parameter viewer clearly illustrated the distribution of compressional velocity, bulk density, and acoustic impedance. The acoustic impedance proved to be highest on the central to the western side of the field at E-CN1 with an average value of 11832 g/cm3s whereas, well F-A13 reservoir in the eastern side of the field proved to have the lowest average acoustic impedance of 9821 g/cm3s. E-M4 reservoir showed almost similar values of bulk density with F-L1, F-A10, F-L11 and F-A13. The effect of porosity on acoustic impedance, bulk density and compressional velocity was thoroughly studied using cross-plots.

There was a good linear negative correlation between acoustic impedance and porosity where the reservoir was homogenous, thick sandstone. Higher porosity values were correlated with lower acoustic impedance values. However, interbedded shale units within the reservoirs appear to hinder a reliable correlation between acoustic impedance and porosity as seen in well E-W1.

The Gassmann equation has been used for the calculation of the effects of fluid substitution on seismic properties using rock frame properties. Three fluid substitution models (brine, oil and gas) were determined for pure sandstones and were used to measure the behaviour of the different sandstone saturations. A significant decrease was observed in Vp when the initial water saturation was substituted with the hydrocarbon (oil or gas) in all the wells. The value of density decreased quite visibly in all the wells when the brine (100% water saturation) was substituted with gas or oil. The fluid substitution affected the rock property significantly. The Vp slightly decreases when brine was substituted with water in well F-A13, F-A10, F-O2, F-O1 F-A11, F-L1 and E-CN1. Wells E-G1, E-W1 and E-M4 contain both oil and gas and therefore showed a notable decrease from brine to oil and from oil to gas respectively. The Vs remained unaffected in all the wells. The acoustic impedance logs showed a decrease when 100% water saturation was replaced with the hydrocarbon (oil or gas) in all the wells.

It can be concluded that porosity and pore fluids are some of the major factors affecting compressional velocity, bulk density, and acoustic impedance.

5.8 REFFERENCES

Becquey, M., Lavergne, M and Willm, M. (1979). Acoustic impedance logs computed from seismic traces. *Geophysics, 44*(9), 1485.

Cemen, I ., Fuschs, J., Coffey, B., Gertson, R and Hager, C. (2014). Correlating porosity with acoustic impedance in sandstone gas reservoirs: Examples from the Atokan Sandstones of the Arkoma basin, Southeastern Oklahoma. *AAPG Bulletin, 41255*, 1-17.

Dunlop, J, and Whichello, A. (1981). Acoustic Impedance of marine sediments. *Marine geophysical researchers, 5*(2), 157-163.

El-Bahiry, M., El-Amir, A and Abdelhay, M. (2017). Reservoir characterization using fluid substitution and inversion methods, offshore West Nile Delta, Egypt. *Egyptian journal of petroleum, 26*(2), 351-361.

Gassmann, F (1951). Über die elastizitätporösermedien. Vierteljahrsschrift der Naturforschenden Gesellschaft in Zurich 96:1–23.

Greenberg, M.L and Castagna, J.P. (1992). Shear -wave velocity estimation in porous rocks: Theoretical formulation, preliminary verification and applications. *Geophysical prospecting, 40*(2), 195–209.

Han, D., Nur, A and Morgani, D. (1986). Effects of porosity and clay content on wave velocities in sandstones. *Geophysics, 51*(11), 2093-2117.

Kassab, M and Weller, A. (2015). Study on P-wave and S-wave velocity in dry and wet sandstones of Tushka region, Egypt. *Egyptian Journal of Petroleum, 24*(1), 1-11.

Kenter, J. (1997). Parameters controlling sonic velocities in a mixed carbonate-siliciclastic Permian shelf-margin (Upper San Andres formation, last canyon, New Mexico). *Geophysics, 62*(2), 505.

Kenter, J.A.M and Ivanov, M. (1995). Parameters controlling acoustic properties of carbonate and volcaniclastic sediments at sites 866 and 869. *Proceedings of the ocean drilling program scientific results, 43*, 287-303.

Khan, N and Rehman, K. (2018). Petrophysical evaluation and fluid substitution modelling for reservoir depiction of Jurassic Datta Formation in the Chanda oil field, Khyber Pakhtunkhwa, northwest Pakistan. *Journal of Petroleum Exploration and Production Technology*, 1-18.

Knackstedt. M., Arns, C and Pinczewski. W. (2005). Velocity-Porosity relationship: Predictive velocity model for cemented sands composed of multiple mineral phases. *Geophysical prospecting, 53*(3), 349-372.

Schlumberger. (2015). *Schlumberger oilfield Glossary.*

Smith, T.M., Sondergeld, C.H and Rai, C.S. (2003). Gassmann fluid substitutions: a tutorial. Geophysics 68(2):430–440.

CHAPTER SIX

6 EFFECT OF MINERALOGY ON VELOCITY, DENSITY AND POROSITY

ABSTRACT

Clay minerals are the most abundant materials in sedimentary basins. Their presence significantly affects the behaviour of the acoustic properties of the reservoir rocks as a function of mineral type, volume, and distribution. Glauconite is a common mineral in sedimentary deposits in marine shelves. The presence of glauconite was observed in all the studied reservoirs. Thirty-two thin sections, XRD and SEM/EDS from eight out of 10 wells were studied to investigate lithology, diagenesis and the effect of mineralogy on porosity and acoustic properties (Compressional velocity and bulk density) within the studied reservoir units. The effect of mineralogy of the two remaining wells (F-A11 and F-L1) could not be determined because of the lack of core and therefore the results of the nearby wells were inferred. Cementation (calcite and quartz), dissolution, compaction, clay mineral authigenesis, and stylolitization were the most significant diagenetic processes affecting porosity, velocity, and density. Well E-CN1 was extensively affected and showed the highest velocity and density readings with the lowest porosity whereas, well F-A13 was the least affected and showed the lowest velocity and density readings with the highest porosity.

6.1 INTRODUCTION

Clay minerals are the most abundant materials in sedimentary basins. The most common clay minerals found in mudstone and clastic and non-clastic reservoir rocks are kaolinite, illite, smectite, and chlorite. Their presence significantly affects the behaviour of the acoustic properties of reservoir rocks as a function of mineral type, volume, and distribution. Two reservoir rocks with the same clay content might have different acoustic properties due to different clay minerals present (Mondol, et al., 2008). The elastic properties of clay minerals are crucial to understanding the response of the sonic log and seismic in both shaley sequence and clay-bearing reservoir rocks (Mondol, et al., 2008).

Glauconite mineral is common in sedimentary deposits in marine shelves (Odon and Matter, 1981). The studied reservoirs are known for the presence of glauconite throughout the field. SEM and EDS, thin section and XRD analysis were conducted to investigate the effect of clay minerals on the acoustic properties of the reservoir rocks.

Glauconites are mixed layer minerals consisting of smectite and glauconite mica (Odin and Matter, 1981). They are K-rich dioctahedral phyllosilicates that usually appear in the shape of the rounded grains (Pestitschek, 2012). Glauconitic mica and Fe-K rich 10 Å illite type are classified as two end members with the characteristics of evolved glauconite (Fe_2O_3 >20%, K_2O >4%) and also glauconite smectite which forms a mixed-layered mineral group consisting of varying proportions of glauconitic, smectitic and also illicit type layers (Bailey, et al., 1979; Chamley 1989).

In order to predict the effect of diagenesis on sandstone reservoirs, it is important to recognize the impact of the compactional and cementation process on sandstone porosity loss (Lundegard, 1992). Studies such as (Benson, 1981; Pittman and Larese 1986, 1991; Kurkjy, et al., 1987) have shown a direct relationship between content of ductile lithic grains such as glauconite and porosity reduction by compaction. Generally, in the clastic sediments, the first control on the quality of the reservoir is a function of the basic presence of sand rather than silt or muds. Although, during the burial process the deposited sand never retains its original porosity, fabric or mineralogy as it becomes sandstone (Worden and Burley, 2003). It is important to carry a detailed study on core samples to understand what diagenetic changes have occurred and what factors are controlling the reservoir quality (Gier, et al., 2008).

Diagenesis is defined as the sum of physical, chemical and biochemical changes that affect sediment after it has been deposited and during or after its lithification. It consists of a broader range of physical, geochemical and biological post-depositional process by which original mineral assemblages intersect with the interstitial pore waters with the aim to reach equilibrium between textural and thermodynamics with their environment. Diagenesis process occurs in different stages of burial cycle. Anadiagenesis is the phase of compaction and maturation that is characterized by the expulsion and upward migration of interstitial water, oil and gas and reduction conditions. This process affects hundreds or even thousands of sediment meters and it is largely responsible for the reduction of porosity. Epidiagenesis is characterized by the modification of interstitial waters because of the penetration of downward migration of meteoritic waters. The dissolution phenomena are usually encountered in this phase. This process usually affects a thin zone close to the surface (Serra, 1986).

Compaction, mineral dissolution and mineral precipitation occur during diagenesis process. Compaction is the mechanical rearrangement of grains under the weight of the above sediments during the burial process. The result is the reduction of the pore volume of the initial porosity. The extent of the compaction depends on the initial porosity and grain size, shape and sorting (Press and Siever, 1978). Cementation is the deposition of minerals within the pore space. This is one of the most common diagenetic phenomenal processes. The deposited minerals may be derived from the sediment itself through leaching and core deposition. They can also be derived from salts dissolved in interstitial or circulating water. Cementation process can either happen over a short or a long period of time. The most common types of cement are calcite, dolomite, silica and clay minerals. Cementation generally results in the reduction of porosity and an increase in velocity.

6.2 AIMS AND OBJECTIVES

The aim of this chapter was to investigate the effect of mineralogy on porosity, velocity and bulk density of the studied reservoir rock. Thin section analysis, XRD and SEM/EDS were used extensively to study mineralogy. A thin section was used to describe the size and shape of the grain size, to observe cementation, mineral overgrowth and differentiate between detrital and authigenic grains. Qualitative XRD analysis was used to identify clay minerals detected through peaks. SEM to reveal microscale features of a rock sample to help understand the

morphology. EDS to help identify minerals present through the identification of major and minor chemical elements present in the rock sample.

6.3 MATERIALS AND METHODS

6.3.1 THIN SECTION ANALYSIS

Thin section analysis is important when learning about a rock, reservoir, or a formation of interest. To fully describe and characterize a rock, it takes varying stages of sample cutting, mounting and smoothing before preparing a slide for thin sections analysis under the microscope.

6.3.2 XRD ANALYSIS SAMPLE PREPARATION

A sample of solid rock was placed into a mortar and pestle (Figure 6-1) to be crushed into a powder form.

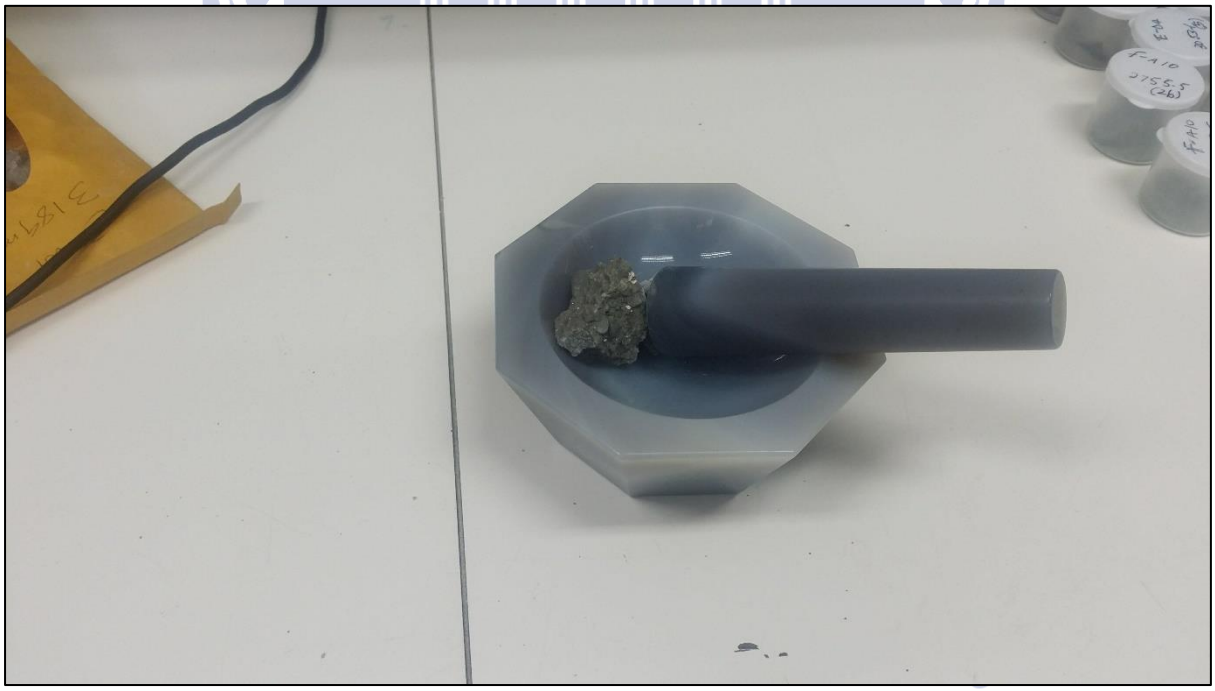

Figure 6-1: Mortar and pestle with a rock sample.

It is necessary to dissolve carbonates in some sediment before clay minerals can be identified. The aim is to remove as many carbonates as possible to separate the materials contained within the carbonate for analysis by using the acetic acid treatment method. The sample preparations followed the methodology outlined by Brandt, et al., 2013: 2cm3 of the undried sample was

placed into a centrifuge tube with a 25ml of acetic acid (10% solution). The solution was mixed well within the centrifuge tube until the reaction stopped (Figure 6-2A). The sample solution was placed into the centrifuge (Figure 6-2B) for 15 minutes at 1500 rpm to spin and the acetic acid solution was decanted and disposed of properly. 25ml of distilled water was added to the centrifuge tube and placed into the centrifuge again for 15min at 1500 rpm. The clear water was decanted and the step was repeated again. The distilled water and sample water from the cube were placed into a beaker and 1% of Calgon solution was added (Figure 6-2C). The ultrasonic bath (Figure 6-2D) was used to effectively mix with the solution. The Calgon solution/ sample mixture was placed into a centrifuge cube to spin for 5 minutes at 1000 rpm to remove the >2µm particle size fraction. The Calgon solution containing a suspended clay was decanted into a new centrifuge tube and placed into a centrifuge to spin for 15 minutes at 1500 rpm to remove the remaining <2µm clay-size fraction. The Calgon solution was decanted and the clay residue left in the centrifuge tube was washed with distilled water in the centrifuge at 1500 rpm for 15 minutes. This step was repeated once again as it was necessary to remove the Calgon. An orientated clay mount was made by placing 2-3 drops (or enough to cover the quartz disk) of the solution into the quartz disk and let dry in the desiccator. The last step was to treat the clay mount sample on the quartz disk with the Ethylene glycol. Ethylene glycol can be used to expand swelling clays (smectite and Montmorillonite), some mixed-layer clays, and vermiculite as an aid to mineral identification. The quick treatment was used which involved using an eye dropper to apply a drop of Ethylene glycol directly to the surface of the clay sample mount. The sample was ready for analysis as soon as glycol is uniformly absorbed on the sample mount (Figure 6-2E). The Rigaku XRD machine (Figure 6-2F) was used to carry out the analysis.

Figure 6-2: Illustration of the clay sample preparation for XRD analysis.

6.3.3 SEM-EDS ANALYSIS

The SEM analyses were conducted using JCM-6000Plus Neoscope Benchtop SEM (Figure 6-3). This equipment complements both optical microscopes and traditional SEMs in the lab and can be configured for advanced analytical applications. The equipment is equipped with the powerful electron optics of an SEM, with up to 60 000X magnification. A small sample of rock was placed inside the JCM-6000Plus for imaging. Both low and high vacuum modes were used to get the best possible results. This analysis helps to identify the morphology and the nature of the clay minerals between the rock grains. The detailed structure of the clay minerals cannot be identified from the petrography; hence it is vital to conduct SEM analysis. Full-featured Energy-Dispersive Spectroscopy (EDS) with SDD technology is optically available for advanced analytical applications. EDS detect the major and minor chemical elements within the rock sample to help identify the minerals.

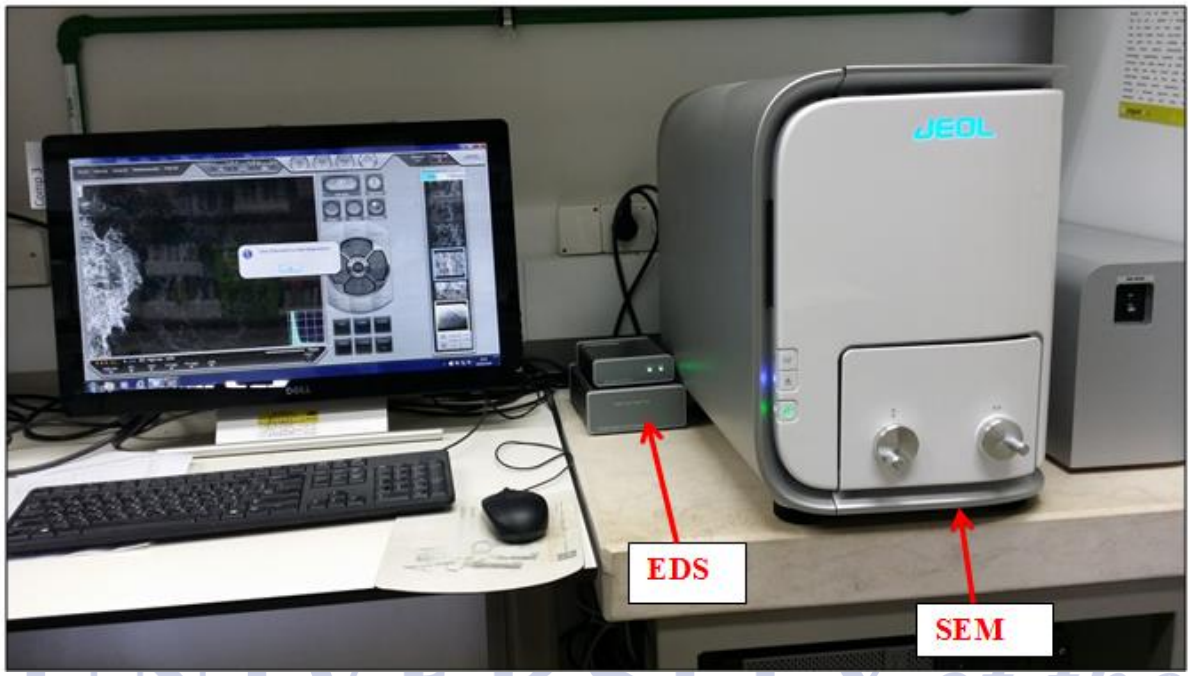

Figure 6-3: SEM/EDS Equipment used for analysis.

6.4 RESULTS AND INTERPRETATION

6.4.1 F-O1 MINERALOGY INTERPRETATION

The lithology F-O1 reservoir is comprised of a sandstone sequence with rare thin claystone. Two cores were cut back to back between 3704-3728m. Thin igneous intrusions were also intersected. The sandstones are predominantly clean, very fine to coarse-grained and poorly to

well sorted. The first core comprises of fine to medium-grained, moderately to well-sorted sandstones. They are lithic, glauconitic, feldspathic and locally slightly shelly. Finer-grained, argillaceous sandstones are locally present and very thin stylolitised; silty, argillaceous laminae are developed. Glauconite mostly appears to have been altered. The second core is similar to the first core but with abundant quartz cement.

The average porosity of 9.1% was recorded from wireline log reading in chapter 4 and the bulk density of 2.573g/cm^3 in chapter 5. Most porosity is secondary after grain dissolution and is commonly illite or chlorite filled as seen in Figure 6-4. Extensive quartz overgrowth cementation or detrital clays result in these pores being poorly interconnected. Below 3711m porosity is good. This is due to better-developed cement dissolution porosity, after calcite. The early calcite cementation was probably sourced by the dissolution of bioclasts. Calcite cement restricted the subsequent quartz overgrowth development and was later leached out to produce well interconnected secondary porosity. Illite and chlorite infill some secondary pores and coat detrital grains in places, but are generally less abundant than in the upper part of the core. Porosity decrease towards the base of the core, due to abundant quartz cement. The abundant quartz cement is also confirmed by high silica content displayed in XRD (Figure 6-5, 6-6 and 6-7). This may be related to the emplacement of the igneous sills, encountered at the bottom of the core. Secondary porosity is well developed towards the top of the interval (above 3745m). The best porosities are developed in the coarser grained, less well sorted, shelly sands, in which leaching of early calcite cement has produced secondary porosity. In the well sorted, less shelly sands quartz overgrowth, illite and chlorite and locally pseudo matrix are more extensively developed, and secondary porosity development is restricted. Microporosity (Figure 6-8), through areas of authigenic illite and chlorite, is commonly the only porosity type present in these sands. Thin chlorite grain coatings are developed in places (Figure 6-9). A few thin, argillaceous sandstones are present, in which detrital clays occlude primary porosity and minimize diagenetic effects.

The presence of bioclastic material on deposition appears to control the distribution of secondary porosity in this interval. Bioclastic calcite sourced the early calcite cementation, which restricted subsequent quartz overgrowth, illite, and chlorite development, and minimized compactional effects. After the burial, the calcite cement was leached to produce well interconnected secondary porosity, resembling primary porosity. In the non-bioclastic sands, less early calcite cementation occurred, allowing for more extensive development of insoluble

quartz, illite, and chlorite. This silicate cement was not removed on deep burial and hence restricted secondary porosity development. This may be related to the emplacement of the igneous sills, encountered at the bottom of the core at 3726.5 and 3727.5m. The igneous intrusions are highly altered, coarse-grained lamprophyres. Extensive calcitisation has occurred with only pseudomorphs of muscovite as seen on the XRD analysis (Figure 6-6). Secondary chlorite was also developed by alteration. More extensive quartz cementation has occurred in the sandstones immediately adjacent to the intrusions, but the effects of the intrusion on the sandstone quality appear to have been much localized, and the overall quality of the reservoir has not been significantly affected.

Common minerals chemical formula:

Glauconite= (K,Na,Ca)1.2-2.0(Fe+3,Al,Fe+2,Mg)4(Si7-7.6Al1-1.9O20) (OH)4 n H2O

Kaolinite= Al4 [Si4 O10] (OH) 8

Chlorite= (Mg, Al, Fe) 12 [(Si, Al) 8 O20] (OH) 16

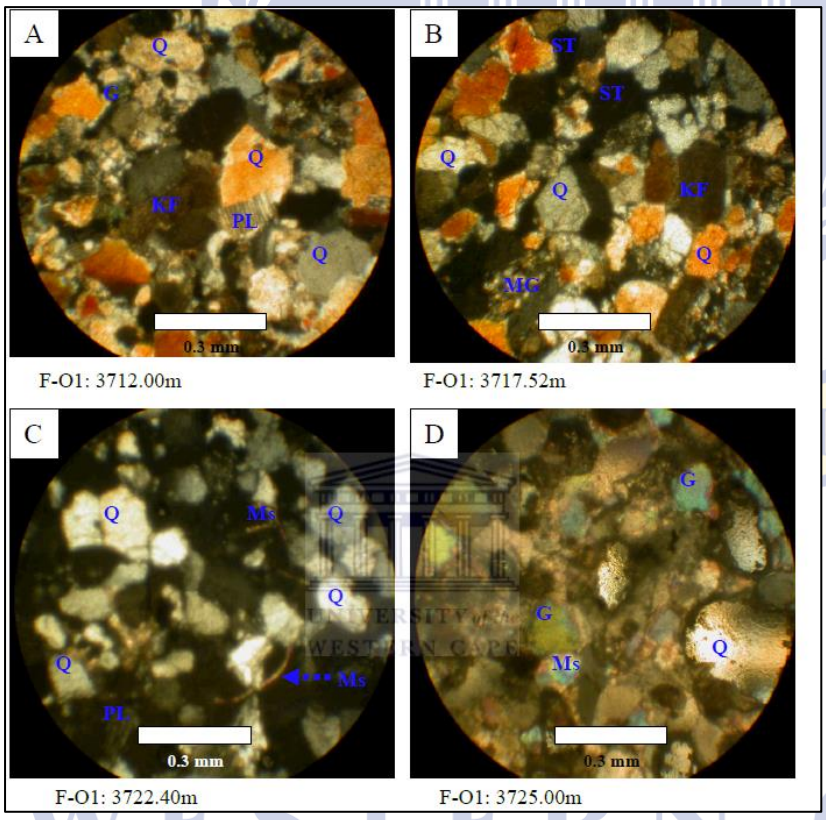

Figure 6-4: F-O1 petrography results (Fadipe, 2012).

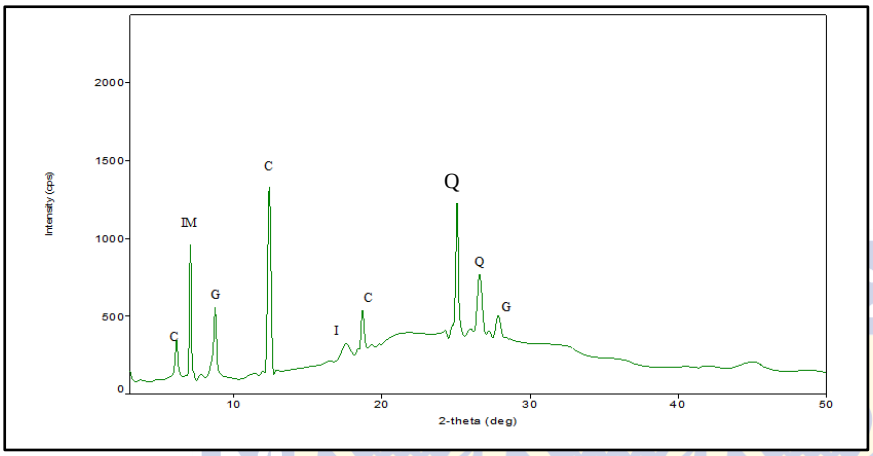

Figure 6-5: F-O1 XRD analysis of 3705m.

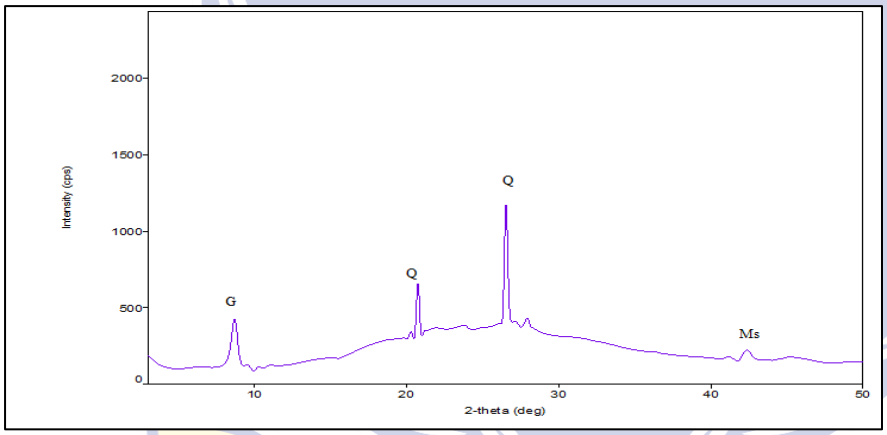

Figure 6-6: F-O1 XRD analysis of 3720.52m.

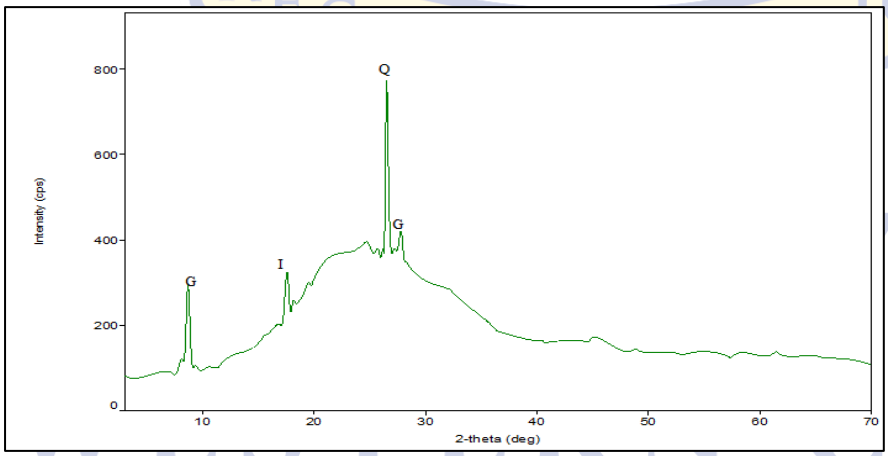

Figure 6-7: F-O1 XRD analysis of 3712.46m.

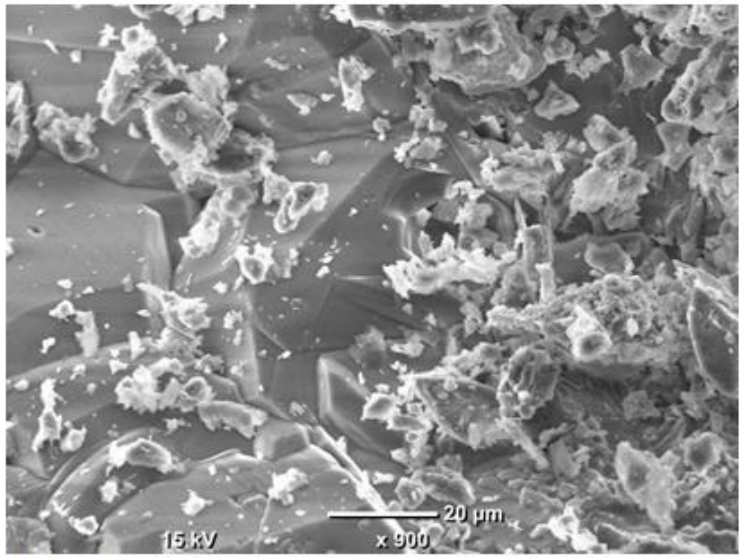

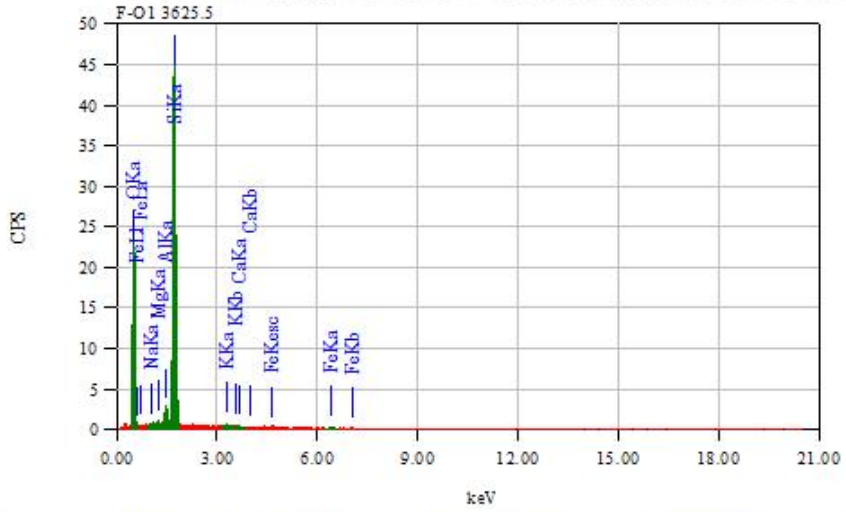

Element	(keV)	Mass%	Sigma	Mol%	Compound	Mass%	Cation	K
O		51.93						
Na K	1.041	0.40	0.17	0.54	Na2O	0.54	0.13	0.6826
Mg K	1.253	0.24	0.14	0.61	MgO	0.40	0.07	0.3384
Al K	1.486	2.03	0.27	2.31	Al2O3	3.84	0.56	4.2610
Si K	1.739	43.21	1.12	94.25	SiO2	92.43	11.37	89.5252
K K	3.312	0.69	0.12	0.54	K2O	0.83	0.13	1.6575
Ca K	3.690	0.25	0.12	0.38	CaO	0.34	0.05	0.6425
Fe K	6.398	1.25	0.23	1.37	FeO	1.61	0.17	2.8927
Total		100.00		100.00		100.00	12.48	

Figure 6-8: SEM and EDS analysis of 3625.5m.

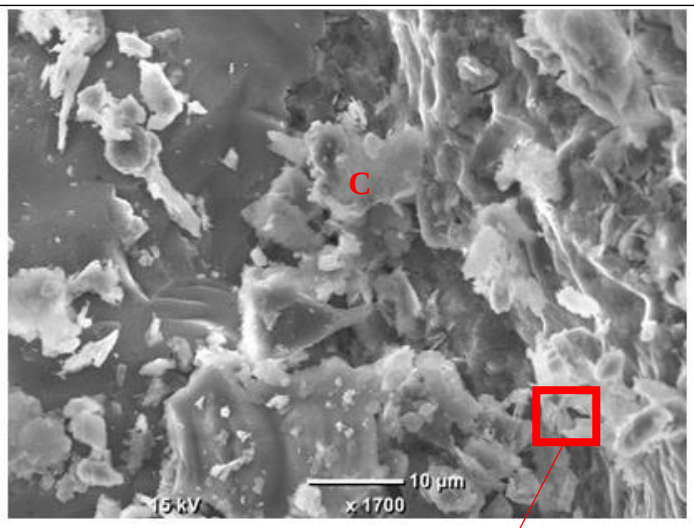

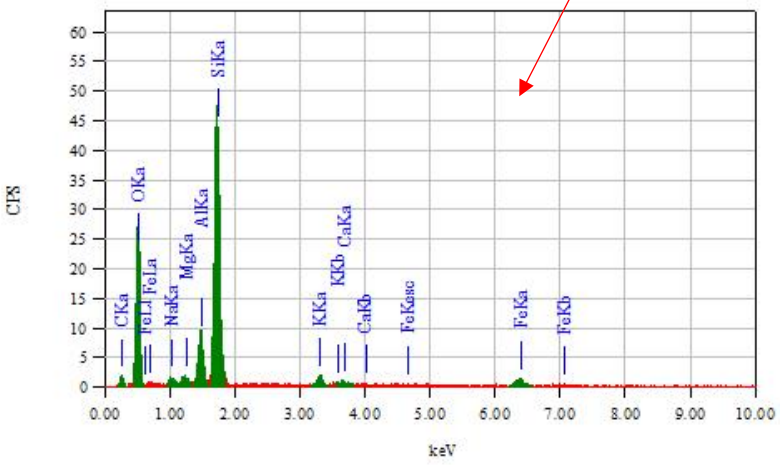

Element	(keV)	Mass%	Sigma	Mol%	Compound	Mass%	Cation	K
C K	0.277	21.72	0.59	59.82	C	21.72	0.00	6.3704
O		38.19						
Na K	1.041	1.22	0.15	0.88	Na2O	1.64	0.53	2.4065
Mg K	1.253	0.52	0.11	0.71	MgO	0.87	0.22	0.8394
Al K	1.486	5.55	0.30	3.40	Al2O3	10.49	2.07	13.3471
Si K	1.739	27.14	0.69	31.97	SiO2	58.07	9.72	60.9697
K K	3.312	1.53	0.11	0.65	K2O	1.84	0.39	4.5999
Ca K	3.690	0.52	0.11	0.43	CaO	0.72	0.13	1.6450
Fe K	6.398	3.61	0.28	2.14	FeO	4.64	0.65	9.8221
Total		100.00		100.00		100.00	13.71	

Figure 6-9: SEM and EDS analysis of 3705m.

6.4.2 F-O2 MINERALOGY INTERPRETATION

Two fairly broadly defined sandstone types were identified petrographically in the pre-1AT1 sediments. The discussion under this reservoir sequence focused on two cores (1 &2). Core 1 was cut from 3620.5m- 3639.1m and it comprises of argillaceous, poorly to moderately sorted, fine-grained sandstones on the upper part of the core just above 3629.5m. They are very lithic, with Cape Supergroup quartzites, claystones, and rarer volcanic clasts. Glauconite, feldspar and carbonaceous material are all abundant. Evidence of possible bioturbation is present locally. Detrital clays resulted in poor primary porosity in these sandstones, and early compaction and pseudo matrix development further reduced porosities. Quartz overgrowths are common. Authigenic Iliite and chlorite are common as pore filling and grain alteration products. A very minor amount of Ferron calcite and feldspar overgrowth are present. Below 3629.5m the sandstones are clean, moderately sorted and medium grained. They are very lithic (with Cape Supergroup quartzites, claystone, siltstone, and rare volcanic clasts) and glauconitic, becoming very glauconitic below 3632m. Detrital feldspar is common. Stylolitised argillaceous and carbonaceous streaks are present in places (Figure 6-10). The lower sandstones of core 1 possess poor to good porosity. Porosity is secondary, after cement and grain dissolution. Quartz overgrowths are the main pore filling mineral, with illite and chlorite commonly lining pore spaces and creating microporosity. The 10.8% average porosity recorded from the wireline logs in chapter 4 was as results of the creation of microporosity. Stylolite resulted from pressure solution and may form barriers between the interconnected pore spaces.

Core 2 is a continuation of core 1 and was cut between 3639.1-3657.5m. The sandstones are similar to those described above, but are locally well sorted and bioturbated, with irregular streaks and patches of detrital clay. A silty, poorly to moderately sorted, fine-grained argillaceous sandstone unit occurs from 3647-3649.5m. Porosity is secondary, after cement and grain dissolution, and as in core 1, quartz cement is the most abundant pore filling mineral. XRD (Figure 6-11) and SEM (Figure 6-12 and 6-13) analyses indicate that chlorite is the most abundant authigenic clay, forming pore linings as is a product of grain alteration. Minor amounts of authigenic feldspar and illite are present. The average porosity recorded in this well was 10.8% with an average velocity of 4038 m/s. and bulk density of 2.5g/cm^3.

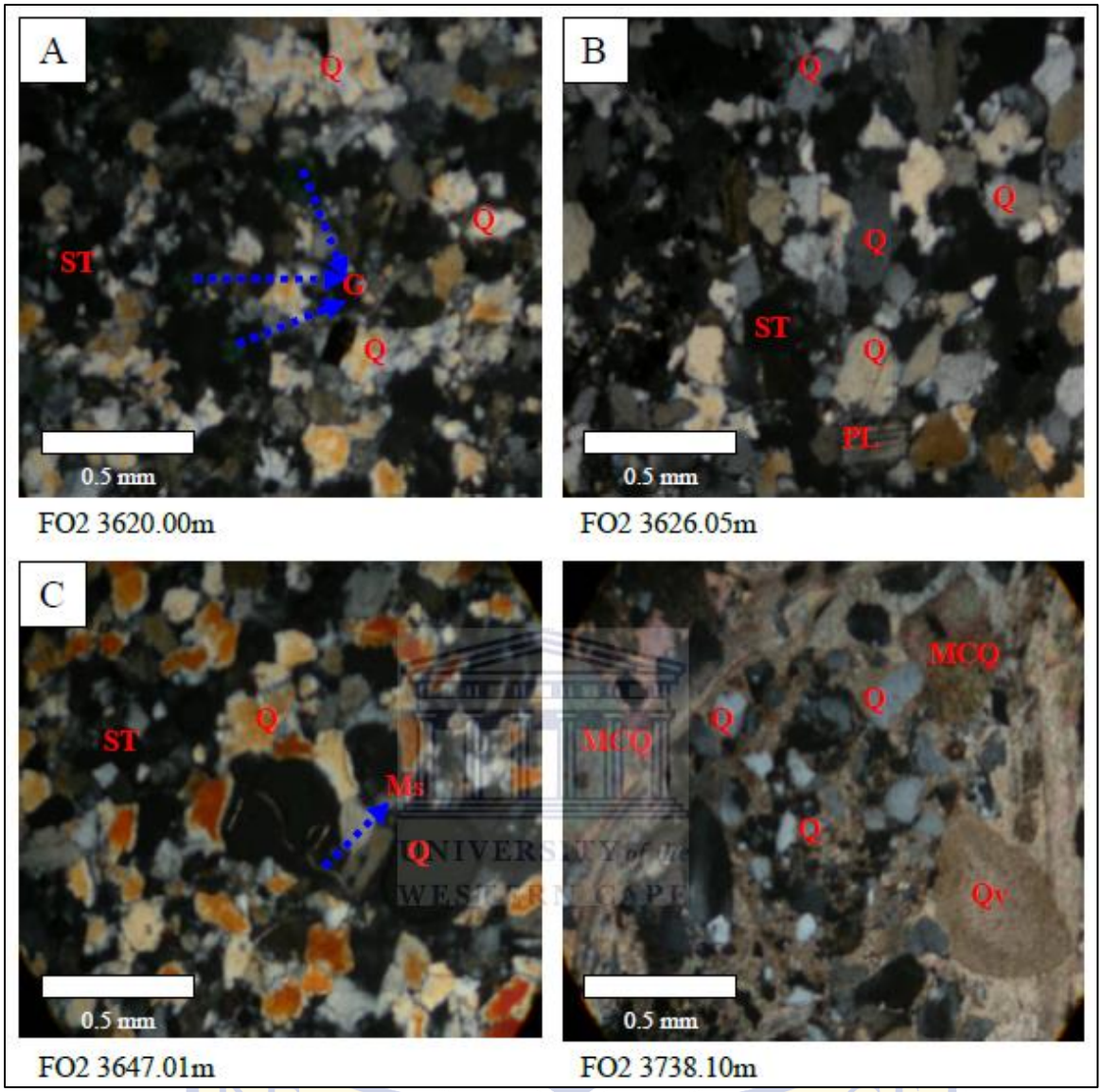

Figure 6-10: F-O2 petrography analysis (Fadipe, 2012).

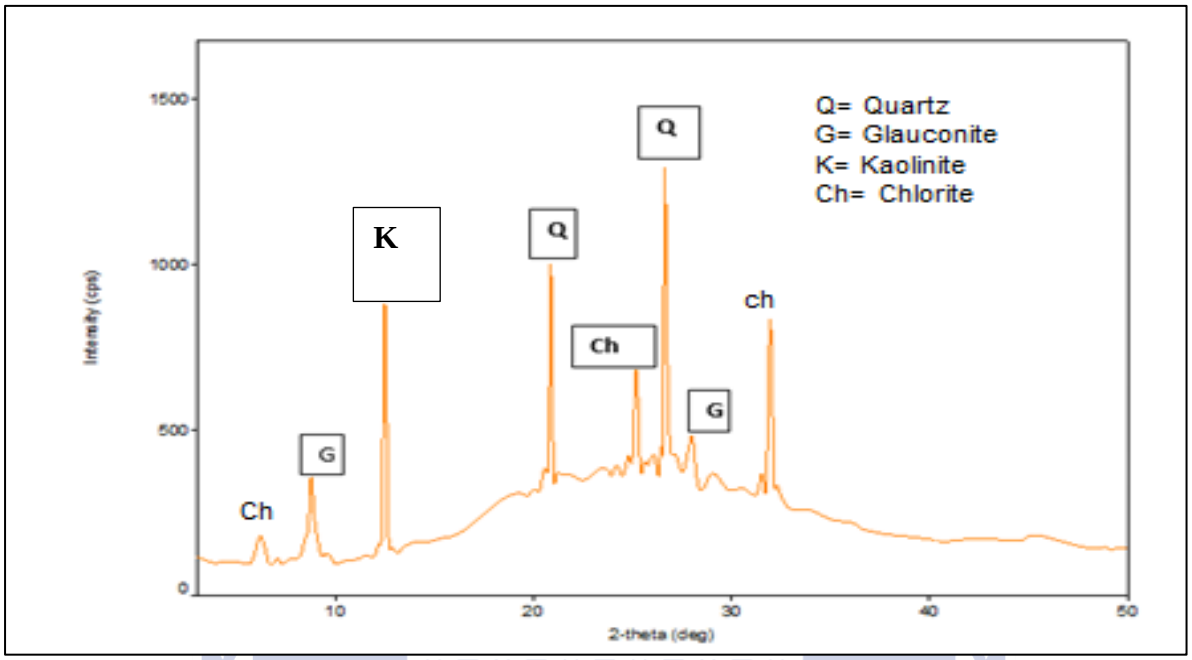

Figure 6-11: F-O2 XRD analysis of 3626.42m.

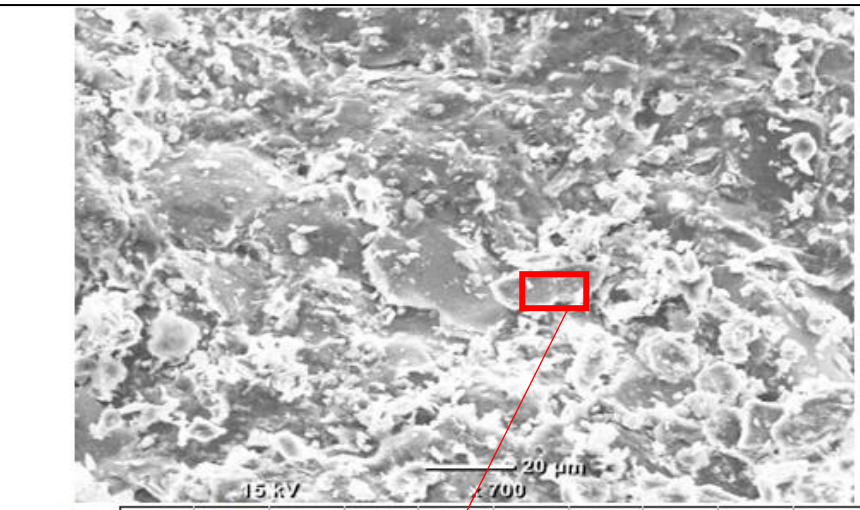

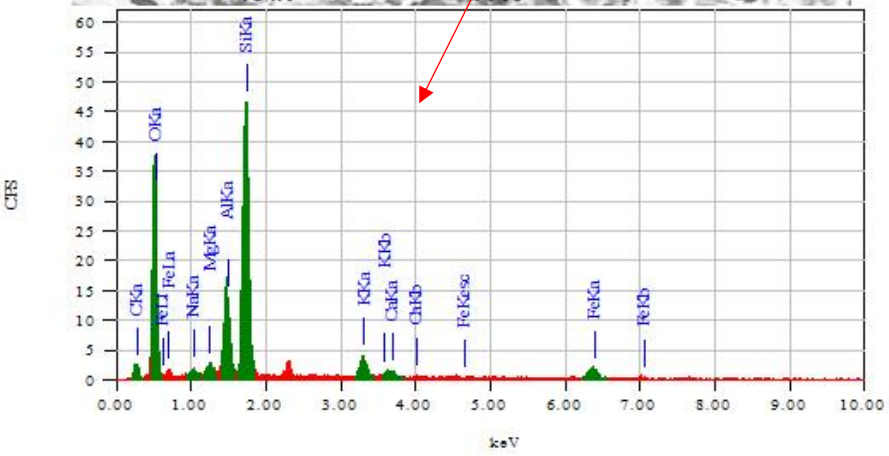

Element	(keV)	Mass%	Sigma	Mol%	Compound	Mass%	Cation	K
C K	0.277	24.16	0.52	63.87	C	24.16	0.00	7.7684
O		35.30						
Na K	1.041	1.02	0.13	0.70	Na2O	1.37	0.48	1.9132
Mg K	1.253	0.83	0.12	1.09	MgO	1.38	0.37	1.2827
Al K	1.486	7.60	0.31	4.47	Al2O3	14.36	3.06	17.4816
Si K	1.739	22.09	0.58	24.97	SiO2	47.26	8.56	46.1914
K K	3.312	2.62	0.12	1.06	K2O	3.15	0.73	7.8508
Ca K	3.690	0.90	0.11	0.71	CaO	1.26	0.24	2.8256
Fe K	6.398	5.48	0.29	3.12	FeO	7.05	1.07	14.6863
Total		100.00		100.00		100.00	14.52	

Figure 6-12: F-O2 SEM and EDS analysis of 3642m showing Glauconite.

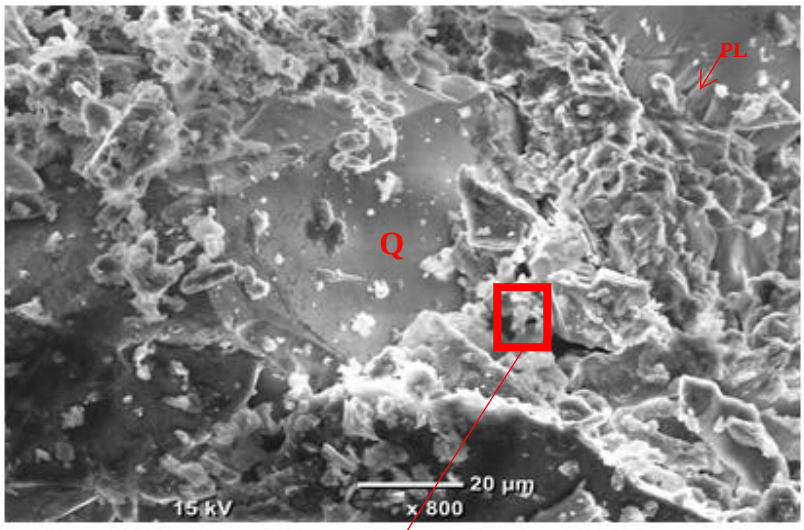

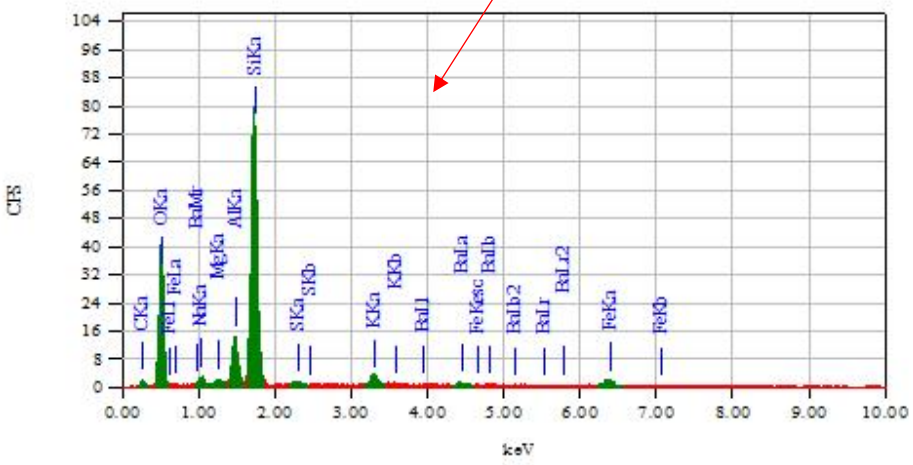

Element	(keV)	Mass%	Sigma	Mol%	Compound	Mass%	Cation	K
C K	0.277	15.81	0.41	50.68	C	15.81	0.00	4.1954
O		40.43						
Na K	1.041	1.53	0.13	1.28	Na2O	2.06	0.63	2.8119
Mg K	1.253	0.51	0.09	0.80	MgO	0.84	0.20	0.7453
Al K	1.486	5.64	0.24	4.02	Al2O3	10.66	1.99	12.4972
Si K	1.739	28.11	0.56	38.53	SiO2	60.15	9.51	58.8641
S K	2.307	0.57	0.11	0.69	SO3	1.43	0.17	1.3613
K K	3.312	1.53	0.09	0.75	K2O	1.85	0.37	4.3971
Fe K	6.398	3.90	0.22	2.69	FeO	5.01	0.66	10.2365
Ba L	4.464	1.96	0.18	0.55	BaO	2.19	0.14	4.8912
Total		100.00		100.00		100.00	13.66	

Figure 6-13: F-O2 SEM and EDS of Chlorite analysis at 3626m. Q= Quartz, PL=Plagioclase.

6.4.3 E-CN1 MINERALOGY INTERPRETATION

The main sandstone interval ranged from 4081-4233m and is a clean, tightly packed, generally moderately sorted and medium grained (Appendix F6). These sandstones are highly lithic, feldspathic to very feldspathic, and slightly carbonaceous and micaceous. Glauconite is present in variable amounts in most samples as seen on thin section (Figure 6-14B) and XRD (Figure 6-15 and 6-16) analysis. A rare leached dolomite shells are present below 4200m. The reservoir quality is very poor due to the destruction of intergranular porosity by extensive quartz and illite cementation, and compaction. Only microporosity through areas of authigenic illite is preserved in most of the samples analyzed, though isolated grain dissolution porosity is present in few places. Lesser amounts of dolomite, siderite and feldspar cement also reduce porosity and increase velocity and density.

The sandstones below 4233m are interbedded. These sandstones are siltier, argillaceous, finer grained and less well sorted than those from above 4233m. They are highly lithic, with sedimentary, metamorphic and rare volcanic clasts, very feldspathic and micaceous. Glauconite can also be observed both in thin section and XRD analysis and also on the EDS (Figure 6-18) by observing the chemicals components that constitute the chemical formula of glauconite. Reservoir quality is very poor due to very poor porosity. No porosity was visible in any of the thin sections and SEM (Figure 6-18 and 6-19) analyses, only very minor microporosity, through aggregates of authigenic clay was observed. Intergranular porosity has been destroyed by extensive dolomite and quartz cementation, and compaction of the sandstones. Lesser amounts of authigenic siderite, pyrite, and feldspar are developed locally. Detrital clays closed pore spaces in places.

The impact of this mineralogy/ diagenesis process was also confirmed by the low average porosity of 8.7% recorded from the wireline logs in chapter 4 and the high velocity of 4530.4m/s and bulk density of 2.578g/cm^3 recorded in chapter 5. This well recorded the lowest average porosity and the highest average porosity as compared to others.

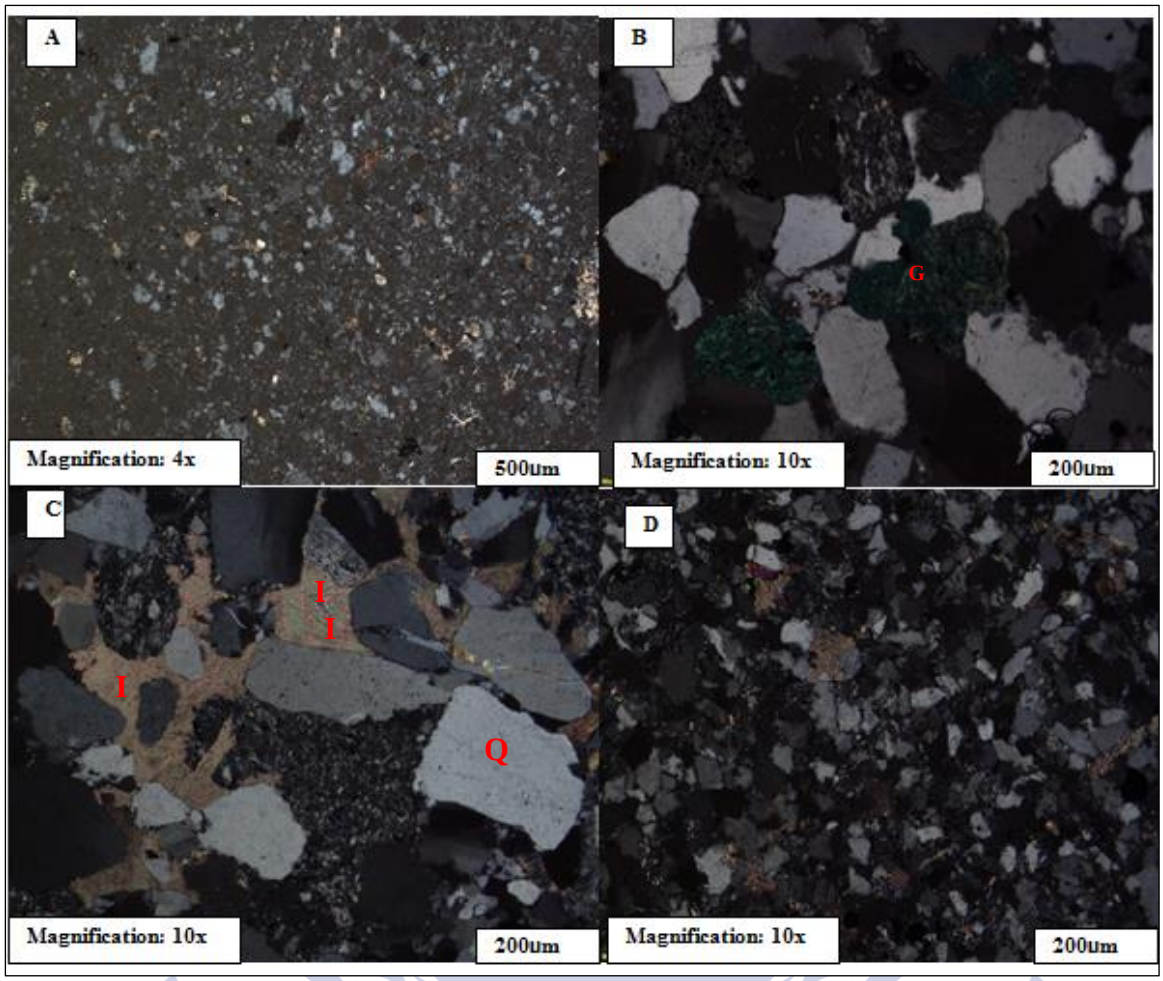

Figure 6-14: E-CN1 petrography analysis of (A) 4006.5m, (B) 4257m, (C) 4254m and (D) 5259.5m.

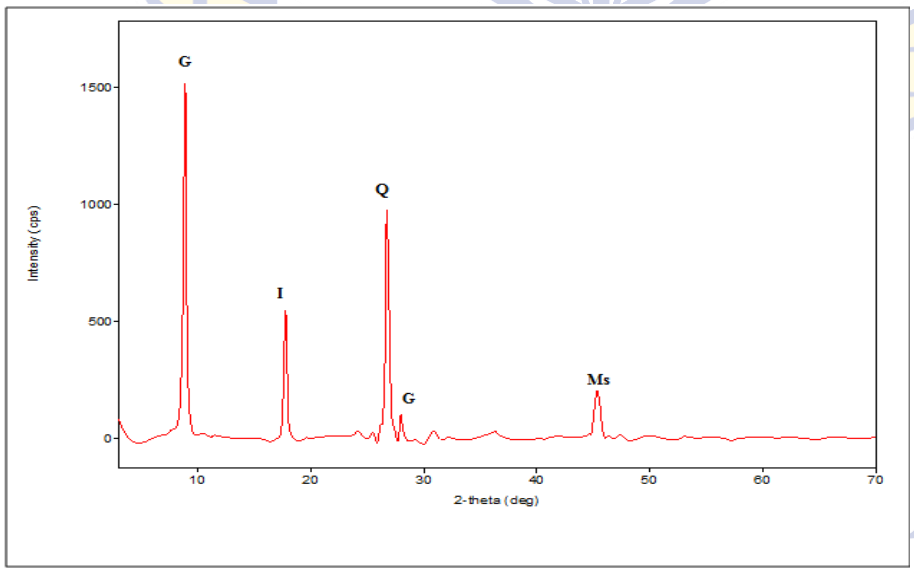

Figure 6-15: E-CN1 XRD analysis of 4006.5m. G= Glauconite, I= Illite, Q= Quartz, and Ms= Muscovite.

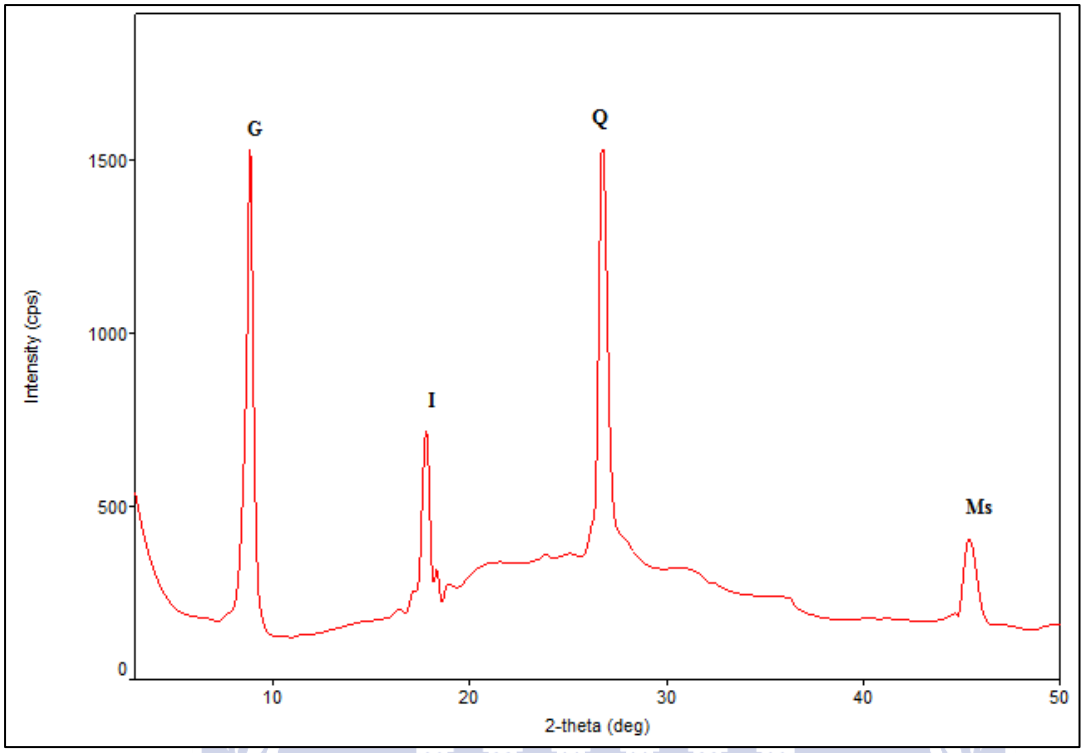

Figure 6-16: E-CN1 XRD analysis of 4253.5m. G= Glauconite, I= Illite, Q= Quartz and Ms= Muscovite.

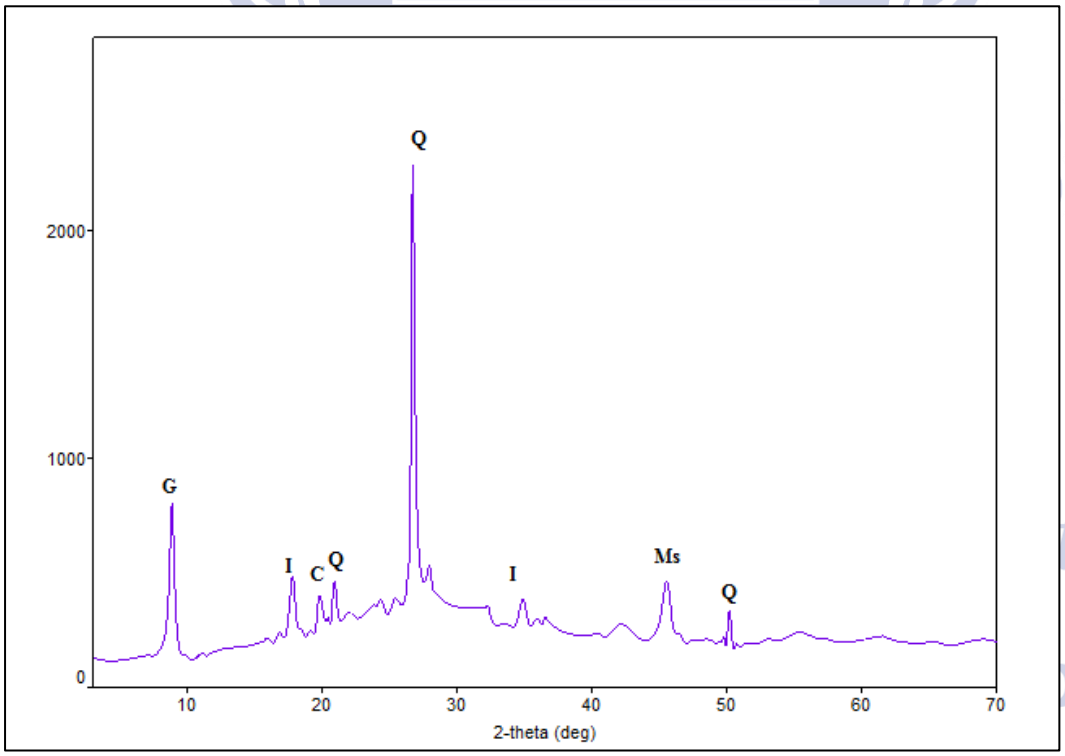

Figure 6-17: E-CN1 XRD analysis of 4257m. G= Glauconite, I= Illite, Q= Quartz, C= Chlorite and Ms= Muscovite.

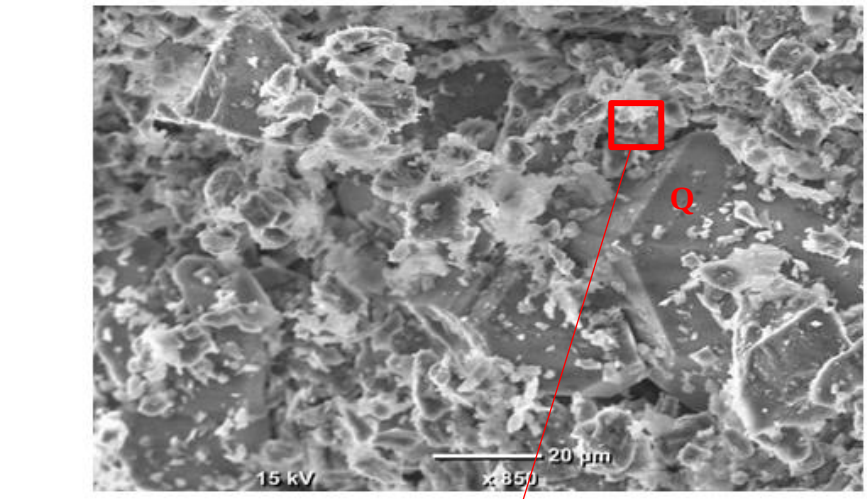

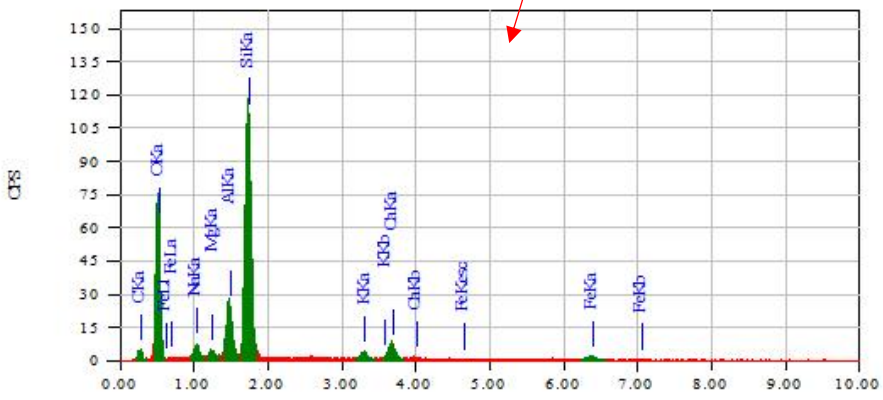

Element	(keV)	Mass%	Sigma	Mol%	Compound	Mass%	Cation	K
C K	0.277	21.17	0.35	58.89	C	21.17	0.00	6.3149
O		37.62						
Na K	1.041	2.54	0.12	1.85	Na2O	3.43	1.13	4.9908
Mg K	1.253	0.74	0.08	1.02	MgO	1.23	0.31	1.1413
Al K	1.486	6.07	0.19	3.76	Al2O3	11.47	2.30	13.9964
Si K	1.739	25.15	0.41	29.92	SiO2	53.81	9.14	53.9387
K K	3.312	1.23	0.06	0.52	K2O	1.48	0.32	3.6187
Ca K	3.690	3.25	0.12	2.70	CaO	4.54	0.83	10.1169
Fe K	6.398	2.23	0.13	1.33	FeO	2.87	0.41	5.8824
Total		100.00		100.00		100.00	14.43	

Figure 6-18: E-CN1 SEM and EDS analysis of illite at 4006.5m.

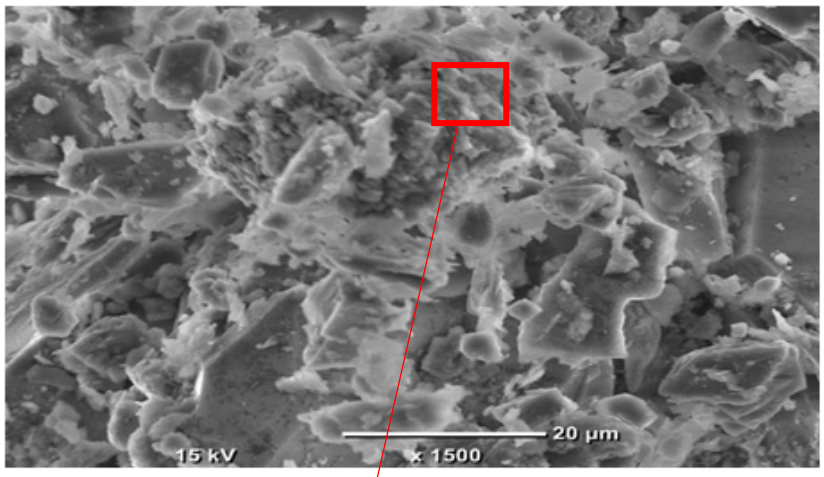

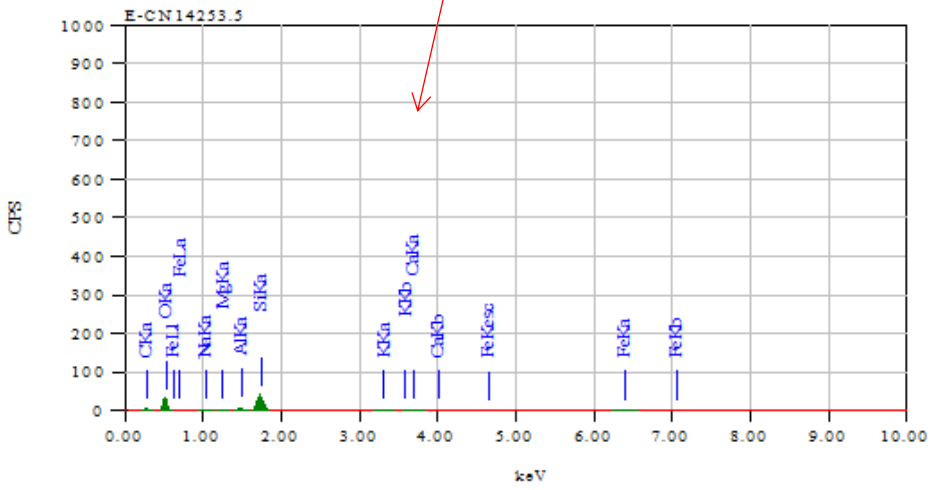

Element	(keV)	Mass%	Sigma	Mol%	Compound	Mass%	Cation	K
C K	0.277	34.73	0.67	73.55	C	34.73	0.00	13.5203
O		31.49						
Na K	1.041	1.40	0.16	0.77	Na2O	1.89	0.74	3.0270
Mg K	1.253	1.02	0.14	1.07	MgO	1.69	0.51	1.7750
Al K	1.486	3.55	0.25	1.67	Al2O3	6.70	1.60	9.1026
Si K	1.739	22.38	0.63	20.27	SiO2	47.88	9.72	55.4936
K K	3.312	1.10	0.10	0.36	K2O	1.32	0.34	3.5926
Ca K	3.690	1.90	0.15	1.21	CaO	2.66	0.58	6.5474
Fe K	6.398	2.42	0.24	1.10	FeO	3.12	0.53	6.9415
Total		100.00		100.00		100.00	14.02	

Figure 6-19: SEM and EDS analysis of 4253.5m.

6.4.4 E-G1 MINERALOGY INTERPRETATION

A single core was cut in the primary target of shallow marine sandstones, immediately beneath horizon 1At1 from 3155.6-3172.3m (100% recovery). The top of the core comprises of 9.4m of slightly porous, fine-grained sandstone (Appendix F4) with visible oil stain and significant fluorescent. The remainder of the core comprises interbedded claystone and siltstone. Figure 6-20B and Figure 6-20C show sandstone rich in glauconite and sub-rounded to angular monocrystalline sandstone quartz grains and calcite cement and few opaque materials. Porosity was not easily detected from the petrography image. Glauconite is easily identifiable in the petrographic image by its green colour. Compaction played a major role in destroying intergranular porosity. This sandstone has undergone compaction and pressure solution. Evidence of pressure solution can be seen in Figure 6-20B at the top left side whereby contacts between grains became sutured due to a more intense pressure solution. Another possible source of intergranular porosity loss may be as a result of silica dissolved during pressure solution which has precipitated as cement away from grain contacts leading to occlusion of porosity. Calcite cement can be observed in Figure 6-20D as brownish in colour towards the top just above the centre. Quartz, feldspar, and rock fragments were observed as detrital minerals and glauconite and chlorite as authigenic minerals. Microporosity was observed from the SEM images. Chlorite must have acted as a grain coating mineral and prevent quartz overgrowth after the dissolution of silica and therefore preserve a secondary microporosity. The EDS shows a large content of silica which is an indication of the presence of quartz and feldspar. The presence of quartz, glauconite, and chlorite is confirmed by XRD (Figure 6-21 and 6-22). Chlorite was also detected by EDS and SEM (Figure 6-23). The occlusion of intergranular porosity resulted in an increase of both bulk density and compressional velocity of the rock. E-G1 recorded a low average effective porosity of 9.2% as presented in chapter 4 and the velocity of 4056.9 m/s as presented in chapter 5. The low porosity, high velocity and high bulk density results are in line with the mineralogy/ diagenesis results which indicated the effect it had in reducing the intergranular porosity and therefore increasing velocity and bulk density.

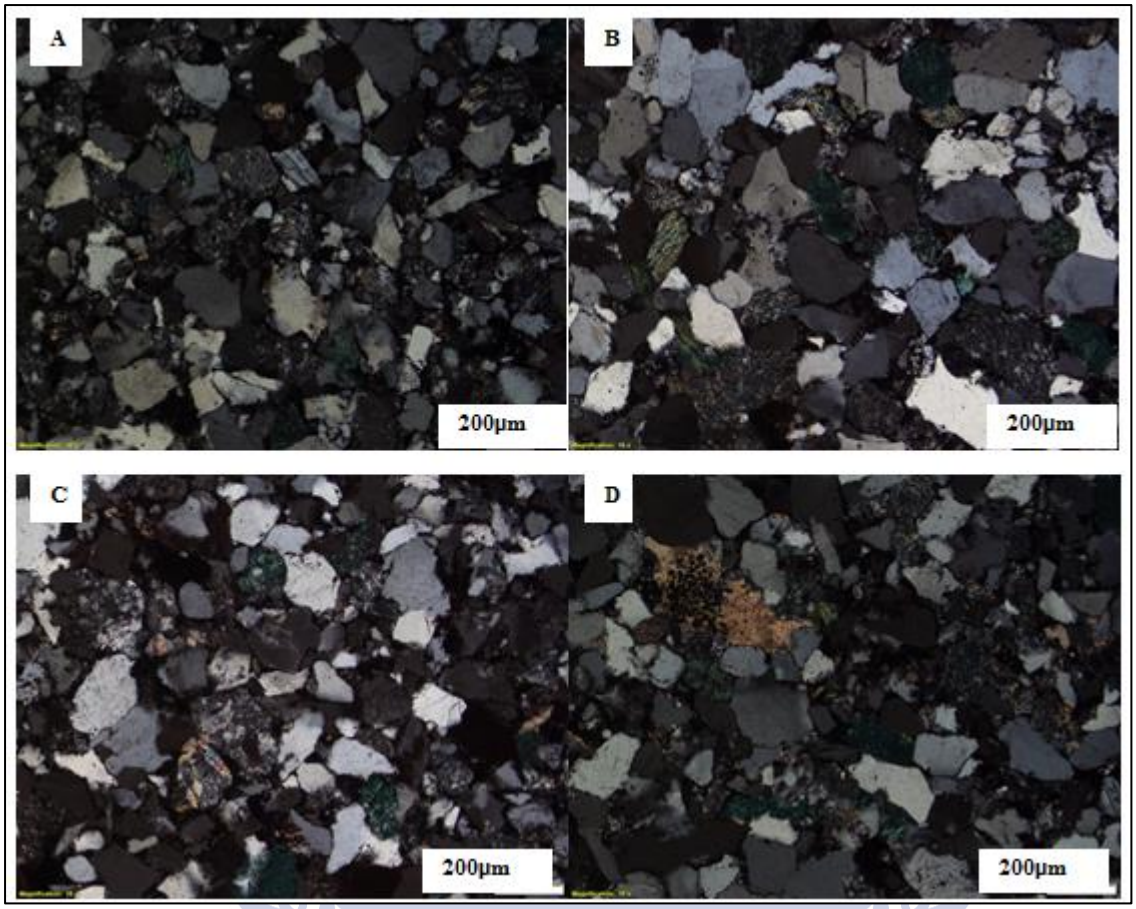

Figure 6-20: E-G1 petrography analysis of (A) 3615.4m, (B) 3161.5m, (C) 3166.5m and (D) 3616m with a magnification of 10X.

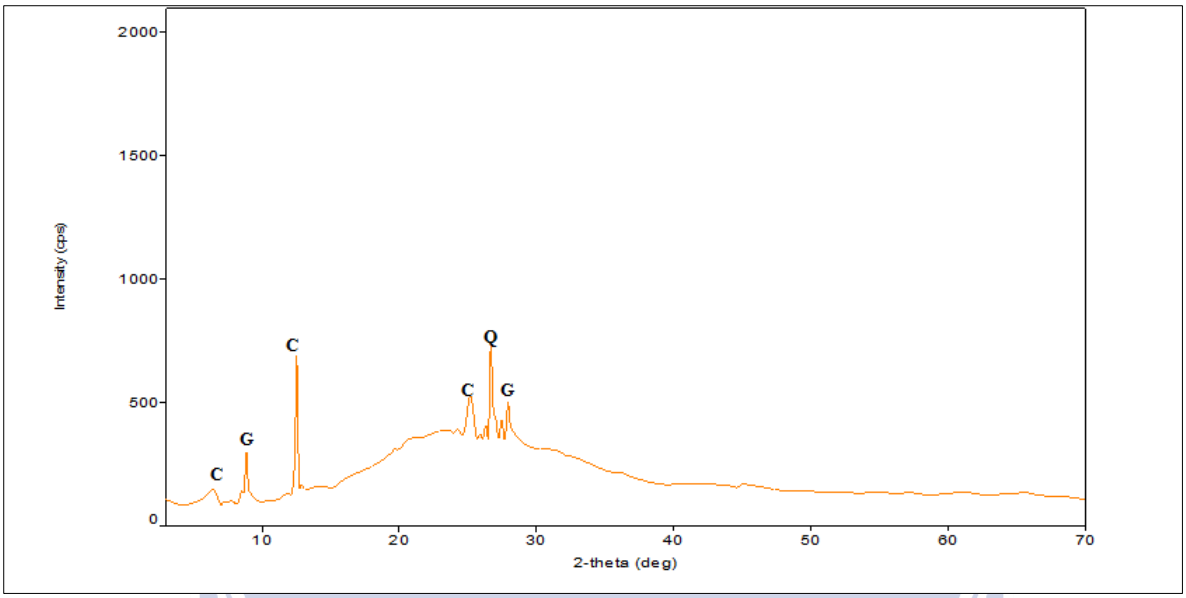

Figure 6-21: E-G1 XRD analysis of 3165.4m.

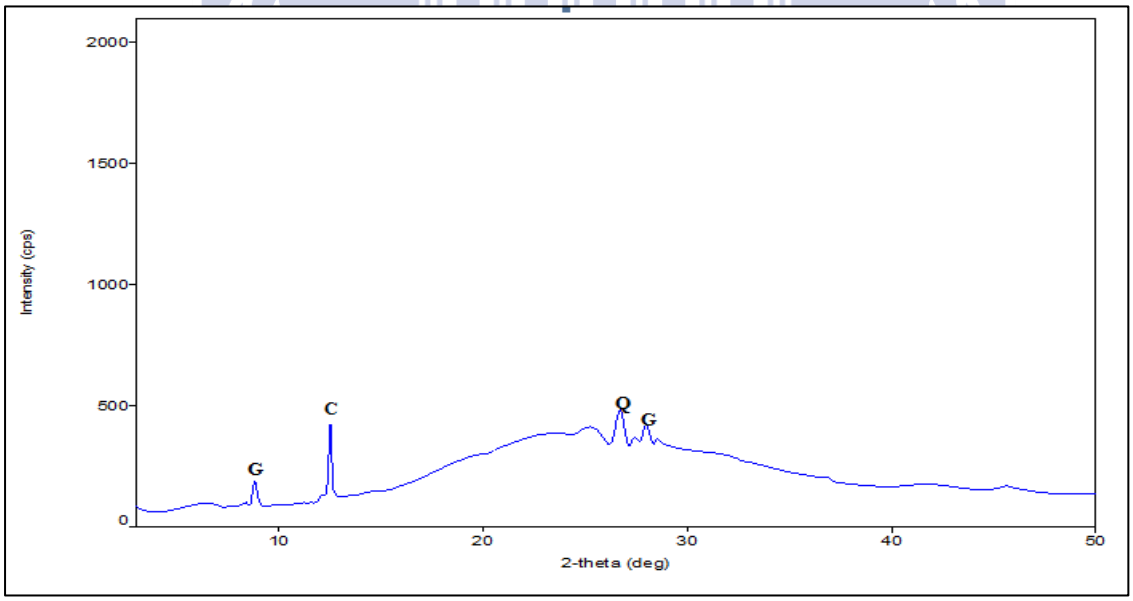

Figure 6-22: E-G1 XRD analysis of 3166.5m.

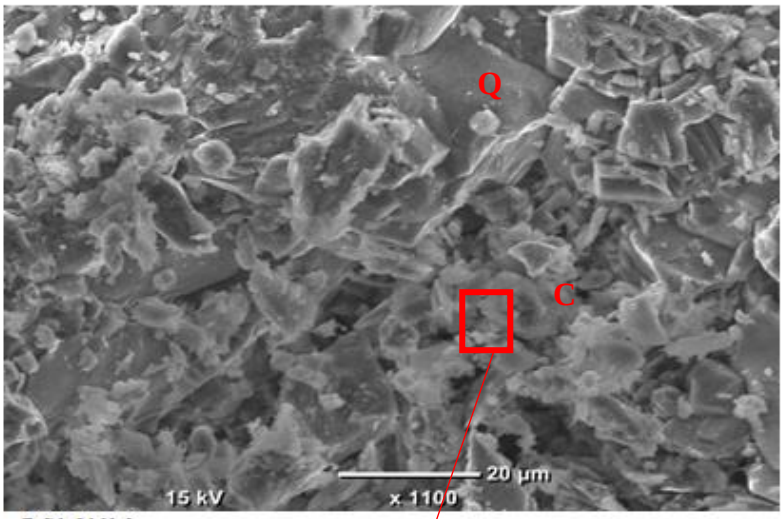

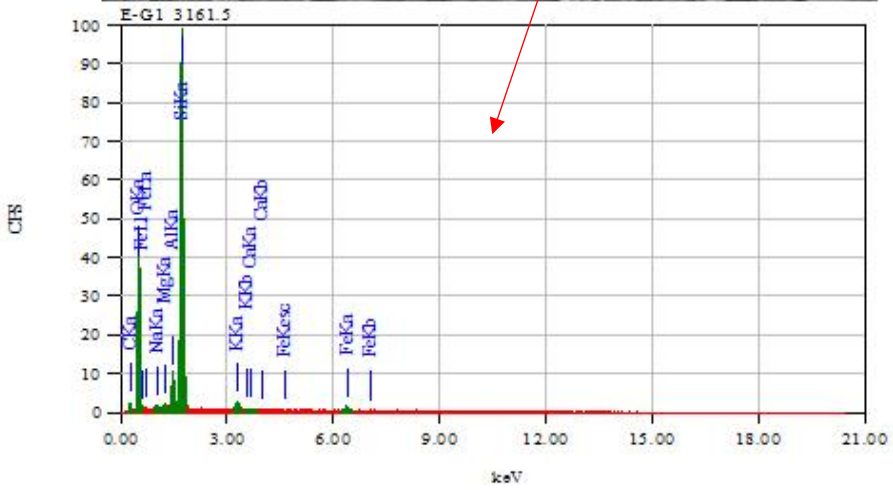

Element	(keV)	Mass%	Sigma	Mol%	Compound	Mass%	Cation	K
C K	0.277	18.58	0.46	54.32	C	18.58	0.00	4.8158
O		41.45						
Na K	1.041	0.60	0.09	0.46	Na2O	0.81	0.24	1.2032
Mg K	1.253	0.35	0.08	0.51	MgO	0.58	0.13	0.5727
Al K	1.486	3.42	0.19	2.23	Al2O3	6.47	1.17	8.3749
Si K	1.739	32.67	0.59	40.85	SiO2	69.89	10.78	76.9196
K K	3.312	1.19	0.08	0.53	K2O	1.43	0.28	3.4668
Ca K	3.690	0.02	0.06	0.01	CaO	0.02	0.00	0.0494
Fe K	6.398	1.72	0.16	1.08	FeO	2.21	0.29	4.5976
Total		100.00		100.00		100.00	12.90	

Figure 6-23: E-G1 SEM and EDS analysis of Chlorite at depth 3161.5m.

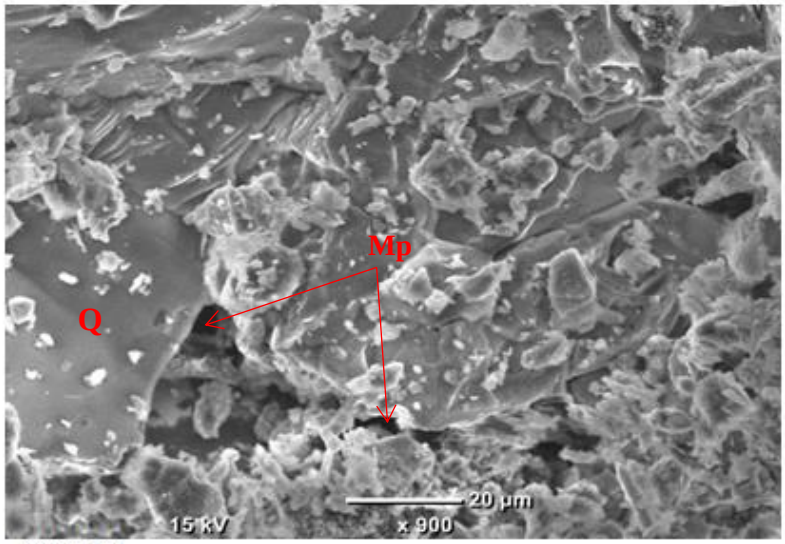

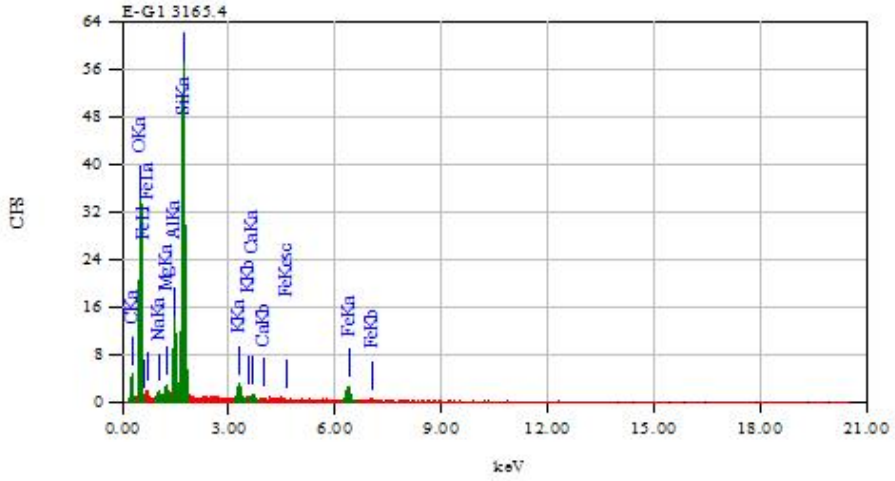

Element	(keV)	Mass%	Sigma	Mol%	Compound	Mass%	Cation	K
C K	0.277	31.98	0.52	71.87	C	31.98	0.00	11.9335
O		32.05						
Na K	1.041	0.94	0.11	0.55	Na2O	1.26	0.49	1.8916
Mg K	1.253	0.85	0.11	0.95	MgO	1.41	0.42	1.4125
Al K	1.486	5.45	0.24	2.73	Al2O3	10.30	2.42	13.4458
Si K	1.739	21.31	0.51	20.48	SiO2	45.60	9.09	49.3930
K K	3.312	1.77	0.09	0.61	K2O	2.13	0.54	5.6658
Ca K	3.690	0.49	0.08	0.33	CaO	0.69	0.15	1.6505
Fe K	6.398	5.16	0.26	2.49	FeO	6.63	1.11	14.6075
Total		100.00		100.00		100.00	14.21	

Figure 6-24: E-G1 SEM and EDS analysis of depth 3165.4m. Q= Quartz, Mp= Microporosity.

6.4.5 E-W1 MINERALOGY INTERPRETATION

The sandstone reservoir of E-W1 is argillaceous sandstone with poor quality, tight and impermeable (Appendix F5). Quartz overgrowth and calcite cementation played a major role in destroying porosity. The lithology becomes clay with depth (Figure 6-25D). Figure 6-25B show a pebble size fragment composed almost entirely of microcline. The sediments surrounding a microcline feldspar contains monocrystalline quartz and brownish clasts and fine-grained materials which are probably shale/claystone. The boundaries between the polycrystalline quartz grains are sutured. This is a characteristic of quartz from a metamorphic source. Figure 6-25C shows tight argillaceous sandstone with opaque materials and accessory of glauconite. The presence of calcite cement can also be observed in Figure 6-25A.

A minor amount of authigenic chlorite is present as shown by XRD (Figure 6-26). Quartz and feldspar are detrital minerals present with glauconite and muscovite mica as accessory minerals. No evidence of extensive compaction due to early calcite cementation. The tight and impermeable state of the rock resulted in a very poor porosity with high velocity and bulk density. The EDX spectrum (Figure 6-28) yields major elements for Feldspar, quartz, and chlorite: Si, Al, Mg, K with minor Ca and Fe. The low average effective porosity of 9.5% and a high velocity of 4395m/s and bulk density 2.59g/cm^3 were recorded. The low reading of 9.5% porosity in this interval was expected because of the presence of calcite cement and sutured grains which restricted the development of pore spaces. This, in turn, resulted in higher velocity and bulk density readings as presented in chapter 4 and 5 respectively.

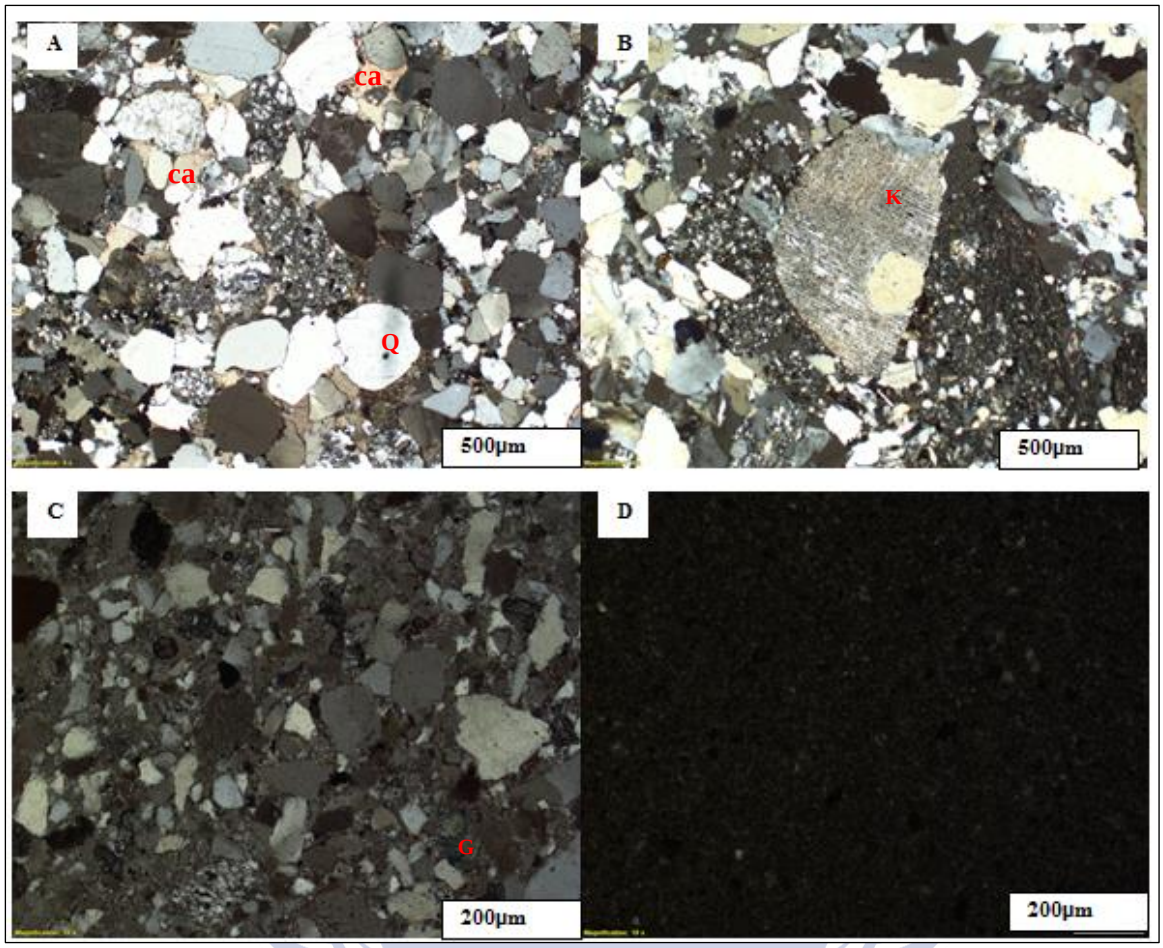

Figure 6-25: E-W1 petrography analysis of (A) 3174m (4X), (B) 3181.5m (4X), (C) 3186.5m (10X) and (D) 3189m (10X) with 4X and 10X magnifications. Ca= calcite cement

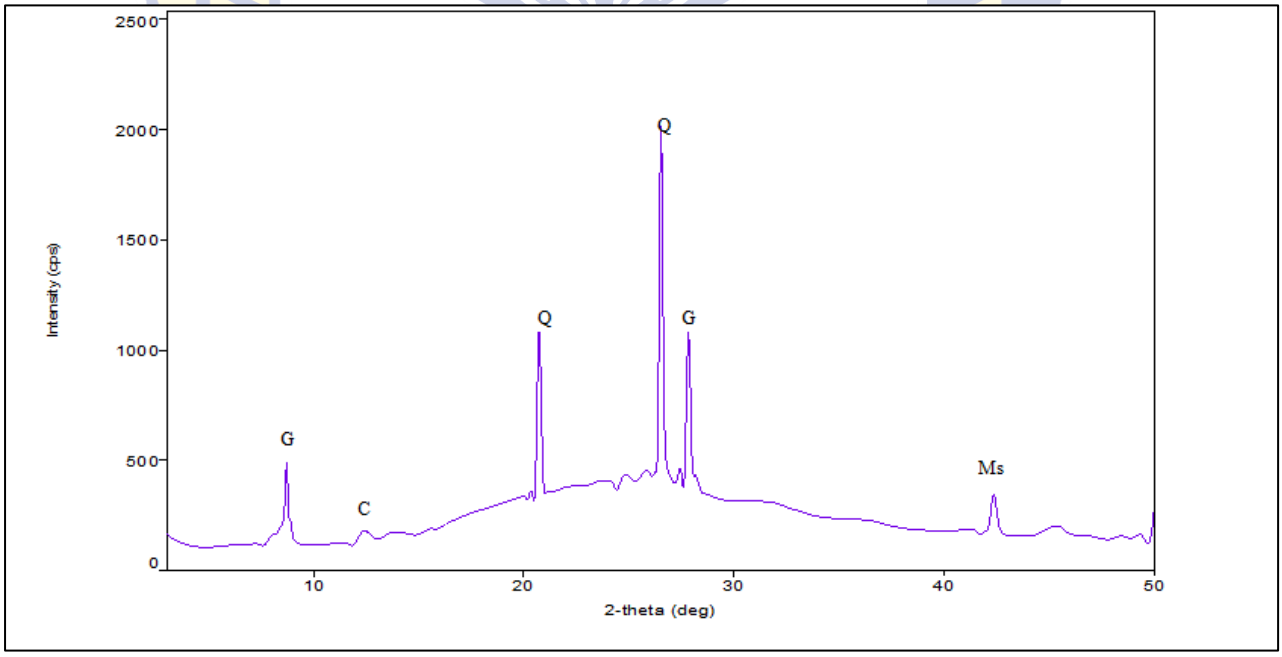

Figure 6-26: E-W1 XRD analysis of 3186.65m.

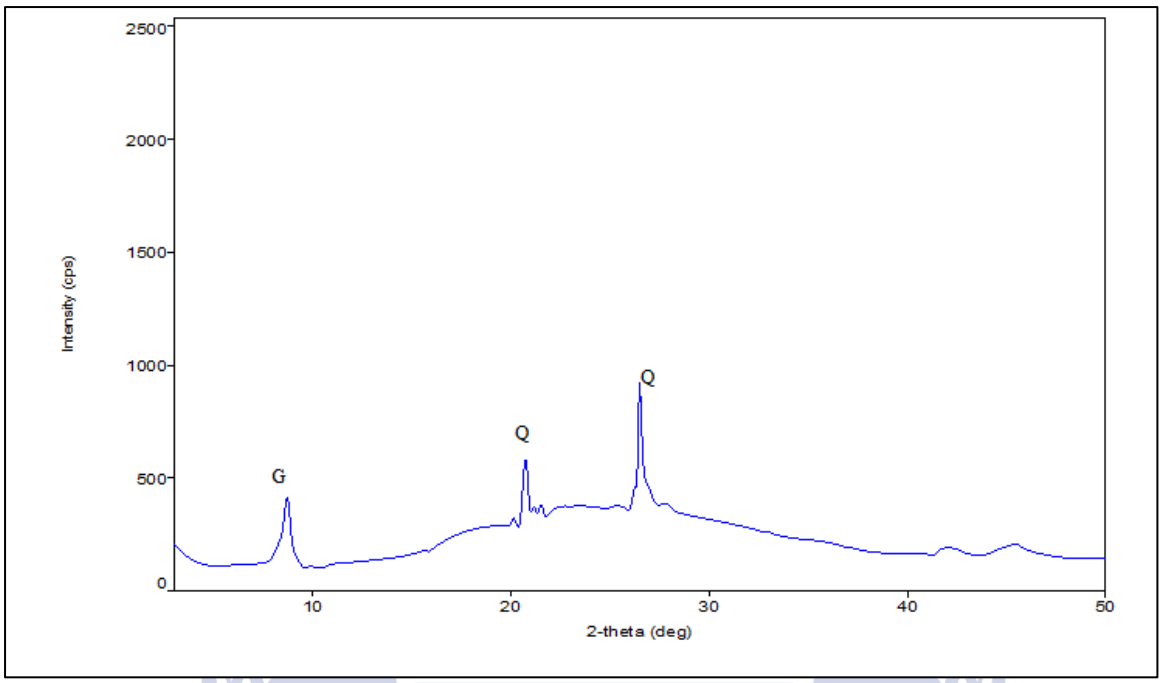

Figure 6-27: E-W1 XRD analysis of 3174m.

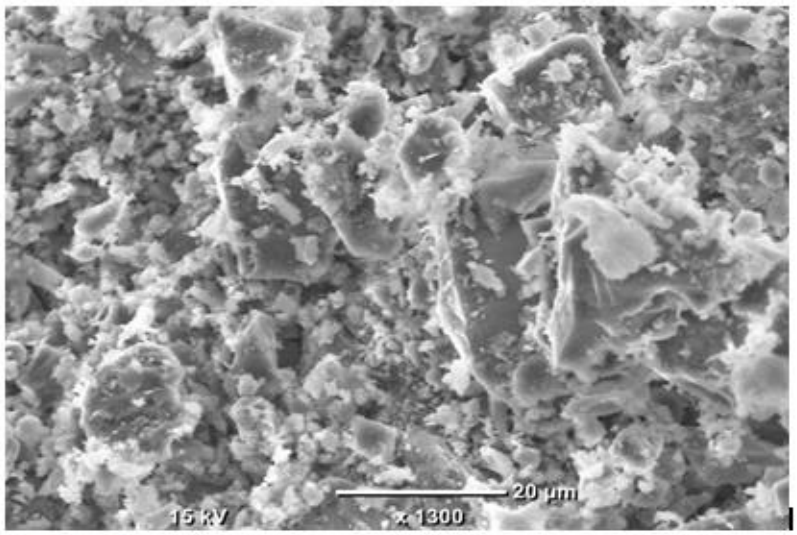

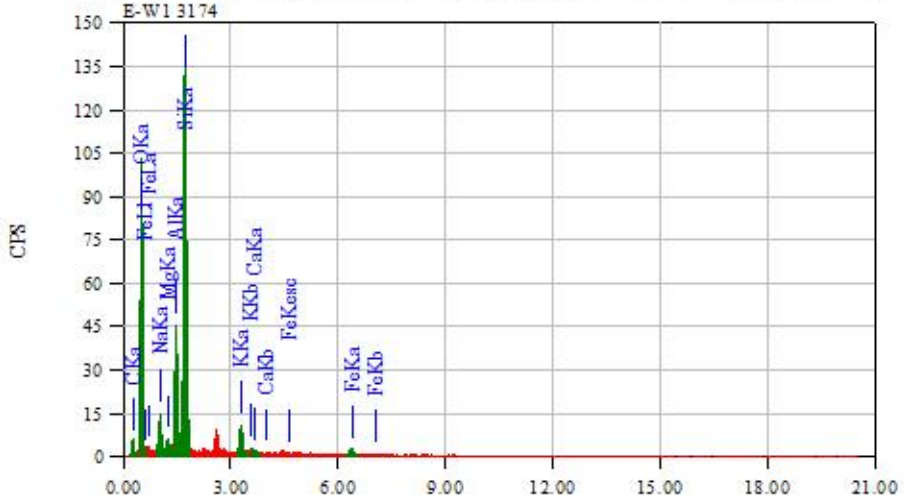

Element	(keV)	Mass%	Sigma	Mol%	Compound	Mass%	Cation	K
C K	0.277	18.15	0.30	54.97	C	18.15	0.00	5.1442
O		38.98						
Na K	1.041	3.99	0.13	3.16	Na2O	5.38	1.71	8.2331
Mg K	1.253	0.73	0.07	1.10	MgO	1.22	0.30	1.1460
Al K	1.486	8.20	0.20	5.53	Al2O3	15.49	2.99	19.1150
Si K	1.739	25.13	0.37	32.55	SiO2	53.76	8.81	52.5757
K K	3.312	2.73	0.08	1.27	K2O	3.29	0.69	8.0883
Ca K	3.690	0.22	0.05	0.20	CaO	0.31	0.05	0.6938
Fe K	6.398	1.86	0.11	1.21	FeO	2.40	0.33	5.0039
Total		100.00		100.00		100.00	14.89	

Figure 6-28: E-W1 SEM and EDS analysis of 3174m.

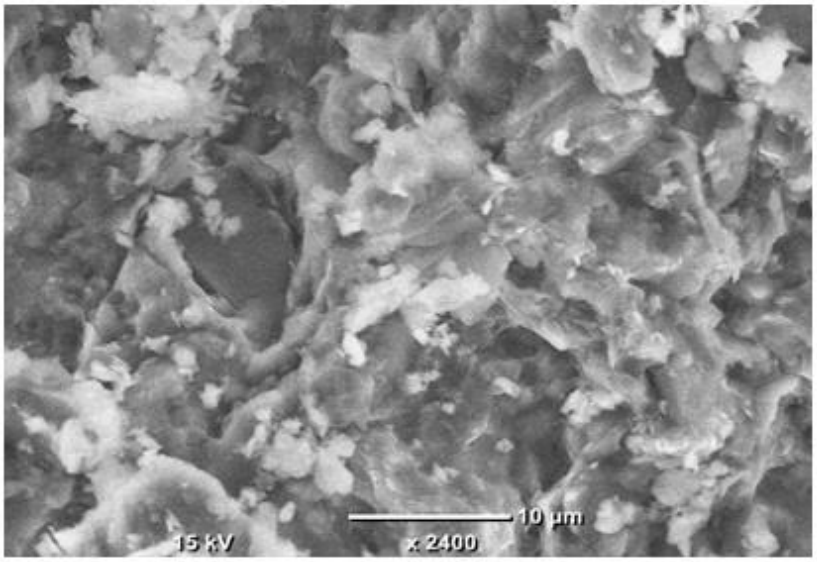

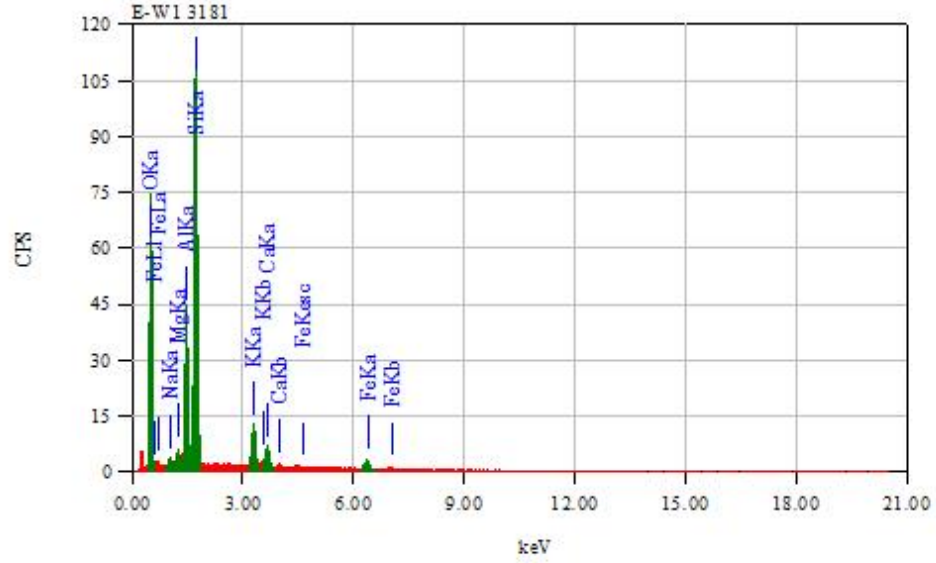

Element	(keV)	Mass%	Sigma	Mol%	Compound	Mass%	Cation	K
O		47.00						
Na K	1.041	0.92	0.10	1.34	Na2O	1.24	0.33	1.4709
Mg K	1.253	1.08	0.10	2.97	MgO	1.79	0.36	1.4158
Al K	1.486	10.84	0.27	13.42	Al2O3	20.47	3.28	21.1191
Si K	1.739	29.21	0.49	69.51	SiO2	62.48	8.50	49.3939
K K	3.312	4.67	0.12	3.99	K2O	5.63	0.98	11.5002
Ca K	3.690	2.62	0.12	4.36	CaO	3.66	0.53	6.7187
Fe K	6.398	3.68	0.18	4.40	FeO	4.73	0.54	8.3815
Total		100.00		100.00		100.00	14.51	

Figure 6-29: E-W1 SEM and EDS analysis of 3181m.

6.4.6 F-A10 MINERALOGY INTERPRETATION

The cores comprise mature uniform sandstones which, is fine to medium grained, occasionally coarse, very well sorted, very slightly carbonaceous, slightly siliceous in places and glauconitic (Appendix F3). Other accessories include minor feldspar, shale and chert clasts and rare shell fragments. Figure 6-30 shows highly porous glauconite sandstone with monocrystalline quartz grains. The remainder of the grains is the feldspar. The pore spaces are indicated by the dark grey colour (Figure 6-30A, B and D) caused by the mounting medium used during the thin section preparations. XRD (Figure 6-31 and 6-32) analysis identified glauconite, chlorite, illite, and quartz as the major rock-forming mineral with an accessory of muscovite. The identification of chlorite mineral and glauconite was confirmed by the EDX analysis which yields a typical EDX spectrum with major elements Si, Al, Mg, Na with minor Fe, K and Ca. The boundaries of quartz grains are clearly defined with no indications of overgrowth. Pore-filling chlorotized biotite can be identified in Figure 6-33 through SEM/EDX analysis of the morphology and chemical composition. This pore filling mineral did not significantly affect the porosity of the rock since it only occurred in a few places. This is supported by a good average effective porosity of 15.8% obtained from wireline logs in this interval as presented in chapter 4. The SEM image in Figure 6-34 shows the ragged-edged, authigenic chlorite platelets stacked face-to-face in a rare beehive-like structure. Individual crystals are circular with lobate or scalloped edges. F-10 recorded an average porosity of 15.8% and velocity of 4587m/s with a bulk density of 2.455g/cm^3.

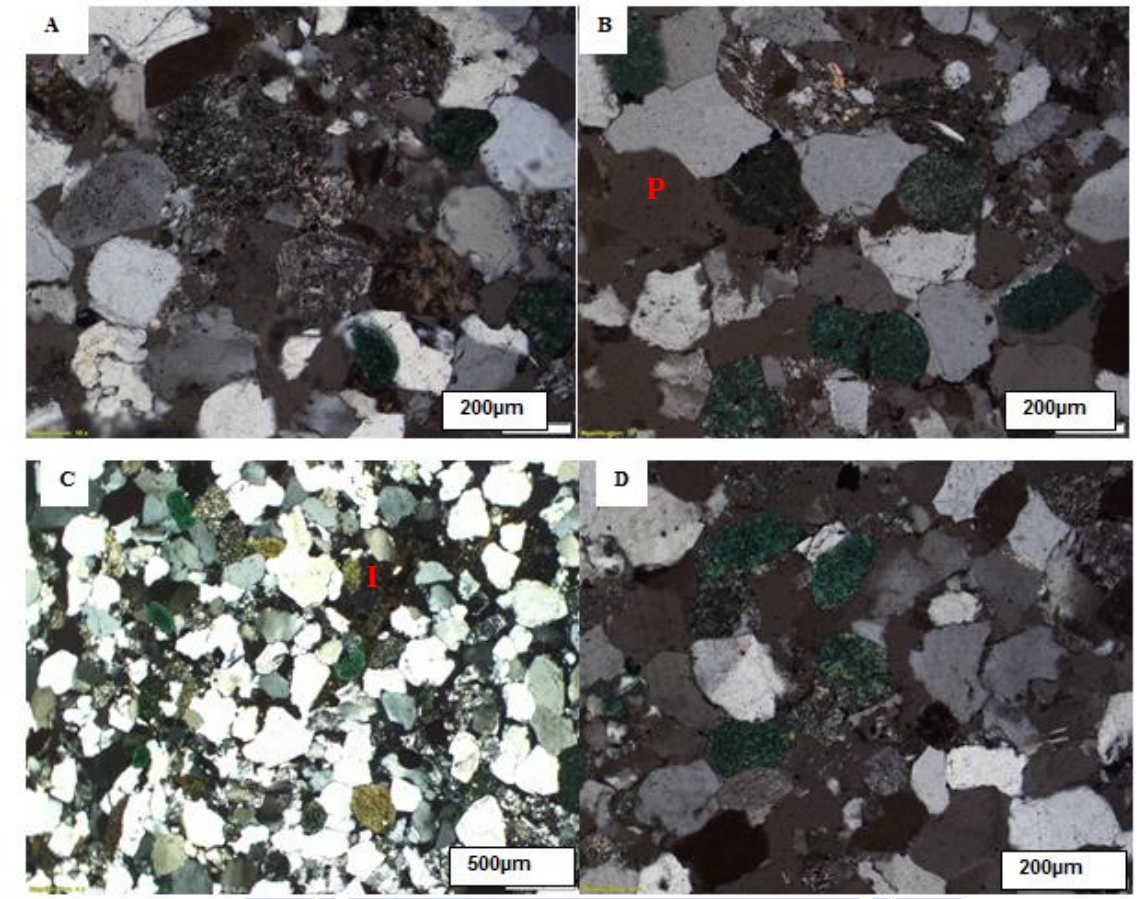

Figure 6-30: Petrographical analysis of (A) 2719.5m (10X), (B) 2730.5m (10X), (C) 2743m (4X), and (D) 2755.5m (10 X) with 4X and 10 X magnifications.

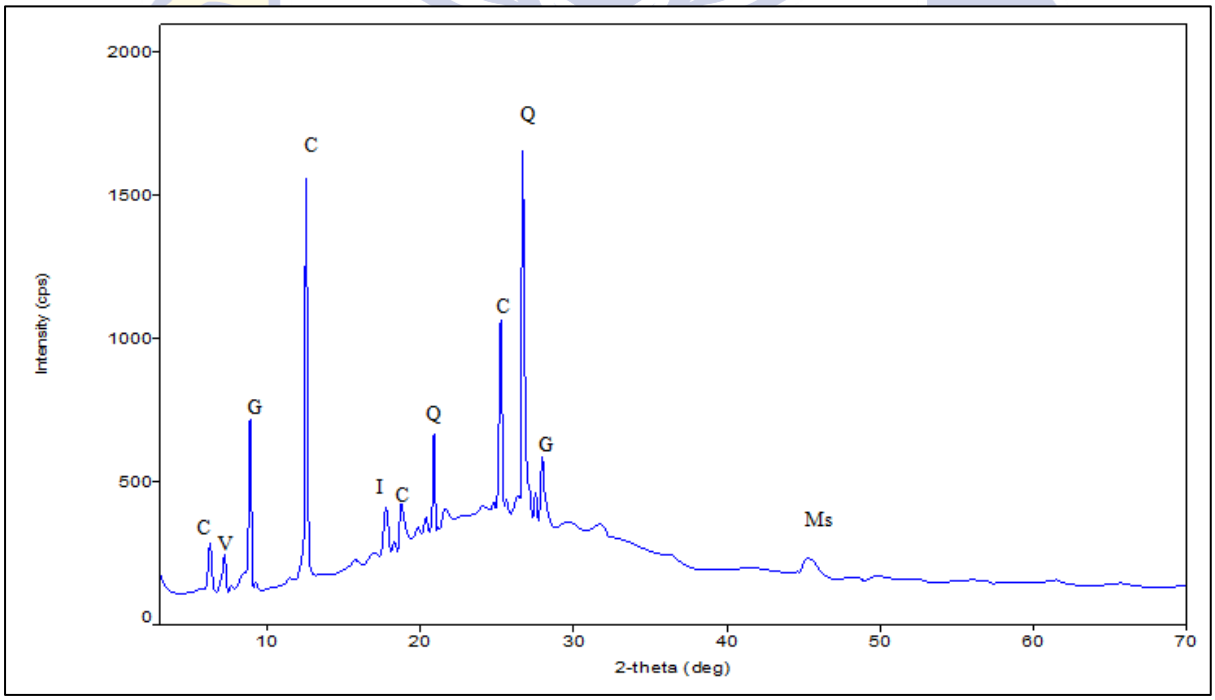

Figure 6-31: F-A10 XRD analysis at 2730.5m. C=Chlorite, V=Vermiculite, G= Glauconite, I= Illite, Q= Quartz and Ms= Muscovite.

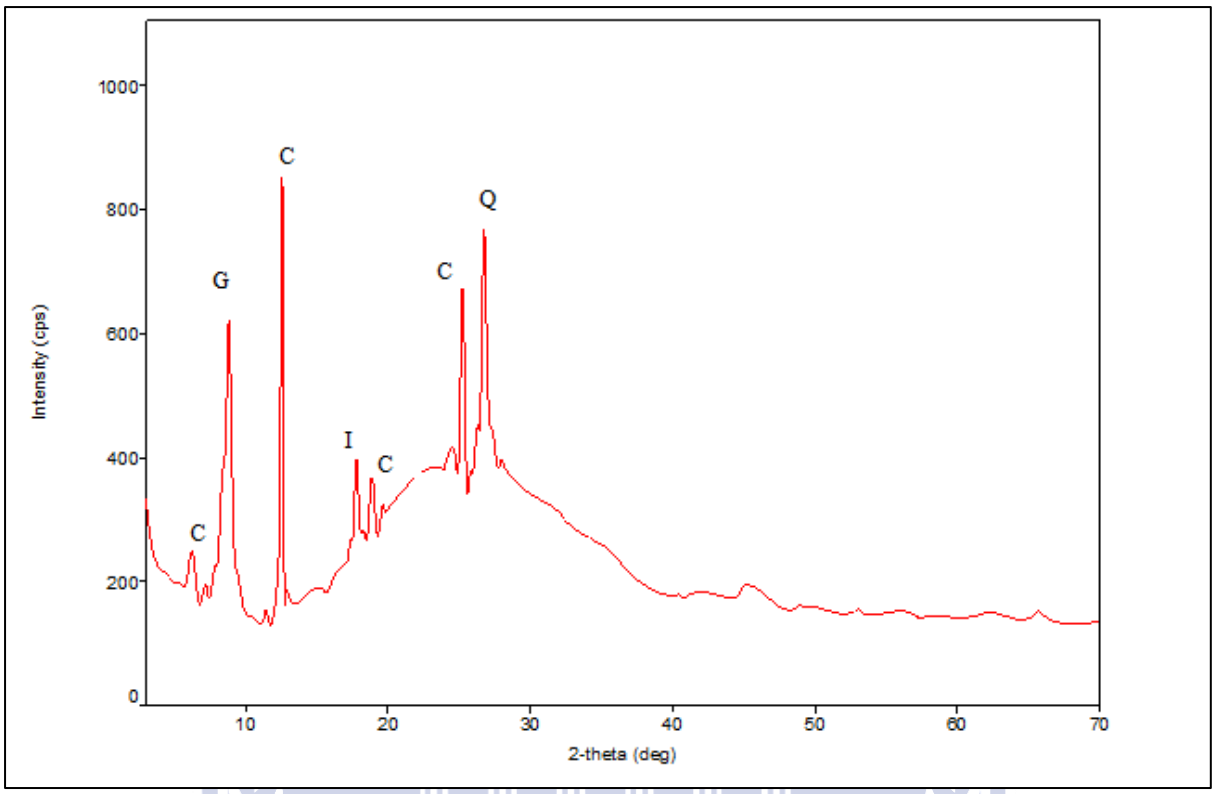

Figure 6-32: F-A10 XRD analysis at 2743m. C=Chlorite, G= Glauconite, I= Illite, Q= Quartz.

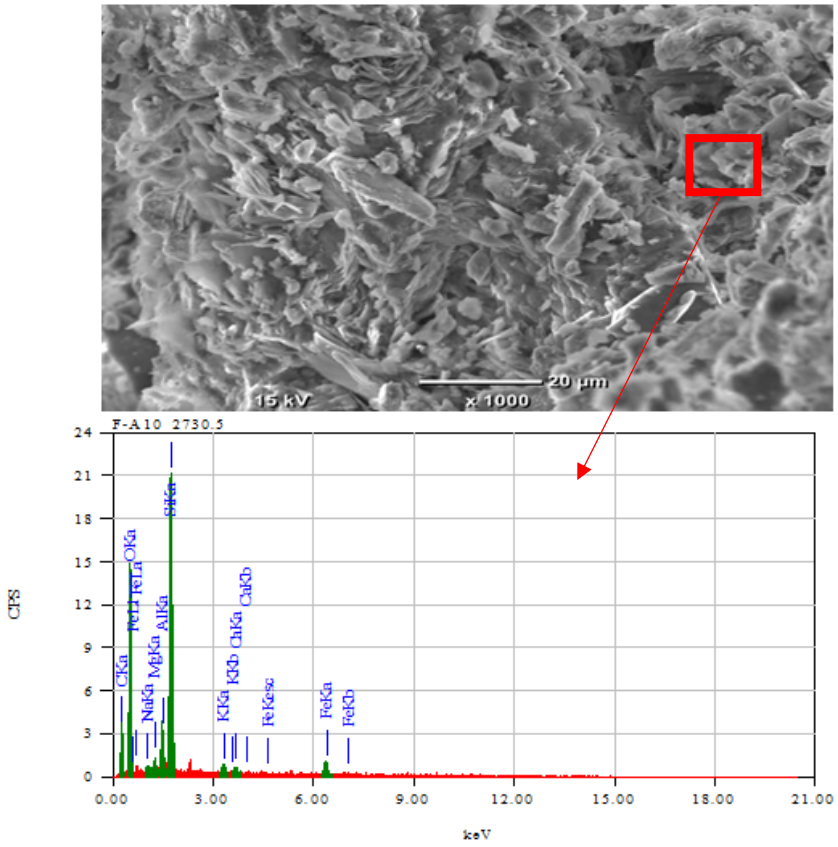

Element	(keV)	Mass%	Sigma	Mol%	Compound	Mass%	Cation	K
C K	0.277	45.42	0.87	81.54	C	45.42	0.00	22.5134
O		25.70						
Na K	1.041	0.60	0.16	0.28	Na2O	0.80	0.39	1.2850
Mg K	1.253	0.68	0.15	0.61	MgO	1.13	0.42	1.2150
Al K	1.486	2.96	0.29	1.18	Al2O3	5.60	1.64	7.8353
Si K	1.739	17.99	0.71	13.81	SiO2	38.49	9.57	46.5207
K K	3.312	0.89	0.11	0.24	K2O	1.07	0.34	3.0729
Ca K	3.690	0.74	0.13	0.40	CaO	1.03	0.27	2.6752
Fe K	6.398	5.01	0.40	1.94	FeO	6.45	1.34	14.8826
Total		100.00		100.00		100.00	13.97	

Figure 6-33: F-A10 SEM and EDS for 2730.5m.

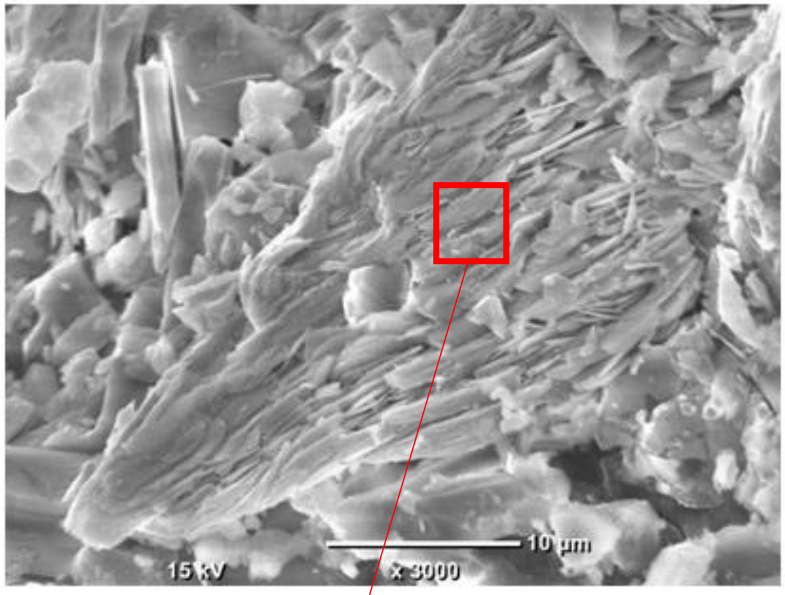

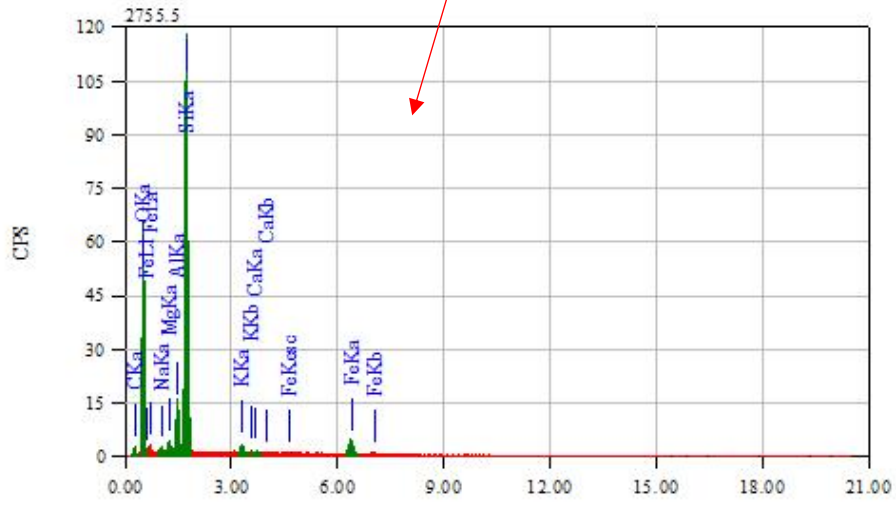

Element	(keV)	Mass%	Sigma	Mol%	Compound	Mass%	Cation	K
C K	0.277	14.04	0.34	46.26	C	14.04	0.00	3.5222
O		41.63						
Na K	1.041	0.55	0.09	0.47	Na2O	0.74	0.22	0.9523
Mg K	1.253	0.99	0.09	1.62	MgO	1.65	0.38	1.4339
Al K	1.486	4.23	0.18	3.10	Al2O3	7.98	1.44	9.1291
Si K	1.739	30.55	0.50	43.06	SiO2	65.37	10.03	64.0339
K K	3.312	1.10	0.07	0.56	K2O	1.33	0.26	3.0831
Ca K	3.690	0.16	0.06	0.16	CaO	0.23	0.04	0.4864
Fe K	6.398	6.73	0.25	4.77	FeO	8.66	1.11	17.3592
Total		100.00		100.00		100.00	13.49	

Figure 6-34: F-A10 SEM and EDS analysis at 2755.5m showing ragged-edged, authigenic chlorite platelets stacked face-to-face in a rare beehive-like structure.

6.4.7 F-A13 MINERALOGY INTERPRETATION

Seven cores were cut back to back between 2613m-2741m. The interval from 2613m-2720m is glauconitic sandstone (Appendix F2) which becomes fossiliferous with depth. Claystone predominates below 2720m. The reservoir is of good quality with an average porosity of 16% from wireline logs as recorded in chapter 4. The porosity tends to decrease with increasing depth as the sandstone becomes more calcareous and fossiliferous. The bottom 10m is very calcareous with an average porosity of 9%. Figure 6-35 shows highly porous sandstone with rounded monocrystalline quartz grains. The remainder of the rock is glauconite (green) and feldspar. The speckled areas which appear black (6-35A and 6-35D) are porous spaces filled the mounting medium used during thin section preparation. Clusters of elongate to disc-like, authigenic chlorite crystals partly filling a depression within an altered detrital grain K can be observed. Individual crystals are rounded in edges. XRD (Figure 6-36 and 6.37) analysis identified glauconite, chlorite, illite, quartz, and accessory of muscovite as the minerals present The EDX (Figure 6-38) spectrum contains elements typical of chlorite: Si, Al, Mg, Fe and Ca. F-A13 recorded the highest average core porosity of 23.1% and lowest average velocity of 4442m/s with a bulk density of 2.427 g/cm3.

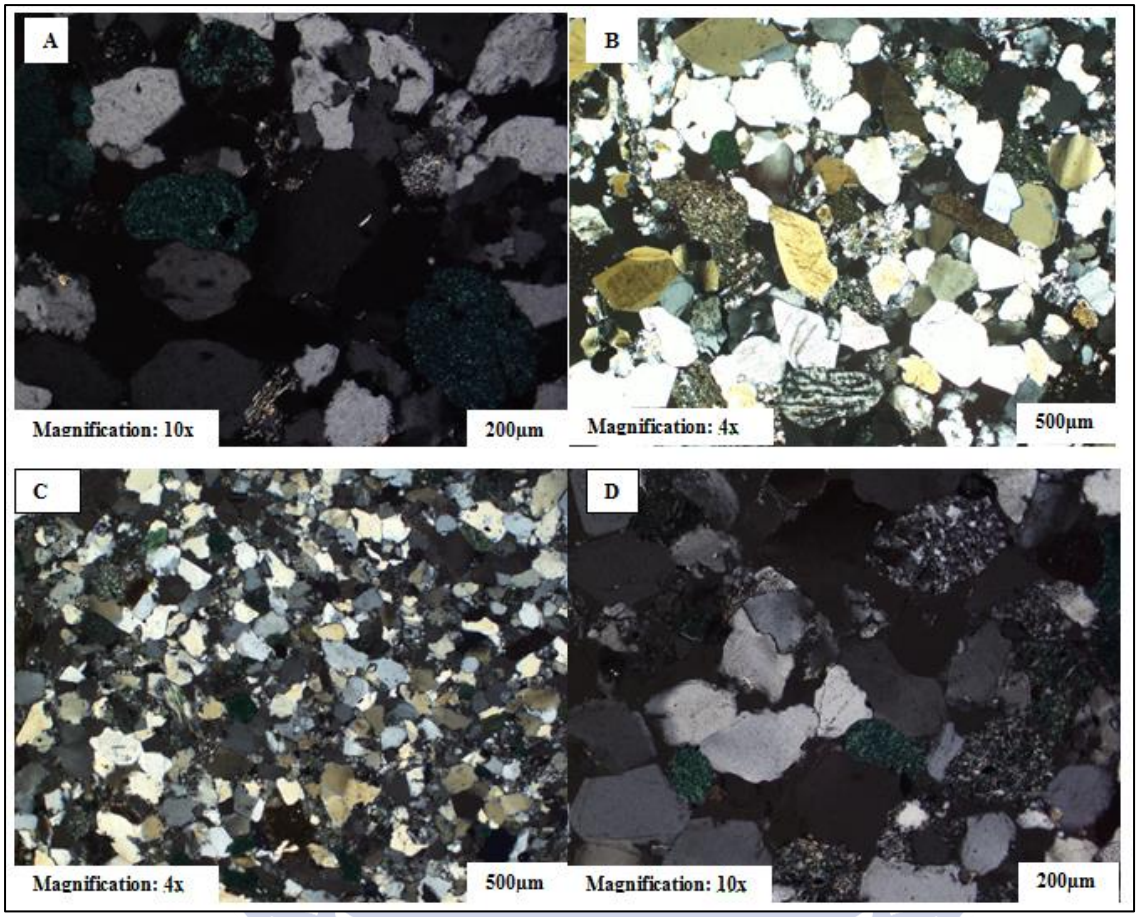

Figure 6-35: F-A13 petrographical analysis of (A) 2615m, (B) 2624.5m, (C) 2646.5m and (D) 2656m.

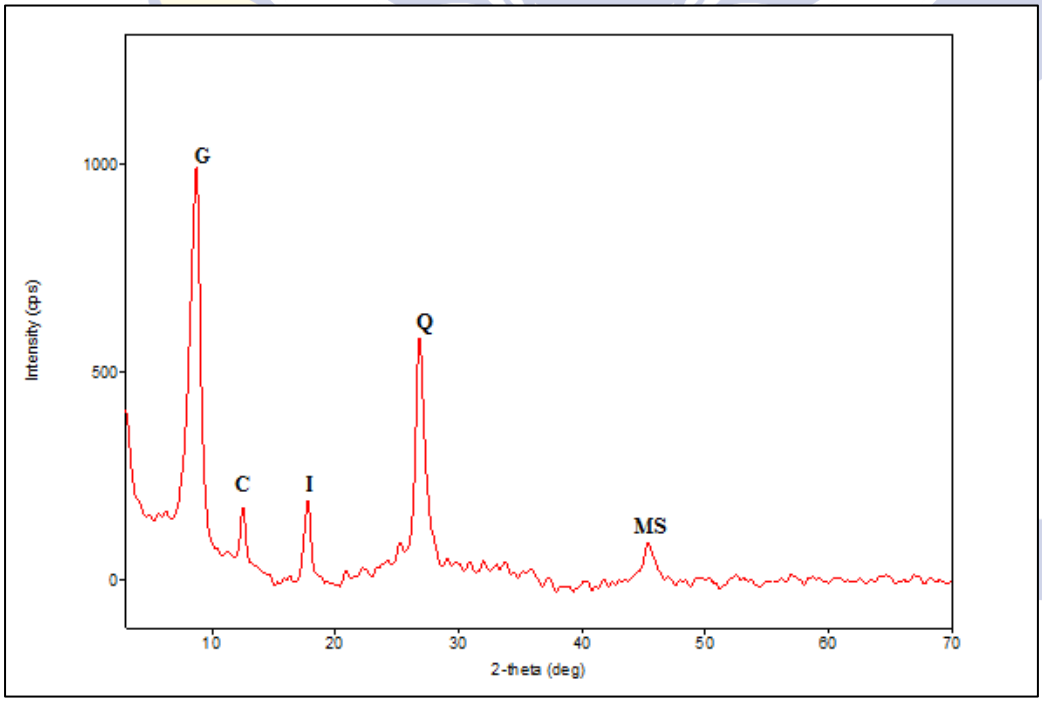

Figure 6-36: F-A13 XRD analysis of 2646.5m. G=Glauconite, C=Chlorite, I=illite, Q=Quartz and MS= Muscovite.

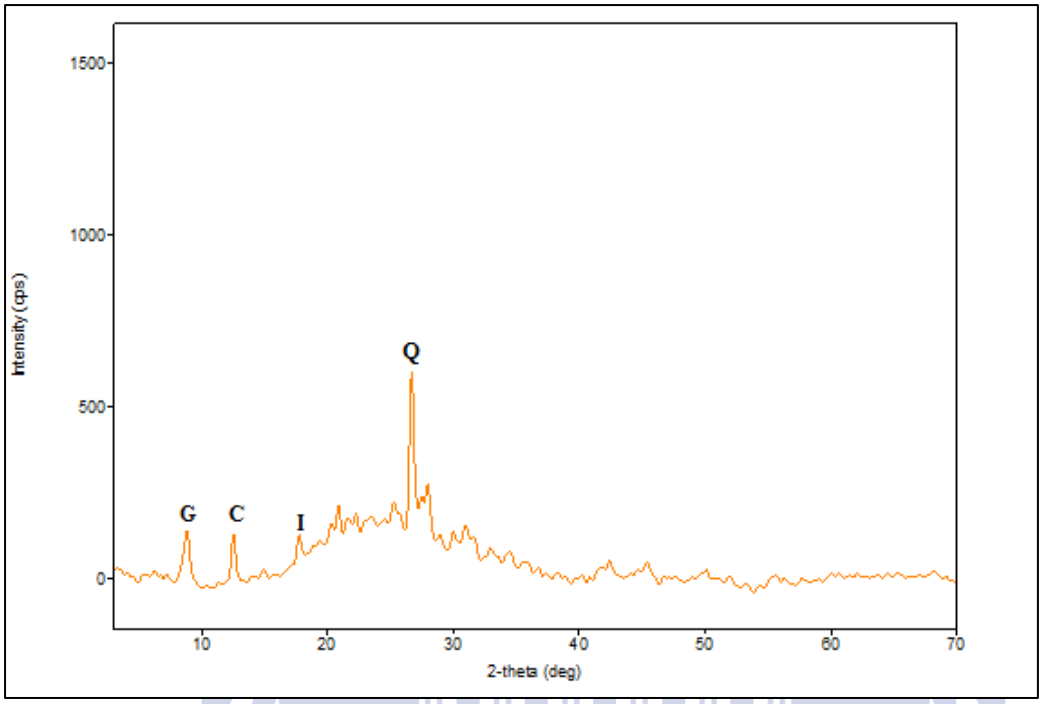

Figure 6-37: F-A13 XRD analysis of 2656m. G=Glauconite, C=Chlorite, I=illite, Q=Quartz

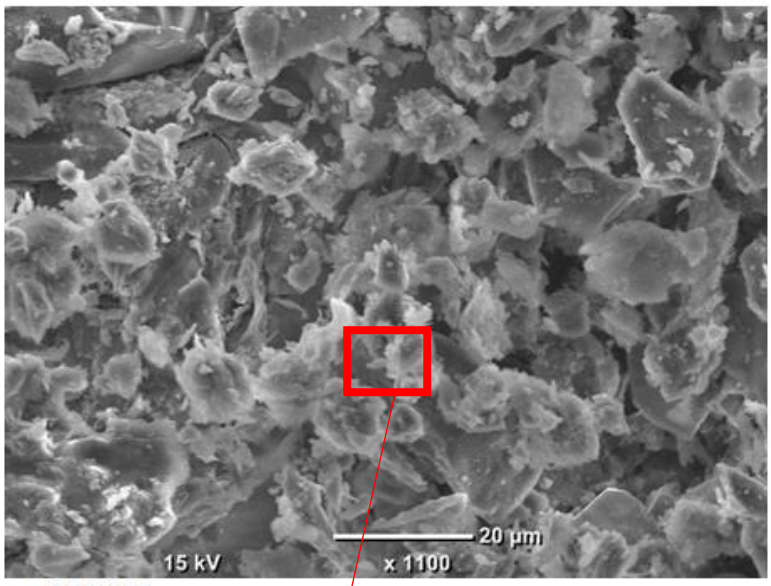

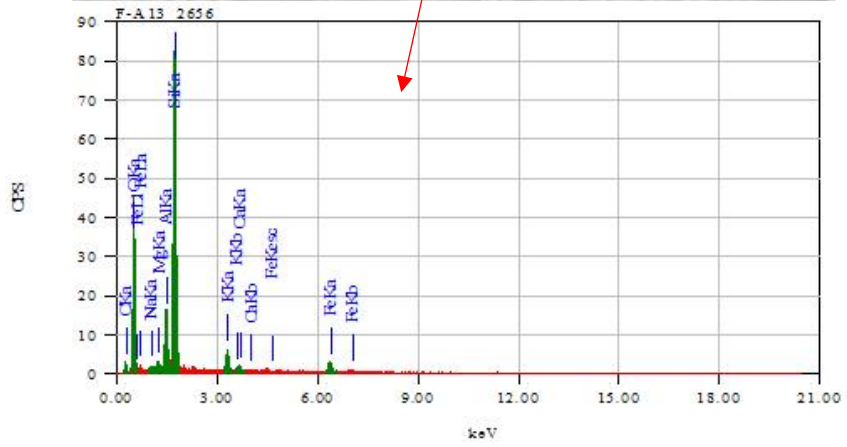

Element	(keV)	Mass%	Sigma	Mol%	Compound	Mass%	Cation	K
C K	0.277	18.89	0.42	55.73	C	18.89	0.00	5.2972
O		38.48						
Na K	1.041	0.70	0.10	0.54	Na2O	0.95	0.31	1.2541
Mg K	1.253	0.65	0.10	0.95	MgO	1.08	0.27	0.9569
Al K	1.486	5.48	0.23	3.60	Al2O3	10.35	2.03	12.1363
Si K	1.739	26.76	0.53	33.77	SiO2	57.26	9.51	55.9557
K K	3.312	2.89	0.11	1.31	K2O	3.48	0.74	8.2300
Ca K	3.690	0.78	0.09	0.69	CaO	1.09	0.19	2.3233
Fe K	6.398	5.37	0.25	3.41	FeO	6.91	0.96	13.8465
Total		100.00		100.00		100.00	14.00	

Figure 6-38: F-A13 SEM/EDS analysis of 2656m.

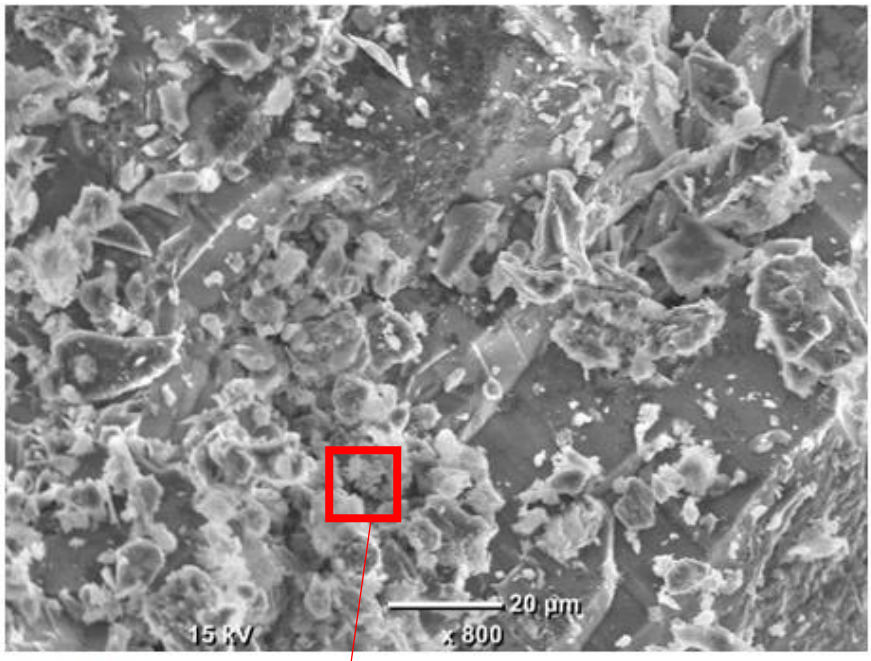

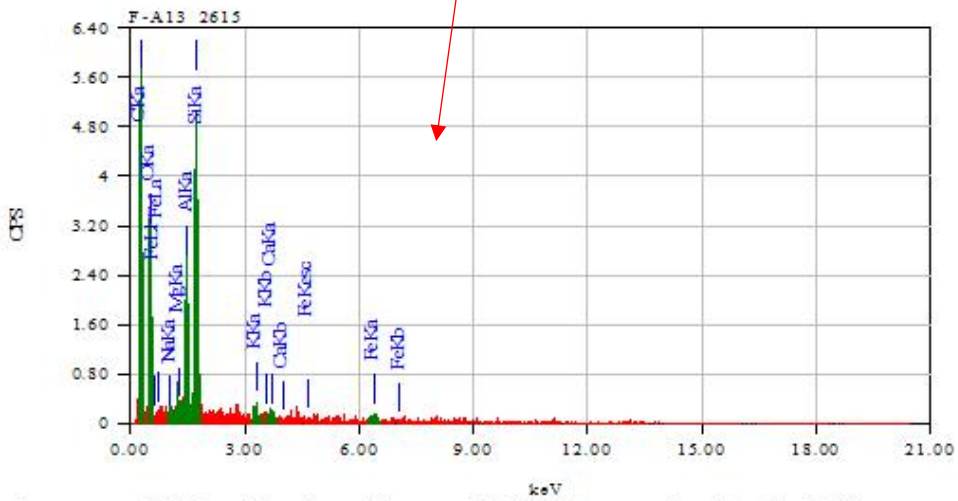

Element	(keV)	Mass%	Sigma	Mol%	Compound	Mass%	Cation	K
C K	0.277	73.45	1.05	94.01	C	73.45	0.00	64.8761
O		12.93						
Na K	1.041	0.30	0.14	0.10	Na2O	0.41	0.39	0.6971
Mg K	1.253	0.55	0.15	0.35	MgO	0.92	0.68	1.0368
Al K	1.486	4.27	0.41	1.22	Al2O3	8.07	4.70	11.5669
Si K	1.739	7.30	0.59	3.99	SiO2	15.61	7.72	18.1457
K K	3.312	0.38	0.10	0.07	K2O	0.46	0.29	1.2662
Ca K	3.690	0.29	0.12	0.11	CaO	0.41	0.22	1.0159
Fe K	6.398	0.52	0.19	0.14	FeO	0.67	0.28	1.3954
Total		100.00		100.00		100.00	14.27	

Figure 6-39: F-A13 SEM/EDS analysis of 2615m.

6.4.8 E-M4 MINERALOGY INTERPRETATION

Seven cores were cut back to back between 2562m- 2647m in the sandstone interval below 1AT1 unconformity. Two intervals of shallow marine are present at 2559.5m to 2610.3m and 2749m to 2821m. The remainder of the core section is made up of fluvial sediments (Appendix F1). Four thin sections were analyzed for this well. Two representative samples at 2567m and 2573m were selected for detailed interpretation and discussion. Interpretation and analyses of other samples are presented in appendix D. Both 2562m and 2647m reveal total rock constituents dominated by detrital quartz and feldspars with minor grains of glauconite. The top left of the thin sections (Figure 6-40A and B) shows a very fine, tight grain section with no evidence of porosity. Dominating grains are large, angular and moderate to well sorted (Figure 6-40C). A clear grain boundary is illustrated under plane-polarized light (Figure 6-40D). Compaction of grains (Figure 6-40A) played a major role in porosity reduction, however, Figure 6-40D shows connected pore spaces between the grains when viewed under Plane Polarised Light (PPL). XRD and SEM/EDS were not available for this well. The rock is basically a moderate to coarse-grained constituted by monocrystalline quartz grains with feldspar and glauconite accessory, slightly porous to porous glauconitic sandstone.

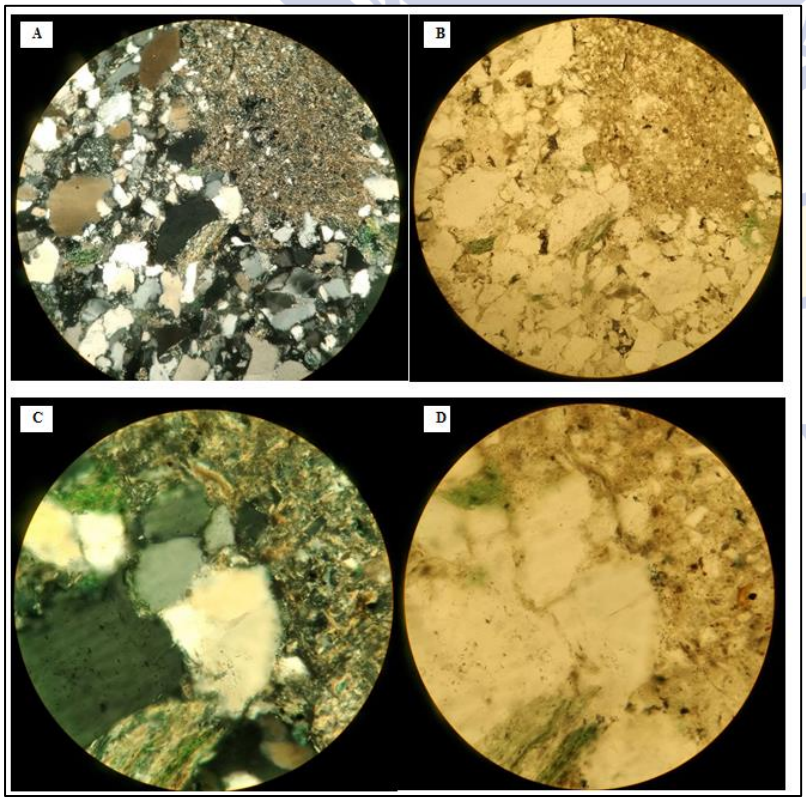

Figure 6-40: E-M4 petrophysical analysis of 2567m (A, B) and 2573m (C, D).

6.5 CONCLUSION

In this chapter, thin section, XRD and SEM/EDS analyses from eight wells were investigated for the effect of mineralogy on porosity and acoustic properties. The effect of mineralogy on the remaining two wells could not be determined because of the lack of core (no core was available) and therefore the results of the nearby wells were inferred to those two wells. Thin sections, XRD and SEM/EDS were extensively interpreted and the following deductions were made:

- The studied formation is comprised of fine to medium grained, moderately to well-sorted sandstones that are lithic, glauconitic and feldspathic. They are porous to very tight. Well F-A10 and F-A13 proved to be the most porous and well E-G1, E-W1 and E-CN1 less porous because they are more tight and argillaceous.
- Petrography studies reveal the presence of stylolite resulting from pressure dissolution and grain compaction in tight, less porous reservoirs (F-O1 and F-O2).
- Authigenic chlorite and illite were identified as the two major clay mineral influencing porosity. Pore filling clays (illite and chlorite) and quartz overgrowth destroyed most of the intergranular porosities. Grain coating chlorite prevented the overgrowth of quartz grains in F-A10 and F-A13 and therefore preserved porosity.
- The dissolution of calcite cement created the secondary micro-porosity in most wells were intergranular porosity was destroyed and decreased velocity and bulk density of the sediments.
- Calcite and quartz cement, pore filling clays (Chlorite and Illite) and quartz overgrowth all reduced intergranular porosity and increased the rock bulk density and velocity. However, where the dissolution of cement occurred, secondary porosity was created and therefore velocity and density was reduced. Well F-A10, F-A11 and F-A13 show clearly that when the porosity is preserved the velocity is lower.
- The notable effect was observed in well E-CN1 where compaction and pore-filling clays destroyed the intergranular pore spaces and resulted in high bulk density and velocity readings.

6.6 REFERENCES

Adams, A.E., Mackenzie, W.S and Guilford, C. (1984). *Atlas of sedimentary rocks under the microscope.* England: Longman Group UK Ltd.

Ardakani P.E., Podivisnky, T.J and Schmitt, D.R. (2014). Lithology discrimination using elastic rock properties and simultaneous seismic inversion in the Leduc reservoir, NE Alberta. *Canadian Society of Exploration Geophysicists*, pp. 42-46.

Bahremandi, M., Mirshahani, M and Saemi, M. (2012). Using of compressional-wave and shear wave velocities ratio in recognition of reservoir fluid contacts case study: A southwest Iranian oil field. *Journal of scientific research and reviews, 1*(2), 15-19.

Bailey, S.W., Brindley, G.W., Kodama, H and Martin, R.T. (1979). Report of the Clay Minerals Society Nomenclature Committee for 1977 and 1978. *Clays and Clay Minerals, 27*, 238-239.

Benson, D. I. (1981). Porosity reduction through ductile grain deformation: an experimental assessment. *Gulf Coast Association of Geological Societies Transactions, 31*, 235-237.

Brandt, L., Barnes, H and Bronk, K. (2013). X-Ray Diffraction (XRD): Quick user guide. *International ocean discovery program*.

Pestitschek, B, Gier, S., Essa, M and Kurzwell, H. (2012). Effects of weathering on glauconite: Evidence from the Abu Tartur Plateau, Egypt. *Clays and Clay Minerals, 60*(1), 76-88.

Chamley, H. (1989). Clay sedimentology. *Springer, Berlin*, 623.

Cheng, A. (2009). Rock physics basics, PetroSA rock physics Course. Cape Town: Rock solid images.

Fadipe, O.A. (2012). Reservoir quality, structural architecture, fluid evolution and their controls on reservoir performance in block9, F-O gas filed, Bredasdorp Basin, Offshore South Africa. Cape Town: University of the Western Cape, Unpublished PhD Thesis.

Hamanda, G.M. (2004). Reservoir fluids identification using Vp/Vs ration. *Oil and Gas Science and Technology, 59*(6), 649-654.

Gier, S. W. (2008). Diagenesis and reservoir quality of Miocene sandstones in the Viena Basin, Austria. *Marine and Petroleum Geology, 25*, 681-695.

Hamada, G. (2004). Reservoir fluids identification using Vp/Vs ratio. *Oil and Gas and Technology, 59*(6), 649-654.

Jain, P. K., Jambhekar, C.V and Pandey, P.B. (2012). Identification of gas using Vp/Vs vis-a-vis Poisson's ratio. *9th Biennial International Conference and Exposition on Petroleum Geophysics*, (pp. 1-6). Hyderabad.

Kurkjy, K. A., Smith, J.c, and Trevena, A.S. (1987). Losses of permeability and porosity in lithic sands assessed with compaction experiments. *American Association of Petroleum Geologists, 71*, 579.

Lundergard, P. D. (1992). Sandstone porosity loss; a "'big picture" view of the importance of compaction. *Journal of Sedimentary Research, 62*(2), 250-260.

Mondol, N.H., Jahren, J and Bjorlykke, K. (2008). Elastic properties of clay minerals. *The leading edge*, 758.

Moore, D.M and Reynolds, Jr. R. C. (1997). X-ray diffraction and the identification and Analysis of Clay minerals (2nd ed.). *New York: Oxford University Press.*

Odin, G.S and Matter, A. (1981). De glauconiarum origine. *Sedimentology, 28*, 611-641.

Picket, G. (1966). Review of current techniques for determination of water saturation from logs. *Journal of Petroleum Technology: SPE, November* 1425-1433.

Pittman, E.D and Larese, R.E. (1986). The importance of ductile deformation of lithic fragments in arenites: evidence from experimental compaction. *Abstracts of the 12th international sedimentology conference*, 243.

Press, F, and Siever, R. (1978). *Earth* (2nd ed.). San Francisco: W.H. Freeman and Co.

Rider, M. (2000). *Geological Interpretation of wireline logs* (second ed.). Sutherland: Rider-French consulting Ltd.

Serra, O. (1986). Chapter 7 Information on diagenesis: Transformation of rocks and sediments. In O.Serra (Ed.), *Fundamentals of Well-Log interpretation* (pp. 341-366). Amsterdam: Elsevier.

Welton, J. (2003). *SEM Petrology Atlas.* USA: The American Association of Petroleum Geologists.

Worden, R.H and Burley, S.D. (2003). Sandstone diagenesis from sand to stone, In: Burley, S.D., Worden, R.H (Eds), Clastic diagenesis: Recent and Ancient. *International Association of Sedimentologists, 4*, 3-44.

CHAPTER SEVEN

7 GENERAL CONCLUSION AND RECOMMENDATIONS

The investigation of petrophysical and acoustic properties of the Upper Shallow Marine sandstone reservoir units encountered by ten wells was made possible by detailed analysis and interpretation of well logs and core data available. The calculated average volume of clay, porosity and water saturation values ranged from 8.6%- 43%, 9%- 16% and 12%- 68% respectively. The distribution of the petrophysical properties across the field was clearly defined with the use of 3D parameter viewer whereby wells F-A10, F-A11, F-O2, E-M4 and F-A13 showed a good porosity and E-CN1, F-O1, F-L1, E-G1 and E-W1 showed a poor porosity of less than 10%. Well E-CN1 showed the lowest volume of clay of 8.6% whereas F-L1 showed the highest volume of clay of 42.8%. Well F-L1 showed the highest water saturation with the value of 68.2% whereas F-O2 showed the lowest value of 12.2%.

The acoustic impedance proved to be highest on the central to the western side of the field at E-CN1 with an average value of 11832 g/cm3s whereas, well F-A13 reservoir in the eastern side of the field proved to have the lowest average acoustic impedance of 9821 g/cm3s. The effect of porosity on acoustic impedance, bulk density, and compressional velocity was thoroughly studied using cross-plots. There was a good linear negative correlation between acoustic impedance and porosity where the reservoir was homogenous, thick sandstone. Higher porosity values were correlated with lower acoustic impedance values. However, interbedded shale units within the reservoirs appear to hinder a reliable correlation between acoustic impedance and porosity as seen in well E-W1. There was no evidence of the effect of reservoir thickness on the acoustic impedance.

The Gassmann equation was used for the calculation of the effects of fluid substitution on acoustic properties using rock frame properties. Three fluid substitution models (brine, oil and gas) were determined for pure sandstones and were used to measure the behaviour of the different sandstone saturations. A significant decrease was observed in Vp when the initial water saturation was substituted with a hydrocarbon (oil or gas) in all the wells. The value of density decreased quite visibly in all the wells when the brine (100% water saturation) was substituted with gas or oil. The fluid substitution affected the rock property significantly. The Vp slightly decreases when brine was substituted with water in well F-A13, F-A10, F-O2, F-

O1 F-A11, F-L1 and E-CN1. Wells E-G1, E-W1 and E-M4 contain both oil and gas and therefore showed a notable decrease from brine to oil and from oil to gas respectively. The Vs remained unaffected in all the wells. The acoustic impedance logs showed a decrease when 100% water saturation was replaced with a hydrocarbon (oil or gas) in all the wells.

Thin section, XRD and SEM/EDS were extensively interpreted and the following deductions were made: The studied formation is comprised of fine to medium grained, moderately to well-sorted sandstones that are lithic, glauconitic and feldspathic. They are porous to very tight. Well F-A10 and F-A13 proved to be the most porous and well E-G1, E-W1 and ECN1 less porous because they are tight and more argillaceous.

Petrography studies revealed the presence of stylolite resulting from pressure dissolution and grain compaction in tight, less porous reservoirs (F-O1 and F-O2). Authigenic chlorite and illite were identified as the two major clay minerals influencing porosity. Pore filling clays (illite and chlorite) and quartz overgrowth destroyed most of the intergranular porosities. Grain coating chlorite prevented the overgrowth of quartz grains in F-A10 and F-A13 and therefore preserved porosity. The dissolution of calcite cement created the secondary micro-porosity in most wells were intergranular porosity was destroyed. Calcite and quartz cement, pore filling clays (Chlorite and Illite) and quartz overgrowth all reduced intergranular porosity and increased the rock bulk density and velocity. However, where the dissolution of cement occurred, secondary porosity was created and therefore velocity and density was reduced. Well F-A10, F-A11 and F-A13 clearly show that when the porosity is preserved the velocity is low. A notable effect was observed in well E-CN1 where compaction and pore filling clays destroyed the intergranular pore spaces and resulted in high bulk density and velocity readings. Overall, the results show that the porosity, lithology, mineralogy, compaction and pore fluid are the major factors causing the acoustic impedance variations in the upper shallow marine sandstone reservoirs.

7.1 RECOMMENDATIONS

I strongly recommend that the compressional velocity log (Vp) be run in future wells to enhance the validity of the calculated acoustic impedance. The Vp measurements from the laboratory using core plugs or whole core are also recommended. This will help with the calibration between the calculated log and the laboratory measurements.

A 3D seismic acquisition will be desirable in the wells intersecting the Upper Shallow Marine reservoirs to further enhance the clarity and understanding of other structures that may also play a role in influencing the acoustic impedance. The 3D seismic data would also help build acoustic impedance inversion model which will give more clarity on the distribution of acoustic impedance across the field taking into account all the geological structures.

The methodology used in chapter six for XRD sample preparation is strongly recommended as it gives a detailed peak results. This method proved to be effective and able to give strong peaks between 0Ɵ-20Ɵ where other authors (E.g Fadipe, 2012) failed to show the peaks between the mentioned interval in F-O1 and F-O2 wells.

APPENDICES

APPENDIX A- GAMMA RAY HISTOGRAM PLOTS

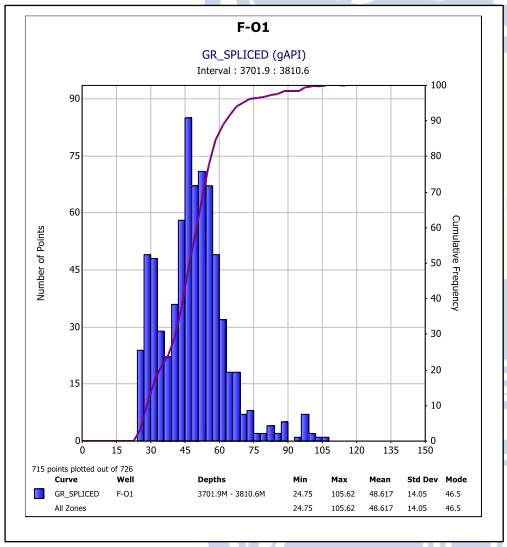

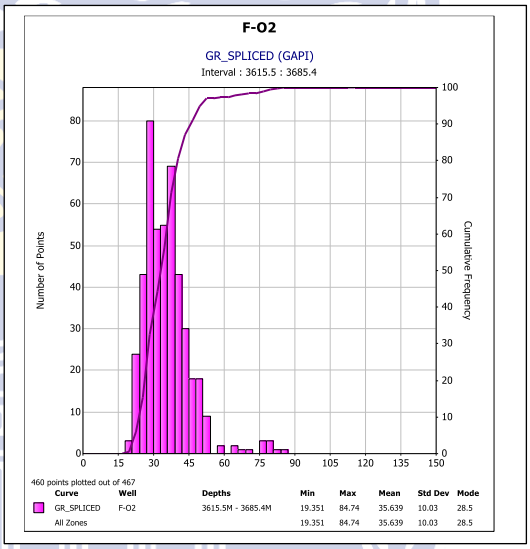

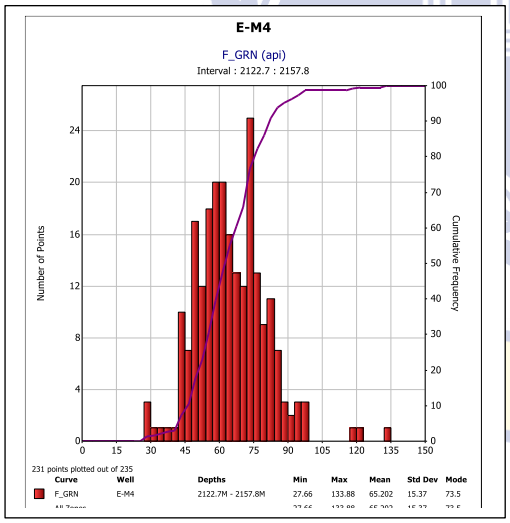

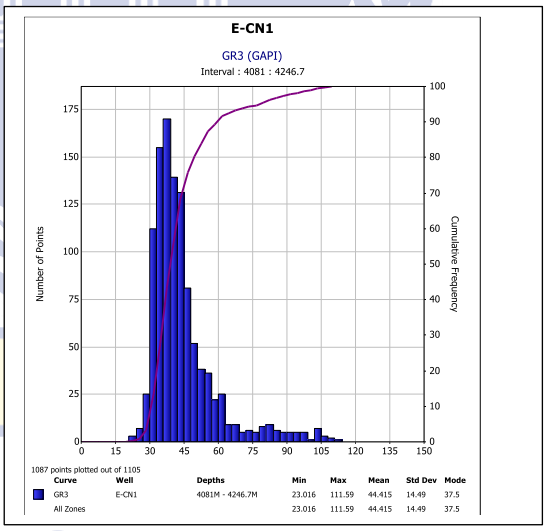

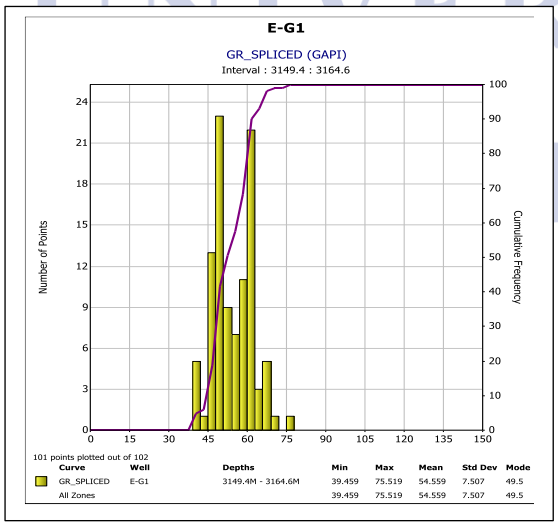

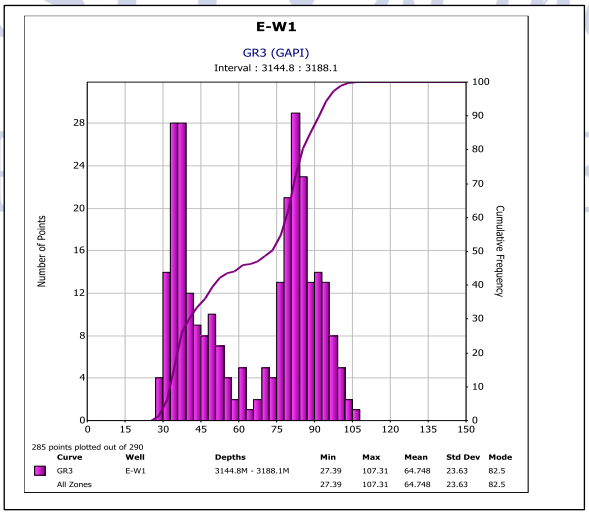

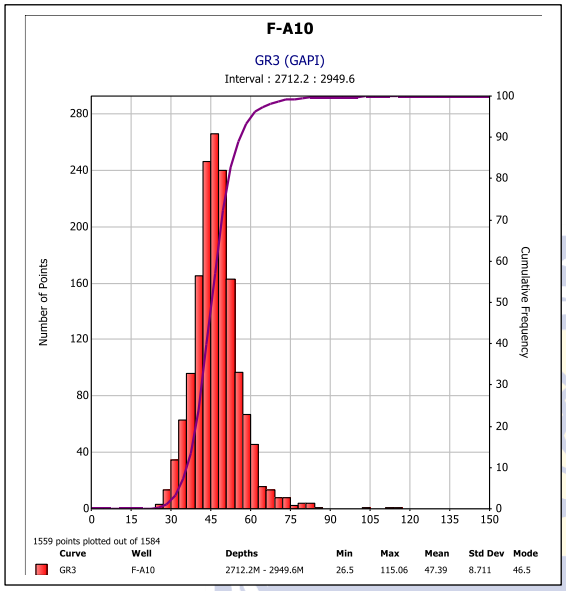

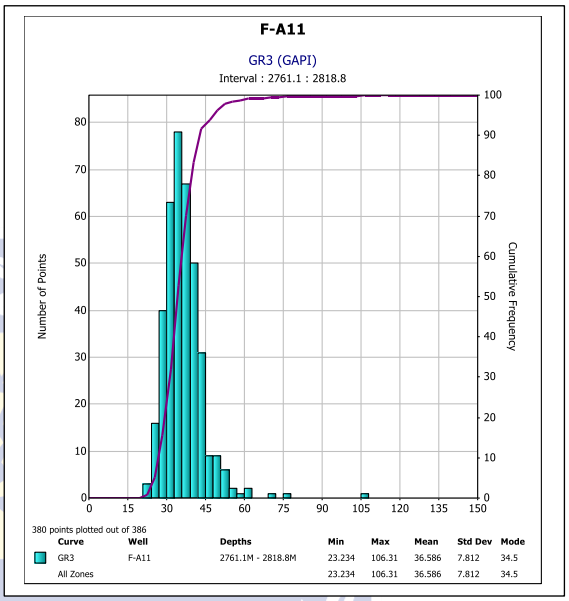

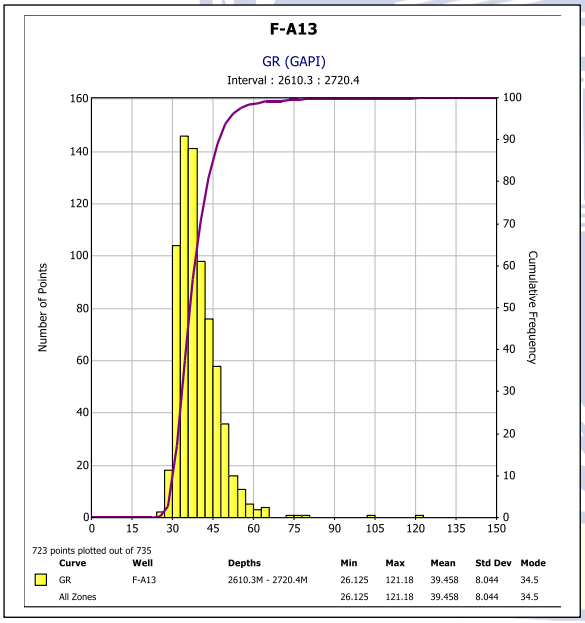

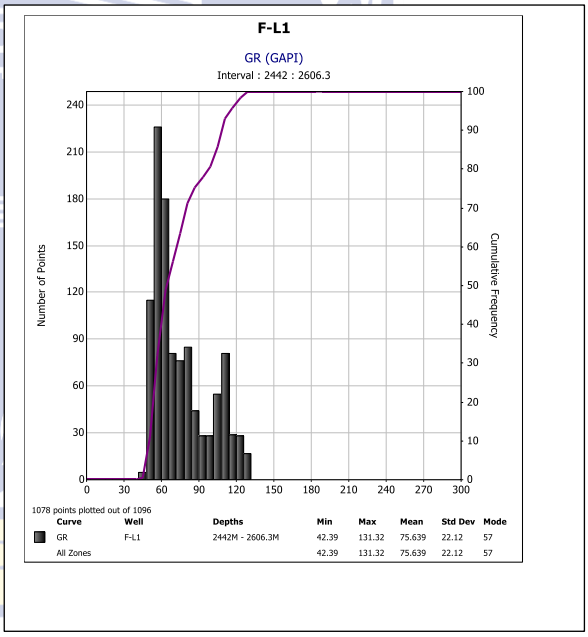

APPENDIX B- CONVENTIONAL CORE ANALYSIS RESULTS

Table B1: Conventional core analysis results of E-G1 well (Soekor core analysis section, 1982).

From (Depth)	porosity	permeability	Sw	So	Sg	Calc	Dol
3159,62	0,121	2				1	3
3159,86	0,117	1,6				1	4
3159,94	0,106	1,2	0,36	0,17	0,47	0	3
3160,25	0,112	0,7				0	3
3160,47	0,109	1	0,36	0,17	0,47	0	3
3160,57							
3160,74	0,109	0,6				1	2
3160,88	0,115	1,7	0,36	0,17	0,47	0	3
3161	0,116	1,8					
3161,37	0,109	0,7					
3161,6	0,105	0,5				0	4
3161,78	0,091	0,2				1	4
3162,05	0,115	0,7				1	4
3162,3	0,105	0,4				0	4
3162,56	0,075	0,1				0	3
3162,65	0,095	0,1	0,37	0,16	0,47	0	1
3163,16	0,105	0,4				0	1
3163,41	0,1128	0,7				0	3
3163,84	0,036	0	0,67	0	0,33	38	3
3164,16	0,017	0				38	0
3164,44	0,012	0				38	0
3164,87	0,039	0				23	0
3165,09	0,058	0				0	2
3165,2	0,09	0,1	0,36	0,15	0,49	0	3
3165,56	0,101	0,6				0	2
3165,9	0,081	0,1				0	1
3166,01	0,1	0,2	0,39	0,13	0,48	0	2
3166,53	0,075	0				0	2
3166,75	0,115	0,5				0	2
3166,96	0,127	0,4				0	3
3167,2	0,082	0,2				0	4
3167,49	0,087	0,5				0	4
3167,63	0,089	0,3				1	
3167,77	0,079	0,2	0,37	0,16	0,47		
3168,1	0,058	0				5	1

Table B2: Core analysis results of E-W1 well (Soekor core analysis section, 1985).

From (depth, m)	To (Depth,m)	porosity	Permeability (KL, mD)	Sw	Sg
3171,05		0,075	0,13		
3171,3		0,119	13		
3171,55		0,106	11		
3171,55	3171,07	0,115	4,8	0,49	0,51
3172,35		0,117	7,8		
3172,6		0,105	3,1		
3172,69	3173,23	0,107	1,4	0,39	0,61
3173,35		0,032	4		
3173,73	3174,2	0,038	0,08	0,8	0,2
3174,05		0,068	0,17		
3174,3		0,057	0,26		
3174,55		0,054	0,6		
3174,04	3175,32	0,058	0,12	0,69	0,31
3175,4		0,06	0,12		
3175,65		0,066	0,1		
3175,03		0,045	0,12		
3176,24	3176,58	0,016	0,05	0,83	0,17
3176,67		0,072	0,1		
3176,93		0,065	0,11		
3177,14	3177,43	0,068	0,06	0,77	0,23
3177,5		0,051	0,09		
3177,75		0,02	0,16		
3178		0,074	0,19		
3178,39	3178,68	0,102	35	0,27	0,73
3178,8		0,066	0,62		
3179,09	3179,42	0,099	5,8	0,44	0,56
3179,5		0,074	5,5		
3179,7		0,07	0,67		
3179,95		0,087	2,2		
3180,23		0,12	24		
3180,58	3180,91	0,113	11	0,36	0,64
3181		0,107	27		
3181,25		0,08	16		
3181,55	3181,76	0,097	9	0,29	0,71
3181,85		0,06	0,4		
3182,1		0,077	7		
3182,43	3182,76	0,095	21	0,41	0,59
3182,83		0,071	4,1		
3183,08		0,083	2,4		
3183,42	3183,73	0,077	4,9	0,4	0,6
3184		0,136	78		

3184,25		0,121	111		
3184,54	3184,82	0,1	2,4	0,51	0,49
3185,2		0,143	112		
3185,55	3185,78	0,127	44	0,39	0,61
3185,88		0,098	9,2		
3186,13		0,065	0,1		
3186,49	3186,76	0,038	0,05	0,57	0,43
3186,85		0,059	0,08		
3187,1		0,035	0,04		
3187,15	3187,47	0,032	0,03	0,57	0,43
3187,55		0,017	0,03		
3229,05		0,074	0,11		
3229,31		0,067	0,14		
3229,55		0,075	0,29		
3229,57	3229,78	0,078	0,71	0,24	0,76
3229,97		0,087	0,19		
3230,22		0,099	14		
3230,34	3230,51	0,092	7,5	0,21	0,79
3230,73		0,096	13		
3230,98		0,092	6,4		
3231,23		0,093	6,5		
3231,48		0,091	5,1		
3231,59	3231,81	0,084	1,6	0,35	0,61
3231,96		0,092	1		
3232,21		0,098	2,5		
3232,46		0,101	7,7		
3232,69	3232,95	0,097	4,3	0,25	0,66
3233,24		0,094	22		
3233,49		0,073	0,31		
3233,76		0,06	0,16		
3234		0,049	0,08		
3234,6		0,085	5,7		
3234,66	3234,95	0,103	22	0,27	0,69
3235,22		0,098	5,8		
3235,47		0,097	3		
3235,52	3235,84	0,102	3,6	0,26	0,64
3236,24		0,083	0,02		
3236,62		0,066	0,1		
3236,87		0,077	0,15		
3236,92	3237,12	0,094	0,3	0,44	0,56
3237,69		0,085	1		
3237,94		0,087	1		
3238,37		0,088	0,91		
3238,5	3238,77	0,101	1	0,32	0,68

3238,89		0,095	0,7		
3239,2		0,078	0,21		
3239,31	3239,53	0,083	0,28	0,33	0,67
3239,8		0,091	0,65		
3240,05		0,08	0,21		
3240,23	3240,45	0,068	0,12	0,25	0,75
3240,7		0,068	0,21		
3240,97		0,066	0,18		
3241,35		0,071	0,25		
3241,42	3241,73	0,078	0,48	0,25	0,75
3242,11		0,084	0,68		
3242,36		0,09	1,4		
3242,6	3242,84	0,101	2,2	0,21	0,69
3243,15		0,077	0,4		
3243,4		0,089	1,3		
3243,53	3243,76	0,09	1,3	0,27	0,68
3245,09		0,084	1		
3245,34		0,081	0,64		
3245,59		0,084	0,71		
3245,64	3245,89	0,088	0,91	0,31	0,58

Table B3: Core analysis results of F-A10 well (Soekor core analysis section, 1983)

From (Depth, m)	Porosity	Permeability (L, mD)	Sw	Sg	Calc %	Dol%
2719	0,166	168	0,3	0,62	0	2
2719,55	0,191	91				
2719,85	0,185	278				
2720,12	0,176	81				
2720,24	0,166	271	0,38	0,62	0	2
2720,64	0,18	293				
2720,94	0,183	298				
2721,03	0,177	456	0,35	0,65	0	2
2721,49	0,191	231				
2721,79	0,192	436				
2721,83	0,191	495	0,45	0,55	0	1
2722,35	0,183	173				
2722,65	0,181	263				
2722,93	0,175	343	0,36	0,64	1	1
2722,94	0,192	306				
2723,3	0,168	126				
2723,64	0,188	338				
2723,95	0,185	491				

2724,22	0,181	210				
2724,23	0,186	282	0,47	0,53	1	1
2724,44		411				
2724,65	0,169	123				
2724,95	0,179	149				
2724,97	0,174	513	0,4	0,6	0	2
2725,37	0,182	210				
2725,67	0,186	350				
2725,8	0,179	241	0,42	0,58	0	1
2726,14	0,195	577				
2726,44	0,186	313				
2726,74	0,177	163				
2727	0,175	222				
2727,03	0,177	511	0,38	0,62	0	2
2727,4	0,171	136				
2727,6	0,165	279				
2727,71	0,174	306	0,4	0,6	1	1
2728,15	0,18	302				
2728,45	0,175	153				
2728,7	0,185	445	0,36	0,54	0	2
2729,04	0,186	333				
2729,29	0,164	428				
2729,54	0,181	341				
2729,79	0,177	362				
2730,06	0,172	924	0,4	0,6	0	1
2730,52	0,166	294				
2730,73	0,165	416	0,34	0,66	0	2
2730,79	0,155	130				
2751,19	0,176	745				
2731,44	0,181	486				
2731,02	0,188	324	0,4	0,6	0	1
2731,95	0,18	298				
2732,2	0,173	278				
2732,45	0,197	440				
2732,51	0,175	503	0,38	0,62	0	2
2732,99	0,174	261				
2733,24	0,191	365				
2733,5	0,173	174	0,38	0,62	1	1
2733,95	0,144	36				
2734,2	0,162	215				
2734,45	0,178	425				
2734,71	0,158	312	0,38	0,62	1	1
2734,75	0,139	19				
2735,12	0,166	247				

2735,37	0,164	201				
2735,67	0,191	473				
2735,92	0,18	435				
2736	0,182	269	0,45	0,55	0	2
2736,35	0,18	290				
2736,6	0,174	323				
2736,74	0,162	240	0,38	0,62	0	1
2737,14	0,165	241				
2737,39	0,171	317				
2737,64	0,17	335				
2737,88	0,17	351				
2737,89	0,156	313	0,36	0,61	1	1
2738,03						
2738,1		237				
2738,3	0,168	340				
2738,55	0,171	383				
2738,8	0,165	228				
2738,92	0,165	73	0,34	0,66	0	3
2739,39	0,152	69				
2739,64	0,117	8,6				
2739,94	0,14	114				
2740,19	0,162	171				
2740,27	0,159	202	0,35	0,65	0	2
2740,39						
2740,45		89				
2740,58	0,16	163				
2740,83	0,16	83				
2741,03	0,159	78				
2741,2	0,167	93	0,11	0,89	0	3
2741,36		81				
2741,55	0,144	55				
2741,6	0,149	51				
2742,03	0,15	74				
2742,29	0,146	58	0,41	0,59	0	2
2742,65	0,14	24				
2742,9	0,14	33				
2743,14	0,154	61	0,37	0,63	0	2
2743,15	0,147	61				
2743,31		30,1				
2743,5	0,141	67				
2743,75	0,15	73				
2744	0,136	21	0,33	0,67	1	1
2744,32	0,161	86				
2744,57	0,15	72				

2744,82	0,15	103				
2745,07	0,15	83				
2745,23	0,143	54				
2745,41	0,154	91				
2745,66	0,149	46				
2745,86	0,14	60	0,37	0,63	1	1
2746,18	0,153	49				
2746,43	0,151	52				
2746,68	0,131	16				
2746,71	0,164	66	0,36	0,64	1	1
2746,85		31				
2727,42	0,141	35				
2747,67	0,138	21				
2747,92	0,123	23	0,32	0,68	1	1
2748,55	0,136	27				
2748,69	0,131	40	0,32	0,68	1	2
2748,92		41				
2749,11	0,127	11				
2749,36	0,142	37				
2749,61	0,144	33				
2749,86	0,144	62				
2750,11	0,143	35				
2750,16	0,133	30	0,39	0,61	0	2
2750,32		30				
2750,47	0,126	45,7				
2750,74		14	0,32	0,68	0	2
2750,88		30				
2751,09	0,121	19,4				
2751,34	0,135	5,3				
2751,63	0,126	21	0,4	0,6	1	2
2751,73	0,131	17				
2751,93	0,103	12				
2752,23	0,134	2,2				
2752,43	0,143	21				
2752	0,131	37				
73	0,139	21				
2752,84		17	0,41	0,59	1	2
2753,01	129	13,4				
2753,19	0,13	15				
2753,44	0,142	16				
2753,67	0,135	27	0,42	0,58	1	3
2754	0,14	15				
2754,25	0,129	50				
2754,5	0,14	27				

2754,75	0,15	35				
2754,98	0,135	34	0,4	0,6	1	2
2755,3	0,133	16				
2755,55	0,133	17				
2750,03	0,143	37				
2756,23	0,146	66				
2756,53	0,136	23				
2756,56	0,135	8	0,62	0,38	1	2
2756,83	0,136	22				
2757,13	0,133	22				
2757,29	0,137	53	0,47	0,53	0	4
2757,6	0,143	41				
2758,5	0,128	15				
2758,1	0,107	3,1				
2758,3	0,085	0,83	0,69		1	1
2758,67	0,096	3,7				
2759,92	0,115	0,91				
2759,17	0,104	2,3				
2759,3	0,115	2	0,58	0,42	1	1
2759,71	0,115	4,6				
2759,96	0,125	6,5				
2760,21	0,131	4,2				
2760,23	0,135	4,9	0,67	0,33	1	3
2760,34	0,126					
2760,4	0,115					
2760,53	0,117	1,6				
2760,78	0,115	3,8				
2761,03	0,104	1,7				
2761,28	0,088	1				
2761,51	0,098	0,23	0,52	0,48	0	3
2761,94	0,099	0,75				
2762,19	0,088	0,54				
2762,44	0,092	0,39				
2762,55	0,126	0,39	0,74	0,26	0	3
2762,84	0,119	3,9				
2763,09	0,125	3,7				
2763,34	0,119	8,1				
2763,59	0,122	3,9				
2763,69	0,112	4,6	0,55	0,45	1	2
2764,04	0,095	2				
2764,29	0,107	0,6				
2764,52	0,123	0,91	0,76	0,24	0	3
2764,88	0,102	1,4				
2765,13	0,098	0,54				

2765,23	0,079	0,46	0,47	0,53	3	2
2765,64	0,098	0,2				
2765,89	0,084	1				
2766,09	0,105	0,39	0,71	0,29	1	3
2766,4	0,1	0,75				
2766,65	0,058	1,3				
2766,9	0,103	0,46				
2767,09	0,093	1	0,5	0,5	7	1
2767,42	0,105	0,31				
2767,69	0,106	0,91				
2767,94	0,091	1,7				
2768,04	0,0141	0,54	0,73	0,27	0	4
2768,49	0,091	0,26				
2768,74	0,071	0,46				
2768,99	0,088	0,26				
2769,22	0,088	0,39	0,59	0,41	1	3
2769,61	0,086	0,26				
2769,86	0,106	0,54				
2770,11	0,105	0,75				
2770,28	0,109	1,1	0,71	0,29	0	3
2770,63	0,101	0,68				
2770,9	0,092	0,6				
2771,13	0,082	0,39	0,51	0,49	1	3
2771,48	0,106	0,26				
2771,73	0,098	2,1				
2771,98	0,104	0,54				
2772,23	0,094	0,91				
2772,48	0,069	0,39				
2772,52	0,106	0,26	0,6	0,2	20	0
2772,83	0,101	0,51				
2773,08	0,093	0,68				
2773,33	0,105	0,51	0,52	0,48	0	2
2773,66	0,116	0,6				
2773,91	0,106	1				
2774,16	0,108	0,6				

Table B4: Core analysis results of F-A13 well (Soekor core analysis section, 1984).

From (M)	Porosity (Dec)	permeability (KL)	Sw (Dec)	Sg (Dec)	Calc (%)	(Dol (%)	Grain density
2627,82	0,215	554					
2682,07	0,205	340					
2628,32	0,207	300					
2628,43	0,181	213	0,38	0,62	0	1	2,68
2629,12	0,197	633					
2629,37	0,2	408					
2629,5	0,181	235	0,39	0,61	0	1	
2629,93	0,203	574					
2630,18	0,206	808					
2630,38	0,188	414	0,36	0,64	1	1	2,69
2630,85	0,192	412					
2631,1	0,203	663					
2631,35	0,187	295					
2631,4	0,204	595	0,39	0,61	0	1	
2631,71	0,18	184					
2631,76	0,195	465	0,34	0,66	0	1	
2632,13	0,184	204					
2632,43	0,149	35					
2632,63	0,191	276					
2632,93	0,204	434					
2633,03	0,213	840	0,4	0,6	0	1	
2633,59	0,207	547					
2633,84	0,21	664					
2634	0,18	255	0,37	0,63	0	2	2,7
2634,54	0,176	179					
2634,79	0,133	227					

2634,67	0,175	54	0,37	0,63	0	5	
2635,29	0,164	78					
2635,54	0,17	894					
2635,95	0,182	53	0,4	0,6	1	1	2,68
2636,15	0,165	42					
2636,4	0,165	15					
2636,67	0,153	38					
2636,92	0,135	27					
2637,03	0,155	32	0,37	0,63	0	2	
2637,51	0,149	29					
2637,76	0,144	243					
2637,95	0,164	4,7	0,29	0,71	0	1	2,68
2638,26	0,131	2,4					
2638,51	0,123	7,2					
2638,76	0,139	5,2					
2639,01	0,135	4,1					
2639,26	0,128	587					
2639,36	0,195	17	0,36	0,64	1	8	
2639,9	0,13	128					
2640,15	0,173	19					
2640,4	0,136	10					
2640,52	0,13	42	0,38	0,62	0	1	2,69
2641,02	0,172	46					
2641,27	0,17	42					
2641,42	0,168	148	0,37	0,63	0	1	
2641,9	0,182	112					
2642,15	0,178	15					
2642,4	0,149	6,8					
2642,67	0,131	14	0,4	0,6	0	1	2,69

2642,85	0,147	22					
2643,39	0,14	26					
2643,64	0,153	2,8					
2643,89	0,119	3,7					
2643,94	0,128	3,8	0,26	0,74	1	13	
2644,48	0,137	2,9					
2644,73	0,156	10					
2644,78	0,149	26	0,36	0,64	1	4	2,71
2645,54	0,11	0,52					
2645,79	0,121	3,1					
2645,86	0,126	1,2	0,3	0,7	25	3	
2646,5	0,159	21					
2646,61	0,16	42	0,3	0,7	0	1	2,68
2647,22	0,133	7,2					
2647,47	0,185	159					
2647,6	0,175	37	0,34	0,66	1	7	
2648,23	0,119	3,7					
2648,48	0,129	7,4					
2648,63	0,14	19	0,34	0,66	1	4	2,68
2648,89	0,137	7,1					
2649,39	0,136	15					
2649,44	0,192	616	0,33	0,67	0	2	
2650,03	0,176	81	0,35	0,65	1	3	
2650,2	0,206	552			0	9	
2650,65	0,174	66			10	18	
2650,9	0,199	272					
2651,1	0,127	243	0,43	0,57	0	9	2,7
2651,35	0,174	98			1	2	
2651,7	0,19	307			0	1	

2651,95	0,133	67			0	6	
2652,02	0,166	24	0,34	0,66	10	18	
2652,35	0,175	57			1	3	
2652,9	0,185	188			0	2	
2653,05	0,192	958	0,34	0,66	1	2	2,69
2653,65	0,219	841			0	2	
2653,9	0,22	848			1	2	
2654,01	0,204	968	0,36	0,64	0	1	
2654,5	0,194	191			1	9	
2654,75	0,183	109			1	2	
2654,91	0,171	454	0,36	0,64	0	6	2,7
2655,25	0,12	17			0	2	
2655,6	0,212	636			0	5	
2655,85	0,194	504			0	4	
2655,99	0,148	54	0,34	0,66	1	3	
2656,1	0,166	182			0	8	
2656,6	0,202	954			1	2	
2656,85	0,209	1032			0	5	
2656,94	0,21	1185	0,38	0,62	0	2	2,69
2657,55	0,215	1142					
2657,8	0,209	989					
2658	0,195	1142	0,36	0,64	0	2	
2658,05	0,215	1109					
2658,6	0,177	288					
2658,85	0,16	107					
2659,01	0,196	729	0,31	0,69	1	2	2,69
2659,65	0,204	722					
2659,9	0,219	668					
2660,04	0,184	397	0,32	0,68	1	9	

2660,6	0,171	273					
2660,88	0,171	317					
2661,13	0,165	106					
2661,16	0,171	253	0,33	0,62	1	2	2,69
2661,6	0,201	419					
2661,85	0,204	644					
2661,96	0,192	372	0,37	0,63	0	2	
2662,95	0,203	656					
2663,13	0,192	494	0,35	0,65	0	6	2,7
2663,68	0,207	447					
2663,93	0,175	36					
2664,18	0,204	365					
2664,19	0,193	290	0,34	0,66	0	5	
2664,7	0,195	335					
2664,95	0,19	380					
2665,03	0,182	385	0,35	0,65	0	4	2,69
2665,65	0,173	184					
2665,9	0,189	182					
2665,97	0,174	296	0,32	0,68	0	8	
2666,55	0,181	196					
2666,8	0,177	273					
2666,94	0,158	79	0,32	0,68	1	2	2,7
2667,5	0,111	3,6					
2667,78	0,155	143					
2667,93	0,162	28	0,34	0,66	0	5	
2668	0,162	43					
2668,43	0,162	150			1	8	
2668,63	0,172	60	0,32	0,68	1	8	
2668,9	0,133	21			0	5	

2669,15	0,098	2			0	4	
2669,4	0,152	84			0	3	
2669,75	0,162	124	0,3	0,7	0	5	2,71
2669,93	0,166	123			0	6	
2670,25	0,159	56			0	2	
2670,57	0,144	12	0,41	0,39	0	4	
2670,9	0,16	49			0	7	
2671,15	0,163	69			0	5	
2671,53	0,176	274	0,32	0,68	0	3	2,7
2671,85	0,157	44			0	4	
2672,1	0,168	78			0	2	
2672,35	0,173	136			0	6	
2672,61	0,18	189	0,37	0,63	0	6	
2672,95	0,123	15			0	2	
2673,2	0,156	84			1	2	
2673,78	0,129	19	0,35	0,65	0	2	2,69
2674,1	0,127	7,5			0	2	
2674,35	0,133	36			1	2	
2674,68	0,156	67	0,41	0,59	0	7	
2674,98	0,127	2,1			0	7	
2675,23	0,135	21			1	7	
2675,53	0,141	11	0,31	0,69	0	5	2,72
2675,83	0,139	10					
2676,08	0,144	63			15	2	
2676,42	0,133	15	0,35	0,65	0	4	2,69
2676,8	0,159	73					
2677,05	0,163	249					
2677,3	0,176	284					
2677,59	0,163	28	0,35	0,65	0	2	

2677,96	0,148	48					
2678,2	0,128	15					
2678,7	0,114	2,6					
2678,76	0,129	15	0,23	0,77	0	6	2,68
2679,1	0,128	9					
2679,35	0,1489	39					
2679,63	0,133	16	0,33	0,67	0	2	2,69
2679,9	0,123	17					
2680,15	0,126	19					
2680,4	0,139	11					
2680,71	0,149	43	0,31	0,69	1	2	
2681,1	0,146	40					
2681,35	0,152	23					
2681,73	0,125	7,1	0,34	0,66	0	2	2,69
2682,05	0,117	5,7					
2682,35	0,142	30					
2685,82	0,166	156	0,33	0,67	1	2	
2683,1	0,167	17					
2683,37	0,175	246					
2683,89	0,157	227	0,39	0,61	0	7	2,67
2684,1	0,177	177					
2684,35	0,136	37					
2684,75	0,15	63					
2685	0,174	620					
2685,06	0,169	122	0,35	0,65	1	7	
2685,45	0,13	79					
2685,8	0,132	46					
2686,5	0,125	17	0,42	0,58	15	2	
2687	0,135	182	0,41	0,59	6	3	

2687,65	0,159	269			6	3	
2687,9	0,117	3,5					
2688,02	0,144	91	0,33	0,67	2	5	2,72
2688,65	0,112	2,7			9	3	
2688,9	0,159	191					
2688,95	0,151	205	0,39	0,61	9	3	
2689,45	0,113	36			1	2	
2689,7	0,141	18					
2689,95	0,111	2,7			9	4	
2689,96	0,148	20	0,37	0,63	13	4	2,74
2690,6	0,138	36					
2690,85	0,134	8,7			9	3	
2691,07	0,145	7,3	0,39	0,61	1	2	
2691,1	0,127	17			21	2	
2691,6	0,148	37			2	6	
2691,85	0,168	49			10	4	
2692	0,142	30	0,38	0,32	21	1	2,7
2692,55	0,069	0,03			10	2	
2692,8	0,111	2			5	9	
2692,87	0,121	4,4	0,37	0,63	9	4	
2693,36	0,047	0,04			2	7	
2693,61	0,049	0,04			8	7	
2693,87	0,11	1,3			2	9	
2693,89	0,104	17	0,4	0,6	20	2	2,73
2694,4	0,119	7,4			11	9	
2694,65	0,067	0,13					
2694,9	0,131	7,7					
2695,09	0,116	3,4	0,34	0,66	9	3	
2695,55	0,12	16					

2695,8	0,098	4,8					
2695,94	0,117	13	0,44	0,56	21	2	2,69
2696,05	0,1	5,2					
2696,55	0,107	17					
2696,8	0,13	35					
2697,05	0,14	31					
2697,07	0,141	46	0,36	0,64	2	6	
2697,75	0,148	20					
2697,99	0,154	4,2					
2698	0,125	8	0,39	0,61	10	4	2,73
2698,5	0,142	20					
2698,75	0,151	28					
2698,82	0,131	34	0,41	0,59	10	2	
2699,22	0,057	0,04					
2699,47	0,152	74					
2699,72	0,147	36					
2699,92	0,141	53	0,37	0,63	5	9	2,68
2700,35	0,049	0,04					
2700,6	0,122	3,8					
2700,85	0,135	14					
2700,88	0,14	25	0,44	0,56	2	7	
2701,45	0,113	3,4					
2701,7	0,055	0,03					
2701,84	0,145	51	0,41	0,59	8	7	2,72
2702,45	0,1	10					
2702,7	0,154	62					
2702,93	0,156	69	0,37	0,63	2	9	
2702,95	0,143	24					
2703,42	0,157	116					

2703,66	0,154	15					
2703,83	0,14	73	0,42	0,58	11	9	
2703,9	0,147	19					
2704,45	0,152	84	0,36	0,64	2	11	
2704,99	0,113	37			2	11	
2705,24	0,11	40			29	1	
2705,45	0,084	1,2			12	7	
2705,43	0,142	57	0,44	0,56	29	1	
2705,97	0,123	89			17	3	
2706,22	0,119	67			6	8	
2706,37	0,154	86	0,34	0,56	12	7	
2706,87	0,106	15			21	1	
2707,14	0,067	0,17			19	1	
2707,31	0,126	47	0,55	0,45	17	3	2,69
2707,52	0,109	20			17	1	
2707,92	0,087	2,2			22	1	
2708,17	0,111	5,8			16	3	
2708,42	0,109	6,4			35	0	
2708,38	0,13	19	0,35	0,55	6	8	
2708,9	0,1	1,6			40	2	
2709,15	0,085	0,52			13	4	
2709,25	0,101	0,75	0,46	0,54	21	1	2,71
2709,65	0,087	0,75			38	1	
2709,9	0,092	1,3			37	0	
2710,15	0,064	0,24					
2710,4	0,072	0,68					
2710,45	0,096	4,4	0,56	0,44	19	1	
2711	0,106	4,8					
2711,25	0,103	10					

2711,41	0,127	0,05	0,51	0,44	17	1	2,72
2711,85	0,054	7					
2712,1	0,111	1,5					
2712,41	0,09	0,1	0,4	0,6	22	1	
2712,9	0,061	0,06					
2713,15	0,063	0,03					
2713,4	0,051	0,29					
2713,48	0,076	0,45	0,45	0,55	16	3	
2713,95	0,082	1,7					
2714,2	0,087	0,05					
2714,34	0,052	0,06	0,49	0,51	35	0	
2715	0,045	0,06					
2715,29	0,061	0,08	0,75	0,25	40	2	2,79
2715,8	0,053	0,04					
2716,05	0,06	0,6					
2716,3	0,103	5,2					
2716,35	0,093	0,23	0,37	0,63	13	4	
2716,55	0,072	0,47					
2717	0,107	6,4					
2717,25	0,087	0,83					
2717,32	0,075	0,03	0,74	0,26	33	1	
2717,8	0,076	0,06					
2718,05	0,057	0,06					
2718,31	0,053	0,04					
2718,37	0,038	0,05	0,53	0,47	37	0	
2718,85	0,061	0,04					

Table B5: Core analysis results of F-O1 well (Soekor core analysis section, 1989)

Depth (M)	Permeability (KL)	Porosity (Dec)	Sg (Dec	Sw (Dec)	Grain Density	Cal (%)	Dol (%)
3652,55	26,62	0,165			2,67		
3652,75	45,87	0,121	0,52	0,48	2,61	0,5	1
3653,04	7,05	0,124			2,66		
3653,29	0,02	0,094			2,68		
3653,54	0,02	0,097			2,68		
3653,75	0,18	0,106	0,33	0,67	2,65	0	1,5
3653,08	0,81	0,126			2,66		
3653,33	0,12	0,117			2,67		
3654,58	0,86	0,121			2,66		
3654,71	0,15	0,087	0,38	0,62	2,65	0,5	1,5
3655	0,02	0,095			2,69		
3655,29	0,09	0,108			2,67		
3655,54	0,01	0,08			2,69		
3655,68	0	0,036	0,17	0,83	2,66	0,5	1
3626	0	0,055			2,69		
3656,25	0,02	0,094			2,68		
3656,5	0,03	0,1			2,72		
3656,66	0,04	0,075	0,27	0,73	2,65	0,5	1,5
3657	0,02	0,094			2,68		
3657,25	0,01	0,086			2,69		
3657,5	0,02	0,09			2,68		
3657,65	0,03	0,084	0,27	0,73	2,64	0	1,5
3657,94	0,03	0,098			2,69		
3658,19	0,03	0,108			2,69		
3658,44	0,02	0,099			2,69		
3658,44	0,02	0,073			2,69		
3658,7	0,03	0,106	0,26	0,74	2,65	0,5	2

3659	0,04	0,109			2,69		
3659,25	0,07	0,113			2,69		
3659,5	0,02	0,085			2,69		
3659,69	0,07	0,118	0,3	0,7	2,65	0	3
3660,03	0,08	0,117			2,7		
3660,28	0	0,057			2,7		
3660,6	0,04	0,107	0,16	0,84	2,66	0,5	3
3660,87	0,02	0,094			2,68		
3661,13	0,01	0,088			2,69		
3661,39	0	0,066			2,68		
3661,6	0,01	0,086	0,17	0,83	2,66	0,5	1
3661,89	0,01	0,089			2,68		
3662,14	0,01	0,085			2,69		
3662,39	0	0,064			2,69		
3662,55	0,01	0,094	0,19	0,81	2,67	0,5	2
3662,85	0,01	0,089			2,69		
3663,1	0,01	0,083			2,69		
3663,35	0	0,035			2,7		
3663,62	0	0,066	0,18	0,82	2,66	1	1
3663,92	0	0,063			2,69		
3664,18	0	0,065			2,68		
3664,41	0	0,052			2,69		
3664,63	0,05	0,108	0,16	0,84	2,7	0,5	1
3665,02	0,02	0,102			2,67		
3665,27	0,03	0,099			2,68		
3665,62	0,26	0,116	0,22	0,78	2,67	0	2
3665,94	0,32	0,11			2,67		
3666,18	0,03	0,101			2,67		
3666,43	0	0,06			2,68		

3666,62	0,02	0,102	0,16	0,84	2,71	0	2
3666,92	0,03	0,107			2,68		
3667,17	0,37	0,125			2,68		
3667,58	0,58	0,128	0,38	0,62	2,67	0	3,5
3668,03	0,37	0,127			2,67		
3668,53	0,81	0,116			2,67		
3668,78	0,15	0,123	0,47	0,53	2,66	0,5	1
3669,09	0,98	0,129			2,67		
3669,34	0,06	0,108			2,66		
3669,59	0,36	0,137			2,7		
3669,78	0,31	0,136	0,46	0,54	2,71	1	2
3670,1	3,8	0,158			2,69		
3670,33	4,36	0,17			2,66		
3670,47	1,67	0,15			2,67		
3670,75	1,33	0,15	0,51	0,49	2,67	0,5	1,5
3671,05	0,44	0,147			2,68		
3671,34	1,64	0,142			2,67		
3671,57	2,55	0,131			2,66		
3671,69	0,72	0,137	0,46	0,54	2,68	1	2
3672,16	0,02	0,133			2,66		
3672,41	0,07	0,082			2,67		
3672,71	0,27	0,135	0,37	0,63	2,68	0	2
3673,08	0,1	0,14			2,69		
3673,33	0,11	0,121			2,68		
3673,69	0,04	0,131	0,38	0,62	2,68	0,5	2
3674	0,08	0,107			2,67		
3674,22	0,16	0,128			2,69		
3674,45	0,11	0,127			2,68		
3674,65	0	0,129	0,37	0,63	2,68	0	3

3675,15	0,06	0,43			2,68		
3675,4	0,09	0,108			2,69		
3675,69	0,05	0,12	0,37	0,7	2,69	1	2
3675,91	0,05	0,111			2,67		
3676,16	0,04	0,116			2,67		
3676,41	0,04	0,094			2,68		
3676,69	0,04	0,101	0,3	0,7	2,68	3	6
3677,05	0,02	0,096			2,88		
3677,29	0,02	0,099			2,67		
3677,52	0,02	0,079			2,67		
3677,77	0,02	0,086	0,32	0,68	2,69	4	5
3678,03	0,01	0,084			2,67		
3678,28	0	0,069			2,67		
3678,53	0	0,022			2,69		
3679,94	0	0,035			2,69		
3680,11	0	0,036	0,15	0,85	2,67	0,5	1,5
3680,23	0	0,034			2,66		
3680	0	0,034			2,67		

Table B6: Core analysis results of F-O2 well (Soekor core analysis section, 1991).

DEPTH (M)	POROSITY (Dec)	PERMEABILITY (KL)	Sg (Dec)	Sw (Dec)	Cal (%)	Dol (%)	Grain Density
3615,19	0,042	0	0,15	0,85	0,5	2,5	2,67
3615,66	0,074	0,04					2,67
3615,92	0,079	0,03					2,66
3616,09	0,09	0,08	0,38	0,62	0	1,5	2,63
3616,38	0,09	0,05					2,66
3616,63	0,103	0,05					2,66
3616,87	0,109	0,13					2,69
3617,05	0,111	0,11	0,43	0,57	1	1	2,68
3617,34	0,1	0,08					2,66
3617,58	0,098	0,08					0,266
3617,86	0,091	0,05					2,66
3618,03	0,1	0,04	0,41	0,59	0	1,5	2,68
3618,28	0,097	0,05					2,66
3618,54	0,094	0,03					2,66
3618,82	0,097	0,11					2,66
3619,05	0,1	0,05	0,41	0,59	0,5	1	2,67
3619,35	0,073	0,01					2,67
3619,61	0,084	0,03					2,67
3619,86	0,082	0,03					2,67
3620,04	0,092	0,03	0,44	0,56	1	0	2,68
3620,37	0,083	0,05					2,66
3620,56	0,065	0,46					2,65
3620,81	0,073	0,03					2,67
3621,03	0,059	0,01	0,35	0,65	0,5	1,5	2,67
3621,35	0,071	0,02					2,66
3621,6	0,08	0,02					2,67

3621,85	0,06	0					2,67
3622,35	0,067	0,01					2,68
3622,6	0,037	0					2,68
3623,03	0,057	0,01	0,31	0,69	1	0	2,66
3623,33	0,068	0,02					2,67
3623,6	0,074	0,03					2,67
3623,83	0,049	0,01					2,69
3624,07	0,042	0,01	0,51	0,49	0	1	2,66
3624,36	0,067	0,03					2,67
3624,62	0,123	5,37					2,68
3624,87	0,149	74,57					2,67
3625,07	0,121	7,98	0,6	0,4	1	0	2,66
3625,35	0,135	55,24					2,65
3625,64	0,091	0,88					2,67
3626,3	0,11	2,63	0,62	0,38	0,5	1	2,67
3626,77	0,111	1,74					2,67
3626,98	0,112	2,2					2,67
3627,14	0,107	1,35	0,59	0,41	1	0,5	2,67
3627,47	0,113	2,83					2,66
3627,72	0,097	0,51					2,67
3627,97	0,113	3,79					2,67
3628,15	0,129	1,8	0,46	0,54	0,5	1	2,67
3628,53	0,101	0,47					2,66
3828,77	0,114	1,25					2,66
3629,14	0,091	0,03	0,49	0,51	0	1	2,69
3629,42	0,144	10,85					2,66
3629,65	0,147	17,61					2,67
3629,91	0,154	45,13					2,66
3630,11	0,136	8,02	0,5	0,5	0	1	2,68

3630,39	0,147	23,82					2,67
3630,64	0,143	17,81					2,66
3630,89	0,159	40,2					2,66
3631,08	0,129	5,88	0,52	0,48	0,5	1	2,68
3631,37	0,149	44,39					2,66
3631,62	0,16	71,65					2,66
3631,87	0,159	64,74					2,66
3632,1	0,159	45,7	0,55	0,45	0,5	1	2,67
3632,36	0,112	4,41					2,67
3632,7	0,062	0,07					2,67
3632,95	0,078	0,14					2,67
3633,14	0,1	0,09	0,52	0,48	1	0	2,67
3633,44	0,106	0,52					2,69
3634,09	0,08	0,19	0,49	0,51	0	1	2,66
3634,31	0,095	0,17					2,67
3634,56	0,087	0,12					2,66
3634,81	0,077	0,02					2,67
3635,11	0,065	0,03	0,39	0,61	0	1	2,64
3635,44	0,096	0,25					2,66
3635,75	0,123	3,31					2,66
3636,02	0,141	14,79	0,53	0,47	0	1	2,67
3636,26	0,137	17,3					2,66
3636,51	0,133	6,08					2,67
3636,77	0,113	1,47					2,67
3637,01	0,114	1,66	0,51	0,49	0,5	1	2,66
3637,23	0,103	0,36					2,66
3637,59	0,101	0,38					2,67
3637,73	0,115	1,03					2,68
3638,14	0,108	0,57	0,45	0,55	1	1	2,68

3638,38	0,104	0,46					2,68
3638,63	0,095	0					2,66
3638,88	0,079	13					2,66
3639,12	0,06	0,05	0,31	0,69	0	1	2,65
3639,34	0,078	0,02					2,67
3639,59	0,097	0,02					2,66
3639,84	0,102	0,21					2,67
3640,07	0,087	0,12	0,39	0,61	0,5	1	2,66
3640,31	0,102	0,12					2,68
3640,56	0,101	0,18					2,66
3640,81	0,099	0,23					2,68
3641,05	0,094	0,13	0,43	0,57	1	1	2,66
3641,33	0,081	0,21					2,65
3641,57	0,073	0,7					2,67
3642,27	0,075	0,01					2,66
3642,52	0,091	0,06					2,68
3642,77	0,078	0,03					2,67
3643,04	0,054	0,02	0,34	0,66	0,5	1	2,65
3643,32	0,069	0,01					2,67
3643,57	0,067	0					2,68
3643,94	0,057	0,01	0,51	0,49	1	1	2,66
3644,32	0,67	0,01					2,67
3611,57	0,088	0,01					2,66
3644,82	0,139	0,3					2,67
3645,05	0,133	2,69	0,72	0,28	0	0	2,66
3645,25	0,126	15,48					2,67
3645,5	0,129	4,65					2,67
3645,75	0,124	3,04					2,67
3645,98	0,138	0,84	0,47	0,53	0	0	2,65

3646,27	0,148	20,94					2,66
3646,52	0,151	22,13					2,67
3646,77	0,153	16,19					2,66
3647,05	0,145	36,84	0,55	0,45	0,5	0,5	2,65
3647,31	0,135	18,33					2,66
3647,56	0,124	7,8					2,67
3647,81	0,126	4,83					2,67
3648,08	0,139	1,82	0,46	0,54	0	0	2,67
3648,32	0,131	16,89					2,67
3648,57	0,127	2,73					2,67
3648,81	0,137	0,42					2,67
3649,06	0,144	0,64	0,52	0,48	0,5	0,5	2,65
3649,3	0,146	8,77					2,66
3649,55	0,109	13,54					2,67
3649,8	0,104	6,94					2,68
3650,05	0,125	0,29	0,52	0,48	1	1	2,65
3650,37	0,133	0,22					2,67
3650,62	0,107	0,84					2,66
3650,95	0,126	1,62	0,47	0,53	0,5	0,5	2,65
3651,23	0,117	0,26					2,66
3651,48	0,131	0,83					2,69
3651,75	0,137	0,22					2,68
3652,05	0,13	2,02	0,42	0,58	1	1	2,65
3652,55	26,62	0,165			2,67		
3652,75	45,87	0,121	0,52	0,48	2,61	0,5	1
3653,04	7,05	0,124			2,66		
3653,29	0,02	0,094			2,68		
3653,54	0,02	0,097			2,68		
3653,75	0,18	0,106	0,33	0,67	2,65	0	1,5

3653,08	0,81	0,126			2,66		
3653,33	0,12	0,117			2,67		
3654,58	0,86	0,121			2,66		
3654,71	0,15	0,087	0,38	0,62	2,65	0,5	1,5
3655	0,02	0,095			2,69		
3655,29	0,09	0,108			2,67		
3655,54	0,01	0,08			2,69		
3655,68	0	0,036	0,17	0,83	2,66	0,5	1
3626	0	0,055			2,69		
3656,25	0,02	0,094			2,68		
3656,5	0,03	0,1			2,72		
3656,66	0,04	0,075	0,27	0,73	2,65	0,5	1,5
3657	0,02	0,094			2,68		
3657,25	0,01	0,086			2,69		
3657,5	0,02	0,09			2,68		
3657,65	0,03	0,084	0,27	0,73	2,64	0	1,5
3657,94	0,03	0,098			2,69		
3658,19	0,03	0,108			2,69		
3658,44	0,02	0,099			2,69		
3658,44	0,02	0,073			2,69		
3658,7	0,03	0,106	0,26	0,74	2,65	0,5	2
3659	0,04	0,109			2,69		
3659,25	0,07	0,113			2,69		
3659,5	0,02	0,085			2,69		
3659,69	0,07	0,118	0,3	0,7	2,65	0	3
3660,03	0,08	0,117			2,7		
3660,28	0	0,057			2,7		
3660,6	0,04	0,107	0,16	0,84	2,66	0,5	3
3660,87	0,02	0,094			2,68		

3661,13	0,01	0,088			2,69		
3661,39	0	0,066			2,68		
3661,6	0,01	0,086	0,17	0,83	2,66	0,5	1
3661,89	0,01	0,089			2,68		
3662,14	0,01	0,085			2,69		
3662,39	0	0,064			2,69		
3662,55	0,01	0,094	0,19	0,81	2,67	0,5	2
3662,85	0,01	0,089			2,69		
3663,1	0,01	0,083			2,69		
3663,35	0	0,035			2,7		
3663,62	0	0,066	0,18	0,82	2,66	1	1
3663,92	0	0,063			2,69		
3664,18	0	0,065			2,68		
3664,41	0	0,052			2,69		
3664,63	0,05	0,108	0,16	0,84	2,7	0,5	1
3665,02	0,02	0,102			2,67		
3665,27	0,03	0,099			2,68		
3665,62	0,26	0,116	0,22	0,78	2,67	0	2
3665,94	0,32	0,11			2,67		
3666,18	0,03	0,101			2,67		
3666,43	0	0,06			2,68		
3666,62	0,02	0,102	0,16	0,84	2,71	0	2
3666,92	0,03	0,107			2,68		
3667,17	0,37	0,125			2,68		
3667,58	0,58	0,128	0,38	0,62	2,67	0	3,5
3668,03	0,37	0,127			2,67		
3668,53	0,81	0,116			2,67		
3668,78	0,15	0,123	0,47	0,53	2,66	0,5	1
3669,09	0,98	0,129			2,67		

3669,34	0,06	0,108			2,66		
3669,59	0,36	0,137			2,7		
3669,78	0,31	0,136	0,46	0,54	2,71	1	2
3670,1	3,8	0,158			2,69		
3670,33	4,36	0,17			2,66		
3670,47	1,67	0,15			2,67		
3670,75	1,33	0,15	0,51	0,49	2,67	0,5	1,5
3671,05	0,44	0,147			2,68		
3671,34	1,64	0,142			2,67		
3671,57	2,55	0,131			2,66		
3671,69	0,72	0,137	0,46	0,54	2,68	1	2
3672,16	0,02	0,133			2,66		
3672,41	0,07	0,082			2,67		
3672,71	0,27	0,135	0,37	0,63	2,68	0	2
3673,08	0,1	0,14			2,69		
3673,33	0,11	0,121			2,68		
3673,69	0,04	0,131	0,38	0,62	2,68	0,5	2
3674	0,08	0,107			2,67		
3674,22	0,16	0,128			2,69		
3674,45	0,11	0,127			2,68		
3674,65	0	0,129	0,37	0,63	2,68	0	3
3675,15	0,06	0,43			2,68		
3675,4	0,09	0,108			2,69		
3675,69	0,05	0,12	0,37	0,7	2,69	1	2
3675,91	0,05	0,111			2,67		
3676,16	0,04	0,116			2,67		
3676,41	0,04	0,094			2,68		
3676,69	0,04	0,101	0,3	0,7	2,68	3	6
3677,05	0,02	0,096			2,88		

3677,29	0,02	0,099			2,67		
3677,52	0,02	0,079			2,67		
3677,77	0,02	0,086	0,32	0,68	2,69	4	5
3678,03	0,01	0,084			2,67		
3678,28	0	0,069			2,67		
3678,53	0	0,022			2,69		
3679,94	0	0,035			2,69		
3680,11	0	0,036	0,15	0,85	2,67	0,5	1,5
3680,23	0	0,034			2,66		
3680,48	0	0,034			2,67		

APPENDIX C- Gassmann fluid substitution results

C1. Gassmann fluid substitution results of F-O1.

Fluid properties

Flushed zone

F-O1	Brine	Oil	Gas
Density (gm/cc)	0.9539	0.6435	0.1644
Bulk modulus (Gpa)	2.3198	0.3283	0.0589
Velocity (m/s)	1559.5	714.3	598.3

Reservoir zone

	Brine	Oil	Gas
Density (gm/cc)	0.9539	0.6435	0.1644
Bulk modulus (Gpa)	2.3198	0.3283	0.0589
Velocity (m/s)	1559.5	714.3	598.3

Matrix properties

Mineral name	Quartz	Wet clay
Density (gm/cc)	2.65	2.6
Modulus (Gpa)	37	21
Velocity (m/s)	6050	3140

Average Gassmann results

Log Inputs

Data from interval: 3701.9-3810.6

	Log value	Value used
Vp (m/s)	4530	4530
Vs (m/s)	2787	2787
Vp/Vs ratio	1.625	1.625
Poison ratio	0.195	0.195
Density (gm/cc)	2.573	2.573
Quartz (dec)	1	1
Wet clay (dec)	0	0
Porosity (dec)	0.065	0.032
Sw (dec)	0.169	0.169
Sxo (dec)	0.049	0.049

Flushed zone fluid mixture is gas/brine

Fluid mixing law is 3

Fluid properties

Fluid Density (gm/cc)	0.203
Fluid Modulus (Gpa)	0.0592
Fluid Velocity (m/s)	539

Dry rock properties

Bulk Modulus (Gpa)	25.989
Shear Modulus (Gpa)	19.985
Poison ratio	0.194
Modulus ratio (K/u)	1.3

C2. Gassmann fluid substitution results of F-O2.

Fluid properties

Flushed zone

F-O2	Brine	Oil	Gas
Density (gm/cc)	0.9527	0.6454	0.1605
Bulk modulus (Gpa)	2.3063	0.3249	0.0571
Velocity (m/s)	1555.9	709.5	596.2

Reservoir zone

	Brine	Oil	Gas
Density (gm/cc)	0.9527	0.6454	0.1605
Bulk modulus (Gpa)	2.3063	0.3249	0.0571
Velocity (m/s)	1555.9	709.5	596.2

Matrix properties

Mineral name	Quartz	Wet clay
Density (gm/cc)	2.65	2.6
Modulus (Gpa)	37	21
Velocity (m/s)	6050	3140

Average Gassmann results

Log Inputs

Data from interval:3615.5-3685.4

	Log value	Value used
Vp (m/s)	4127	4127
Vs (m/s)	2487	2487
Vp/Vs ratio	1.659	1.659
Poison ratio	0.215	0.215
Density (gm/cc)	2.501	2.501
Quartz (dec)	1	1
Wet clay (dec)	0	0
Porosity (dec)	0.076	0.073
Sw (dec)	0.169	0.169
Sxo (dec)	0.556	0.556

Flushed zone fluid mixture is gas/brine

Fluid mixing law is 3

Fluid properties

Fluid Density (gm/cc)	0.601
Fluid Modulus (Gpa)	0..4435
Fluid Velocity (m/s)	859

Dry rock properties

Bulk Modulus (Gpa)	20.866
Shear Modulus (Gpa)	15.468
Poison ratio	0.203

1.349

C3. Gassmann fluid substitution results of E-M4.

Fluid properties

Flushed zone

E-M4	Brine	Oil	Gas
Density (gm/cc)	0.988	0.6446	0.1861
Bulk modulus (Gpa)	2.5874	0.0.3979	0.0615
Velocity (m/s)	1618.3	785.7	574.6

Reservoir zone

	Brine	Oil	Gas
Density (gm/cc)	0.988	0.6446	0.1861
Bulk modulus (Gpa)	2.5874	0.0.3979	0.0615
Velocity (m/s)	1618.3	785.7	574.6

Matrix properties

Mineral name	Quartz	Wet clay
Density (gm/cc)	2.65	2.6
Modulus (Gpa)	37	21
Velocity (m/s)	6050	3140

Average Gassmann results

Log Inputs

Data from interval: 2558.1m-2.665.8m

	Log value	Value used
Vp (m/s)	4296	4296
Vs (m/s)	2599	2599
Vp/Vs ratio	1.653	1.653
Poison ratio	0.211	0.211
Density (gm/cc)	2.464	
Quartz (dec)	1	1
Wet clay (dec)	0	0
Porosity (dec)	0.102	0.099
Sw (dec)	0.187	0.187
Sxo (dec)	0.732	0.732

Flushed zone fluid mixture is gas/brine

Fluid mixing law is 3

Fluid properties

Fluid Density (gm/cc)	0.773
Fluid Modulus (Gpa)	1.0508
Fluid Velocity (m/s)	1166

Dry rock properties

Bulk Modulus (Gpa)	21.607
Shear Modulus (Gpa)	16.647
Poison ratio	0.193
Modulus ratio (K/u)	1.298

C4. Gassmann fluid substitution results of E-G1.

Fluid properties

Flushed zone

E-G1	Brine	Oil	Gas
Density (gm/cc)	0.9734	0.5961	0.2448
Bulk modulus (Gpa)	2.5625	0.4534	0.1152
Velocity (m/s)	1622.5	872.2	686.1

Reservoir zone

	Brine	Oil	Gas
Density (gm/cc)	0.9734	0.5961	0.2448
Bulk modulus (Gpa)	2.5625	0.4534	0.1152
Velocity (m/s)	1622.5	872.2	686.1

Matrix properties

Mineral name	Quartz	Wet clay
Density (gm/cc)	2.65	2.6
Modulus (Gpa)	37	21
Velocity (m/s)	6050	3140

Average Gassmann results

Log Inputs

Data from interval:3149.4-3164.6

	Log value	Value used
Vp (m/s)	4433	4433
Vs (m/s)	2709	2709
Vp/Vs ratio	1.636	1.636
Poison ratio	0.202	0.202
Density (gm/cc)	2.566	2.566
Quartz (dec)	1	1
Wet clay (dec)	0	0
Porosity (dec)	0.11	0.044
Sw (dec)	0.494	0.494
Sxo (dec)	0.364	0.364

Flushed zone fluid mixture is Oil/brine

Fluid mixing law is 3

Fluid properties

Fluid Density (gm/cc)	0.733
Fluid Modulus (Gpa)	0.5551
Fluid Velocity (m/s)	870

Dry rock properties

Bulk Modulus (Gpa)	23.875
Shear Modulus (Gpa)	18.53
Poison ratio	0.188
Modulus ratio (K/u)	1.268

C5. Gassmann fluid substitution results of E-CN1.

Fluid properties

Flushed zone

E-CN1	Brine	Oil	Gas
Density (gm/cc)	0.9496	0.6276	0.1514
Bulk modulus (Gpa)	2.2513	0.2708	0.055
Velocity (m/s)	1539.7	656.9	602.5

Reservoir zone

	Brine	Oil	Gas
Density (gm/cc)	0.9546	0.5976	0.2017
Bulk modulus (Gpa)	2.3465	0.3352	0.0856
Velocity (m/s)	1567.9	748.9	651.5

Matrix properties

Mineral name	Quartz	Wet clay
Density (gm/cc)	2.65	2.6
Modulus (Gpa)	37	21
Velocity (m/s)	6050	3140

Average Gassmann results

Log Inputs

Data from interval:4081-4256.7

	Log value	Value used
Vp (m/s)	4598	4598
Vs (m/s)	2842	2842
Vp/Vs ratio	1.618	1.618
Poison ratio	0.191	0.191
Density (gm/cc)	2.581	2.581
Quartz (dec)	1	1
Wet clay (dec)	0	0
Porosity (dec)	0.05	0.036
Sw (dec)	0.2723	0.273
Sxo (dec)	0.729	0.729

Flushed zone fluid mixture is gas/brine

Fluid mixing law is 3

Fluid properties

Fluid Density (gm/cc)	0.733
Fluid Modulus (Gpa)	0.9044
Fluid Velocity (m/s)	1111

Dry rock properties

Bulk Modulus (Gpa)	23.339
Shear Modulus (Gpa)	20.849
Poison ratio	0.167
Modulus ratio (K/u)	1.167

C6. Gassmann fluid substitution results of E-W1.

Fluid properties

Flushed zone

E-W1	Brine	Oil	Gas
Density (gm/cc)	0.9852	0.5963	0.2502
Bulk modulus (Gpa)	2.6525	0.4444	0.1153
Velocity (m/s)	1640	863.3	678.9

Reservoir zone

	Brine	Oil	Gas
Density (gm/cc)	0.9852	0.5963	0.2502
Bulk modulus (Gpa)	2.6525	0.4444	0.1153
Velocity (m/s)	1640	863.3	678.9

Matrix properties

Mineral name	Quartz	Wet clay
Density (gm/cc)	2.65	2.6
Modulus (Gpa)	37	21
Velocity (m/s)	6050	3140

Average Gassmann results

Log Inputs

Data from interval: 3144.8m-3188.1m

	Log value	Value used
Vp (m/s)	4502	4502
Vs (m/s)	2765	2765
Vp/Vs ratio	1.628	1.628
Poison ratio	0.197	0.197
Density (gm/cc)	2.535	2.535
Quartz (dec)	1	1
Wet clay (dec)	0	0
Porosity (dec)	0.124	0.067
Sw (dec)	0.637	0.637
Sxo (dec)	0.927	0.927

Flushed zone fluid mixture is gas/brine

Fluid mixing law is 3

Fluid properties

Fluid Density (gm/cc)	0.931
Fluid Modulus (Gpa)	2.1356
Fluid Velocity (m/s)	1514

Dry rock properties

Bulk Modulus (Gpa)	21.027
Shear Modulus (Gpa)	19.378
Poison ratio	0.147
Modulus ratio (K/u)	1.085

C7. Gassmann fluid substitution results of F-A10.

Fluid properties

Flushed zone

F-A10	Brine	Oil	Gas
Density (gm/cc)	0.9828	0.6446	0.1851
Bulk modulus (Gpa)	2.5546	0.3953	0.0613
Velocity (m/s)	1612	783.1	572.4

Reservoir zone

	Brine	Oil	Gas
Density (gm/cc)	0.9828	0.6446	0.1851
Bulk modulus (Gpa)	2.5546	0.3953	0.0613
Velocity (m/s)	1612	783.1	572.4

Matrix properties

Mineral name	Quartz	Wet clay
Density (gm/cc)	2.65	2.6
Modulus (Gpa)	37	21
Velocity (m/s)	6050	3140

Average Gassmann results

Log Inputs

Data from interval:2712.2-2949.8

	Log value	Value used
Vp (m/s)	4335	4335
Vs (m/s)	2630	2630
Vp/Vs ratio	1.648	1.648
Poison ratio	0.209	0.209
Density (gm/cc)	2.455	2.455
Quartz (dec)	1	1
Wet clay (dec)	0	0
Porosity (dec)	0.104	0.098
Sw (dec)	0.512	0.512
Sxo (dec)	0.593	0.593

Flushed zone fluid mixture is gas/brine

Fluid mixing law is 3

Fluid properties

Fluid Density (gm/cc)	0.658
Fluid Modulus (Gpa)	0.582
Fluid Velocity (m/s)	940

Dry rock properties

Bulk Modulus (Gpa)	22.64
Shear Modulus (Gpa)	16.989
Poison ratio	0.2
Modulus ratio (K/u)	1.333

C8. Gassmann fluid substitution results of F-A11.

Flushed zone

F-A11	Brine	Oil	Gas
Density (gm/cc)	0.9868	0.6213	0.2194
Bulk modulus (Gpa)	2.6188	0.4016	0.0836
Velocity (m/s)	1629.1	804	617.3

Reservoir zone

	Brine	Oil	Gas
Density (gm/cc)	0.9868	0.6213	0.2194
Bulk modulus (Gpa)	2.6188	0.4016	0.0836
Velocity (m/s)	1629.1	804	617.3

Matrix properties

Mineral name	Quartz	Wet clay
Density (gm/cc)	2.65	2.6
Modulus (Gpa)	37	21
Velocity (m/s)	6050	3140

Average Gassmann results

Log Inputs

Data from interval: 2761.1 - 2818.8

	Log value	Value used
Vp (m/s)	4392	4392
Vs (m/s)	2676	2676
Vp/Vs ratio	1.641	1.641
Poison ratio	0.205	0.205
Density (gm/cc)	2.472	2.472
Quartz (dec)	1	1
Wet clay (dec)	0	0
Porosity (dec)	0.114	0.09
Sw (dec)	0.465	0.465
Sxo (dec)	0.601	0.601

Flushed zone fluid mixture is gas/brine

Fluid mixing law is 3

Fluid properties

Fluid Density (gm/cc)	0.681
Fluid Modulus (Gpa)	0.6347
Fluid Velocity (m/s)	966

Dry rock properties

Bulk Modulus (Gpa)	23.143
Shear Modulus (Gpa)	17.696
Poison ratio	0.195
Modulus ratio (K/u)	1.308

C9. Gassmann fluid substitution results of F-A13.

Fluid properties

Flushed zone

F-A13	Brine	Oil	Gas
Density (gm/cc)	0.9903	0.6206	0.223
Bulk modulus (Gpa)	2.6441	0.4071	0.0848
Velocity (m/s)	1634	809.9	616.6

Reservoir zone

	Brine	Oil	Gas
Density (gm/cc)	0.9924	0.6202	0.2253
Bulk modulus (Gpa)	2.6581	0.4103	0.0856
Velocity (m/s)	1636.6	813.4	616.4

Matrix properties

Mineral name	Quartz	Wet clay
Density (gm/cc)	2.65	2.6
Modulus (Gpa)	37	21
Velocity (m/s)	6050	3140

Average Gassmann results

Log Inputs

Data from interval:2610.3-2720.1

	Log value	Value used
Vp (m/s)	4034	4034
Vs (m/s)	2388	2388
Vp/Vs ratio	1.689	1.689
Poison ratio	0.23	0.23
Density (gm/cc)	2.426	2.426
Quartz (dec)	1	1
Wet clay (dec)	0	0
Porosity (dec)	0.142	0.104
Sw (dec)	0.122	0.122
Sxo (dec)	0.362	0.362

Flushed zone fluid mixture is gas/brine

Fluid mixing law is 3

Fluid properties

Fluid Density (gm/cc)	0.501
Fluid Modulus (Gpa)	0.2065
Fluid Velocity (m/s)	642

Dry rock properties

Bulk Modulus (Gpa)	20.655
Shear Modulus (Gpa)	13.838
Poison ratio	0.226
Modulus ratio (K/u)	1.493

C10. Gassmann fluid substitution results of F-L1.

Fluid properties

Flushed zone

F-L1	Brine	Oil	Gas
Density (gm/cc)	1.0024	0.6462	0.204
Bulk modulus (Gpa)	2.6716	0.4512	0.06534
Velocity (m/s)	1632.6	835.5	557.5

Reservoir zone

	Brine	Oil	Gas
Density (gm/cc)	1.0024	0.6462	0.204
Bulk modulus (Gpa)	2.6716	0.4512	0.06534
Velocity (m/s)	1632.6	835.6	557.5

Matrix properties

Mineral name	Quartz	Wet clay
Density (gm/cc)	2.65	2.6
Modulus (Gpa)	37	21
Velocity (m/s)	6050	3140

Average Gassmann results

Log Inputs

Data from interval: 2442-2695

	Log value	Value used
Vp (m/s)	4058	4058
Vs (m/s)	2407	2407
Vp/Vs ratio	1.686	1.686
Poison ratio	0.228	0.228
Density (gm/cc)	2.529	2.529
Quartz (dec)	1	1
Wet clay (dec)	0	0
Porosity (dec)	0.063	0.063
Sw (dec)	0.799	0.799
Sxo (dec)	0.667	0.667

Flushed zone fluid mixture is gas/brine

Fluid mixing law is 3

Fluid properties

Fluid Density (gm/cc)	0.737
Fluid Modulus (Gpa)	0.8374
Fluid Velocity (m/s)	1066

Dry rock properties

Bulk Modulus (Gpa)	19.523
Shear Modulus (Gpa)	14.657
Poison ratio	0.2
Modulus ratio (K/u)	1.332

Appendix D- XRD ANALYSIS

D1. F-O2 XRD ANALYSIS OF 3617m, 3623m and 3642m

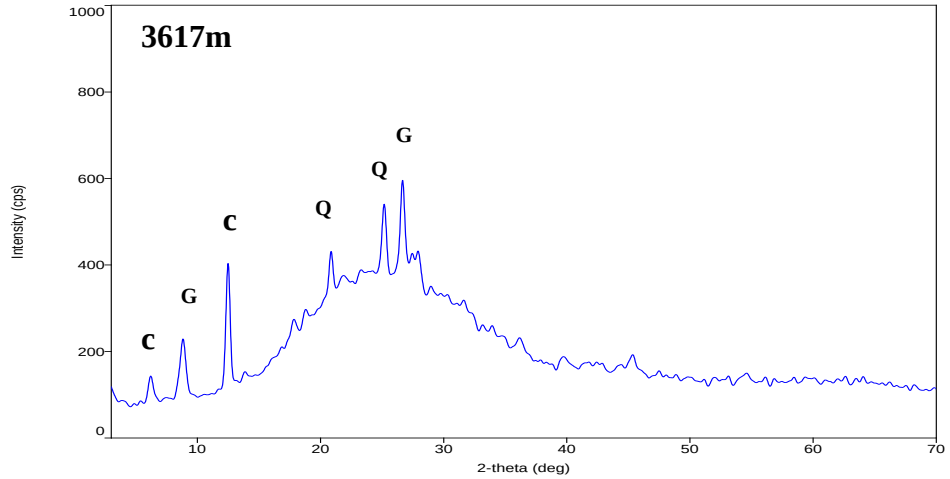

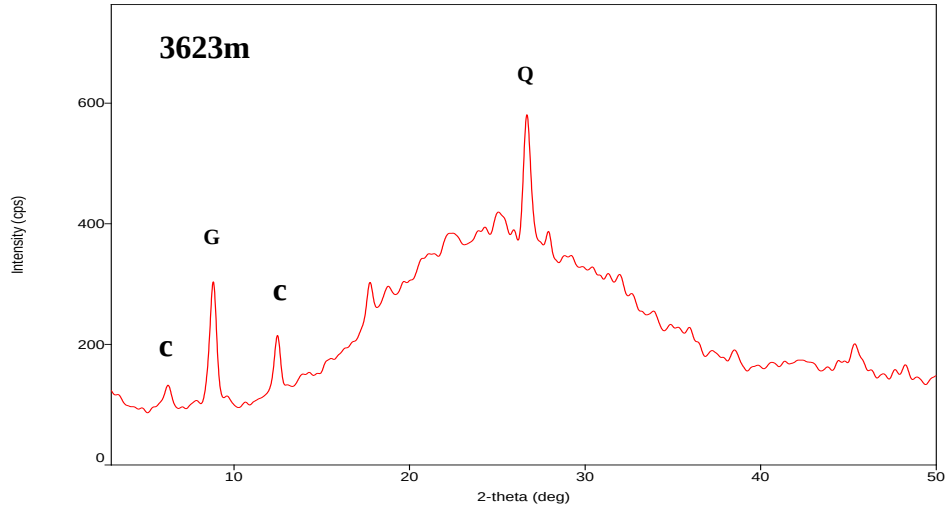

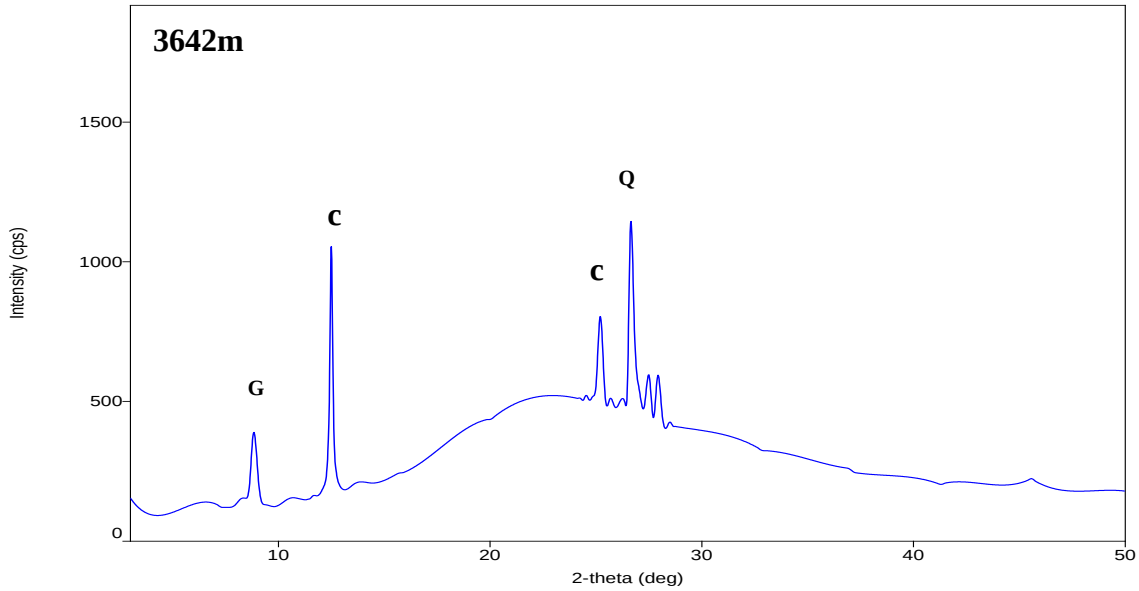

D2. E-CN1 XRD ANALYSIS OF 4259.5m

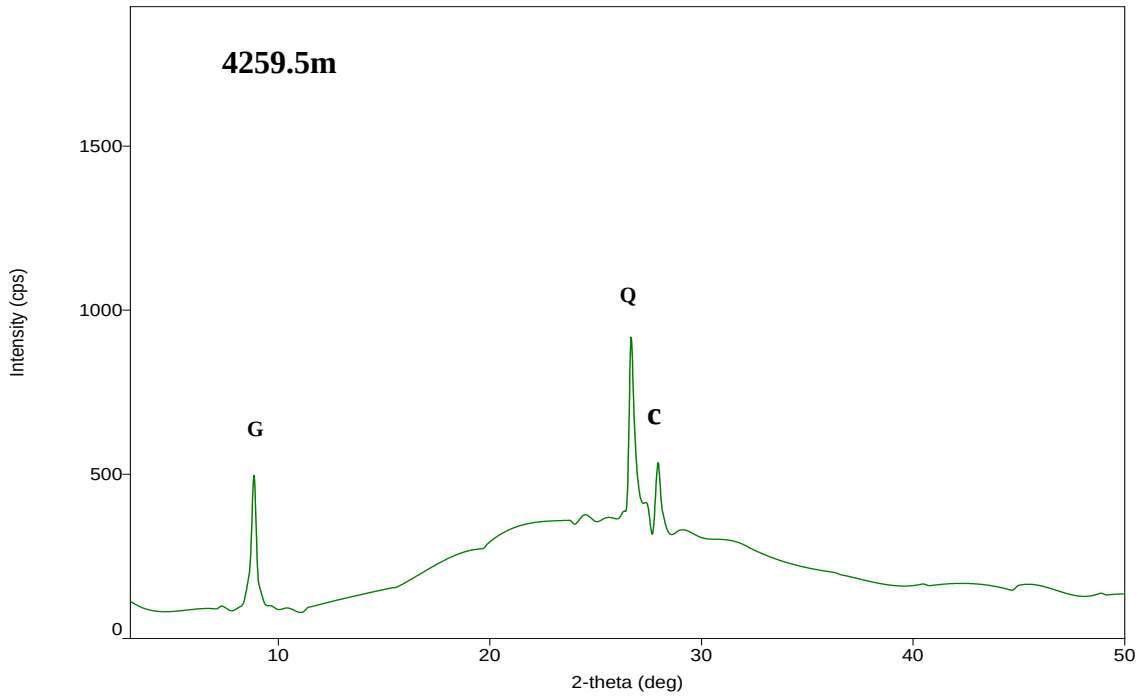

D3. E-G1 XRD ANALYSIS OF 3161.5m and 3161m

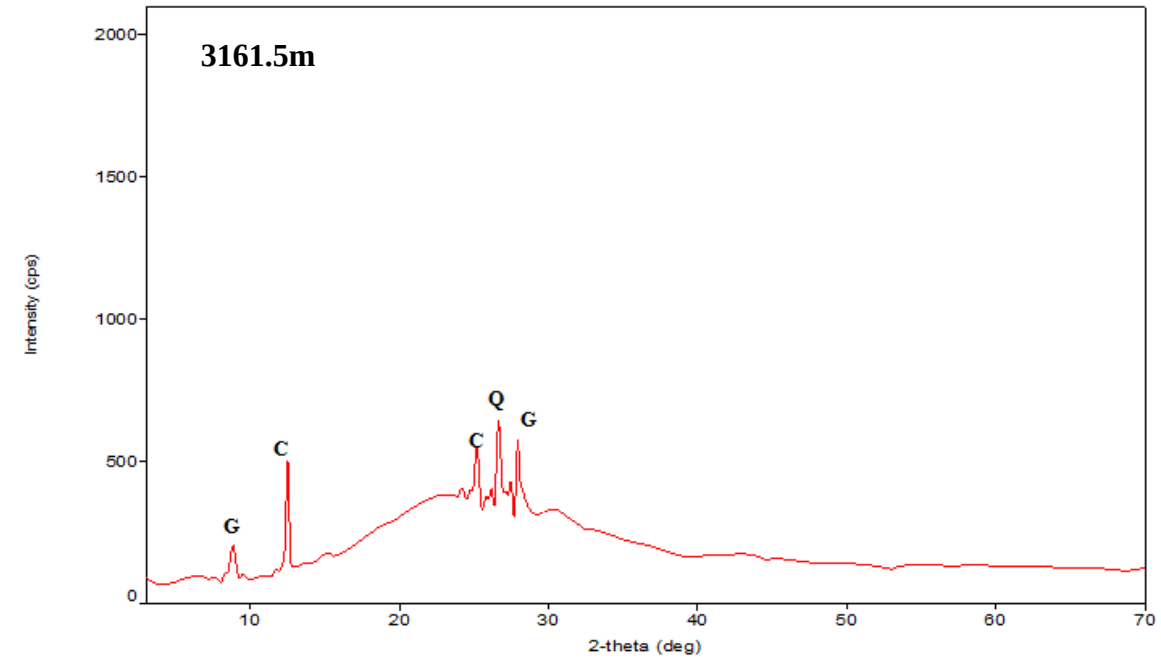

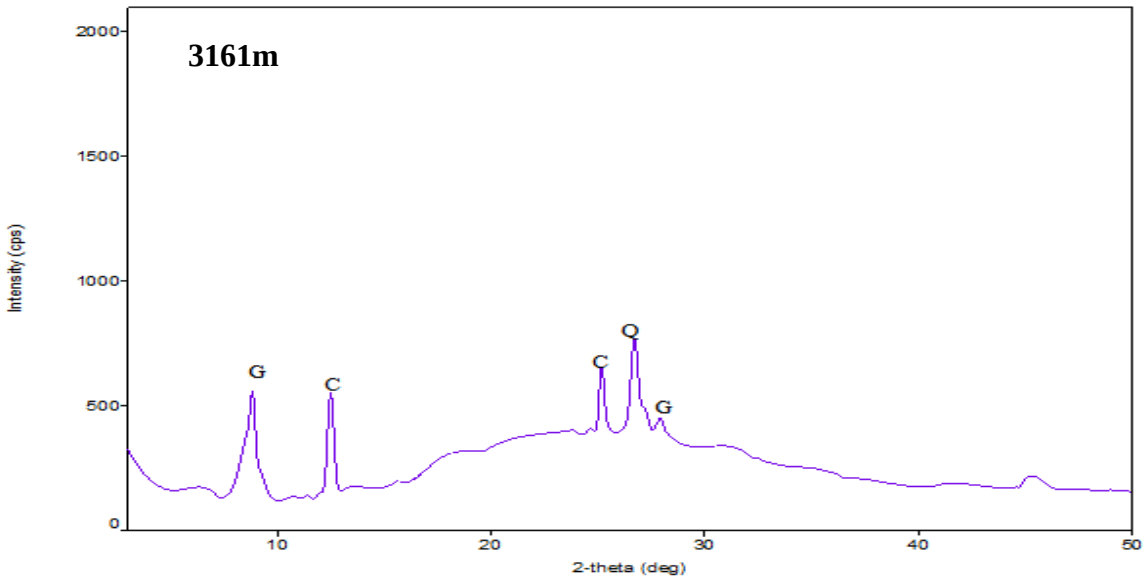

D4. E-W1 XRD ANALYSIS OF 3181m and 3189m

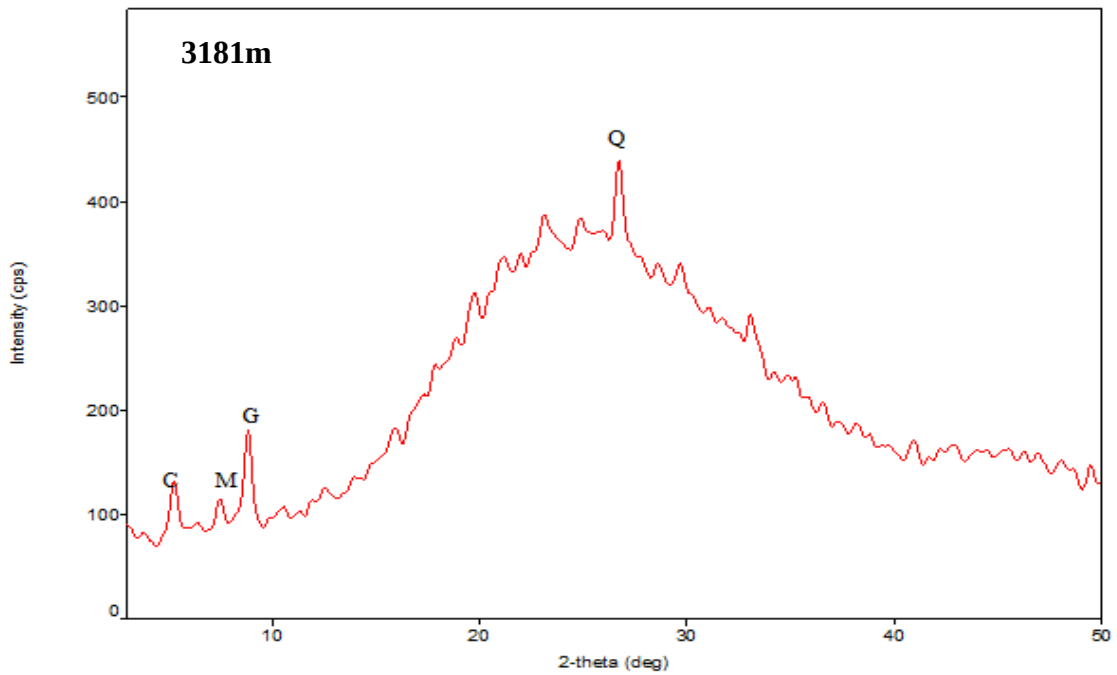

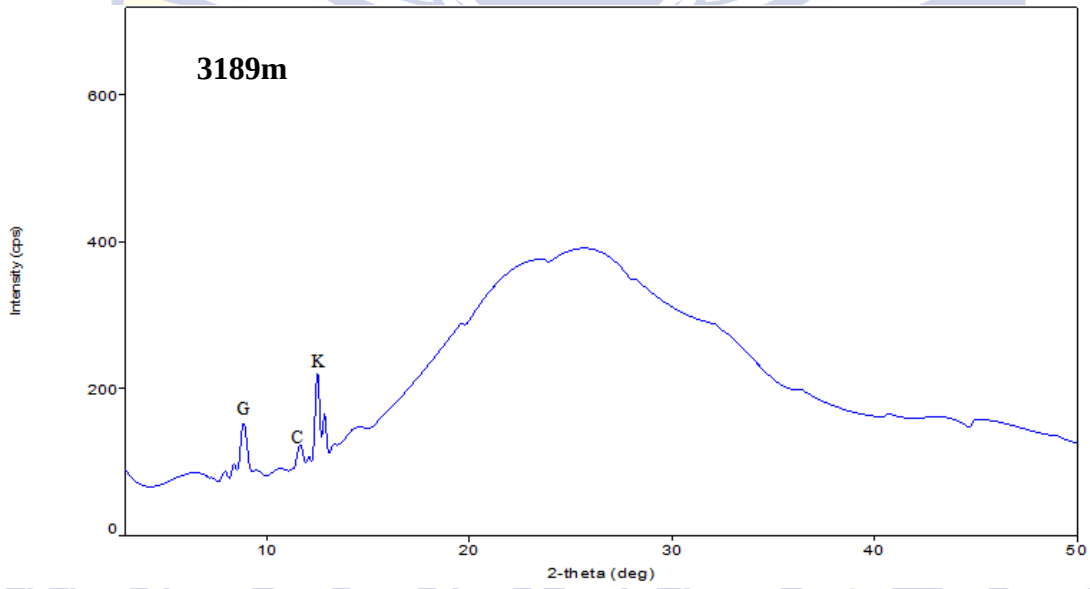

D5. F-A10 XRD ANALYSIS OF 2719.5m and 2755.5m

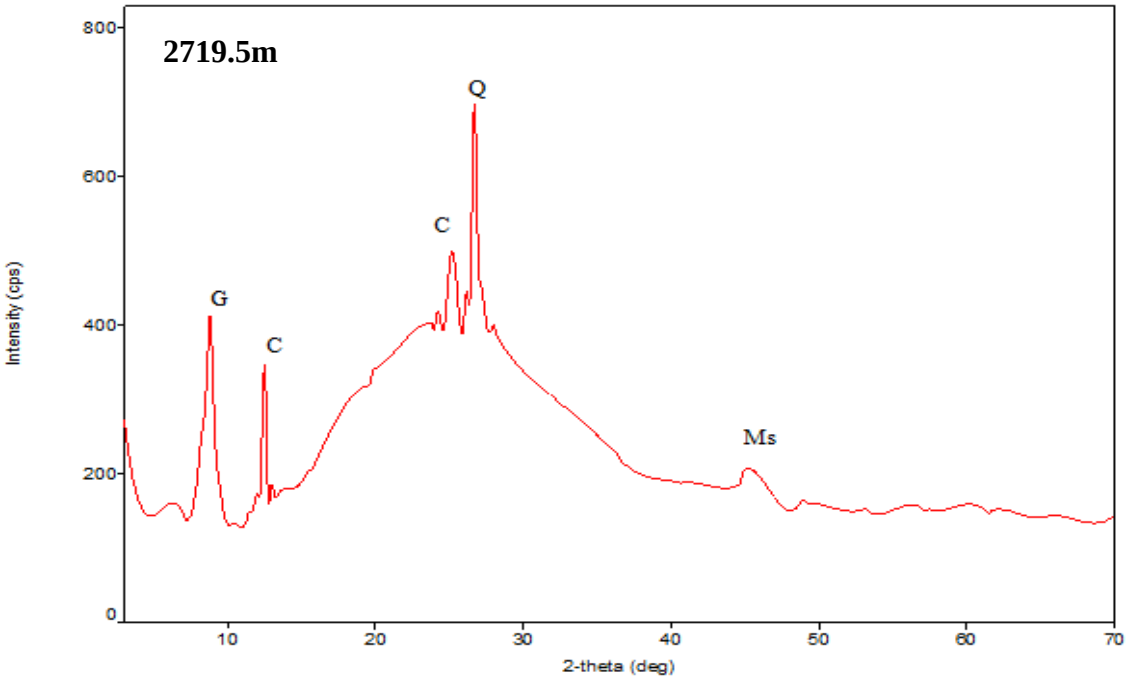

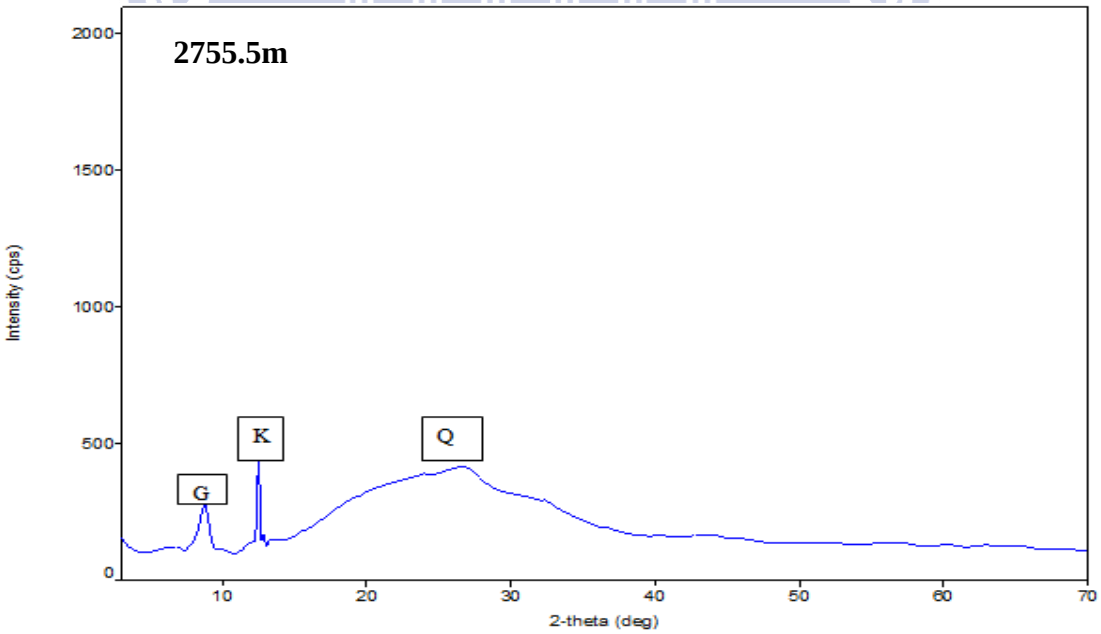

D6. F-A13 XRD ANALYSIS OF 2624.5m and 2615m

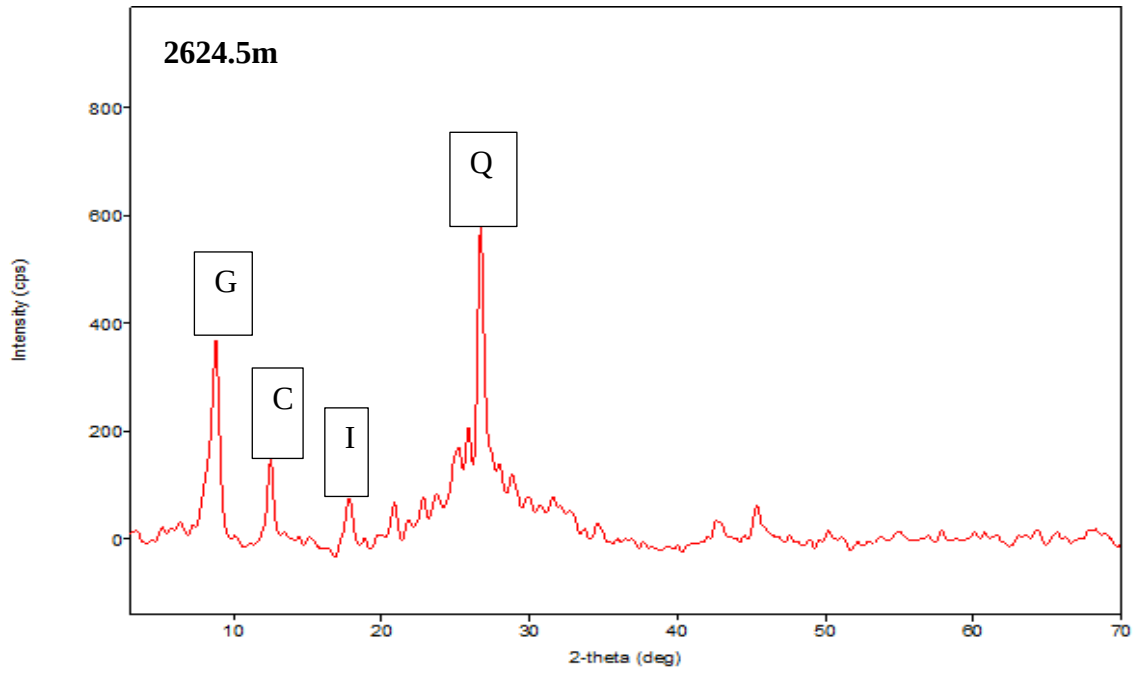

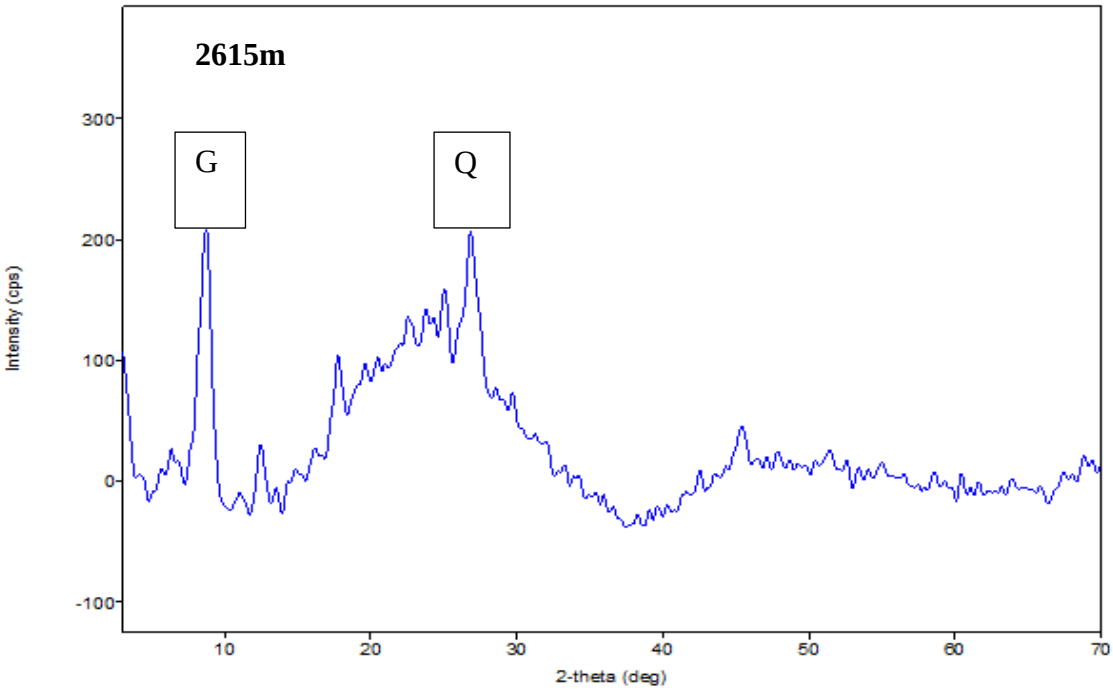

APPENDIX E- SEM/EDS ANALYSIS

E1. F-O1 SEM/EDS ANALYSIS 3712.46m

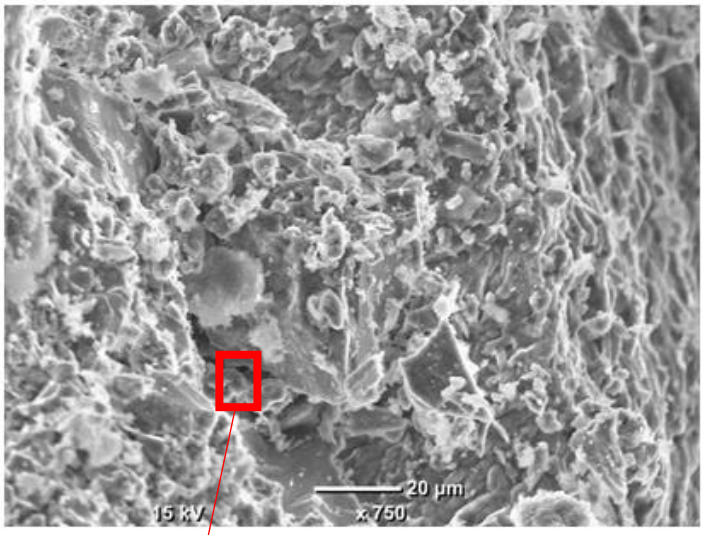

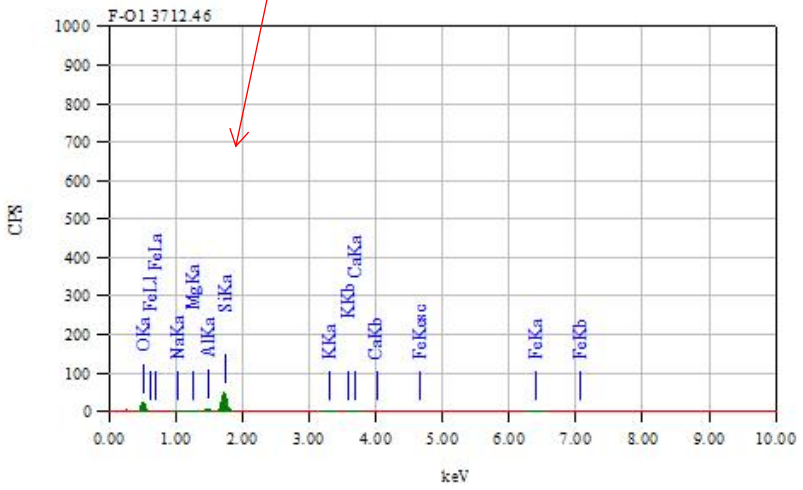

Element	(keV)	Mass%	Sigma	Mol%	Compound	Mass%	Cation	K
O		50.22						
Na K	1.041	1.42	0.20	1.94	Na2O	1.91	0.47	2.4436
Mg K	1.253	0.54	0.14	1.41	MgO	0.90	0.17	0.7541
Al K	1.486	5.21	0.35	6.09	Al2O3	9.85	1.48	10.8718
Si K	1.739	38.18	0.99	85.71	SiO2	81.69	10.39	74.9675
K K	3.312	1.75	0.15	1.41	K2O	2.11	0.34	4.3557
Ca K	3.690	0.96	0.16	1.52	CaO	1.35	0.18	2.5705
Fe K	6.398	1.71	0.26	1.93	FeO	2.20	0.23	4.0368
Total		100.00		100.00		100.00	13.27	

E2. F-O2 XRD/EDS ANALYSIS OF 3617m

3617m

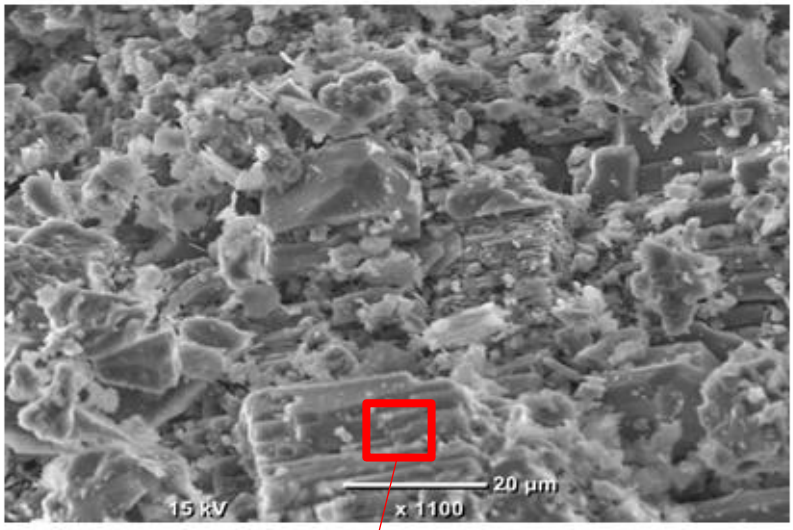

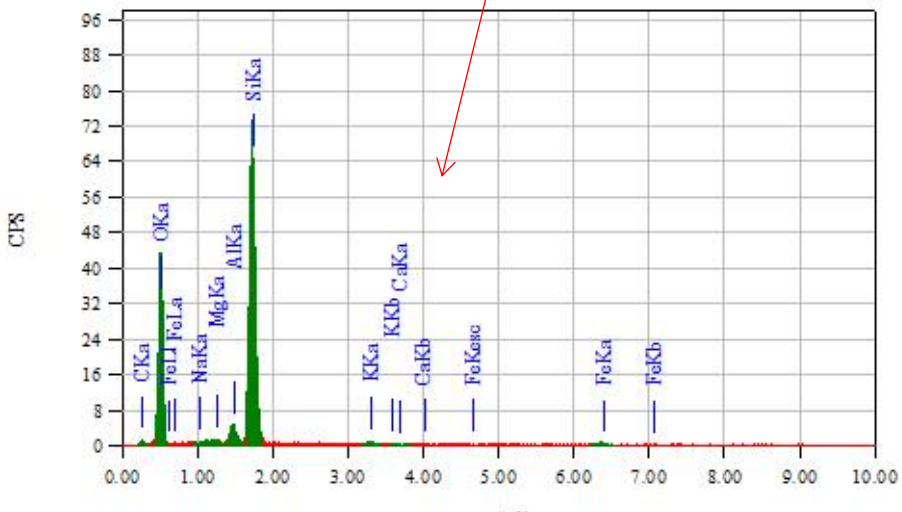

Element	(keV)	Mass%	Sigma	Mol%	Compound	Mass%	Cation	K
C K	0.277	16.82	0.56	50.90	C	16.82	0.00	4.0829
O		43.04						
Na K								
Mg K	1.253	0.35	0.10	0.52	MgO	0.58	0.13	0.5681
Al K	1.486	2.28	0.20	1.53	Al2O3	4.30	0.75	5.5123
Si K	1.739	35.26	0.74	45.64	SiO2	75.43	11.20	83.7630
K K	3.312	0.51	0.08	0.24	K2O	0.62	0.12	1.4523
Ca K	3.690	0.10	0.08	0.09	CaO	0.14	0.02	0.3030
Fe K	6.398	1.64	0.20	1.07	FeO	2.11	0.26	4.3184
Total		100.00		100.00		100.00	12.48	

E3. F-O2 SEM/EDS XRD ANALYSIS OF 3623m

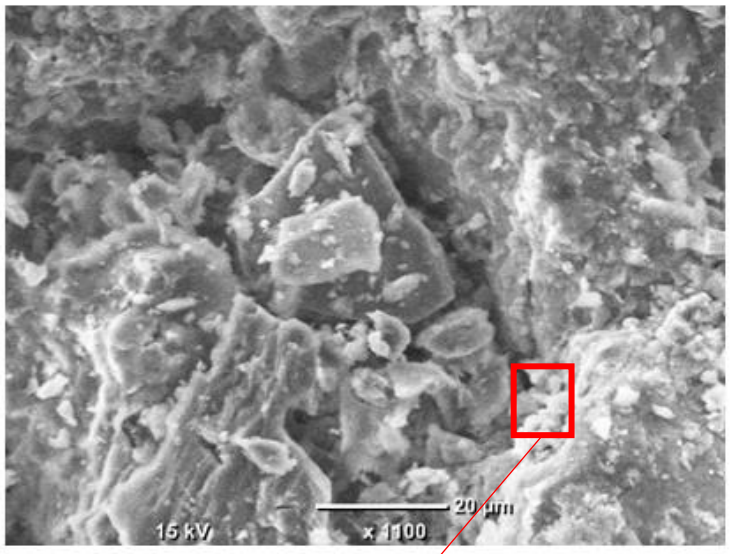

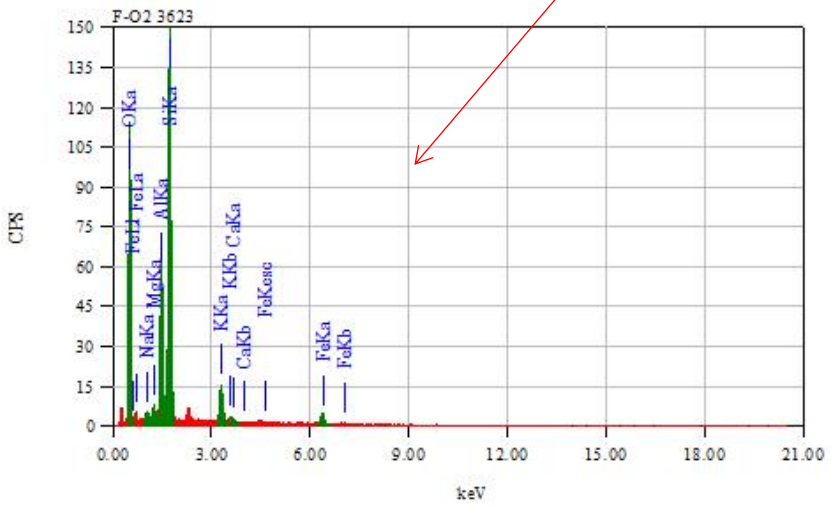

Element	(keV)	Mass%	Sigma	Mol%	Compound	Mass%	Cation	K
O		47.42						
Na K	1.041	0.92	0.09	1.35	Na2O	1.24	0.32	1.5179
Mg K	1.253	1.07	0.08	2.99	MgO	1.78	0.36	1.4547
Al K	1.486	12.04	0.25	15.13	Al2O3	22.75	3.61	24.2356
Si K	1.739	29.30	0.43	70.73	SiO2	62.67	8.45	50.1510
K K	3.312	4.52	0.10	3.92	K2O	5.45	0.94	11.4019
Ca K	3.690	0.26	0.06	0.44	CaO	0.36	0.05	0.6883
Fe K	6.398	4.47	0.17	5.42	FeO	5.75	0.65	10.5506
Total		100.00		100.00		100.00	14.38	

E4. E-CN1 SEM/EDS ANALYSIS OF 4259m

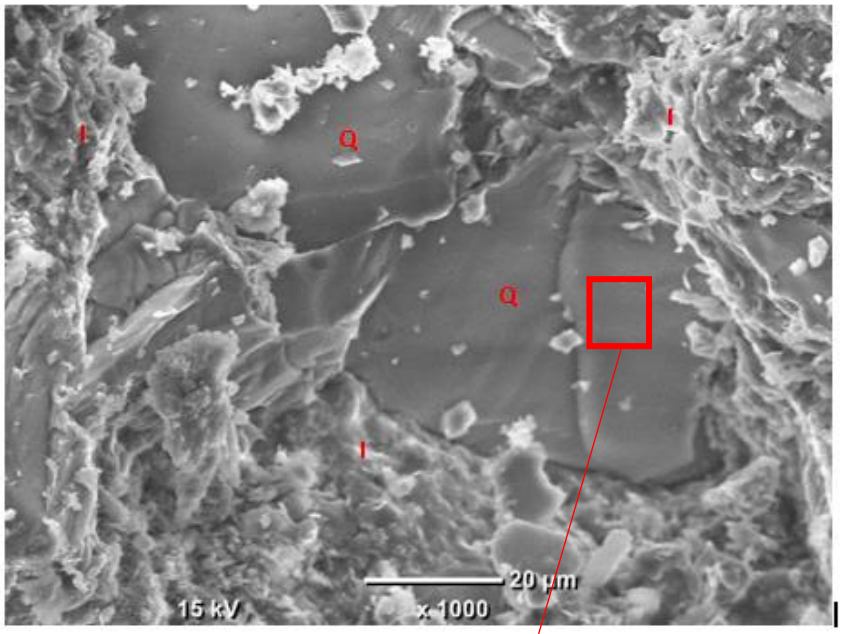

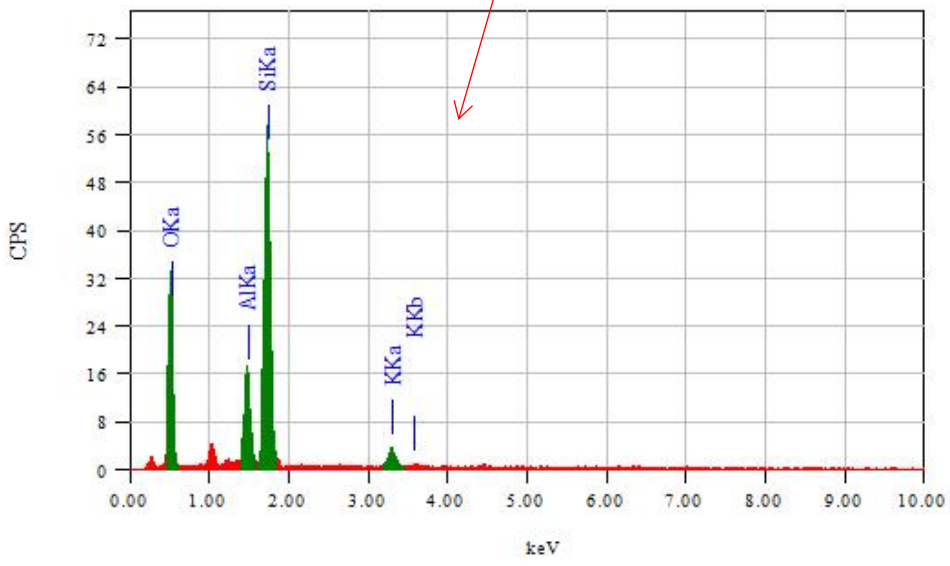

Element	(keV)	Mass%	Sigma	Mol%	Compound	Mass%	Cation	K
O		50.55						
Al K	1.486	10.48	0.40	12.91	Al2O3	19.80	2.95	23.6080
Si K	1.739	35.59	0.84	84.22	SiO2	76.13	9.62	67.8109
K K	3.312	3.38	0.17	2.87	K2O	4.07	0.66	8.5811
Total		100.00		100.00		100.00	13.23	

E5. E-G1 SEM/EDS ANALYSIS OF 3166.5

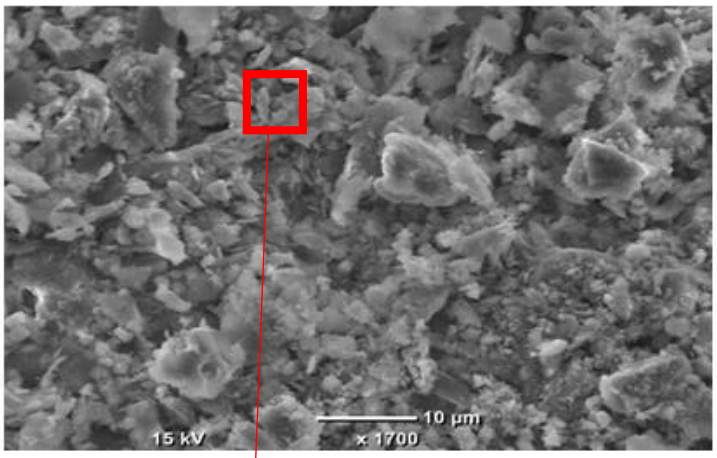

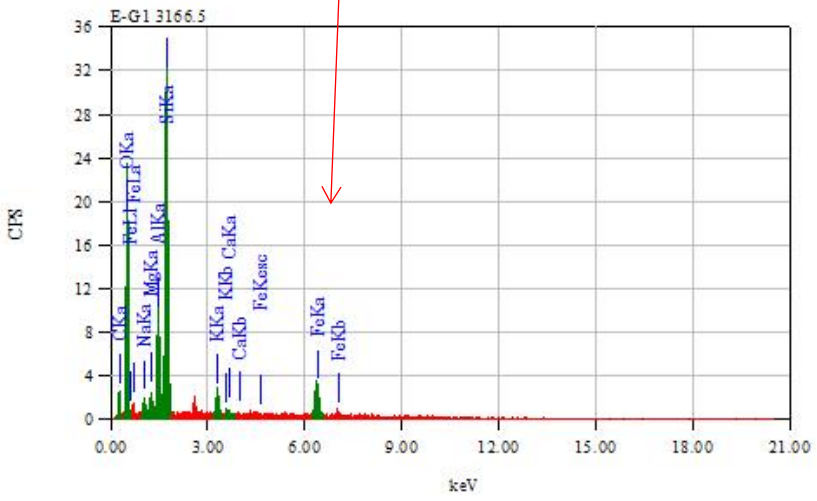

Element	(keV)	Mass%	Sigma	Mol%	Compound	Mass%	Cation	K
C K	0.277	26.01	0.58	66.04	C	26.01	0.00	8.8899
O		32.68						
Na K	1.041	1.76	0.18	1.17	Na2O	2.37	0.90	3.0063
Mg K	1.253	1.21	0.15	1.52	MgO	2.01	0.58	1.6936
Al K	1.486	6.34	0.33	3.58	Al2O3	11.98	2.76	13.3702
Si K	1.739	19.49	0.62	21.16	SiO2	41.70	8.16	39.0047
K K	3.312	2.14	0.12	0.83	K2O	2.58	0.64	6.3806
Ca K	3.690	0.12	0.09	0.09	CaO	0.17	0.04	0.3880
Fe K	6.398	10.25	0.44	5.60	FeO	13.18	2.16	27.2666
Total		100.00		100.00		100.00	15.23	

E6. E-G1 SEM/EDS ANALYSIS 3161m

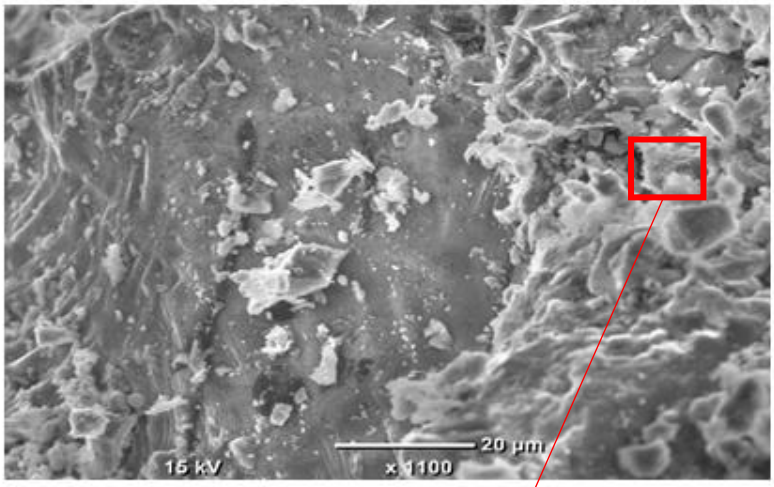

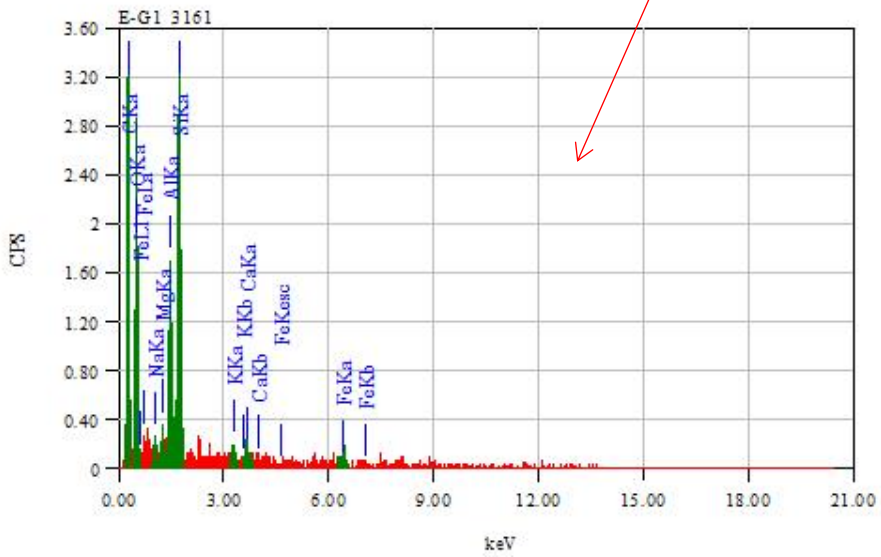

Element	(keV)	Mass%	Sigma	Mol%	Compound	Mass%	Cation	K
C K	0.277	71.57	1.35	93.38	C	71.57	0.00	61.6016
O		13.47						
Na K	1.041	0.63	0.23	0.21	Na2O	0.85	0.78	1.4450
Mg K	1.253	0.73	0.21	0.47	MgO	1.21	0.86	1.3491
Al K	1.486	4.18	0.54	1.21	Al2O3	7.89	4.41	11.1684
Si K	1.739	7.43	0.78	4.15	SiO2	15.90	7.54	18.4333
K K	3.312	0.40	0.13	0.08	K2O	0.48	0.29	1.3341
Ca K	3.690	0.42	0.18	0.16	CaO	0.58	0.30	1.4471
Fe K	6.398	1.19	0.36	0.33	FeO	1.53	0.61	3.2215
Total		100.00		100.00		100.00	14.78	

E7. E-W1 SEM/EDS ANALYSIS 3186.65m.

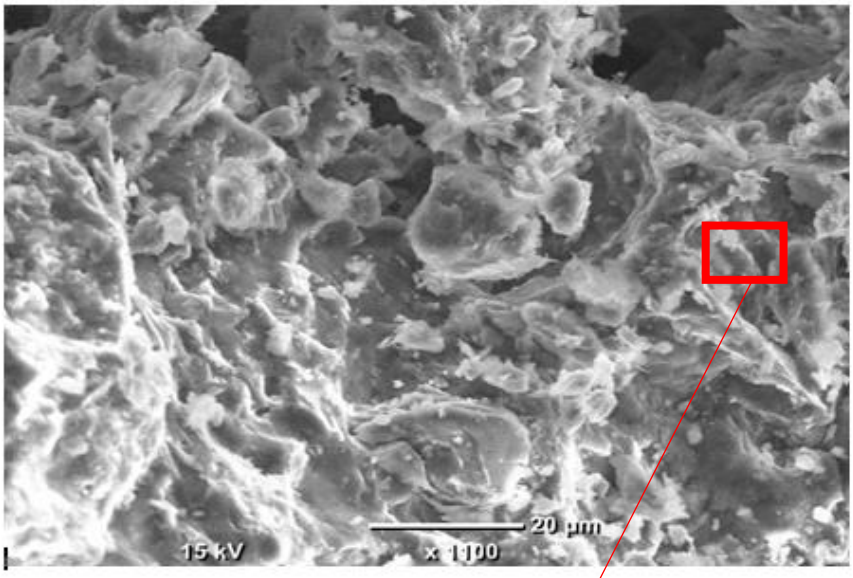

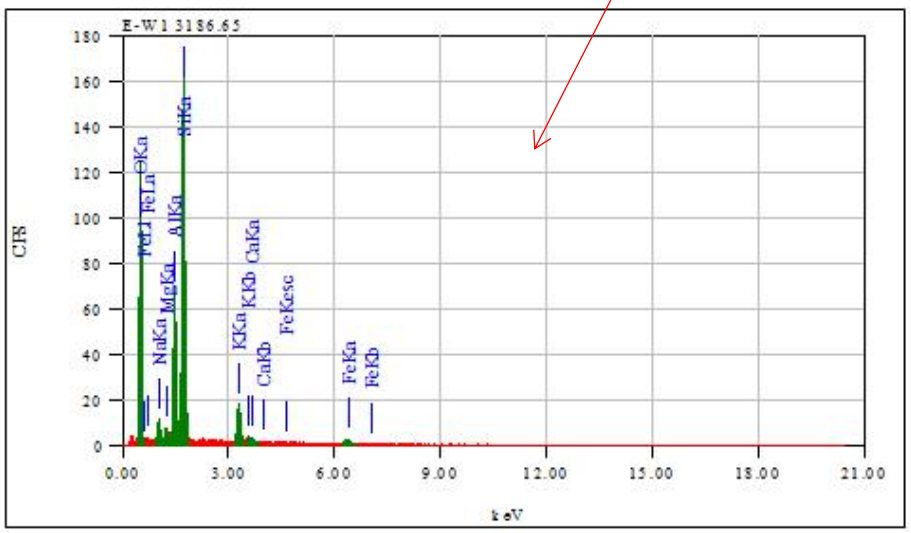

Element	(keV)	Mass%	Sigma	Mol%	Compound	Mass%	Cation	K
O		47.47						
Na K	1.041	2.63	0.11	3.88	Na2O	3.55	0.93	4.6116
Mg K	1.253	1.01	0.08	2.80	MgO	1.67	0.33	1.3794
Al K	1.486	12.12	0.23	15.20	Al2O3	22.90	3.63	24.7063
Si K	1.739	29.20	0.41	70.34	SiO2	62.46	8.41	50.3954
K K	3.312	4.84	0.10	4.19	K2O	5.83	1.00	12.2757
Ca K	3.690	0.61	0.06	1.03	CaO	0.86	0.12	1.6191
Fe K	6.398	2.12	0.12	2.57	FeO	2.72	0.31	5.0125
Total		100.00		100.00		100.00	14.74	

E8. E-W1 SEM/EDS ANALYSIS 3189m.

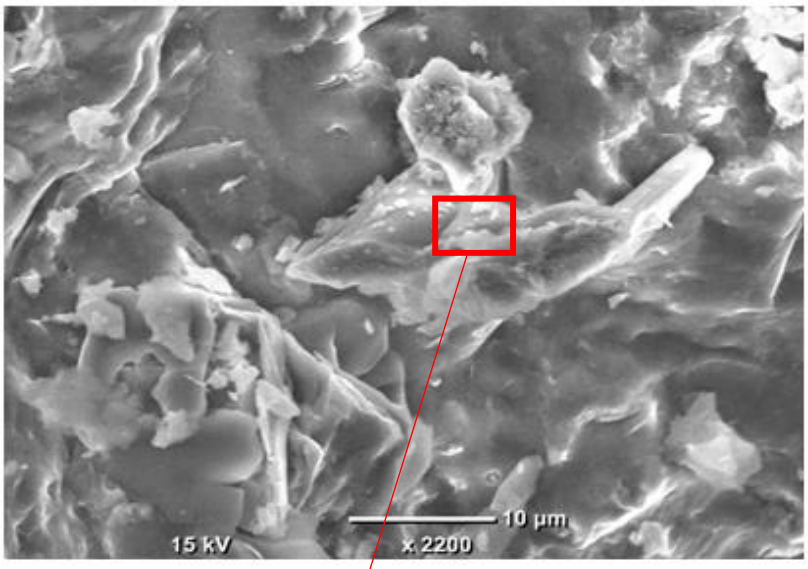

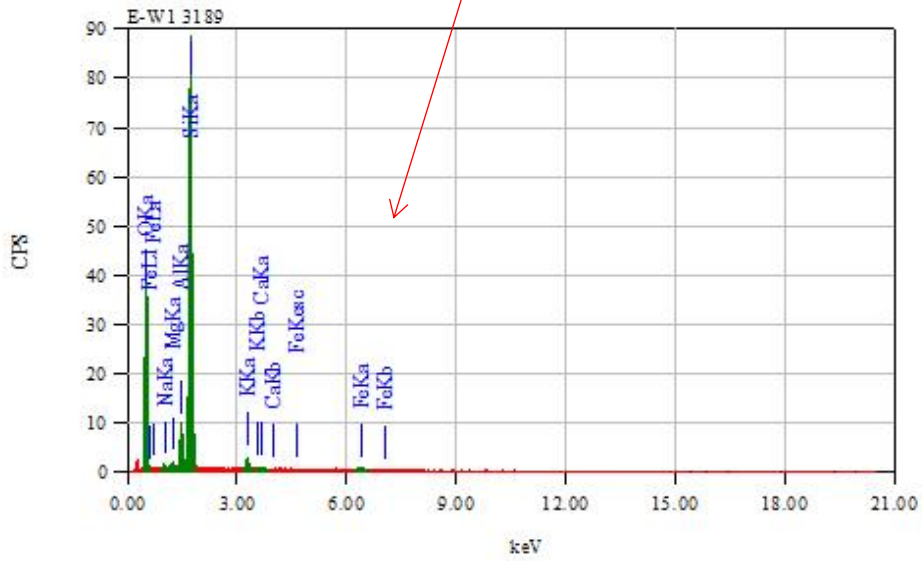

Element	(keV)	Mass%	Sigma	Mol%	Compound	Mass%	Cation	K
O		51.18						
Na K	1.041	0.39	0.11	0.53	Na2O	0.53	0.13	0.6741
Mg K	1.253	0.41	0.10	1.07	MgO	0.69	0.13	0.5899
Al K	1.486	4.48	0.25	5.20	Al2O3	8.46	1.25	9.5398
Si K	1.739	40.37	0.77	90.10	SiO2	86.36	10.78	81.4633
K K	3.312	1.72	0.11	1.38	K2O	2.07	0.33	4.2509
Ca K	3.690	0.21	0.09	0.33	CaO	0.29	0.04	0.5512
Fe K	6.398	1.24	0.18	1.40	FeO	1.60	0.17	2.9306
Total		100.00		100.00		100.00	12.82	

E9. F-A13 SEM/EDS ANALYSIS

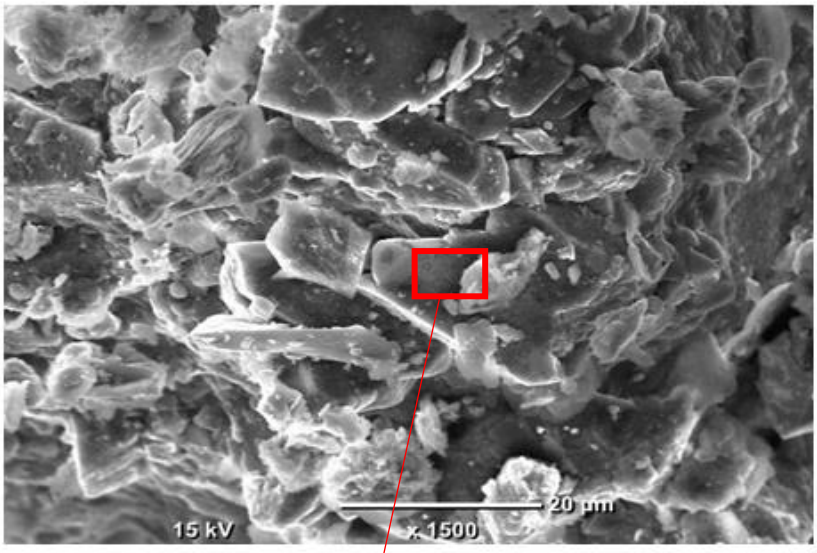

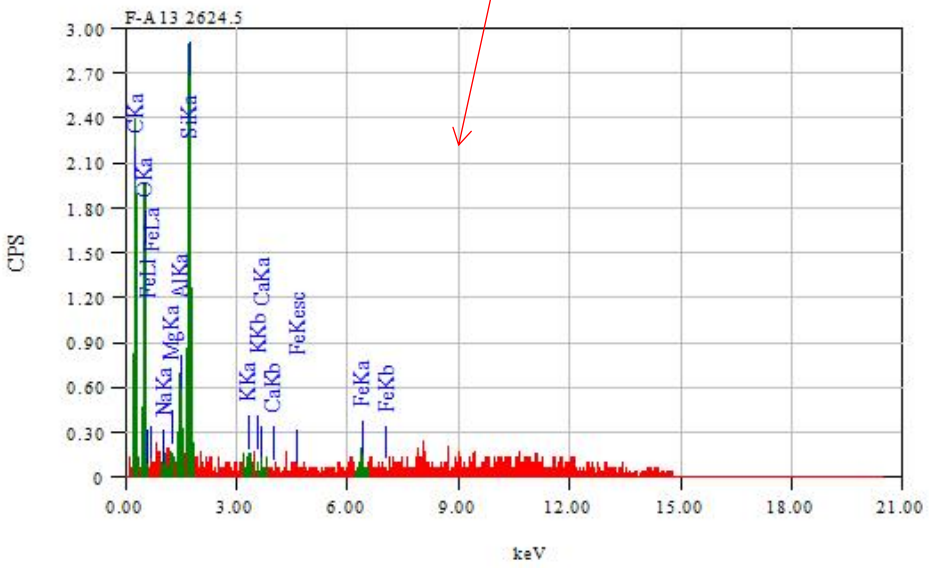

Total Oxide : 24.0

Element	(keV)	Mass%	Sigma	Mol%	Compound	Mass%	Cation	K
C K	0.277	72.54	1.67	93.47	C	72.54	0.00	62.5467
O		13.07						
Na K	1.041	0.46	0.24	0.15	Na2O	0.61	0.58	1.0063
Mg K	1.253	0.21	0.19	0.13	MgO	0.34	0.25	0.3686
Al K	1.486	2.04	0.48	0.58	Al2O3	3.85	2.22	5.3870
Si K	1.739	8.98	1.02	4.95	SiO2	19.21	9.39	23.0665
K K	3.312	0.50	0.16	0.10	K2O	0.60	0.38	1.6699
Ca K	3.690	0.03	0.15	0.01	CaO	0.04	0.02	0.0912
Fe K	6.398	2.18	0.59	0.60	FeO	2.80	1.15	5.8639
Total		100.00		100.00		100.00	13.98	

APPENDIX F-CORE PHOTOS

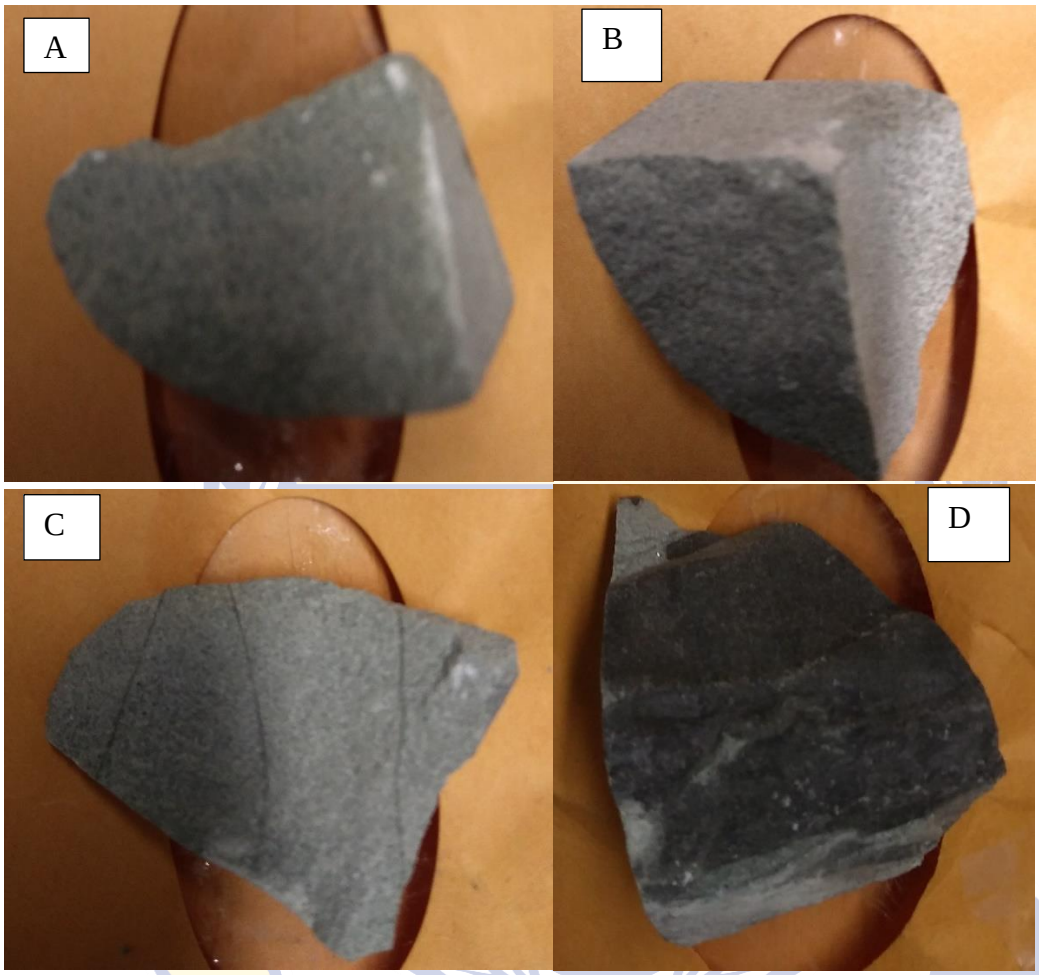

F1. E-M4 CORE PHOTOS (A=2569m, B=2572.14m, C=2575m, D=2577m).

F2. F-A13 CORE PHOTOS (A=2616.5m, B=2656.5m).

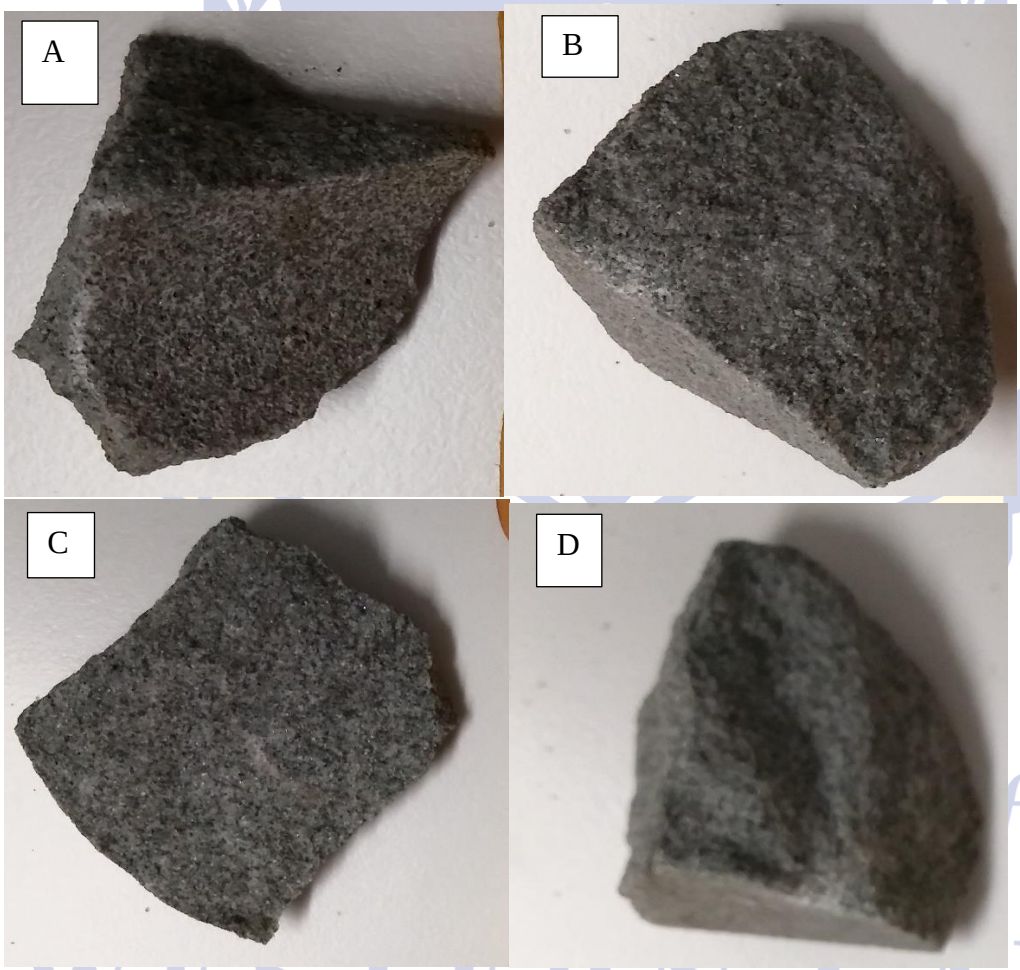

F3. F-A10 CORE PHOTOS (A=2720m, B=2731.5m, C=2742.5m, D=2744m)

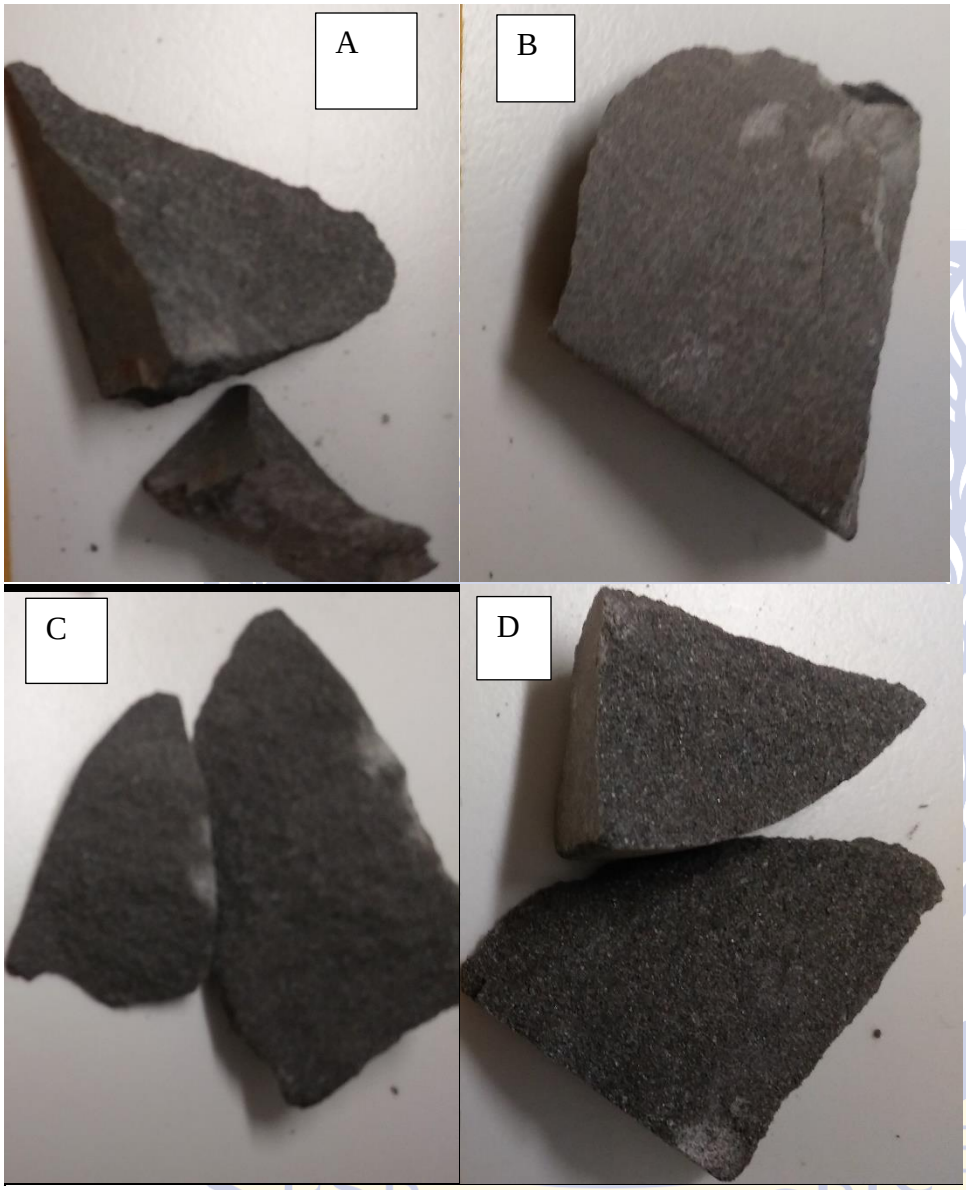

F4. E-G1 CORE PHOTOS (A=3160m, B=3162.5m, C=3166.5m, D=3165).

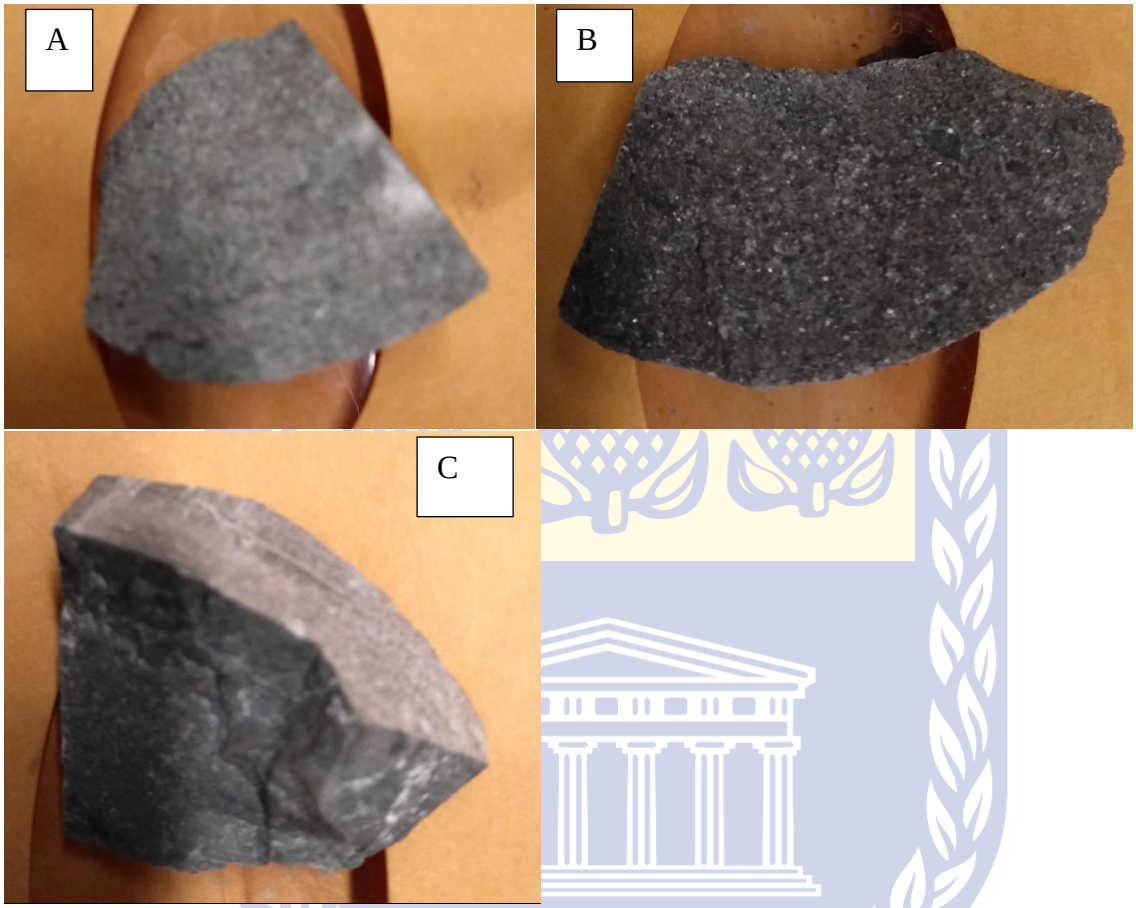

F5. E-W1 CORE PHOTOS (A=3173.5m, B=3186m, C=3188.1m)

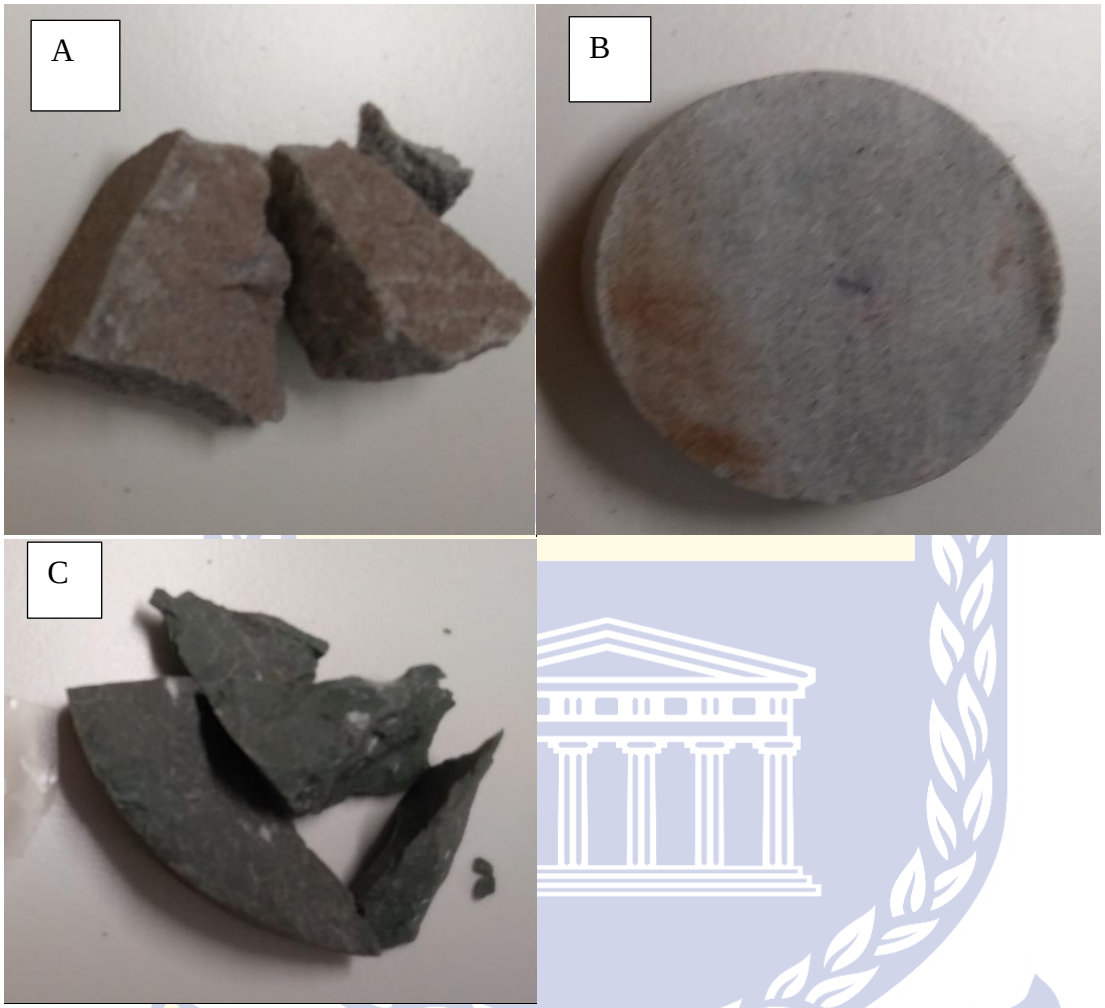

F6. E-CN1 CORE PHOTOS (A=4007m, B=4253m, C=4258m).

APPENDIX G- SHEAR VELOCITY QC